ProQuest LLC.
789 East Eisenhower Parkway
P.O. Box 1346
Ann Arbor, MI 48106 – 1346

NUMERICAL SIMULATION OF ELECTROHYDRODYNAMIC EFFECT ON SINGLE AND TWO-PHASE HEAT TRANSFER

HONGBO ZHANG

A thesis submitted in partial fulfilment of the
requirements of The Nottingham Trent University
for the degree of Doctor of Philosophy

This research programme was carried out in the
School of Computing and Technology,
Faculty of Construction, Computing and Technology,
The Nottingham Trent University,
Burton Street, Nottingham NG1 4BU, UK.

May 2004

NUMERICAL SIMULATION OF ELECTROHYDRODYNAMIC EFFECT ON SINGLE AND TWO-PHASE HEAT TRANSFER

By
Hongbo Zhang

ABSTRACT

The effects of an electric field on single- and two-phase heat transfer have been numerically investigated. The aim of this work is to establish analytical and mathematical models for the coupled electric, flow and thermal fields in single- and two-phase flows and to analyze the EHD effects on natural convection and nucleate boiling and provide numerical predictions of temperature, electric and velocity fields both in pure liquid and in the vicinity of single bubbles attached to a heat transfer surface under the application of electric fields.

Physical and mathematical models to describe the phenomenon of EHD effects on natural convection are proposed. A current in a dielectric field is physically modelled as a directed motion of electrically charged particles injected into a fluid. The Navier-Stokes equations, with an electric body force and the Joule heat are added to the momentum and energy equations respectively, are coupled with the electric field equations. The governing equations for the coupled electric, flow and thermal fields are discretized using Finite Volume Method (FVM) and solved using the SIMPLE method with a non-staggered grid arrangement. A modified momentum interpolation scheme is proposed to eliminate the defects of Rhie and Chow's interpolation scheme. The algorithm is developed into a FORTRAN code and is validated.

Natural convection enhanced by electric fields is widely investigated. This includes the natural convection in rectangular and cylindrical enclosures, enhanced by uniform and non-uniform electric fields respectively. The effects of the Rayleigh number and the fluid viscosity and electrical conductivity on the obtaining of good heat transfer enhancement are numerically investigated.

In order to understand the mechanism of EHD enhancement of heat transfer at the gas-liquid interface during nucleate boiling, a simplified physical model for a bubble attached to a heated wall is considered. Treatments at the gas-liquid interface and the triple-phase point are applied. Based on these, numerical study of EHD effect on heat and flows around a single R134a bubble attached to a superheated wall are carried out. Analysis is carried out for the flow and heat transfer at the vicinity of the gas-liquid interface when different electric voltages are applied. The bubble model is further employed to study the EHD effects on the fluids with different charge relaxation time. Four refrigerants, R134a, R123, R12 and R113, are studied and compared.

The numerical methods and the models for the coupled electric, flow and thermal fields are employed to carry out a preliminary study of the EHD effect on a growing bubble at different stages.

ACKNOWLEDGMENTS

The author would like to acknowledge Dr. Yuying Yan for the supervision and lots of encouragement during the research. Dr Yan initiated the project and obtained the Research Enhancement Fund; and he also supported my application for the ORS awards. These should be specially appreciated.

I would also very much like to acknowledge Professor Barry Hull for the guidance and encouragements during the research.

The author would also like to acknowledge the administrators and technicians from the School of Computer and Technology for their technical support, especially Mrs. Doreen Corlett and Mr. Gary Griffiths for their help during the three-year study.

Thanks should be given to my colleagues for their timely support and help. The author finally gratefully acknowledges the financial support from Research Enhancement Fund (REF) of the Nottingham Trent University and the Overseas Research Studentship (ORS) award from the CVCP.

PBLICATIONS ARISING FROM THIS WORK

1. Yan, Y.Y., Zhang, H. and Hull, J., "Numerical Modelling of Electrohydrodynamic (EHD) Effect on Natural Convection in an Enclosure", Accepted by *Numerical Heat Transfer, Part A (Applications).*
2. Zhang, H, Yan, Y.Y. and Hull, J., "Numerical Simulation of Electrohytrodynamics effects on a single bubble during nucleate boiling on a horizontal surface", *8th UK national heat transfer conference,* Oxford, 9th-10th September 2003.
3. Zhang, H. and Yan, Y. Y. "Numerical simulation of electrohydrodynamics effects on natural convection in vertical cylindrical encloses", *2003 international conference on energy and the environment*, May 22-24, Shanghai, China.
4. Zhang, H., Yan, Y. Y. and Hull, J., "A modified momentum interpolation scheme and its application in numerical modelling of natural convection in enclosed cavities," *7th UK national heat transfer conference,* Nottingham, 11th-12th September 2001
5. Zhang, H., Yan, Y. Y. and Hull, J., "Numerical Simulation of Electrohytrodynamics effect on a single bubble during nucleate boiling on a horizontal surface", submitted to *Numerical Heat Transfer, Part A (Applications).*

TABLE OF CONTENTS

	Page
Abstract	**i**
Acknowledgments	**ii**
Publications arising from this work	**iii**
Table of contents	**iv**
Lists of Tables	**ix**
Lists of Figures	**x**
Nomenclature	**xiv**
Chapter 1: Introduction	1
1.1 Nucleate boiling	1
1.2 Background	2
1.3 Starting Point of This Research	4
1.4 Aims and Objectives	5
1.5 Outline of the Work	6
Chapter 2: Literature Review	9
2.1 Introduction	9
2.2 EHD Enhancement of Convective Heat Transfer	11
2.2.1 Experimental study	11
2.2.2 Numerical Study	14
2.3 EHD effect on Two-Phase Heat Transfer	15
2.3.1 Experimental Study	16
2.3.2 Numerical Study	25

2.3.2.1 Mathematical models and boundary treatment for bubbles 26

2.3.2.2 Findings of numerical investigations 27

2.4 Numerical Methods for Natural Convection and Gas-Liquid Interfacial Flows 30

2.4.1 Numerical Algorithm for Natural Convection 30

2.4.2 Numerical Algorithm for Gas-Liquid Interfacial Flows 33

2.5 Summary 39

Chapter 3: Basic Equations for Electric, Flow and Thermal Fields 41

3.1 Introduction 41

3.2 Physical Model 42

3.3 Equations of Electric field 42

3.4 Basic Governing Equations 49

3.5 Normalisation of Governing Equations 52

3.6 Governing Equations in Body-Fitted Coordinate (BFC) System 54

3.7 Summary 61

Chapter 4: Numerical Methods for Solving Coupled Electric, Flow and Thermal Fields 62

4.1 Introduction 62

4.2 Grid Generation 63

4.2.1 Algebraic Method 63

4.2.2 Partial Differential Method 65

4.3 Discretization of Governing Equations 69

4.3.1 Discretization of Transport Equations 71

4.3.2 Discretization of Conservation of Charge Equation 74

4.3.3 Discretization of Electric Potential Equation 77

4.3.4 QUICK Scheme and Deferred Correction 79

4.4 Pressure Correction Technique 83

4.4.1 Non-Staggered Grid Arrangement 83

4.4.2 Pressure Correction Equation and Momentum Interpolation Scheme 85

4.4.2.1 Pressure Correction Equation 85

4.4.2.2 Modified Momentum Interpolation Scheme 90

4.4.3 SIMPLE Method 97

4.5 Code Validation 98

4.5.1 Roache Channel Flow 98

4.5.2 Natural Convection in an Annulus 100

4.5.3 Natural Convection in an Inclined Cavity 104

4.5.4 Natural Convection in a Squeezed Cavity 116

4.5.5 Laminar Flow through a Circular Pipe with Constriction 120

4.6 Summary 122

Chapter 5: Numerical Study of EHD effect on Natural Convection Heat Transfer 124

5.1 Introduction 124

5.2 EHD effect on Natural Convection in rectangular encloses 125

5.2.1 EHD effect at Different Rayleigh Number 126

5.2.2 EHD effect at Uniform or Non-Uniform Electric Fields 135

5.3 EHD effect on Natural Convection in a Cylindrical encloses 141

5.4 EHD effect on Different Working Fluids 148

5.5 Summary 161

Chapter 6: EHD effect on Heat and Flow around R134a Bubble during Nucleate Boiling 163

6.1 Introduction 163

6.2 Problem Statement and Assumptions 166

6.3 Mesh, Boundary Conditions and Interfacial Treatment 171

6.3.1 Non-Orthogonal Body-Fitted Mesh 171

6.3.2 Boundary Conditions 172

6.3.3 Interfacial Treatment 174

6.3.4 Temperature Singularity at Triple Point 176

6.4 Results and Analysis 177

6.5 Summary 186

Chapter 7: EHD effect on Refrigerants with Different Relaxation time 188

7.1 Introduction 188

7.2 Relaxation Time 188

7.3 Numerical Results 191

7.4 Summary 200

Chapter 8: EHD effect on Bubble Growth 201

8.1 Introduction 201

8.2 Assumption of Constant Angle 202

8.3 EHD effect on a Growing Bubble 206

8.4 Summary 213

Chapter 9: Conclusions and Recommendations for Further Work 214

9.1 Establishment of Physical and Mathematical Models 215

9.1.1 Physical Aspect of Coupled Electric, Flow and Thermal Field 215

9.1.2 Mathematical Descriptions of Coupled Electric, Flow and Thermal fields 216

9.1.3 Analysing Models for Heat and Flows in Vicinity of Gas-Liquid Interface around a Single Bubble 216

9.2 Numerical Methods and CFD Codes 217

9.2.1 Finite Volume Method (FVM) with QUICK schemes 217

9.2.2 Development of FORTRAN Codes 217

9.3 Numerical Results 218

9.3.1 EHD effect on Natural Convection 218

9.3.2 EHD Enhancement of Heat Transfer around a Single R134a Bubble 220

9.3.3 EHD effect on Refrigerants with Different Charge Relaxation Time 220

9.3.4 EHD effect on Different Stages of Bubble Growth 220

9.4 Recommendation for Further Work 221

References 224

Appendix A: Derivation of Electric Equation 239

Appendix B: List of FORTRAN Codes 241

LISTS OF TABLES

Tables

4.1 Comparison with benchmark solutions

4.2 Model Geometries

4.3 Comparison of the present results with experiments

5.1 Grid independent test

5.2. The comparison of mean Nusselt number at different Rayleigh number

5.3. The mean Nusselt number

5.4 Mean Nusselt number along the hot wall

5.5 Working fluid properties

5.6 Non-dimensional parameters

5.7 Comparison of the Nusselt Number of the three fluids at voltage of 5000v

5.8 Properties of the three fluids (2)

6.1 Physical properties of R134a at 20°C

6.2 dimensionless numbers

7.1 Electrical properties of refrigerants

7.2 Dimensionless parameters for flow and thermal fields

7.3 Dimensionless parameters for electric field at $\varphi = 5000v$

8.1 Nu_{av} increase at different contact angles

LISTS OF FIGURES

Figures

2-1 Electrode system applied to an inner tube

2-2 EHD effects on boiling process

2-3 Bubble behaviours in an electric field

3-1a Coulomb force

3-1b Dielectrophoretic force

3-2 Mapping an irregular simply-connected region into the computational domain as a rectangle

3-3 Mapping of a doubly-connected region in to a simply connected region by using a branch cut

4-1a Physical domain of a simple body fitted coordinate system

4-1b Computational domain of a simple body fitted coordinate system

4-2 The discretized geometry

4-3 Discrete checkerboard pressure distribution

4-4 Geometry of the Roache channel

4-5 Pressure distribution at wall (Re=100)

4-6 Vorticity distribution at wall (Re=100)

4-7 Computational domain and boundary conditions for annulus

4-8 Comparison of K_{eq} on annulus walls

4-9 Comparison of temperature

4-10 Comparison of circumferential velocity

4-11 Temperature contour and streamlines in the annulus

4-12 Geometry of inclined cavity

4-13a Temperature Isothermal at Ra=10^3

4-13b Temperature Isothermal at Ra=10^4

4-13c Temperature Isothermal at Ra=10^5

4-13d Temperature Isothermal at Ra=10^6

4-14a Streamlines at Ra=10^3

4-14b Streamlines at Ra=10^4

4-14c Streamlines at Ra=10^5

4-14d Streamlines at Ra=10^6

4-15 Local Nussult Number along the hot wall at different Rayleigh number

4-16 Convergent path of the inclined cavity at φ=30°

4-17 Comparison of *u*-velocity distribution at X/D=0.5

4-18a Thermal Contour distribution for Ra=10^6 at φ=19°

4-18b Thermal Contour distribution for Ra=10^6 at φ=20°

4-18c Thermal Contour distribution for Ra=10^6 at φ=30°

4-18d Thermal Contour distribution for Ra=10^6 at φ=40°

4-18e Thermal Contour distribution for Ra=10^6 at φ=60°

4-18f Thermal Contour distribution for Ra=10^6 at φ=80°

4-18g Thermal Contour distribution for Ra=10^6 at φ=90°

4-18h Thermal Contour distribution for Ra=10^6 at φ=120°

4-18i Thermal Contour distribution for Ra=10^6 at φ=140°

4-18j Thermal Contour distribution for Ra=10^6 at φ=160°

4-18k Thermal Contour distribution for Ra=10^6 at φ=180°

4-19a Streamlines distribution for Ra=10^6 at φ=19°

4-19b Streamlines distribution for Ra=10^6 at φ=20°

4-19c Streamlines distribution for Ra=10^6 at φ=30°

4-19d Streamlines distribution for Ra=10^6 at φ=40°

4-19e Streamlines distribution for Ra=10^6 at φ=60°

4-19f Streamlines distribution for Ra=10^6 at φ=80°

4-19g Streamlines distribution for Ra=10^6 at φ=90°

4-19h Streamlines distribution for Ra=10^6 at φ=120°

4-19i Streamlines distribution for Ra=10^6 at φ=140°

4-19j Streamlines distribution for Ra=10^6 at φ=160°

4-19k Streamlines distribution for Ra=10^6 at φ=180°

4-20 Local Nusselt number at some angles of inclination for Ra=10^6

4-21 A squeezed cavity

4-22 A mesh of the squeezed cavity

4.23-1a Benchmark (Demirdzic, 1992) of Predicted streamlines at Pr=0.1

4.23-1b Present work of Predicted streamlines at Pr=0.1

4.23-2a Benchmark (Demirdzic, 1992) of Predicted isotherms s at Pr=0.1

4.23-2b Present work of Predicted isotherms at Pr=0.1

4.24-1a Benchmark (Demirdzic, 1992) of Predicted streamlines at Pr=10

4.24-1b Present work of Predicted streamlines at Pr=10

4.24-2a Benchmark (Demirdzic, 1992) of Predicted isotherms s at Pr=10

4.24-2b Present work of Predicted isotherms at Pr=10

4-25 Geometric configuration of the pipe with a constriction

4-26 Flow pattern for Model M-3 at Re=40

5-1 The horizontal rectangular chamber (where a/b=3)

5-2.1a The temperature distribution without EHD effect at Ra = 3000

5-2.1b The temperature distribution with EHD effect at Ra = 3000

5-2.2a The streamlines without EHD effect at Ra = 3000

5-2.2b The streamlines with EHD effect at Ra = 3000

5-2.3 The local Nusselt number along the hot wall at Ra =3000

5-3.1a The temperature distribution without EHD effect at Ra = 4000

5-3.1b The temperature distribution with EHD effect at Ra = 4000

5-3.2a The streamlines without EHD effect at Ra = 4000

5-3.2b The streamlines with EHD effect at Ra = 4000

5-3.3 The local Nusselt number along the hot wall at Ra =4000

5-4.1a The temperature distribution without EHD effect at Ra = 5000

5-4.1b The temperature distribution with EHD effect at Ra = 5000

5-4.2a The streamlines without EHD effect at Ra = 5000

5-4.2b The streamlines with EHD effect at Ra = 5000

5-4.3 The local Nusselt number along the hot wall at Ra =5000

5-5 Force analysis (The Gravity isn't shown in this figure)

5-6 Comparison of mean Nusselt number for with and without EHD effect

5-7.1a The temperature distribution without EHD effect

5-7.1b The temperature distribution with EHD effect at uniform electric density injection

5-7.1c The temperature distribution with EHD effect at non-uniform electric density injection

5-7.2a The comparison of streamline without EHD effect

5-7.2b The comparison of streamline with EHD effect at uniform electric density injection

5-7.2c The comparison of streamline with EHD effect at non-uniform electric density injection

5-7.3 The comparison of local *Nu* along the bottom wall

5-7.4a Distribution of the electric density *q* at uniform electric density injection

5-7.4b Distribution of the electric density *q* at non-uniform electric density injection

5-8 The geometry of the cylindrical enclosure (b=3a)

5-9a Temperature distribution of natural convection in a cylindrical enclosure at *Ra*=3000

5-9b Streamlines of natural convection in a cylindrical enclosure at *Ra*=3000

5-10a Temperature distribution of natural convection in a cylindrical enclosure at *Ra*=4000

5-10b Streamlines of natural convection in a cylindrical enclosure at *Ra*=4000

5-11a Temperature distribution of natural convection in a cylindrical enclosure at *Ra*=6000

5-11b Streamlines of natural convection in a cylindrical enclosure at *Ra*=6000

5-12a Temperature distribution of natural convection in a cylindrical enclosure at *Ra*=10000

5-12b Streamlines of natural convection in a cylindrical enclosure at *Ra*=10000

5-13 Computer generated mesh

5-14a Comparison of thermal contours of Fluid Beta at φ=5000v

5-14b Comparison of streamlines of Fluid Beta at φ=5000v

5-14c Comparison of local Nusselt number along the hot wall of Fluid Beta at φ=5000v

5-15a Comparison of thermal contours of fluid ECO-C at φ=5000v

5-15b Comparison of streamlines of fluid ECO-C at φ=5000v

5-15c the comparison of local Nusselt number along the hot wall of fluid ECO-C

5-16a Comparison of thermal contours of fluid PAO at φ=5000v

5-16b Comparison of streamlines of fluid PAO at φ=5000v

5-16c Comparison of local Nusselt Number along the hot wall at φ=5000v(fluid PAO)

6-1 A vapour bubble attached to a heated wall

6-2a Body-fitted mesh for calculation

6-2b Illustration of mesh and boundaries

6-2c Grid treatments at triple point

6-3 convergence paths

6-4a Streamlines around the bubble at φ = 0

6-4b Streamlines around the bubble at φ =2000v

6-4c Streamlines around the bubble at φ =4000v

6-4d Streamlines around the bubble at φ =5000v

6-4e Streamlines around the bubble at φ =8000v

6-4f Streamlines around the bubble at φ =10000v

6-5a Contours of temperature around the bubble at φ = 0

6-5b Contours of temperature around the bubble at φ =2000v

6-5c Contours of temperature around the bubble at φ =4000v

6-5d Contours of temperature around the bubble at φ =5000v

6-5e Contours of temperature around the bubble at φ =8000v

6-5f Contours of temperature around the bubble at φ =10000v

6-6 Average value of Nusselt number

6-7 Local Nusselt number around the bubble they

6-8a Distribution of electric potential at φ = 2000V

6-8b Distribution of electric potential at φ = 10000V

6-9a Distribution of charge density at φ = 2000V

6-9b Distribution of charge density at φ = 10000V

7-1 Local Nusselt number along the bubble surface at $\varphi = 5000V$

7-2 Increase of average Nusselt Number at different voltages

7-3a The comparisons of thermal contours of R134a

7-3b The comparisons of thermal contours of R123

7-3c The comparisons of thermal contours of R113

7-3d The comparisons of thermal contours of R12

7-4a The comparisons of Streamlines of R134a

7-4b The comparisons of Streamlines of R123

7-4c The comparisons of Streamlines of R113

7-4d The comparisons of Streamlines of R12

8-1a Thermal contours at different contact angles at $\theta_c = 15^\circ$

8-1b Thermal contours at different contact angles at $\theta_c = 30^\circ$

8-1b Streamlines at different contact angles at $\theta_c = 60^\circ$

8-2a Streamlines at different contact angles at $\theta_c = 15^\circ$

8-2b Streamlines at different contact angles at $\theta_c = 30^\circ$

8-2b Streamlines at different contact angles at $\theta_c = 60^\circ$

8-3 Nu_{av} increase at different contact angles

8-4a Temperature distribution at different bubble growing stages $R = 0.5R_d$

8-4b Temperature distribution at different bubble growing stages $R = 0.6R_d$

8-4c Temperature distribution at different bubble growing stages $R = 0.75R_d$

8-4d Temperature distribution at different bubble growing stages $R = R_d$

8-5a Streamlines distribution at different bubble growing stages $R = 0.5R_d$

8-5b Streamlines distribution at different bubble growing stages $R = 0.6R_d$

8-5c Streamlines distribution at different bubble growing stages $R = 0.75R_d$

8-5d Streamlines distribution at different bubble growing stages $R = R_d$

8-6a Contours of the dimensionless electric potential at different bubble growing stages $R = 0.5R_d$

8-6b Contours of the dimensionless electric potential at different bubble growing stages $R = 0.6R_d$

8-6c Contours of the dimensionless electric potential at different bubble growing stages $R = 0.75R_d$

8-6d Contours of the dimensionless electric potential at different bubble growing stages $R = R_d$

8-7a Charge distributions at different bubble growing stages $R = 0.5R_d$

8-7b Charge distributions at different bubble growing stages $R = 0.6R_d$

8-7c Charge distributions at different bubble growing stages $R = 0.75R_d$

8-7d Charge distributions at different bubble growing stages $R = R_d$

8-8 Local Nusselt Number at the bubble surface

8-9 Increase of Nu_{av} at different bubble growth stages at $\varphi = 5000V$

NOMENCLATURE

Symbol	Meaning	SI unites
a'_P	coefficient of discretisation	-
a	acceleration	ms^{-2}
	thermal diffusivity	m^2s^{-1}
	coefficient in discretisation equation for variable ϕ	-
a'_{NB}	coefficients of discretisation	-
b	ionic mobility	$m^2s^{-1}V^{-1}$
B	numerical parameter	-
c_p	specific heat capacity	$kJkg^{-1}K^{-1}$
C	coefficient of pressure correction equation	-
D	charge diffusive conductivity	m^2s^{-1}
	diffusion flux	m^3s^{-1}
$\vec{E}, E, E_x, E_y, E^\xi, E^\eta$	electric field strength and its components	Vm^{-1}
E_2 , E_3	relative errors of calculation	-
E_C	Eckert number	-
f_1, f_2	geometrical interpolation factors	-
$\vec{F}_E$	Electric body force	N
F	convection flux	m^3s^{-1}
g	acceleration due to gravity	ms^{-2}
Gr	Grashof number	-
$\vec{J}$	electric current density	Am^{-2}
$\tilde{J}$	Jacobian determinant	
	dielectric constant	-
$\mathcal{J}$	convection-diffusion flux	m^3s^{-1}
k	iteration step	-
l	length scale	m

L	the gap of electrodes	m
$\dot{m}_P$	imbalance of mass source	m^3s^{-1}
N_E	electric field number	-
Nu	Nusselt Number	-
p	pressure	Pa
q	electric charge density	Cm^{-3}
$\dot{Q}$	heat source	J
r	radial coordinate in the cylindrical system	-
R_d	bubble departure radius	m
Re	Reynolds number	-
S, $\overline{S}$, $\overline{\overline{S}}$, S_1, S_2	source terms in general governing equations	-
$S(\phi)$	source term related to transport variable ϕ	-
S_E	Lorentz force number	-
T	temperature	K
u, v	Cartesian components velocity $\vec{V}$	m/ s
$\vec{V}$	Eulerian velocity	m/ s
W	diameter of electrodes	m
W_1, W_2	curvilinear component velocity	-
x, y	Cartesian coordinates	-
x	horizontal coordinate	m
x_r	separate point	m
y	vertical coordinate	m

Greek symbols

α	relaxing factor	-
	coordinates transform metric	-
α	coefficient of convective heat transfer	$Wm^{-2}[K]^{-1}$
α_ϕ , α_p	relaxation factors	-
β	coefficient of expansion	K^{-1}
	coordinates transform metric	-
γ	coordinates transform metric	-
Γ	diffusion coefficient of ϕ	-
ε	permittivity	Fm^{-1}
ξ, η	curvilinear coordinates	-
θ	circumferential angle	degree
θ_c	contact angle	degree
λ	heat conductivity	$W\ m^{-1}\ K^{-1}$
ν	viscosity	$kg\ m^{-1}s^{-1}$
	curvilinear coordinate	-
ρ	density	$kg\ m^{-3}$
σ	electric conductivity	$A\ m^{-1}\ V^{-1}$
	the coefficient of surface tension	$N\ m^{-1}$
ϕ	general variable	-
	volume fraction of fluid	-
φ	electric field potential	kV
	inclined angle of a square cavity	degree
γ	metric parameter	-
η	curvilinear coordinate	-
μ	dynamic viscosity	$kg\ m^{-1}\ s^{-1}$
ν	kinetic viscosity	$m^2\ s^{-1}$
ξ	curvilinear coordinate	-
κ	numerical parameter	-
Γ	diffusion coefficient	-

Δ	finite difference operator	-
∇	gradient (Hamilton) operator	-

Subscripts

0	reference value for normalisation
av	average value
c	cold wall
H	hot wall
max	maximum value
$\vec{n}$	pertain to normal direction
NB	neighbour points to node P, (*N, S, E, W*)
n, s, e, w	pertaining cell faces *n, s, e, w*
$\vec{t}$	pertain to tangential direction
ξ, η	derivatives respect to ξ and η respectively

Superscripts

ξ,η	pertaining to ξ and η, respectively
H	values from QUICK scheme
U	upwind scheme

Top Scripts

*	correction value
	intermediate iteration value
–	normalised variables (omitted after chapter 3)
→	vector
~	intermediate value

Dimensionless Parameters

$D_e = \frac{\mu_0}{\rho_0 D_0}$	Charge diffusivity number
$E_c = \frac{u_0^2}{c_p \Delta T}$	Eckert number
$Gr = \frac{\rho_0{}^2 g \beta \Delta T l_0{}^3}{\mu_0{}^2}$	Grashof number
$N_E = \frac{q_0 l_0^2}{\varepsilon \Delta \varphi_0}$	Electric field number
$Nu = \frac{\alpha \cdot l_0}{\lambda}$	Nusselt number
$\mathrm{Pr} = \frac{\mu_0 / \rho_0}{a}$	Prandtl number
$\mathrm{Pr}_E = \frac{\mu_0}{\rho_0 b_0 \Delta \varphi}$	Electric Prandtl number
$\mathrm{Re} = \frac{\rho_0 u_0 l_0}{\mu_0}$	Reynolds number
$S_E = \frac{q_0 \Delta \varphi}{\rho_0 u_0^2}$	Lorentz force number

Chapter 1

Introduction

This chapter gives an introduction to the research work of this thesis. An explanation to the background of the project and concise descriptions of the aims and the objectives of the research are also presented.

1.1 Nucleate boiling

Nucleate boiling is defined as a process, in which addition heat from a solid surface to a liquid in such a way that generation of bubble on the solid surface occurs at low superheat. The heat transfer associated with nucleate boiling process makes them highly advantageous in traditional refrigeration and power industries from a thermodynamic efficiency standpoint. Moreover, the high heat transfer rate has made nucleate boiling process even attractive in the thermal control of compact devices that have high heat dissipation rates. The applications of this include cooling electronic components in computer manufacturing industry and the use of compact evaporators for thermal control of aircraft and spacecraft environments. Nucleate boiling is also of critical importance to nuclear power plant design, chemical and petroleum.

The considerable economic importance of nucleate boiling process, along with its fashionably complex phenomena involved, has attracted the attention of the researchers from all relevant disciplines since more than a century ago. This process has all the complexity of single phase convective transport, plus additional elements resulting from the phase change, the motion of the interface, non-equilibrium effects, and dynamic interactions between the phases. Due to the highly complex nature of this process, development of methods to accurately predict the associated heat and mass transfer is often a formidable task.

1.2 Background

Since the use of an electric field to enhance convective heat transfer was firstly reported in the UK over eighty years ago, a number of significant works on Electrohydrodynamic (EHD) enhanced heat transfer and mass transport has been performed by researchers from all over the world. EHD effect on nucleate boiling have particularly drawn researchers' attention due to the potential applications for renewable sources (Yan, Karayiannis, Allen, Collins and Neve, 1996). Attractive experimental outcomes on EHD enhancement of nucleate boiling can be identified in a number of research papers; and these include the elimination of boiling hysteresis, the initiation of bubbles at low superheat and the enhancement of heat transfer at low superheat (Yan, 1996a; Yan, 1996b), and other compound effects of using EHD and passive methods (Neve and Yan 1996). However, the mechanism behind these attractive results has not yet been clearly explained. For example, the past theoretical studies of EHD effect on

nucleate boiling, which had mainly focused on derivation and analysis of the EHD body force in a dielectric system, show that EHD enhancement of two-phase heat transfer lies in additional body forces exerted by the electric field in the Navier-Stokes equations; however, the important work of implanting the electric body force to the Navier-Stokes equations and establishing the computational model for the EHD enhanced nucleate boiling and two-phase flow problems have not yet been done.

Furthermore, from experimental studies (Yan, 1996b), the mechanism of EHD enhancement of nucleate boiling on a heating surface was recently assumed to be due to EHD forces pressed the newly generated bubbles onto the heat transfer surface, instead of breaking away from it. In the meantime, bubbles around the heating surface will grow when the superheat is increased and tend to move up by the action of buoyancy. The EHD effect and buoyancy forces disintegrate bubbles into many smaller ones. As a result, the area of the thin liquid film under the bubbles increases, and the heat transfer rate is enhanced. To validate such an EHD mechanism experimentally, the UK Engineering and Physical Sciences Research Council (EPSRC) has invested a huge amount of money in Oxford during the last seven years. Nevertheless, the researchers at Oxford have recognised that, due to the limitation of experimental conditions, it would be difficult to explain the complex mechanism without combining with computing techniques to carry out numerical analysis (Kenning, 1999).

The research works carried out in this thesis are financially supported by an Overseas Research Scholarship (ORS) Award and a Research Enhancement Fund (REF) of The

Nottingham Trent University. The research will be entirely theoretical and numerical. The outcome will be significant for improving related industrial processes, such as refrigeration, air conditioning, industrial evaporators/condensers in thermal and power systems, and some gas-liquid related chemical reactors. These will also have a direct influence on process economics and optimisations.

1.3 Starting Point of This Research

The Heat and Fluid Flow Group at the Nottingham Trent University has been engaged in heat transfer enhancement and multi-phase flow for several years and has established a good base for the current research. Prior to the current study, two PhD research programmes relevant to numerical simulation of gas-liquid two-phase flows have been finished in this group. Based on these works, available supports for the current research are as follows:

1). Basic software package for development of computational codes. These include the Digital Visual FORTRAN software and the post-processing and flow-visualising package TECPLOT;

2). The FORTRAN code for generation of body-fitted staggered grids for simply-connected geometries (Li, Yan and Hull, 2003);

3). The FORTRAN codes for calculating of heat and fluid flows in rising single bubbles (Li and Yan, 2002; Yan, Lai, Gentle and Smith, 2002; Lai, Yan and Gentle, 2003).

With these supports, necessary contributions for the current study are:

1). Because of the shortcomings of the staggered grid system, to be analysed in chapters 2 and 4 later, this study will use a non-staggered grid system; FORTRAN codes generating such grids for the problems considered in this thesis need be developed;

2). The aforementioned codes for rising bubbles can only be used to calculate heat and fluid flows without EHD effect; special mathematical and computational models for describing the coupled thermal, flow and electric fields need be established and realised in codes;

3). In order to analyse the EHD effect and the relevant mechanism of heat transfer enhancement, the using of numerical methods with especially high resolution is a basic requirement. The resolution of codes in the research group have been improved by using second-order total variation diminishing (TVD) schemes (Yan, Lai, Gentle and Smith, 2002; Lai, Yan and Gentle, 2003); but the employment of Rhie and Chow's (1983) momentum interpolation scheme may introduce instability to the calculation and smearing to the resolution (Zhang, Yan and Hull, 2001). Modification to this scheme and further improvement of the numerical accuracy must be carried out in this thesis.

1.4 Aims and Objectives

Aims:

To complete an analysis of EHD effect on nucleate boiling and provide numerical predictions of temperature and velocity fields both in pure liquid and in the vicinity of single bubbles attached to a heat transfer surface under the application of electric fields.

Objectives:

1) To develop analytical and mathematical models for describing the EHD enhancement on heat transfer. These models should be formulated and coupled with the Navier-Stokes equations;
2) Based on the codes developed in the research group, to further modify and improve the numerical methods, and develop FORTRAN codes for the analytical and mathematical models so as to simulate EHD effect on single-phase and two-phase flows;
3) To numerically study the EHD effect on single phase flows in natural convection;
4) To enhance the numerical algorithm to make it capable of simulating the EHD effect on the heat and flows at the vicinity of a single bubble in nucleate boiling; and study the mechanism of EHD enhancement of heat transfer.

1.5 Outline of the Work

As stated earlier, this research is entirely theoretical and numerical. The main works are organised and presented in seven chapters after the current introductions.

In order to fully understand the work published on electrohydrodynamic enhancement on single and two phase heat transfer, chapter 2 gives a review of the literature. In this chapter, both the theoretical and experimental studies on EHD effect on heat transfer of single and two phase flow are reviewed and summarised. Special attentions have been

given to review the analytical models and numerical methods for studying natural convection and single bubbles because of the tasks of current research.

Physical and mathematical models for the coupled electric, flow and thermal fields are presented in chapter 3. The electric field, heat and fluid flows around the bubble are physically modelled. Based on the physical model, full Navier-Stokes equations for incompressible heat and fluid flows are coupled with the controlling equations for the electric field in terms of an electric body force and the Joule heat. The controlling equations are normalised and presented in a non-orthogonal body-fitted coordinates system.

Chapter 4 presents a complete numerical procedure to solve the coupled controlling equations for electric, flow and thermal fields. The transport and electric field equations are discreted using Finite Volume Method (FVM). The discretizatioin yields a large system of non-linear algebraic equations. The method of solution depends on the problem; therefore an appropriate method has to be chosen. In this work, the SIMPLE method with non-staggered grid arrangement is selected to solve the discretized equations. The algorithm is developed into a FORTRAN code and is validated.

The EHD effect on single phase heat transfer was studied in chapter 5. The EHD effect on natural convection in rectangular and cylindrical enclosures was numerically investigated. As revealed by experiments, the electrical properties of the working fluid have effects on the heat transfer rate once the electric field was applied; chapter 5 also

carried out a study of the EHD effect on working fluids which have different conductivities and viscosities.

It is clear that the heat transfer rate of nucleate boiling is determined by the characteristics of the bubbles that depart from the superheated surfaces. In order to understand the mechanism of EHD enhancement of heat transfer at the gas-liquid interface during nucleate boiling, simulations of EHD effect on heat and flows around a single bubble attached to a superheated wall during nucleate boiling of R134a are conducted in Chapter 6.

The charge relaxation time of fluids plays an important role in heat transfer enhancement by the meanings of an electric field. Four refrigerants, R134a, R123, R12 and R113 are chosen to study the effects of the charge relaxation time in chapter 7.

Bubble growth is a very importance of the heat transfer rate of nucleate boiling. The complex process involving coupling between mass, momentum and heat transfer between an expanding bubble and the surrounding fluid; it also involves the coupling of electric, flow and thermal fields when electric fields are applied. Chapter 8 simulate the EHD effect on a growing bubble at different stages. The studies also checked the assumption of the constant contact angle.

Finally, the conclusions of the research and recommendations for further work are given in chapter 9.

Chapter 2
Literature Review

2.1 Introduction

The heat transfer objectives can usually be stated by either

a). removing large rates of energy generated through small surface areas with moderate surface extended; or

b). reducing the size of a boiler for a given rating.

The desire to promote high heat fluxes has been the major driving force for the study of boiling heat transfer and the development of methods to enhance boiling heat transfer.

Nucleate boiling has long been recognized as a very effective mode of heat transfer. The early work of Jacob and Fritz (1931) demonstrated high heat fluxes could be obtained with pool boiling of water at low temperature differences, in effect, representing very high heat transfer coefficients. Thus it was established more then 70 years ago that nucleate boiling had the promise to satisfy the two main objectives noted above. Furthermore, the possibility of enhancing boiling performance was strong.

For many years, various techniques for heat transfer enhancement have been applied to practical heat exchangers. In general, heat transfer enhancement methods are categorized as "passive" or "active" (Bergles, 1987). The first category includes the high heat-treated, rough or extended surfaces, displaced enhancement devices, additives, etc. Porous surfaces with re-entrant cavities

are currently the most effective boiling heat transfer surfaces for commercial heat exchangers. The "active" category includes the methods such as *mechanical aids*, stirring or vibrating the fluid by mechanical means or by rotating the surface. Surface "scraping", which is widely used for batch processing of viscous liquids in the chemical process industry, is applied to the flow of such diverse fluids as high viscosity plastics and air. Equipment with rotating heat exchanger ducts is found in commercial practice. *Electric fields* are applied in many different ways to dielectric fluids. The effects of an electric field (AC or DC) on heat transfer are mainly to cause greater bulk mixing or fluid, or disruption of flow in the vicinity of the heat transfer surface and also the boiling process, which enhances heat transfer. Other active methods are *suction* or *injection* by suction or injecting the similar fluid through a porous heated surface. Injection is only used in single-phase flow.

Among the heat transfer enhancement methods, the application of an electric field is very attractive and has been studied extensively over the last 30 years because of its advantages:

1). rapid and smart control of enhancement by varying the applied electric field strength;

2). non-mechanical and simple in design;

3). suitable for special environments (space);

4). applicable to single and multi-phase flows;

5). minimal power consumption;

6). it is a more efficient technique at low degrees of superheat.

Furthermore, because of reduced gravity in space, the specific weights of liquid and vapour could become equal. In such an environment, the bubbles generated during boiling cannot be smoothly moved from the boiling surface, which can cause deterioration of heat transfer. Electric forces can be the ideal replacement for gravity in the space, which makes EHD more desirable than other techniques.

This chapter gives a brief review of the available research work on EHD enhancement of heat transfer, which includes single-phase flow (natural convection) and gas-liquid interfacial flow (boiling). The review is organised according to investigating methods applied such as experimental and numerical studies. As this study is entirely numerical and theoretical, attention will be mainly paid to numerical simulations. Further to these, because good and reliable physical and numerical models are the key issues when a computational fluid dynamic (CFD) method is used to study the heat transfer phenomena, this chapter will also review the numerical methods on natural convection and gas-liquid interfacial flows.

2.2 EHD Enhancement of Convective Heat Transfer

2.2.1 Experimental Study

The application of EHD effect was firstly seen in 1911 with colloidal separation and in the late 1920's with the deposition of insulating materials on metal electrodes. It is well known that when an impermeable solid surface interacts with the flow over it, a boundary layer will form over the surface; this exerts the main resistance to convective

heat transfer. The thicker boundary layer the lower the thermal conductivity of the working fluid, the lower heat transfer coefficient.

Using an electric field can induce secondary motions (Lacroix, Atten and Hopfinger, 1975; Worraker and Richardson, 1979; Shu and Lai, 1995; Darabi, Ohadi and Desiatoun, 2000) and increase flow velocities; these have been considered the main reason for the augmentation on heat transfer rate for single phase flow. Probably the earliest demonstration of these phenomena applied to a heat transfer situation was those of Senftlenben (1931, 1932, and 1934) and Senftlenbenand & Braun (1936). In their studies, the influence of an externally applied radial electrostatic field on free convection from heated wire was examined, and increases in heat transport of 50% were reported with gases including air and oxygen. Arajs and Legrold (1958) reported large improvements with gaseous N_2, CO_2, NH_3, SO_2 and CCI_3F using a similar radial field configuration. Field strengths up to 10^5 volts/cm were applied resulting in forty-fold increases in heat transfer with SO_2.

Other earlier experiments on convection were reported in 1949 by Kroning and Ahsman (1949), when both *dc* and 40-Hz voltages were employed. With *dc* voltages, polarity dependent effects were observed which they attributed to electrolysis. The alternating voltage eliminated the observed electrolytic gas evolution. Kroning and Ahsman (1949) extended their work to other liquids and developed a Nusselt correlation.

These initial experiments soon drew more attentions. Weber and Halsey (1953)

demonstrated experimentally that electric field disrupted laminar thermal boundary and produced turbulence. In a brief theoretical treatment, they noted three types of forces and pointed out the conservation nature of electrostriction. The work on electric field-coupled thermal convection was reported about the same time in Germany by Schmidt and Leidenfrost (1953), who used an elaborate arrangement of two concentric electrode cylinders and measured the effective thermal conductivity of the liquid in an annular region as a function of the voltage. The principal conclusion, based on visual observation, was that electro-convection was the cause of the increased heat transfer, rather than changes in the thermal conductivity caused by dipole alignment. An electrically induced convection experiment was carried out in 1966 (Gross and Porter, 1966), which showed the convection patterns under non-uniform electric field were similar to the familiar "Bénard" cells in normal natural convection.

Martin and Richardson (1984) experimentally demonstrated that a *dc* voltage applied across a thermally stabilized plane layer of dielectric field could induce both stationary and oscillatory instabilities, and thereby significantly augmented heat transfer. Electro-convection seems an attractive tool for enhancing convective heat transfer, particularly in a low Reynolds number flow of a weakly conducting liquid through a narrow space, where the application of any conventional passive enhancement methods is neither easy nor effective.

Fujino, Yokoyama and Mori (1989) experimentally examined the effect of a uniform electric field on laminar force-convective heat transfer, which showed the degree of

enhancement might be significantly extended by appreciably adjusting the conductivity of the liquid.

2.2.2 Numerical Study

A numerical prediction of the EHD effect on laminar mixed convection in a vertical channel was reported by Wang, Collins and Allen (1990). The numerical results showed that in convective heat transfer, the non-uniformity of the temperature field produces the non-uniformity of the dielectric permittivity. The electrically induced secondary flow was rather weak.

Another paper about the EHD enhancement on laminar heat transfer was reported by Dulikravich and Ahuja (1993), which treated the Coulomb force as the electric body force for a single-specie eletrorheological fluid and took the effects of Joule heat into account. The numerical investigations showed that EHD was a significant alteration of the flow field and consequently it redistributed surface convective heat fluxes. When viscosity was treated as a constant, the predicted increase of the convective heat transfer rate due to EHD phenomena was between 12% and 64% for the cases studied. The importance of accounting for increased viscosity of the electrorheolohical fluid due to the chaining effect of the electrically charged particles was been clearly demonstrated.

Numerical simulations of EHD-enhanced heat transfer for laminar natural convection in an enclosure with differentially heated vertical walls was also reported by Shu and Lai

(1995). Attention was also focused on the effect of added electric field on the flow stability. The electrical field was generated by positive corona from a wire electrode located at the centre of the enclosure and charged with a high *dc* voltage (10 ~17.5 kV). The thermal buoyancy effects considered were in the range of $Ra = 10^3 \sim 10^6$. For a given Rayleigh number, the flow and temperature fields changed from a steady state to periodic and non-periodic convection as the applied voltage increases. It was found that heat transfer enhancement increased with the applied voltage but decreased with the Rayleigh number. Due to the existence of secondary flows, there was an improvement in heat transfer, which was the most significant for flows at a small Rayleigh number. In their work, the charge convection is neglected and the EHD and fluid dynamic equations was decoupled.

EHD-enhanced forced convection in a horizontal channel was studied by Huang and Lai (2003) using stream-function/vorticity method. The difference of the results obtained using one-way and two-way coupling is insignificant, therefore it is concluded that one-way coupling assumption is valid for the convection heat transfer problems. The results show heat transfer rate can be as high as 350% and also the existence of oscillatory flows, which is considered the main reason for the high heat transfer enhancement.

2.3 EHD effect on Two-Phase Heat Transfer

Nucleate boiling is a vapour-liquid phase changing procedure associated with bubble

formation. As it is a very efficient mode of heat transfer, the boiling process has been studied extensively during the last century.

2.3.1 Experimental Study

In the last 30 years the great potential of EHD in enhancing two-phase heat transfer rates has been realised by more and more industrial and academic researchers. The research of EHD enhanced nucleate boiling heat transfer appeared in 1960s and 1970s, which focused on the influence of electric field on the critical heat flux and on film boiling from electro-resistance-heated wires. One of the quantitative studies on EHD enhancement of nucleate boiling was carried out by Bochirol et al. (1960), which was

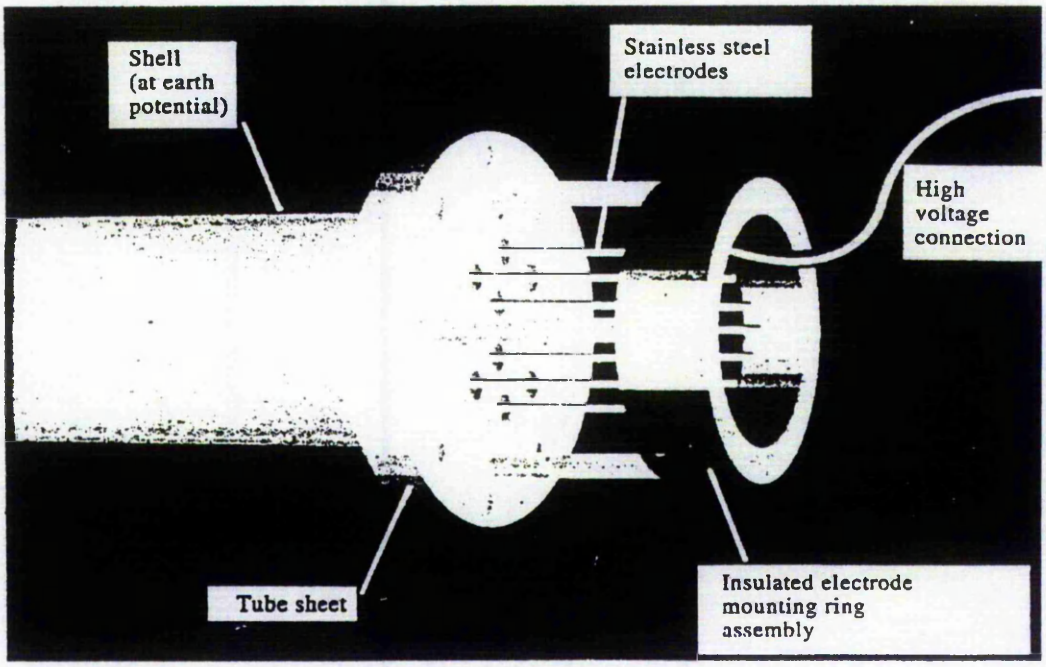

Figure 2-1 Electrode system applied to an inner tube

concerned with the dramatic EHD enhancement of the film boiling regime and a consequent increase in the critical heat flux. Theoretical analysis was also applied to help explaining the phenomena of EHD enhanced heat transfer.

Since 1980s the study of EHD enhanced nucleate boiling has been carried out with more emphasis on the industrial applications (Yabe and Maki, 1988; Ogata and Yabi ,1991, 1993a, 1993b; Kawahira, Kubo, Yokoyama and Ogata, 1990; Karayiannis et al. 1993; Salehi, Ohadi and Dessiatoun, 1997; Darabi, Ohadi and Dessiatoun, 1998; Yan and Neve, 1996; 1997; Yan, 2000). Figure 2-1 shows an electrode system designed and used to apply an electric field at the inner surface of tubes by Poulter and Allen (1986).

EHD effect on bubble dynamics

Applying an electric field can strongly affect the boiling process. The major effects of an electric field on boiling are considered to include the shift of the boiling curve; eliminate boiling hysteresis; the delay of ONB (Onset of Nucleate Boiling) and CHF (Critical Heat Flux) to a higher heat flux; and more importantly the electric field can strongly enhance heat transfer rate by influencing bubble behaviour such as the faster bubble frequency, reduced bubble size, bubble deformation, and also by disturbing the thermal layer on the heated surface.

Figure 2-2 shows a typical boiling characteristic curve (Seyed-Yagoobi and Bryan,

1995) in terms of thermal flux per unit area q'', versus superheat ΔT_{sat}. A-E is the EHD enhanced boiling curve, the boiling hypsteresis is eliminated; and the CHF is increased as well as the onset of nucleation is delayed.

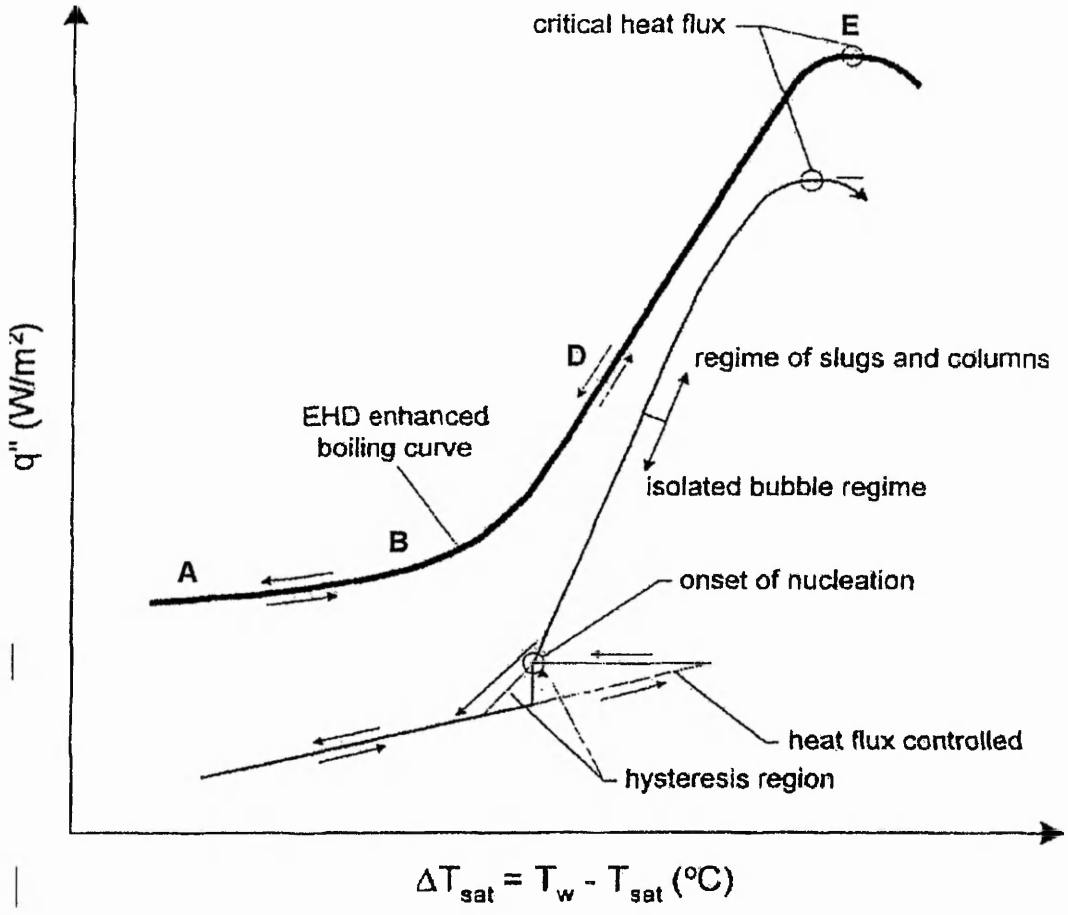

Figure 2-2 EHD effect on boiling process

DiMarco and Grassi (1993) gave a good review of the effect of an imposed electric field on regime transitions in boiling heat transfer. The major effects of EHD were proven to

be exerted on CHF and MFB (minimum film boiling); film and transition boiling may even disappear.

Cooper (1990) experimentally studied the EHD enhancement of nucleate boiling of R114. The results show that boiling hysteresis is completely eliminated through the electrical activation of nucleation sites on the heat transfer surface following a brief application of a modest electric field; the augmentation of heat transfer coefficients is up to an order of magnitude.

Seyed-Yagoobi, Geppert and Gerppert (1996) studied the EHD enhanced heat transfer in pool boiling of R123. They found that the average of convective heat transfer at a voltage of 10kV was about 4.6 times higher than without an electric field; and with the increase of the applying voltage, the onset of boiling came later; by contrast to all references, which implied that the higher voltage, the higher the enhancement of heat transfer coefficient, the best results were achieved at 5 to 10 kV range. They suggested two reasons. First, below 5kv, the turbulence generated due to the electrostriction force in small. Second, at high voltages (above 10kV), the dielectrophoretic forces are large, pushing the bubbles away from the electrodes. This effectively results in restricting the path available for the bubbles to depart.

Kweon and Kim (2000) gave thorough experimental results on the EHD effect on nucleate boiling and bubble dynamic behaviour in saturated pool boiling using a non-uniform DC electric field. The results showed the shift of the boiling curve, including

the increase of critical heat flux, the delay of onset of nucleate boiling, and the suppression of the hysteresis phenomenon. Significantly changes of boiling parameters (including the nucleation site, bubble frequency, bubble velocity and departure size) in the presence of a non-uniform electric field were also observed using a high speed camera. It was confirmed that the mechanism of EHD nucleate boiling was closely connected with the dynamic behaviour of bubbles. Also at a very high voltage, the amount of latent heat transported bubbles nearly corresponds to the total heat flux and only a small amount of the heat was transported by convection.

Zagpdoudi and Lallemand (2001) experimentally studied the influence of a DC uniform electric field on nucleate boiling heat transfer. They found that for an applied voltage below 10kV, the vapour bubbles were not much influenced by the electric field and the boiling phenomenon was similar to that observed without the electric field. When the voltage exceeds 20kV, the bubbles became smaller, the departure frequency increased and the bubbles had a very rectilinear path.

Iacona, Herman and Chang (2002) recorded the bubble detachment with different electric field magnitude ranging from 0kV to 10kV using high speed camera. They found that the bubble is increasingly elongated in the direction parallel to the applied field and the bubble axis is vertical. As a result of bubble shape changes, the aspect ratio and the contact angle increase by 27% and 32%, respectively; and the bubble volume at detachment is also affected by the presence of an electric field and it decreases by 51%.

The period of bubble formation t_d (the time between bubble apparition and its detachment) decreases 50%.

Electrode geometry and non-uniform electric field effects

Markels and Durfee (1964, 1965) studied enhanced boiling heat transfer in semi-insulating liquids with DC and AC voltages up to 10kV. The increments of CHF up to five times were measured with applied DC voltages up to 8kV. DC fields were found more effective than AC ones, and the field frequency was reported to have a very low effect in the range of 50-5000HZ.

Kweon, Kim, Cho and Kang (1998) examined the nouniformity effects of electric fields on bubble deformation and departure by using three types of electrode systems. For a DC electric field, as the applied voltage increases the bubble attached to a wall is more extended in the direction parallel to the imposed electric field, thus the aspect ratio and contact angle also increase. The bubble departure volume in a nonuniform electric field decreases continuously, while that in a uniform electric field is nearly constant. Their results show that bubble behaviour is significantly affected by the inhomogeneity of the electrode configuration. For an AC electric field, that bubble departure occurs near a resonant frequency.

Karayiannis and Xu (1998b) focused on the effects of electrode geometry. They suggested novel electrode geometry for single tube and tube bundles. The geometry can

produce a resultant force tangential to the tube surface on most of the bubbles on the boiling surface. The tangential force can have sliding boiling effects, which is regarded as a dominant mechanism for tube exchangers. They also verified the designed geometry using a shell-and-tube heat exchanger of R123. The EHD enhancement of R123 boiling heat transfer was significant.

More recently, Kweon & Kim (2000) focused on the effects of non-uniform electric field on nucleate boiling. Their results also showed that the EHD effect are more remarkable when the electric field is strong and non-uniform. Due to the increased liquid motion, the onset of nucleation is delayed when the EHD forces are applied. The increased liquid motion re-supplies the heated surface with cooler surrounding liquid, thus condensing bubbles as they are formed and lowering the wall superheat. They also found out that at the lower part of the heated wire, as the increase of the electric strength, the bubbles are pulled off from the heated wire towards the region of weaker electric field. The direction of the electric force acting on bubbles is the electric field line.

Zagpdoudi and Lallemand (2001) also found that the tangential component force is the Coulomb stress generated by the electric field on the liquid-vapour surface. It induces liquid movements around the bubble and vapour movements within the bubble. And it is not dependent on the electric field polarity. The factor determining the bubble shape is the product of the permittivities and resistivities ratio of the bubble and liquid.

Relaxation time and Fluid properties effects

In nucleate boiling, the charge relaxation time plays an important role during bubble growth and departure in an electric field. When fluid is placed in an electric field, electric charge is generated. It takes a certain time for the influence of the electric field to take place. This time is called the relaxation time of the electric charge and it is related to the electrical properties of the fluid (it is defined as the ratio of electric permittivity and electric conductivity of the fluid: $\tau = \varepsilon/\sigma$).

The studies by Ogata and Yabi (1993a, 1993b) and Ohadi (1991) focused on the charge relaxation time effects on nucleate boiling by EHD. For pure R11 the charge relaxation time is about 1.3s, while the characteristic time of the boiling fluid (the generation frequency of boiling bubbles of R11) is about 2×10^{-2} s, which means that the generated bubbles float to the free surface without being effected by the electric field. When ethanol is added to the dielectric R11 (with only several percents of the total weight), the relaxation time decreases and it becomes much smaller than the bubble frequency. As a result, the enhancement of boiling heat transfer was about 8.5 times higher than the case for a pure R11. Figure 2-3 shows the results of augmentation of heat transfer for air bubble and R11. They also found that if the charge relaxation time is far greater than the bubble detachment period, the bubbles are not affected by the electric field.

The influence of fluid properties on EHD enhancement heat transfer behaviour has been experimentally investigated by Oh and Kwak (1996) and Paschkewitz and Pratt (2000). The experimental results show that for a given Reynolds number forced flow and

electrical power input the fluid with a larger charge relaxation time will yield greater heat transfer enhancement. The experiments also show that decreasing viscosity reduces both the electrical and pressure drop penalty for a desired heat transfer enhancement via secondary flow. Using a low viscosity, high charge relaxation time working fluid with low Reynolds number forced flow gives optimal performance and an early onset of significant EHD enhancement.

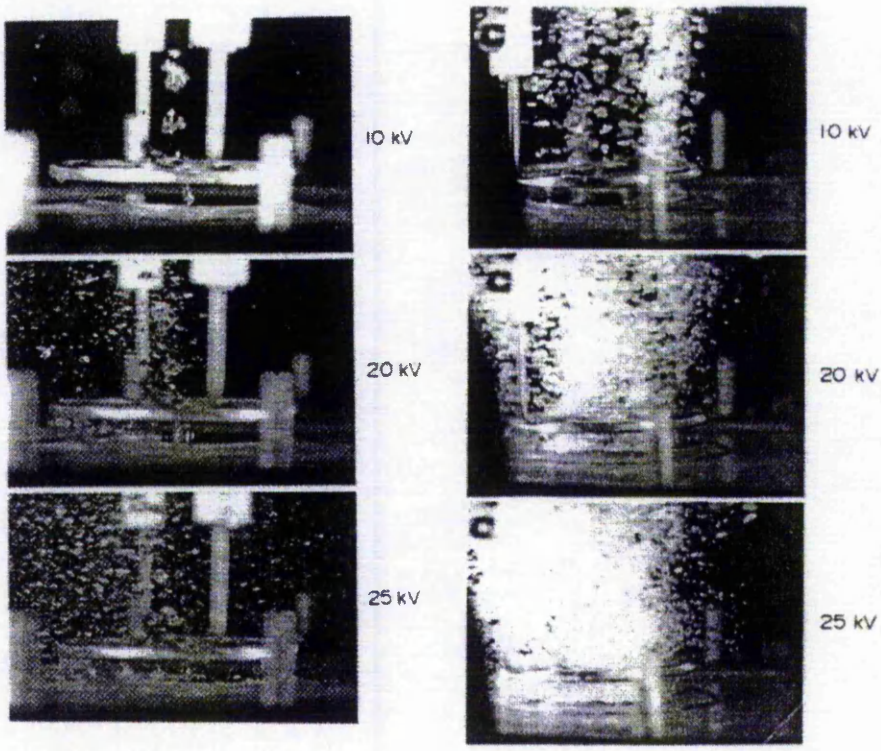

(a) Air bubble behaviour (b) Boiling behaviour of R11/ethanol mixture

Figure 2-3 Bubble behaviours in an electric field

Zagpdoudi and Lallemand (2001) also studied the influence of fluid properties. R113, R123 and n-pentane were chosen as working fluids. The results showed 17% and 23%

of increase of CHF for n-pentane and R113, respectively. However, for R123 a threefold increase was reached. The charge relaxation time for R123 is only about 1.76×10^{-3} s, for R113 it is about 2.12s.

As far as EHD bubble dynamics is concerned, only limited papers can be identified, in which bubble departure diameter or volume are normally derived and discussed. Typically, such analysis is only on the basis of the assumption of one-dimensional spherical bubble. Although there are a few recently published papers which deal with numerical analysis of electric field distribution around a bubble by solving Laplace's or Poisson's equations in conjunction with relevant boundary conditions (Ogata and Yabe, 1993a, b; Yan, 1996b and Karayiannis, 1998), the significant effects of the established fields on bubble-liquid interface have not yet been taken into account. In fact, based on experimental observations, it has been suggested that the mutual interaction between a dielectric liquid and an imposed electric field leads to a change in the bubble dynamics, in particular, near or on the heating surface; which is believed to be one of the major reasons why nucleate boiling can be significantly enhanced by applying the EHD. All these works contribute to possible industrial applications in the future.

2.3.2 Numerical Study

Due to the complicated interactions among the electric, flow and temperature fields, studies on two-phase heat transfer enhancement by electric fields are mostly accomplished by experiments. Numerical solutions are possible but usually subject to

some simplifications of the heat transfer phenomena by EHD. So far only a few of numerical studies have been published; these studies were focused on the mathematical model of calculating the electric field when bubbles appeared in the flow field.

2.3.2.1 Mathematical models and boundary treatment for bubbles

Ogata and Yabe (1991) and (1993a) reported an attempt to simulate a single bubble in an originally uniform electric field. They used the Laplacian equation to simulate the electric field profile; the bubble surface was defined as a part of the boundary and assumed that the electric strength E in the direction normal to the bubble surface to equal zero. Yan et al. (1996) made the same assumption in calculating the electric field distribution. The shortcoming of these studies is that the electric field inside the bubble is neglected, and the assumption of zero-electric-strength normal to the bubble surface is possibly untrue in reality.

The study of electric field with the presence of multiple bubbles was firstly reported by Karayiannis and Xu (1998). In their work, the bubbles were included as a part of the domain of interest; and the electric field at the bubble surface was decided by the actual calculations. And also the domain of interest is inhomogenous, the properties, such as the electric conductivity and permittivity, are functions of the temperature. The bubble surface is characterised by the significantly different permittivity on both sides. The electric force acting on bubbles was evaluated by surface integration of the electric stress over the bubble surface. This method was also applied to an EHD shell-and-tube

heat exchanger to predict the electric field and force field distribution. The effect of departed bubbles was also taken into account. The mathematical model established by Karayiannis and Xu (1998) is simple and easy to be applied to calculate the EHD effect on heat transfer enhancement; and more importantly, a group of bubbles can be considered in the same time without assumption on the electric strength at the bubble surface. However, the thickness of a bubble surface is physically zero and therefore there is a sharp jump of permittivity across the bubble surface; this impose a difficulty in numerical calculation when differential operations, such as the Laplacian and divergent operators, are applied to calculate the charge density. Moreover, the advection of electric charges by the flow is neglected and therefore the interaction between the electric and flow fields can not be included in this model; because the flow field will not be calculated in this model, the physical coupling of the flow and electric fields which is possibly be very strong (Takata, Shirakawa, Tanaka, Kuroki and Ito, 1996), is decoupled.

2.3.2.2 Findings of numerical investigations

Cheng and Chaddock (1985) theoretically studied the effects of an electric field on bubble growth rate using a heat diffusion controlled growth model, which assumed that the temperature field around the bubble was uniform and the bubble grows as a result of evaporation at the liquid vapour interface. The analyses showed that by elongating the bubbles, an electric field reduced the area of contact between the bubbles and the heated surface. This reduced the surface tension force which held the bubble to the heating

surface, and resulted in smaller bubble departure size. Cheng and Chaddock (1985) suggested that the smaller departure size and faster growth rate were two mechanisms by which a uniform electric field enhanced the nucleate boiling heat flux of a liquid.

Takata, Shirakawa, Tanaka, Kuroki and Ito (1996) carried out a numerical analysis on bubble growth and deformation under an electric field in order to elucidate the mechanisms of boiling heat transfer enhancement by EHD means. Transient Navier-Stokes and Maxwell's equations were solved simultaneously for liquid and vapour phases in a two-dimensional cylindrical co-ordinate system using VOF (Volume of Fluid) method. Bubble growth in liquid R113 under atmospheric pressure has been simulated. In their study, elongation of a single bubble under uniform electric field was simulated and the final shapes of the bubble were found to be in good agreement with Garton's analytical and experimental results. Further to this, the bubble deformation process under non-uniform electric field was simulated. A bubble initially attached to the lower electrode was observed to deform and finally detaches from the lower electrode. This study unveiled that the shape of bubbles depends on the intensity of the electric field. The behaviour of bubbles, the velocity vectors, and the contours of electric field were also shown and compared with experimental data. However, the temperature field was not studied in this paper; therefore the effects of temperature and Joule heat were not included.

A numerical study using a finite element method on bubbles behaviour and boiling heat transfer under the electric field was given by Oh and Kwak (1996). In their study, there

was no free charge and the electric permittivity of medium was a constant in the domain considered. Numerical study in this paper revealed that the bubbles were forced away from the heating surface, then toward the electrostatic stagnation point by the dielectrophoretic force. Such modified bubble motion turns out to promote the boiling heat transfer if an appropriate electrode configuration is used.

Cho, Kang, Kweon and Kim (1996) numerically and experimentally studied the behaviour of a bubble attached to a wall in a uniform electric field; they found that the bubble was elongated in the direction parallel to the applied electric field, the elongation increases with the strength increase of the electric field. The results were obtained by employing the finite-difference method in an orthogonal curvilinear coordinate system. The steady bubble shape was given under fixed contact radius condition as part of the solution of the free boundary problem. The bubble shape was determined by the normal stress condition. Since the temperature and flow fields were not given in this paper, it is hard to know how the bubble shape was determined in detail.

Karayiannis and Xu (1998a) used their aforementioned mathematical model to account for the presence of multiple bubbles, the thermal boundary layer and the generated free charges. The electric field distribution, the electric body force and according the resultant force acting on the bubbles were calculated for a shell and tube exchanger. The effect of different electrode geometries on boiling heat transfer was also presented in this paper.

2.4 Numerical Methods for Natural Convection and Gas-Liquid Interfacial Flows

As mentioned above, the main aim of this investigation is to study the EHD effect on single-phase convection (natural convection) and gas-liquid interfacial flows (boiling), so the numerical methods for simulation of both natural convection and gas-liquid interfacial flows are reviewed here.

2.4.1 Numerical Algorithm for Natural Convection

Natural convection is generally at low speed of fluid flow and is described by the coupled Navier-Stokes and energy equations. For the coupled Navier-Stokes equations system, the numerical methods can be categorized as "primitive-variable" methods and "non-primitive-variable" methods.

The vorticity/ stream-function method and vorticity/ velocity method (which originated from the vorticity/ stream-function method) are the most popular methods in the "non-primitive-variable" methods category and they are widely used to solve two-dimensional flow heat transfer problems. In a vorticity/ stream-function method, the vorticity is the primary variable, and its boundary value is provided by the stream-function. The advantage of this method is that the pressure is eliminated by taking cross differentiation for the momentum equations in the two coordinate directions and subtracting each other; these lead to the transport equation of vorticity. Therefore, the issues related to the coupling of pressure and velocity are avoided in the numerical

calculation. However, the vorticity/ stream-function method has its disadvantage: it cannot easily be extended to three-dimensional situations because of the non-existence of a three-dimensional stream-function. A possible remedy for this problem is the introduction of vectored potential function (Raul, 1990), or the three-dimensional stream-like function (Hamed and Abdanah, 1983). These strategies actually cannot reduce the complexity because four dependent variables are involved in a three-dimensional incompressible flow problem. Thus, the complexity is just the same with dealing with the three velocities component and pressure directly. Comparing with the vorticity/ stream-function method, a vorticity/ velocity method also does not need to calculate the pressure, and no introduction of stream-functions for a three-dimensional problem. The disadvantage of this method is that the boundary values for the vorticity are difficult to pose.

"Primitive-variable" methods can be classified as the density-based methods and pressure-based methods. The representatives for these two categories are the time-marching methods and the pressure correction methods (such as the SIMPLE method). Density-based methods are very successful in simulation of compressible flows at high Mach numbers; but for flows at low Mach value, these methods become incapable because the density is weakly coupled with the velocity and temperature at this time. On the other hand, because the pressure is decided by the equations of state and continuity, the small change of the density in an incompressible flow will result in an inaccurate change of the pressure, therefore the pressure field obtained using this method is not correct. For incompressible flows, the pressure and density will not be present in the

continuity equation, and the equations of gas state and the continuity are completely decoupled. In the meanwhile it is also difficult to couple the velocity with pressure because the continuity is only a constraint for velocity this time. Because of these reasons, the density-based methods are seldom used to solve incompressible flows.

In the family of the pressure-based methods, the SIMPLE method, which is the abbreviation for Semi-Implicit Method for Pressure-Linked Equations, has become a mature and successful method for incompressible flows and heat transfer since it was proposed by Patankar and Spalding (1972). Due to the development of the computer power, the SIMPLE method has undergone from fully parabolic forms, partially parabolic forms to elliptic forms. Nowadays, the computer resources are not restrictive and therefore, the SIMPLE method has become a very popular method to simulate incompressible heat and fluid flows.

To couple the pressure and velocity is a key issue in the SIMPLE method. Using of central differences scheme for discretisation of the pressure gradient in the momentum equation will result in a non-physical wavy pressure field (also called checkerboard pressure distribution); and once such a wavy pressure is generated, it will never be corrected since the pressure at the adjacent grid points are not related to each other (Patankar and Spalding, 1972). The staggered grid arrangement was a remedy for the wavy pressure field problem. However, the three sets of grids are needed for two-dimensional problems; and for a three-dimensional problem, the sets of grids are even four. The using of this multi-set of grid mesh is not a welcome issue for CFD coding

because of the storage and the geometrical interpolation. In the meanwhile, when the grids are highly non-orthogonal, the staggered grid arrangement is also possible to result in a wavy pressure field (Rhie and Chow, 1983).

The non-staggered grid arrangement with a momentum interpolation technique was proposed by Rhie and Chow (1983). Corresponding to its name, the non-staggered grid arrangement only use one set of grids in the calculation procedure. Compared with the staggered grid, the non-staggered grid method has the following advantages (Peric et al, 1988):

(i) all variables share the same location; hence, only one set of grids is needed;

(ii) in a discretised equation, the convection contribution to the coefficients is the same for all variables;

(iii) for a complex geometry, Cartesian velocity components can be used in conjunction with non-orthogonal coordinates, yielding simpler equations than when numerical coordinate-oriented velocity components are employed.

The non-staggered method has been widely employed in the past 20 years because of its conciseness and is relatively straightforward to implement. But there are also some flaws in this method, such as the accuracy of the simulation depends on the relaxation factors, which are chosen manually, and the extent of the non-linearity ness of the pressure field (Lai, Zhang and Wu, 1996).

2.4.2 Numerical Algorithm for Gas-Liquid Interfacial Flows

From the view point of CFD, a gas-liquid interface is a moving boundary problem, which is one of the most challenging problems to researchers (Shyy, Udaykumar, Rao and Smith, 1996). The key to solve a moving boundary problem is that it should be able to track the moving-boundary or interface that changes with time. Some methods have been developed to solve such a complicated problem. These techniques can be classified in two categories:

(i) surface tracking or predominantly Lagrangian methods. This category includes the arbitrary Lagrangian-Eulerian (ALE) method (Hirt, Amsden and Cook, 1974), the unstructured moving mesh method (Welch, 1995; Welch, 1998) and the Front tracking method (Unverdi and Tryggvason, 1992).

(ii) volume tracking or Eulerian methods. The representatives of this category are the well known volume of fluid (VOF) method (Hirt and Nichols, 1981), the level-set method (Osher and Sethian, 1988; Sussman, Smereka and Osher, 1994) and the Marker-and-Cell (MAC) method (Harlow and Welch 1965).

In this thesis, the gas-liquid interface of the bubbles attached to the heated wall will be assumed to be spherical caps, so the determination of the bubble shape is not a main task. Therefore, only may a brief review for the typical representativemay s for the above two categories, the ALE and the VOF methods, respectively is presented.

Arbitrary Lagrangian-Eulerian (ALE) method

Hirt, Amsden and Cook (1974) proposed an algorithm for solving invicid time-

dependent flows. Ramaswamy (1990) developed this method for modelling unsteady viscous flows with free surfaces. According to Ramaswamy (1990), a physical time marching cycle, from the (n)th instant to the (n+1)th instant with a time increase Δt, can be divided into four sub-steps. These are Lagrangian calculation, rezoning, convective flux calculation, and scalars (temperature for example) calculation. In the Lagrangian calculation, the computational grid vertices are advected by a divergence-free flow velocity. This velocity is used to update the coordinates of the vertices (especially, to update the position of interface). For the rezoning, the interior grids (and therefore the whole mapping meshes) are regenerated using Thompson, Warsi and Mastin's (1985) method, to conform the new boundary and eliminate the highly contorted deformation of internal grid lines by the Lagrangian advect, and the moving velocity of meshes are obtained. Thirdly, convective flux through the cells of updated meshes (not Lagrangian meshes any more) are calculated and the velocity field is redistributed to the new meshes. Finally, the scalars such as temperature are obtained by solving their controlling equations on the moving meshes.

Fujita and Bai (1998) employed the ALE method to study the growth of an isolated bubble in nucleate boiling, quantitative description of the fluid and thermal fields surrounding the bubble was achieved. In order to improve the numerical accuracy of ALE, Li and Petzold (1997) tried to combine the moving mesh with high-order upwind schemes for the convection term, and good results were achieved in their simulation of discontinuous interface. Although the rearrangement of grid at every time step is

needed, and the calculations may experience difficulties when the interface becomes multiple-valued (this corresponds to the topological changes of interface), the ALE moving mesh methods are still attractive because of their capability of highlighting the fields near interface, and the result of physical zero thickness of interface, which are always necessary to study the interface-related mechanism.

When the terminal steady state is calculated, the ALE moving mesh method becomes the body-fitted coordinates transformation method, proposed by Ryskin and Leal (1984a, 1984b). The moving mesh methods employed to track bubble surface and study bubble behaviour by Takagi and Matsumoto (1993, 1995) and Lee and Nydahl (1989) was the time-dependent form of Ryskin and Leal's (1984a, 1984b) method; it also belong to ALE in fact though implicit time-marching scheme was employed to replace the sub-step explicit time-marching.

The principal limitation of Lagrangian methods is that they cannot be used to track an interface which is changeable in topology. Even large amplitude surface motions are difficult to track without introducing regridding techniques.

Volume of fluid (VOF) method

VOF (Volume of Fluid) method was initially proposed by Hirt and Nichols (1981). In VOF, a volume of fluid function with assigned values of 1 for cells contain one phase and 0 for those contain the other, is used to identify the location of interface as it is obvious that the interface lies in those cells take a function value in between. The VOF

function F, is a Lagrangian invariant of fluid, and its controlling equation (Hirt and Nichols, 1981) is an advection equation as follows

$$\frac{\partial F}{\partial t} + \nabla \cdot \left(\vec{V} F\right) = 0, \tag{2.1}$$

where $F = \begin{cases} 1, & in\ \ liquid\ \ side \\ 0, & in\ \ gas\ \ side \end{cases}$ is the void fraction. It is noticeable that equation (2.1) is an advection equation since the volume fraction F is discontinuous there.

According to equation (2.1), which is based on concepts of continuous functions, the VOF function should vary continuously in spatial dimensions. In reality however, F changes discretely from 1 to 0 over the interface whose physical thickness in space is zero, and therefore in computation, it is expected the calculated thickness of interface is as infinitesimal as possible to get valid information of fields in the vicinity of interface. Consequently, special methods must be used to solve equation (2.1), which are the right tasks for CFD researchers.

Over the past years, more accurate schemes have been developed for equation (2.1) in VOF methods. For those calculations with direct differentiations of equation (2.1), Rudman (1997) employed a so-called flux-corrected transport (FCT) algorithm and put forward the FCT-VOF in which equation (2.1) is differenced using a combination of first-order upwind and downwind scheme, a comparison of this new scheme against other well-known schemes was undertaken in his work. Garrioch and Baliga (1998)

developed a skewed subadvection scheme for multidimensional problems. However, the majority of VOF methods do not directly difference equation (2.1) but use a two-stage process, namely, free surface reconstruction and boundary flux integration. To recover the interface shape, piecewise constant schemes (SUFEER by Lafaurie, Nardone, Scardovelli, Zaleski and Zanetti, 1994) and piecewise linear schemes (Ashgriz and Poo (FLAIR), 1991; Puckett, Almgren, Bell, Marcus and Rider, 1997; Rider and Kothe, 1998) of high resolutions, have been developed. Sou, Tomiyama, Zun and Yabushita (1997) compared the FLAIR with traditional "donor-acceptor" scheme (Hirt and Nichols, 1981) and found better accuracy for interface calculation can be achieved with FLAIR. To calculate the boundary cell flux accurately, Harvie and Fletcher (2000) developed a "Stream Scheme", and a good review of VOF algorithms is available in their paper.

VOF methods have been widely employed in the simulations of gas-liquid bubble interface. Tomiyama, Sou, Minagawa and Sakaguchi (1993) analyse a bubble rising in stagnant liquid; Takata, Shirakawa, Tanaka, Kuroki and Ito (1996) simulated bubble growth under electric field; Krishna and Baten (1999) studied the rise characteristics of gas bubbles in a two-dimensional column; Bugg, Mack, and Rezkallah (1998) simulated the Taylor bubbles rising in vertical tubes. All of these investigations have employed the VOF methods and generally good results have been obtained.

However, the weaknesses of VOF methods are also obvious. Firstly, the stability of computation always arises from the varying of bubble volume when VOF is employed

to simulate the bubble growth (Barkhudarov and Chin, 1994). In the second, a smeared interface is inevitable because of the numerical diffusion resulted from the "donor-acceptor" (Hirt and Nichols, 1981) or other schemes (for example, the FCT-VOF by Rudman, 1997), which are only first-ordered in accuracy. For higher order schemes, smearing can come from non-physical oscillations in the vicinithey ty of interface. The thickness of interface is of a magnitude of 1.5 times, which is the mesh size. The uncertainties about interface shape and location have decided that VOF cannot be used for analysing the mechanisms of interface related phenomena. VOF is really not a method designed with intention to capture local physics near phase interfaces (Welch, 1998).

2.5 Summary

The status quo of the research on EHD enhancement of natural convection and gas-liquid interfacial heat transfer are reviewed. Because the study in this thesis is entirely theoretical and numerical, the review has also paid attention to the numerical methods for studying natural convection and heat and fluid flows relevant to a gas-liquid interface of a bubble. The aspects of the review are as follows:

1. The EHD is very promising in practical application for enhancing heat transfer in engineering applications. In nucleate boiling, experiments have revealed noticeable increases in heat transfer coefficient and critical heat flux in the presence of an electric field. Under an electric field, the bubble departure size becomes smaller and the departure frequency increases.

2. The enhancement of heat transfer by EHD effect can be influenced by both the geometry of the electrodes and the properties of the working fluid. The more inhomogeneous the electric field is, the better enhancement. The smaller charge relaxation time, the fluid achieves the better augmentation.
3. Due to the complexity, only a few numerical results have been published so far. These numerical simulations of EHD enhanced heat transfer are based on a number of assumptions such as the zero electric field inside a bubble, decoupling of the flow and electric fields or negligible temperature field. Even for single-phase heat transfer (natural convection), a proper model for describing the physically coupled thermal, flow and electric fields model has not yet been established.
4. In numerical studies, the EHD effect on different working fluid have not yet been studied.
5. The SIMPLE method is a mature and widely employed method for numerical study of heat transfer and fluid flow. The non-staggered grid arrangement with a momentum interpolation technique has many advantages over staggered grid arrangement.
6. For calculation of gas-liquid interfacial flows, the Lagrangian methods use grids configured to conform the shape of the interface; the flow and heat transfer in the vicinity of a gas-liquid interface can be highlighted and with good fidelities. On the other hand, the VOF method employs a fixed Cartesian grid and the interface between two phases is not explicitly tracked but is reconstructed from the properties of appropriate field variables, such as fluid fractions. The fidelities to flow detail and heat transfer phenomena in the vicinity of an interface are poor in the VOF method.

Chapter 3

Basic Equations for Electric, Flow and Thermal Fields

3.1 Introduction

In order to study an industrial or academic problem using CFD method, the following issues are fundamental:

(a). a good understanding of physical phenomenon for the problem;

(b). a proper and accurate mathematical model for describing the given problem;

(c). an efficient numerical procedure to solve the mathematical model.

In this chapter the electric body force, which induces the fluid motion and gives a higher heat transfer rate, and the Joule heat are considered. The electric, flow and thermal fields are coupled in order to give more accurate resolution. A full mathematical model for describing the coupled electric, flow and thermal fields are presented. The governing equations are non-dimensionalised and transformed to a body fitted coordinates (BFC) system using generalized curvilinear coordinates; which give flexibilities and a wide range of applications of the present code for solving many fluid flow and heat transfer problems in an arbitrary computational domain with complicated geometry boundaries. Well posed boundary conditions and their relevant treatment are presented so as to solve the mathematical model numerically.

3.2 Physical Model

EHD is an interdisciplinary phenomenon dealing with the interaction between the electric fields and flow fields in a dielectric medium. This interaction, which causes induced fluid motion and interfacial instabilities, can result in electrically induced pumping, mixing or enhancement of heat transfer.

Physically, when an electric field is applied to a flow, the factors relevant to the problem can be summarised as a current, an electric body force and Joule heat. In order to establish an analytical model for the coupled electric, flow and thermal fields, a current in a dielectric field is physically modelled as a directed motion of electrically charged particles injected into a fluid in this thesis. Based on this modelling, the electric field can be coupled with the flow and thermal fields through the electric body force and Joule heat, while the flow and thermal fields play their effects on the electric field through the transport of the charged particles.

3.3 Equations of Electric Field

To predict the EHD effect on fluid flow and heat transfer requires a simultaneous solution of the coupled equations of fluid flow, temperature and electric fields. In order

to do so, the electric field must be firstly determined from the Maxwell's relation and the Gauss' law. The combination of them yields:

$$\nabla \cdot \varepsilon \vec{E} = q, \tag{3.3.1}$$

where the electric field strength E is defined by the negative gradient of electrical field potential φ,

$$\vec{E} = -\nabla \varphi \ , \tag{3.3.2}$$

and q, the electric charge density, is determined from the conservation of charge:

$$\nabla \cdot \vec{J} + \frac{\partial q}{\partial t} = 0, \tag{3.3.3}$$

where $\vec{J}$ represents the electric current density. Experimental studies have demonstrated that an electric field applied across a thermally stabilized plane layer of a dielectric liquid can induce instability of the layer and thereby significantly augment heat transfer (Bergles, 1978; Allen & Karayiannis, 1995). A dominant destabilizing force in the experiments is the Coulomb force resulting from the interaction of the electric field and free charges. There are two generally accepted versions about the origin of the distribution of the net charges: One is a conductivity model (Martin, 1984), which considered that a temperature gradient in the liquid is an indispensable condition for the convection to occur, and the intensity of the convection is dependent on the magnitude of the temperature gradient; the other is a mobility model (Worraker &

Richardson, 1979), in which the electro-convection is assumed to occur irrespective of the presence or absence of a temperature gradient in the liquid.

Experimental results seem to show that the mobility model is more reasonable for a free charge origination. According to the mobility model, the electric current density can be written as (Worraker & Richardson, 1981; Fujino, Yokoyama and Mori, 1989):

$$\vec{J} = q\vec{V} + \sigma \vec{E} - D\nabla q \ , \tag{3.3.4}$$

where the terms on the right hand side represent the convection, conduction and the diffusion components, respectively; σ is the electrical conductivity; the charge diffusivity coefficient D is related by Einstein's formula (Babski *et al.*,1989).

Equation (3.3.4) was substituted into equation (3.3.3) and developed into a dimensionless form according to the method, which will be introduced later, and then expanded into a Cartesian coordinates system (x, y)

$$\frac{\partial \overline{q}}{\partial \overline{t}} + \overline{u}\frac{\partial \overline{q}}{\partial \overline{x}} + \overline{v}\frac{\partial \overline{q}}{\partial \overline{y}} + \frac{1}{\mathrm{Re}\,\mathrm{Pr}_E}\left[\overline{q}\left(\frac{\partial \overline{E}_x}{\partial \overline{x}} + \frac{\partial \overline{E}_y}{\partial \overline{y}}\right) + \vec{E}_x\frac{\partial \overline{q}}{\partial \overline{x}} + \vec{E}_y\frac{\partial \overline{q}}{\partial \overline{y}}\right] = \frac{1}{\mathrm{Re}\,D_e}\left(\frac{\partial^2 \overline{q}}{\partial \overline{x}^2} + \frac{\partial^2 \overline{q}}{\partial \overline{y}^2}\right), \tag{3.3.4a}$$

where variables with top bars are dimensionless. The right hand side of equation

(3.3.4a) is the diffusion term of $\overline{q}$, and $\frac{1}{\mathrm{Re}\, D_e}$ is the diffusion coefficient. D_e is a dimensionless charge diffusivity number defined by $D_e = \frac{\mu_0}{\rho_0 D_0}$, where μ_0, ρ_0 and D_0 are reference value. As D_0 is in $O(10^{-14})$ (Babski, et al., 1989), the magnitude of D_e is normally a large number, for example of pure water, $D_e = 2.5\times10^7$. Therefore, taking into account of the effect of diffusion coefficient $\frac{1}{\mathrm{Re}\, D_e}$ in equation (3.3.4a), the diffusion term is much smaller than other terms and can be neglected. Similarly, the diffusion term $D\nabla q$ in equation (3.3.4) is also much smaller than other terms and is negligible as well. In addition, as the temperature gradient for a natural convection is not steep, σ and q in the convection term can be assumed to have a linear relationship (Kraus, 1992) as:

$$\sigma = qb, \tag{3.3.5}$$

so that the charge density in equation (3.3.4) is simplified as:

$$\vec{J} = q\vec{V} + qb\vec{E}, \tag{3.3.4b}$$

where b is the ironic mobility (Babskii, et al., 1989).

It is commonly accepted that the physical basis of electrically-enhanced heat transfer lies in the EHD body forces $\vec{F}_E$; and the first step to establish the mathematical model for the EHD enhanced heat transfer is to model these body force. Generally saying, once an electric field is applied, the heat transfer phenomenon becomes complicated because

of the various interactions among the electric field, flow and temperature field. According to Yabe's (1993) study, these interactions include the body forces, interfacial stresses, the variation of physical properties due to temperature distribution, and the combined body forces such as the dielectrophoretic force due to the mutual effect of temperature and electric fields. Mathematically, the electric body force density acting on the molecules of a fluid in the presence of an electric field consists of three terms (Landau and Lifshiz, 1963):

$$\vec{F}_E = q\vec{E} - \frac{1}{2}E^2\nabla\varepsilon + \frac{1}{2}\nabla\left[E^2\left(\frac{\partial\varepsilon}{\partial\rho}\right)_T\rho\right], \tag{3.3.6}$$

where q is free electric charge density, ε is permittivity, T is temperature and E is the electric field strength. The three terms in equation (3.3.6) stand for two primary force densities acting on the fluid. The electrophoretic component $q\vec{E}$ is the Coulomb force exerted by an electric field upon the free charges; the second term depends on the spatial variation of permittivitty ε and the magnitude of E^2. The third term comprises the dielectrophoretic and electrostrictive components; it represents the polarization forces induced in the fluid.

The importance of the three components of the electric body force in equation (3.3.6) varies in practices. All of them can be significant, or one can dominate over the others. However, the expression for the body force in equation (3.3.6) and the interactions are simpler if the working fluid or electric field is subjected to concrete situations. For example, in single-phase heat transfer enhancement using EHD, the Coulomb force

could be the dominant electric body force term; the second term in equation (3.3.6) which is due to the nonuniform electric field is usually weaker. The second term can only dominate when the electric field is imposed on an insulating dielectric liquid. Due to the damage caused by Coulomb force in real applications, researchers are trying to eliminate the free charge in the system. In two-phase heat transfer enhancement using EHD, the second and third electric force term are the dominate ones due to the spatial change in permittivity at the liquid-vapour surface, the variation of physical properties due to temperature distribution.

There are two examples which show that the electric body force density components defined in equation (3.3.6) are responsible for the induced forces on the dielectric field (Seyed-Yagoobi and Bryan, 1995):

- A charged body in a non-uniform or uniform electric field will move along the electric field lines and impart momentum to the surrounding fluid. This Coulomb force (schematically shown in Figure 3-1a) is expressed by the first term in Equation (3.3.6). Free charges can either be directly injected from the energized electrode or induced with the fluid in the presence of an electric field due to non-uniformity in the electrical conductivity of the fluid. The non-uniformity can be caused by a temperature gradient and/ or an inhomogeneous fluid.
- If an interface exists, such as a liquid-vapour interface in a non-uniform electric field, an attraction force is created, which pushes the fluid of higher permittivity (liquid) towards the region of higher electric field strength. This force is called

dielectrophoretic force (schematically shown in Figure 3-1b) results from the application of a non-uniform electric field with the existence of a permittivity gradient and is described in the second term in equation (3.3.6).

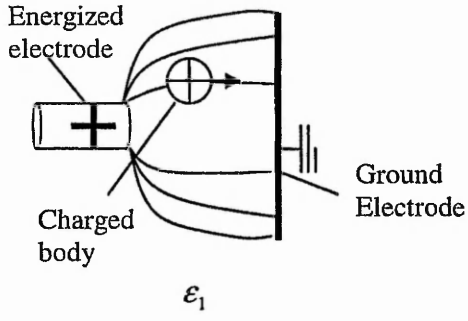

Figure 3-1a Coulomb force

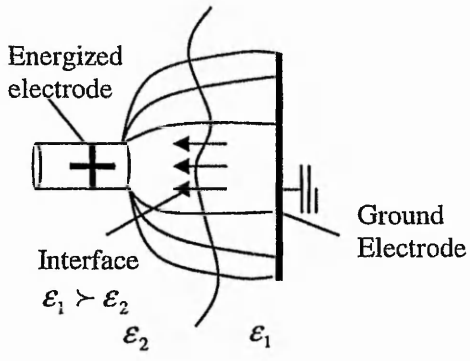

Figure 3-1b Dielectrophoretic force

Because we have physically modelled the current in a dielectric field as a directed motion of electrically charged particles injected into a fluid, the electric body force is therefore in the form of Coulomb force and is calculated as follows:

$$\vec{F}_E = q\vec{E} \ . \tag{3.3.7}$$

It must be clarified that the body force in equation (3.3.7) is different from that in equation (3.3.6) because of the different physical meanings of q. In equation (3.3.6), as we explained earlier, q is the free charge induced by the electric field. On the other hand, the q in equation (3.3.7) is the charged particles released from the positive electrode to model the current; it is only a modelled (imaginary) carrier for both the

electric charge and the electric body force. In other words, the body force in equation (3.3.7) can be a result of any term or a summation of terms of the right hand of equation (3.3.6), but we formulate this result in a form of the Coulomb force in our mathematical model. It is obvious the expression of body force in equation (3.3.7) will not lose generality because all the forces in equation (3.3.6) can be considered if the fluid properties under an electric field can be made available. In the case of the second and the third terms in equation (3.3.6) are neglected, these two equations become equivalent and the q take a same value.

Besides the electric body force, another result of applying an electric field on the working liquid is the Joule heat,

$$\dot{Q} = \vec{J} \cdot \vec{E} . \tag{3.3.8}$$

3.4 Basic Governing Equations

To take an electric field into account in the transport equations, the electric body force $\vec{F}_{\mathrm{E}}$ is added into momentum equation and the Joule heat is added into the energy equation. Based on these, the mathematical model of EHD effect on two-phase flow is described as follows; the flow is considered as two-dimensional and incompressible:

Continuity equation:

$$\frac{\partial(ru)}{\partial r}+\frac{\partial(rv)}{\partial y}=0\,; \tag{3.4.1}$$

x-momentum equation:

$$\frac{\partial(ru)}{\partial t}+\frac{\partial(ruu)}{\partial x}+\frac{\partial(rvu)}{\partial y}=\frac{\partial}{\partial x}\left(r\upsilon\frac{\partial u}{\partial x}\right)+\frac{\partial}{\partial y}\left(r\upsilon\frac{\partial u}{\partial y}\right)+rS(u)\ ; \tag{3.4.2}$$

y-momentum equation:

$$\frac{\partial(rv)}{\partial t}+\frac{\partial(ruv)}{\partial x}+\frac{\partial(rvv)}{\partial y}=\frac{\partial}{\partial x}\left(r\upsilon\frac{\partial v}{\partial x}\right)+\frac{\partial}{\partial y}\left(r\upsilon\frac{\partial v}{\partial y}\right)+rS(v)\,; \tag{3.4.3}$$

Energy equation:

$$\frac{\partial(rT)}{\partial t}+\frac{\partial(ruT)}{\partial x}+\frac{\partial(rvT)}{\partial y}=\frac{\partial}{\partial x}\left(r\frac{\lambda}{\rho C_P}\frac{\partial T}{\partial r}\right)+\frac{\partial}{\partial y}\left(r\frac{\lambda}{\rho C_P}\frac{\partial T}{\partial y}\right)+rS(T)\quad ; \tag{3.4.4}$$

Conservation of charge:

$$\frac{\partial(rq)}{\partial t}+\frac{\partial[r(u+b\,E_x)]}{\partial x}+\frac{\partial[r(u+b\,E_y)]}{\partial y}=r\left\{\frac{q[u\,E_x+v\,E_y+b(E_x{}^2+E_y{}^2)]}{\rho C_P}\right\}\ ; \tag{3.4.5}$$

Electric field potential equation:

$$\frac{\partial}{\partial x}\left(r\frac{\partial \varphi}{\partial x}\right)+\frac{\partial}{\partial y}\left(r\frac{\partial \varphi}{\partial y}\right)=r\left(-q/\varepsilon\right), \tag{3.4.6}$$

Electric field strength equation:

$$E_x=-\frac{\partial \varphi}{\partial x}, \qquad E_y=-\frac{\partial \varphi}{\partial y}. \tag{3.4.7}$$

Equations (3.4.1~3.4.4) can be written in a general form as following:

$$\frac{\partial(r\phi)}{\partial t}+\frac{\partial}{\partial x}(ru\phi)+\frac{\partial}{\partial y}(rv\phi)=\frac{\partial}{\partial x}\left(r\Gamma\frac{\partial \phi}{\partial x}\right)+\frac{\partial}{\partial y}\left(r\Gamma\frac{\partial \phi}{\partial y}\right)+rS(\phi), \tag{3.4.8}$$

where for Cartesian coordinates, *i.e.*, $r=1$,

$$\phi=\begin{bmatrix}1\\ u\\ v\\ T\end{bmatrix}, \qquad \Gamma=\begin{bmatrix}0\\ \upsilon\\ \upsilon\\ \dfrac{\lambda}{\rho c_p}\end{bmatrix}, \quad rS=\begin{bmatrix}0\\ r\left(-\dfrac{1}{\rho}\dfrac{\partial p}{\partial x}+\dfrac{qE_x}{\rho}\right)\\ r\left(-\dfrac{1}{\rho}\dfrac{\partial p}{\partial y}+g\beta(T-T_0)+\dfrac{qE_y}{\rho}\right)\\ r\left\{\dfrac{q}{\rho c_p}\left[uE_x+uE_y+b\left(E_x^2+E_y^2\right)\right]\right\}\end{bmatrix};$$

And for axisymmetric system, i.e., $r=x$, we have

$$\phi=\begin{bmatrix}1\\u\\v\\T\end{bmatrix},\qquad \Gamma=\begin{bmatrix}0\\\upsilon\\\upsilon\\\dfrac{\lambda}{\rho c_p}\end{bmatrix},\qquad rS=\begin{bmatrix}0\\r\left(-\dfrac{1}{\rho}\dfrac{\partial p}{\partial x}+\dfrac{qE_x}{\rho}-\dfrac{\upsilon\ u}{r^2}\right)\\r\left(-\dfrac{1}{\rho}\dfrac{\partial p}{\partial y}+g\beta(T-T_0)+\dfrac{qE_y}{\rho}\right)\\r\left\{\dfrac{q}{\rho c_p}\left[uE_r+uE_y+b\left(E_x^2+E_y^2\right)\right]\right\}\end{bmatrix}.$$

3.5 Normalisation of Governing Equations

It is advisable to cast the governing equations in a dimensionless form before carrying out a numerical solution. This enables the flow variables to be normalized so that their values fall between prescribed limits such as 0 and 1. Also, the characteristic parameters such as Reynolds number, Prandtl number, etc., can be varied independently. Non-dimensionless parameters are obtained by the reference values denoted by a subscript "0", they are defined as:

$$\bar{u}=\frac{u}{u_0},\quad \bar{v}=\frac{v}{u_0},\quad \bar{x}=\frac{x}{l_0},\quad \bar{y}=\frac{y}{l_0},\quad \bar{t}=\frac{t\,u_0}{l_0},\quad \bar{p}=\frac{p}{\rho u^2},\quad \bar{T}=\frac{T-T_0}{T_1-T_0}$$

$$\bar{q}=\frac{q}{q_0},\quad \bar{E}=\frac{E}{E_0},\quad \bar{\varphi}=\frac{\varphi-\varphi_0}{\varphi_1-\varphi_0}, \qquad (3.6.1)$$

where T_1 and T_0 are the hot and cold wall's temperature, φ_1 and φ_0 are the potentials of electrodes. Therefore, the equation (3.4.8) can be expressed as:

$$\frac{\partial(\bar{r}\phi)}{\partial\bar{t}}+\frac{\partial}{\partial\bar{x}}(\bar{r}\bar{u}\phi)+\frac{\partial}{\partial\bar{y}}(\bar{r}\bar{v}\phi)=\frac{\partial}{\partial\bar{x}}\left(\bar{r}\Gamma\frac{\partial\phi}{\partial\bar{x}}\right)+\frac{\partial}{\partial\bar{y}}\left(\bar{r}\Gamma\frac{\partial\phi}{\partial\bar{y}}\right)+\bar{r}S(\phi). \qquad (3.6.2)$$

Similar to equation (3.4.8), when $\bar{r}=1$, equation (3.6.2) is for Cartesian system:

$$\phi=\begin{bmatrix}1\\ \bar{u}\\ \bar{v}\\ \bar{T}\end{bmatrix},\qquad \Gamma=\begin{bmatrix}0\\ \frac{1}{\mathrm{Re}}\\ \frac{1}{\mathrm{Re}}\\ \frac{1}{\mathrm{Re\,Pr}}\end{bmatrix},\quad \bar{r}S(\phi)=\begin{bmatrix}0\\ \bar{r}\left(-\frac{\partial\bar{p}}{\partial\bar{x}}+S_E\,\bar{q}\,\bar{E}_x\right)\\ \bar{r}\left(-\frac{\partial\bar{p}}{\partial\bar{y}}+S_E\,\bar{q}\,\bar{E}_y+\frac{Gr}{\mathrm{Re}^2}\bar{T}\right)\\ \bar{r}\left\{S_E E_C\left[\bar{u}\bar{E}_x+\bar{v}\bar{E}_y+\frac{\left(\overline{E_x^2}+\overline{E_y^2}\right)}{\mathrm{Re\,Pr}_E}\right]\right\}\end{bmatrix};$$

and when $\bar{r}=\bar{x}$, it is for axisymmetric system:

$$\phi=\begin{bmatrix}1\\ \bar{u}\\ \bar{v}\\ \bar{T}\end{bmatrix},\qquad \Gamma=\begin{bmatrix}0\\ \frac{1}{\mathrm{Re}}\\ \frac{1}{\mathrm{Re}}\\ \frac{1}{\mathrm{Re\,Pr}}\end{bmatrix},\quad \bar{r}S(\phi)=\begin{bmatrix}0\\ \bar{r}\left(-\frac{\partial\bar{p}}{\partial\bar{x}}+S_E\,\bar{q}\,\bar{E}_x-\frac{1}{Re}\frac{\bar{u}}{\bar{r}^2}\right)\\ \bar{r}\left(-\frac{\partial\bar{p}}{\partial\bar{y}}+S_E\,\bar{q}\,\bar{E}_y+\frac{Gr}{Re^2}\bar{T}\right)\\ \bar{r}\left\{S_E E_C\left[\bar{u}\bar{E}_x+\bar{v}\bar{E}_y+\frac{\left(\overline{E_x^2}+\overline{E_y^2}\right)}{Re\,Pr_E}\right]\right\}\end{bmatrix};$$

Equations (3.4.5), (3.4.6) and (3.4.7) are changed into as follows:

$$\frac{\partial(\bar{r}\,\bar{q})}{\partial \bar{t}}+\frac{\partial}{\partial \bar{x}}\left[\bar{r}\left(\bar{u}+\frac{\bar{E}_x}{\mathrm{Re}\,\mathrm{Pr}_E}\right)\bar{q}\right]+\frac{\partial}{\partial \bar{y}}\left[\bar{r}\left(\bar{v}+\frac{\bar{E}_y}{\mathrm{Re}\,\mathrm{Pr}_E}\right)\bar{q}\right]=0, \tag{3.6.3}$$

$$\frac{\partial}{\partial \bar{x}}\left(\bar{r}\frac{\partial \bar{\varphi}}{\partial \bar{x}}\right)+\frac{\partial}{\partial \bar{y}}\left(\bar{r}\frac{\partial \bar{\varphi}}{\partial \bar{y}}\right)=\bar{r}\left(-N_E\,\bar{q}\right), \tag{3.6.4}$$

$$\bar{E}_x=-\frac{\partial \bar{\varphi}}{\partial \bar{x}}, \qquad \bar{E}_y=-\frac{\partial \bar{\varphi}}{\partial \bar{y}}. \tag{3.6.5}$$

3.6 Governing Equations in Body-Fitted Coordinate (BFC) System

It is frequently convenient to write and solve the governing equations in generalized, non-orthogonal curvilinear coordinates, especially when complex geometries are involved. Furthermore, in many applications it may be desirable to preferentially improve resolution in certain region of the flow. In these regions, the flow or other physical phenomena may evolve dynamically and, therefore the local grids may need to be adjusted manually during the calculation; a general body fitted coordinates system is a commonly used remedy for satisfying this requirement of adjusting local grids.

The employment of BFC needs a transformation from the physical plane (x, y) to the computational plane (ξ, η). This one-to-one transformation can be easily carried out for simply-connected domain, as shown in figure 3.2. For a doubly-connected domain, one-to-one transformation can also be found by using a branch cut; figure 3.3 gives an example of such a transformation. In figures 3.2 and 3.3, a bound in the irregular physical plane is always transformed to its counterpart with a same name in the computational plane. For example, bound AD in figure 3.4a has its counterpart bound AD in figure 3.4b.

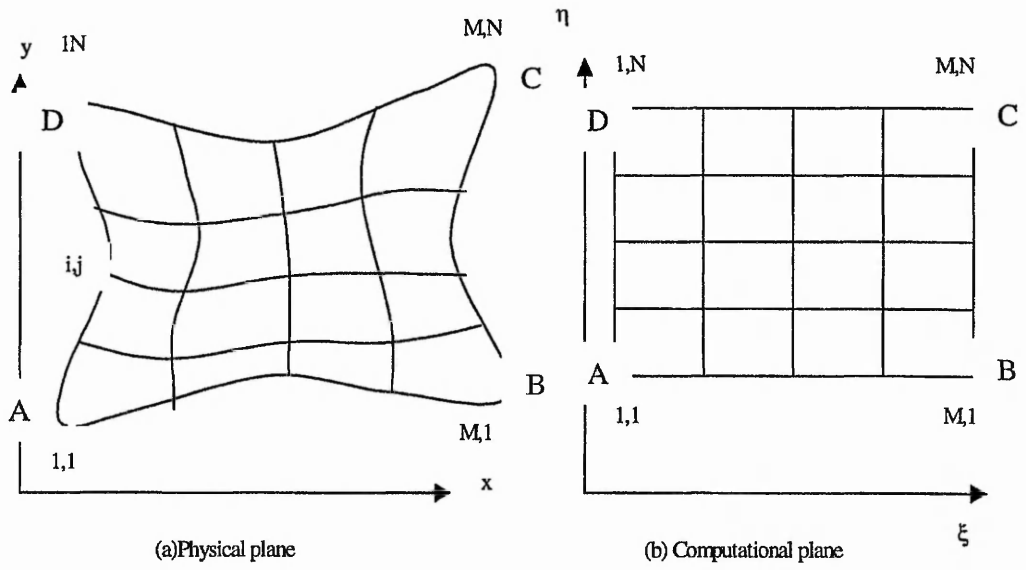

Figure 3.4 Mapping an irregular simply-connected region into the computational domain as a rectangle

The transformation of coordinates systems between the (x, y) and the (ξ, η) can be expressed as:

$$\xi \equiv \xi(x, y), \quad \eta \equiv \eta(x, y) \quad ; \tag{3.6.6}$$

$$x \equiv x(\xi, \eta), \quad y \equiv y(\xi, \eta) \quad ; \tag{3.6.7}$$

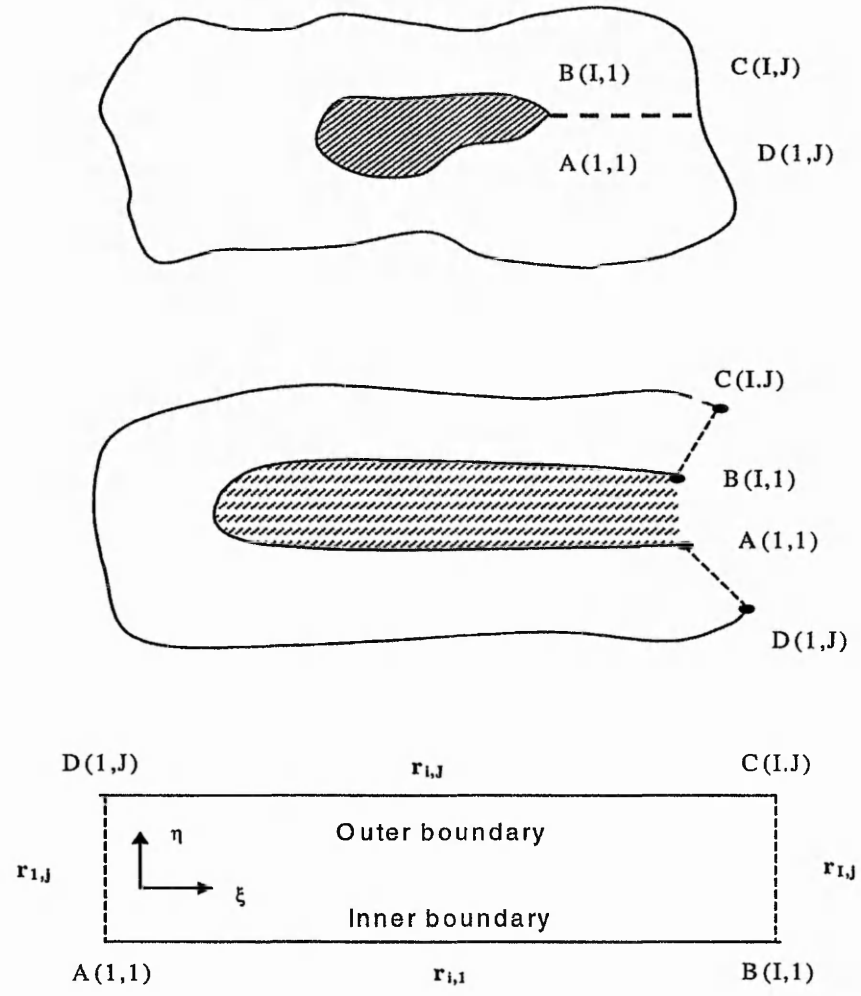

Figure 3.3 Mapping of a doubly-connected region in to a simply connected region by using a branch cut

The basis of the transformation of the partial differential equations is the availability of the relations for the transformation of various differential operators such as the first derivative, gradient, Laplacian, *etc.*

The *Jacobian* of the transformation $\tilde{J}$ is given by Courant (1956) as:

$$\tilde{J} = \tilde{J}\left(\frac{x,y}{\xi,\eta}\right) = \begin{vmatrix} x_\xi & y_\xi \\ x_\eta & y_\eta \end{vmatrix} = x_\xi y_\eta - x_\eta y_\xi \neq 0 \tag{3.6.8}$$

where the subscripts denote differentiation with respect to the variable considered i.e.,

$$x_\xi = \frac{\partial x}{\partial \xi}, x_\eta = \frac{\partial x}{\partial \eta}, y_\eta = \frac{\partial y}{\partial \eta}, y_\xi = \frac{\partial y}{\partial \xi} \tag{3.6.9}$$

The transformation relations can be developed by application of the chain rule of differentiation or by making a use of the method in differential geometry and tensor analysis. Consider, for example, the first derivatives $\frac{\partial \phi}{\partial x}$ *and* $\frac{\partial \phi}{\partial y}$. With the chain rule of differentiation, $\frac{\partial \phi}{\partial x}$ and $\frac{\partial \phi}{\partial y}$ can be written as follows:

$$\begin{cases} \dfrac{\partial \phi}{\partial x} = \xi_x \dfrac{\partial \phi}{\partial \xi} + \eta_x \dfrac{\partial \phi}{\partial \eta} \\ \dfrac{\partial \phi}{\partial y} = \xi_y \dfrac{\partial \phi}{\partial \xi} + \eta_y \dfrac{\partial \phi}{\partial \eta} \end{cases} \tag{3.6.10}$$

Interchange x and ξ, and y and η, yields

$$\begin{cases} \dfrac{\partial \phi}{\partial \xi} = x_\xi \dfrac{\partial \phi}{\partial x} + y_\xi \dfrac{\partial \phi}{\partial y} \\ \dfrac{\partial \phi}{\partial \eta} = x_\eta \dfrac{\partial \phi}{\partial x} + y_\eta \dfrac{\partial \phi}{\partial y} \end{cases} \tag{3.6.11}$$

The solution of equations (3.8.6) for $\dfrac{\partial \phi}{\partial x}$ *and* $\dfrac{\partial \phi}{\partial y}$ with Cramer's rule gives the transformation relations for the first derivatives as

$$\begin{cases} \dfrac{\partial \phi}{\partial x} = \dfrac{1}{\tilde{J}} \left(y_\eta \dfrac{\partial \phi}{\partial \xi} - y_\xi \dfrac{\partial \phi}{\partial \eta} \right) \\ \dfrac{\partial \phi}{\partial y} = \dfrac{1}{\tilde{J}} \left(-x_\eta \dfrac{\partial \phi}{\partial \xi} + x_\xi \dfrac{\partial \phi}{\partial \eta} \right) \end{cases} \tag{3.6.12}$$

where the *Jacobian* of the transformation is defined in equation (3.7.3). A comparison of equations (3.7.5) and (3.7.7) gives:

$$\begin{cases} \xi_x = \dfrac{1}{\tilde{J}} y_\eta , \quad \xi_y = -\dfrac{1}{\tilde{J}} x_\eta , \\ \eta_x = -\dfrac{1}{\tilde{J}} y_\xi , \quad \eta_y = \dfrac{1}{\tilde{J}} x_\xi , \end{cases} \tag{3.6.13}$$

the above relations are called contravariant metrics.

The generalized form of governing equations for the flow field given in section 3.6 is transformed from Cartesian coordinates to non-orthogonal body-fitted coordinates as follows:

$$\begin{aligned} &\frac{\partial}{\partial \xi}(W_1 \phi) + \frac{\partial}{\partial \eta}(W_2 \phi) \\ &= \frac{\partial}{\partial \xi}\left[\frac{\Gamma}{\tilde{J}}\left(\alpha \frac{\partial \phi}{\partial \xi} - \beta \frac{\partial \phi}{\partial \eta}\right)\right] + \frac{\partial}{\partial \eta}\left[\frac{\Gamma}{\tilde{J}}\left(-\beta \frac{\partial \phi}{\partial \xi} + \gamma \frac{\partial \phi}{\partial \eta}\right)\right] + \tilde{J} S(\phi) \end{aligned} , \tag{3.6.14}$$

where

$$\phi = \begin{bmatrix} 1 \\ u \\ v \\ T \end{bmatrix}, \quad \Gamma = \begin{bmatrix} 0 \\ \dfrac{1}{Re} \\ \dfrac{1}{Re} \\ \dfrac{1}{Re\,Pr} \end{bmatrix}, \quad S(\phi) = \begin{bmatrix} 0 \\ -\dfrac{\partial p}{\partial x} \\ -\dfrac{\partial p}{\partial y} + \dfrac{Ra}{Pr\,Re^2} T \\ 0 \end{bmatrix},$$

$$\alpha = x_\eta^2 + y_\eta^2 ; \tag{3.6.15}$$

$$\beta = x_\xi x_\eta + y_\xi y_\eta; \tag{3.6.16}$$

$$\gamma = x_\xi^2 + y_\xi^2; \tag{3.6.17}$$

the curvilinear velocity components, W_1 and W_2, are defined as:

$$\begin{cases} W_1 = uy_\eta - vx_\eta \\ W_2 = vx_\xi - uy_\xi \end{cases}. \tag{3.6.18}$$

Conservation of charge equation (3.6.3) is changed into:

$$\frac{\partial(\tilde{J}rq)}{\partial t} + \frac{\partial}{\partial \xi}\left[r\left(W_1 + \frac{1}{Re\, Pr_E} E_1 \right) q \right] + \frac{\partial}{\partial \eta}\left[r\left(W_2 + \frac{1}{Re\, Pr_E} E_2 \right) q \right] = 0; \tag{3.6.19}$$

where

$$\begin{cases} E_1 = E_x y_\eta - E_y x_\eta \\ E_2 = E_y x_\xi - E_x y_\xi \end{cases}. \tag{3.6.20}$$

Electric field potential equation (3.6.4) is changed into:

$$\frac{\partial}{\partial\xi}\left(\frac{r}{\tilde{J}}\alpha\frac{\partial\varphi}{\partial\xi}\right)+\frac{\partial}{\partial\eta}\left(\frac{r}{\tilde{J}}\gamma\frac{\partial\varphi}{\partial\eta}\right)+\frac{\partial}{\partial\xi}\left(\frac{-r}{\tilde{J}}\beta\frac{\partial\varphi}{\partial\eta}\right)+\frac{\partial}{\partial\eta}\left(\frac{-r}{\tilde{J}}\beta\frac{\partial\varphi}{\partial\xi}\right)$$
$$=\tilde{J}r(-N_E q) \qquad (3.6.21)$$

Electric field strength equation (3.6.5) is changed into:

$$\begin{cases} E_x=-\dfrac{\partial\varphi}{\partial x}=-\dfrac{1}{\tilde{J}}\left(\varphi_\xi y_\eta-\varphi_\eta y_\xi\right) \\ E_y=-\dfrac{\partial\varphi}{\partial y}=-\dfrac{1}{\tilde{J}}\left(\varphi_\xi x_\eta+\varphi_\eta x_\xi\right) \end{cases} \qquad (3.6.22)$$

3.7 Summary

The mathematical model for coupled electric, flow and thermal fields are presented. A current in a dielectric field is physically modelled as a directed motion of electrically charged particles injected into a fluid; the factors for the coupling include the electric body force, Joule heat and the transport of the charged particles. Governing equations for the coupled fields are normalised and transformed into body-fitted coordinates system so as to develop numerical method for solving these equations in the next chapter.

Chapter 4

Numerical Methods for Solving Coupled Electric, Flow and Thermal Fields

4.1 Introduction

Once the physical and mathematical models are established, the followed steps for numerically solving the coupled electric, flow and thermal fields are to discretise the mathematical model and establish the calculating methods for these discretised equations. For the first step, the discretisation includes two parts, namely, the *space* discretization (grid generation) and the equation discretisation. In this chapter, the grid generation is carried out by using a combined algebraic and partial differential equation method; the algebraic method is applied to give the initial values of the grid points, and then the partial differential equation grid generation method is employed to generate a grid system with second order smoothness. While for the discretisation of the governing equations, the finite volume method (FVM) is applied. In order to obtain high numerical resolution, the quadratic upwind interpolation for convective kinematics (QUICK) scheme (Leonard, 1979) is employed for the discretisation of the convection term.

The discretizatioin of transport and electric field equations yields a large system of non-

linear algebraic equations. The method of solution depends on the problem; therefore an appropriate method has to be chosen. In this work, the SIMPLE method with non-staggered grid arrangement is chosen to solve the discretized equations.

4.2 Grid Generation

The numerical grid generation at which the variables are to be calculated is essentially a discrete representation of the geometric domain in which the problem is to be solved. The generation of a fine grid system is very important for giving an accurate solution. There are many approaches to generate a grid system.

4.2.1 Algebraic Method

Using algebraic methods to generate grid can take arbitrarily shaped physical regions into a rectangular computational domain. The basics of generating a grid using the algebraic method can be explained as follows:

Consider an irregular geometry shown in figure 4.1. The describing function for the upper bound is given as

$$y_s = f(x) \tag{4.2.1}$$

In figure 4.1, curve *de* is the upper wall; *fg* is the centreline. The grid shown in figure 4.1(a) exactly fits these boundaries. A computational grid can easily be generated by choosing equally spaced increments in the x direction and using uniform division in the y direction. This may be described as

$$\xi = x \tag{4.2.2}$$

$$\eta = \frac{y}{y_s} \tag{4.2.3}$$

where $y_s = f(x)$.

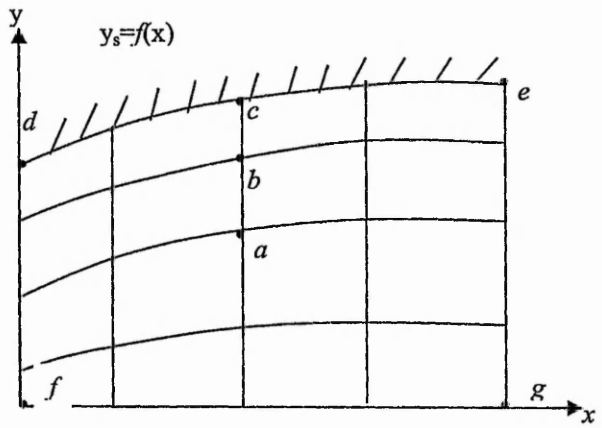

(a)

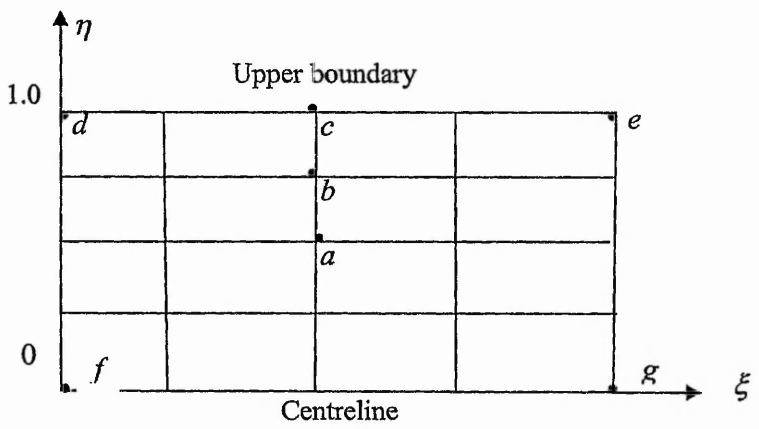

(b)

Figure 4.1 a simple body fitted coordinate system

(a) Physical domain (b) Computational domain

From the above equations (4.2.2) and (4.2.3) at curvilinear upper wall, $\eta_d = \frac{y_d}{y_{sd}} = 1$, so do the η_c and η_e. It is clear that all the points along the curved upper boundary in the physical domain are transformed along the horizontal line $\eta = 1$ in the computational domain. Once the ξ and η are given, the values of x and y can be easily recovered. The mesh generated in the physical domain is shown in figure 4.1(a).

The main advantages of using algebraic methods are that they are direct and the metrics of the transformation can be analytically computed. However, the grid will sometimes not have second order smoothness, for some certain problems, it can cause chaos during the computing. Also for this method, a certain amount of ingenuity is required to produce a grid with points properly positioned.

4.2.2 Partial Differential Equations

A more general approach of grid generation is presented by the solution of Possion equations:

$$\begin{cases} \dfrac{\partial^2 \xi}{\partial x^2} + \dfrac{\partial^2 \xi}{\partial y^2} = P(\xi, \eta) \\ \dfrac{\partial^2 \eta}{\partial x^2} + \dfrac{\partial^2 \eta}{\partial y^2} = Q(\xi, \eta) \end{cases} \tag{4.2.4}$$

where $P(\xi,\eta)$ and $Q(\xi,\eta)$ are known as control functions used to control clustering of interior grid points and angles at the boundaries. Specification of desired grid points (x, y) on the boundary of the physical domain provides the boundary conditions for the solution of (4.2.4). The use of an elliptic partial differential equation to generate the interior grid points has some advantages. Firstly, the grid is smoothly varying even if the domain boundary has a slope discontinuity. Secondly, an equation like (4.2.4) satisfy the maximum principle for reasonable values of $P(\xi,\eta)$ and $Q(\xi,\eta)$, implying thereby that the maximum and minimum values of ξ and η must occur on the boundary. According to Tompson (1982), this normally guarantees the grid is not overlapping.

By an appropriate selection of the $P(\xi, \eta)$ and $Q(\xi, \eta)$ functions, the coordinate lines ξ and η can be concentrated toward a specified coordinate line or about a specific grid point. In the absence of these functions, for example while $P(\xi,\eta)=Q(\xi,\eta)=0$, the equation (4.2.4) become Laplace's equation, the coordinate lines will tend to be generally equally spaced in the regions away from the boundaries regardless of the concentration of the grid points along the boundaries.

While Equation (4.2.4) describes the basic coordinate transformation between (x, y) and (ξ, η) coordinate system, all numerical computations of the governing differential

equations for a physical problem are to be performed in the computational (ξ, η) space since the transformed region has a simple regular geometry. Then, the problem becomes one of seeking the (x, y) values of the physical space corresponding to the known (ξ, η) grid locations of the computational space. For this reason, equation (4.2.4) should be transformed to the computational domain by interchanging the roles of the dependent and the independent variables.

The actual solution is carried out in the computational domain (ξ, η). In this domain (4.2.4) transform to

$$\begin{cases} \alpha\dfrac{\partial^2 x}{\partial\xi^2}-2\beta\dfrac{\partial^2 x}{\partial\xi\partial\eta}+\gamma\dfrac{\partial^2 x}{\partial\eta^2}+\tilde{J}^2\left(P(\xi,\eta)\dfrac{\partial x}{\partial\xi}+Q(\xi,\eta)\dfrac{\partial x}{\partial\eta}\right)=0 \\ \alpha\dfrac{\partial^2 y}{\partial\xi^2}-2\beta\dfrac{\partial^2 y}{\partial\xi\partial\eta}+\gamma\dfrac{\partial^2 y}{\partial\eta^2}+\tilde{J}^2\left(P(\xi,\eta)\dfrac{\partial y}{\partial\xi}+Q(\xi,\eta)\dfrac{\partial y}{\partial\eta}\right)=0 \end{cases}, \qquad (4.2.5)$$

where the convariant metrics α, β, γ and the Jacobian have been defined in equations (3.8.10-3.8.11) and equations (3.8.3) respectively.

The determination of the grid control function $P(\xi, \eta)$ and $Q(\xi, \eta)$ is very useful to concentrate the interior grid lines in regions, where large gradients occur. For example, in problems of natural convection large gradients occur near the walls, hence grid points need to be concentrated in such locations. Thomas and Middlecoff (1980) proposed a

method to determine $P(\xi, \eta)$ and $Q(\xi, \eta)$. This method is employed in the present research because it is easy to control the grid concentration as pre-specified by the user and to achieve the orthogonal coordinate lines to the boundary lines. The function of $P(\xi, \eta)$ and $Q(\xi, \eta)$ are constructed as follows:

$$\begin{cases} P(\xi,\eta) = \phi(\xi,\eta)\left(\xi_x^2 + \xi_y^2\right) \\ Q(\xi,\eta) = \psi(\xi,\eta)\left(\eta_x^2 + \eta_y^2\right) \end{cases}, \tag{4.2.6}$$

where $\phi(\xi,\eta)$ and $\psi(\xi,\eta)$ are unknown functions. With this convention, the Possion's equation may be written

$$\begin{cases} \alpha\left(x_{\xi\xi} + \phi x_{\xi}\right) - 2\beta x_{\xi\eta} + \gamma\left(x_{\eta\eta} + \psi x_{\eta}\right) = 0 \\ \alpha\left(y_{\xi\xi} + \phi y_{\xi}\right) - 2\beta y_{\xi\eta} + \gamma\left(y_{\eta\eta} + \psi y_{\eta}\right) = 0 \end{cases}, \tag{4.2.7}$$

$\phi(\xi,\eta)$ and $\psi(\xi,\eta)$ can be determined by setting the quantities in parentheses equal to zero. For example, at the boundaries of $\xi=0$ and $\xi=\xi_{max}$:

$$\begin{cases} x_{\eta\eta} + \psi(\xi,\eta)x_{\eta} = 0 \\ y_{\eta\eta} + \psi(\xi,\eta)y_{\eta} = 0 \end{cases}. \tag{4.2.8}$$

Similarly, at the boundaries of η =0 and $\eta = \eta_{max}$ may be determined by:

$$\begin{cases} x_{\xi\xi} + \phi(\xi,\eta)x_{\xi} = 0 \\ y_{\xi\xi} + \phi(\xi,\eta)y_{\xi} = 0 \end{cases} \tag{4.2.9}$$

Since x and y are known at all boundary points, the function $\phi(\xi,\eta)$ and $\psi(\xi,\eta)$ can be obtained by using central differences for the required derivatives. The function $\phi(\xi,\eta)$ and $\psi(\xi,\eta)$ on the interior are obtained by interpolation from boundary values. This method provides a means of control for the interior point's distribution based upon the requirement at the boundary.

In this thesis, an algebraic method was used to generate the initial grid system, then a grid system with second order smoothness was obtained by applying the partial differential equations method. This combination of the grid generation methods gives second order smoothness to the mesh for calculation.

4.3 Discretization of Governing Equations

The finite volume method (FVM) was first introduced by McDonald (1971) and MacCormack and Paullay (1972) for the solution of two-dimensional Euler equations and extended by Rizzia and Inouye (1973) into three-dimensional flows. This method is using the technique by which the integral formulation of the conservation laws is

discretized directly in the physical space. Thus, this approach employs numerical balances of a conserved variable over small control volumes, thereby ensuring that the basic quantities like mass, momentum and energy remain conserved at the discrete level. This is the fundamental advantage of the FVM methods.

The finite form of the conservation laws may be obtained by integrating equations (3.6.2)~ (3.6.4) over appropriately non-staggered control volumes leading to a five point differential stencil centred around the point P with neighbouring node points N, S, E and W; the letters e, s, w, and n denotes the interfaces with neighbouring control volumes shown in figure 4.2, the values of the variables at the interfaces are obtained by interpolation from the node points; the interfaces are halfway from the node points.

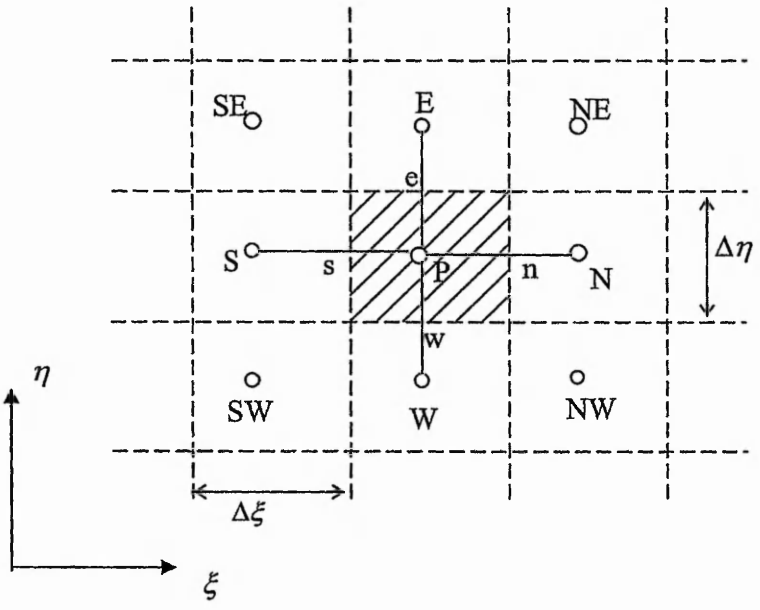

Figure 4.2 The discretized geometry

4.3.1 Discretization of Transport Equations

The integration of the generalized form of governing equation (3.6.14) over the control volume shadowed in figure 4.2 can be achieved as follow:

$$\begin{aligned} & r\left(W_1\phi-\frac{\Gamma}{\tilde{J}}\alpha\frac{\partial\phi}{\partial\xi}\right)\Delta\eta\Big|_s^n+r\left(W_2\phi-\frac{\Gamma}{\tilde{J}}\gamma\frac{\partial\phi}{\partial\eta}\right)\Delta\xi\Big|_w^e \\ & =\left[\tilde{J}rS(\phi)\Delta\xi\Delta\eta+S'(\phi)\right]_P \\ & =\overline{S(\phi)} \end{aligned} \quad , \tag{4.3.1}$$

where

$$S'(\phi)=\left[r\frac{\Gamma}{\tilde{J}}(-\beta)\frac{\partial\phi}{\partial\eta}\Delta\eta\right]_s^n+\left[r\frac{\Gamma}{\tilde{J}}(-\beta)\frac{\partial\phi}{\partial\xi}\Delta\xi\right]_w^e . \tag{4.3.2}$$

For simplicity, the symbols $F_i \ \ (i=n,s,e,w)$, $D_i \ \ (i=n,s,e,w)$, and $\mathcal{F}_i \ \ (i=n,s,e,w)$ are defined as:

$$F_n=(W_1)_n\Delta\eta, \qquad D_n=\left(\frac{\Gamma}{\tilde{J}}\alpha\right)_n\frac{\Delta\eta}{\xi_N-\xi_P}, \qquad \mathcal{F}_n=F_n\phi_n-D_n(\Delta\phi)_n;$$

$$F_s=(W_1)_s\Delta\eta, \qquad D_s=\left(\frac{\Gamma}{\tilde{J}}\alpha\right)_s\frac{\Delta\eta}{\xi_P-\xi_S}, \qquad \mathcal{F}_s=F_s\phi_s-D_s(\Delta\phi)_s;$$

$$F_e = (W_2)_e \Delta\xi, \qquad D_e = \left(\frac{\Gamma}{\tilde{J}}\gamma\right)_n \frac{\Delta\xi}{\eta_E - \eta_P}, \qquad \mathcal{J}_e = F_e\phi_e - D_e(\Delta\phi)_e;$$

$$F_w = (W_2)_w \Delta\xi, \qquad D_w = \left(\frac{\Gamma}{\tilde{J}}\gamma\right)_w \frac{\Delta\xi}{\eta_P - \eta_W}, \qquad \mathcal{J}_w = F_w\phi_w - D_w(\Delta\phi)_w,$$

equation (4.3.1) becomes

$$\mathcal{J}_n - \mathcal{J}_s + \mathcal{J}_e - \mathcal{J}_w = \overline{S(\phi)} \ . \tag{4.3.3}$$

For the case of $\phi = 1, \Gamma_\phi = 0, S(\phi) = 0$, the equation (4.3.3) can be written as:

$$F_n - F_s + F_e - F_w = 0 \tag{4.3.4}$$

Multiply equation (4.3.4) with ϕ_P and subtract equation (4.3.3) gives:

$$(\mathcal{J}_n - F_n\phi_P) - (\mathcal{J}_s - F_s\phi_P) + (\mathcal{J}_e - F_e\phi_P) - (\mathcal{J}_w - F_w\phi_P) = \overline{S(\phi)} \tag{4.3.5}$$

According to Patankar's (1980) derivation,

$$\begin{cases} \mathcal{J}_n - F_n\phi_P = a_N(\phi_P - \phi_N) \\ \mathcal{J}_s - F_s\phi_P = a_S(\phi_S - \phi_P) \\ \mathcal{J}_e - F_e\phi_P = a_E(\phi_P - \phi_E) \\ \mathcal{J}_w - F_w\phi_P = a_W(\phi_W - \phi_P) \end{cases}, \tag{4.3.6}$$

the discretization form of the governing equation (3.6.14) is :

$$a_P\phi_P = a_N\phi_N + a_S\phi_S + a_E\phi_E + a_W\phi_W + \overline{S(\phi)}, \tag{4.3.7}$$

where the convection and diffusion coefficients, a_N, a_S, a_E , a_W and a_P , are calculated using discretization schemes. For example, the well known upwind scheme,

$$\begin{cases} a_N = D_n + max(-F_n, 0) \\ a_S = D_s + max(F_s, 0) \\ a_E = D_e + max(-F_e, 0) \\ a_W = D_w + max(F_w, 0) \\ a_P = (a_N + a_S + a_E + a_W) \end{cases} ; \tag{4.3.8}$$

Using the under relaxation technique, which is essential for an iterative process and a classical method for solving the above elliptic problems, yields:

$$a_P\phi_P = \alpha_P\left[a_N\phi_N + a_S\phi_S + a_E\phi_E + a_W\phi_W + \overline{S(\phi)}\right] + (1-\alpha_P)a_P\phi_P^* \ , \tag{4.3.9}$$

where ϕ_P^* is the value of last iteration; α_P is the under relaxation factor. Introducing $a_P' = a_P/\alpha_P$, the above equation (4.3.9) becomes:

$$a'_P\phi_P = a_N\phi_N + a_S\phi_S + a_E\phi_E + a_W\phi_W + \overline{S(\phi)} + (1-\alpha_\phi)a'_P\phi^*_P \qquad (4.3.10)$$

For simplicity, writing a'_P as a_P,

$$a_P\phi_P = a_N\phi_N + a_S\phi_S + a_E\phi_E + a_W\phi_W + \overline{\overline{S(\phi)}} \quad , \qquad (4.3.11)$$

where

$$a_P = (a_N + a_S + a_E + a_W)/\alpha_\phi \quad , \qquad (4.3.12)$$

the source term is given by:

$$\overline{\overline{S(\phi)}} = \overline{S(\phi)} + (1-\alpha_P)a_\phi\phi^*_P \quad . \qquad (4.3.13)$$

Equation (4.3.11) is the final form of discretized equations solved by computer code using FORTRAN language.

4.3.2 Discretization of conservation of charge equation

To integrate the generalized conservation of charge equation (3.6.19) over the control volume shadowed in figure 4.2

$$\left(W_1 + \frac{E_1}{\mathrm{Re}\,\mathrm{Pr}_E}\right)\nabla\eta \;\; q\Big|_s^n + \left(W_2 + \frac{E_2}{\mathrm{Re}\,\mathrm{Pr}_E}\right)\nabla\xi \;\; q\Big|_w^e = 0 \qquad (4.3.14)$$

Similarly to the procedure of discretization of the transport equations:

$$\begin{cases} F_n = r_n\left(W_1 + \dfrac{E_1}{Re\,Pr_E}\right)_n \Delta\eta \\ F_s = r_s\left(W_1 + \dfrac{E_1}{Re\,Pr_E}\right)_s \Delta\eta \\ F_e = r_e\left(W_2 + \dfrac{E_2}{Re\,Pr_E}\right)_e \Delta\xi \\ F_w = r_w\left(W_1 + \dfrac{E_2}{Re\,Pr_E}\right)_w \Delta\xi \end{cases}, \tag{4.3.15}$$

then:

$$F_n q_n - F_s q_s + F_e q_e - F_w q_w = 0 \tag{4.3.16}$$

Since the equation (3.6.19) is a pure convective transport equation, no diffusion terms are involved, the up-wind discretization scheme can be applied:

$$\begin{cases} F_n q_n = q_P\, max(F_n, 0) - q_N\, max(-F_n, 0) \\ F_s q_s = q_S\, max(F_s, 0) - q_P\, max(-F_s, 0) \\ F_e q_e = q_P\, max(F_e, 0) - q_E\, max(-F_e, 0) \\ F_w q_w = q_W\, max(F_w, 0) - q_P\, max(-F_w, 0) \end{cases}, \tag{4.3.17}$$

equation (4.3.16) then becomes:

$$a_P q_P = a_N q_N + a_S q_S + a_E q_E + a_W q_W \ , \tag{4.3.18}$$

where

$$\begin{cases} a_N = max(-F_n, 0) \\ a_S = max(F_s, 0) \\ a_E = max(-F_e, 0) \\ a_W = max(F_w, 0) \\ a_P = max(F_n, 0) + max(-F_s, 0) + max(F_e, 0) + max(-F_w, 0) \\ \quad = \ a_N + a_S + a_E + a_W + (F_n - F_s + F_e - F_w) \end{cases} \tag{4.3.19}$$

The coefficient a_P in equation (4.3.19) can be further changed into the following (see the appendix for derivation),

$$a_P = a_N + a_S + a_E + a_W + \frac{\tilde{J}r}{Re\,Pr_E} N_E q \Delta\xi\Delta\eta \tag{4.3.20}$$

Using under relaxation technique gives:

$$a_P q_P \ = \ a_N q_N + a_S q_S + a_E q_E + a_W q_W + a_P (1 - \alpha_\phi) q_P \tag{4.3.21}$$

where

$$a_P = \left[a_N + a_S + a_E + a_W + \frac{\tilde{J}r}{Re\,Pr_E} N_E q \Delta\xi \Delta\eta \right] \Big/ \alpha_\phi \tag{4.3.22}$$

4.3.3 Discretization of Electric Potential Equation

Similar to the procedure for the discretization of transport equations, the generalized electric potential equation (3.6.21) is integrated over the control volume shadowed in figure 4.2 with the centre point P as follows:

$$\frac{r\alpha}{\tilde{J}} \frac{\partial \varphi}{\partial \xi} \Delta\eta \Big|_s^n + \frac{r\gamma}{\tilde{J}} \frac{\partial \varphi}{\partial \eta} \Delta\xi \Big|_w^e + S'(\varphi) + \tilde{J}r(N_E q)\Delta\xi\Delta\eta = 0, \tag{4.3.23}$$

where

$$S'(\varphi) = \left(\frac{-r\beta}{\tilde{J}} \frac{\partial \varphi}{\partial \eta} \right) \Delta\eta \Big|_s^n + \left(\frac{-r\beta}{\tilde{J}} \frac{\partial \varphi}{\partial \xi} \right) \Delta\xi \Big|_w^e \quad . \tag{4.3.24}$$

The centre difference scheme is used to approximate $\frac{\partial \varphi}{\partial \xi}$ and $\frac{\partial \varphi}{\partial \eta}$ as follows:

$$\left(\frac{r\alpha}{\tilde{J}} \right)_n \Delta\eta \frac{\varphi_N - \varphi_P}{\xi_N - \xi_P} - \left(\frac{r\alpha}{\tilde{J}} \right)_s \Delta\eta \frac{\varphi_P - \varphi_S}{\xi_P - \xi_S} +$$

$$\left(\frac{r\gamma}{\tilde{J}} \right)_e \Delta\xi \frac{\varphi_E - \varphi_P}{\eta_E - \eta_P} - \left(\frac{r\gamma}{\tilde{J}} \right)_w \Delta\xi \frac{\varphi_P - \varphi_w}{\eta_P - \eta_w} + S(\varphi) \quad . \tag{4.3.25}$$

$$= 0$$

The above equation (4.3.25) can be written as:

$$a_P\varphi_P = a_N\varphi_N + a_S\varphi_S + a_E\varphi_E + a_W\varphi_W + S(\varphi) \quad , \tag{4.3.26}$$

where

$$\begin{cases} a_N = \left(\dfrac{r\alpha}{\tilde{J}}\right)_n \Delta\eta \dfrac{1}{\xi_N - \xi_P} \\ a_S = \left(\dfrac{r\alpha}{\tilde{J}}\right)_s \Delta\eta \dfrac{1}{\xi_P - \xi_S} \\ a_E = \left(\dfrac{r\gamma}{\tilde{J}}\right)_e \Delta\xi \dfrac{1}{\eta_E - \eta_P} \\ a_W = \left(\dfrac{r\gamma}{\tilde{J}}\right)_w \Delta\xi \dfrac{1}{\eta_P - \eta_W} \\ a_P = (a_N + a_S + a_E + a_W) \end{cases} , \tag{4.3.27}$$

the source term is given by:

$$S(\varphi) = \tilde{J}r(N_E q)\Delta\xi\Delta\eta + \left(\frac{-r\beta}{\tilde{J}}\frac{\partial\varphi}{\partial\eta}\right)\Delta\eta\Big|_s^n + \left(\frac{-r\beta}{\tilde{J}}\frac{\partial\varphi}{\partial\xi}\right)\Delta\xi\Big|_w^e . \tag{4.3.28}$$

Again, using the under relaxation scheme:

$$a_P\varphi_P = a_N\varphi_N + a_S\varphi_S + a_E\varphi_E + a_W\varphi_W + S(\varphi) + a_P(1-\alpha_\phi)\varphi_P , \tag{4.3.29}$$

where

$$a_P = \left[a_N + a_S + a_E + a_W\right]/\alpha_\phi \quad , \tag{4.3.30}$$

$\alpha_\phi \leq 1$ is the under relaxation factor.

4.3.4 QUICK scheme and Deferred Correction

To apply the control-volume method, the value of ϕ and its normal derivative at the interfaces are often required. There are many approximation approaches for this purpose, such as upwind difference scheme (UDS) which has been used in above, linear interpolation scheme or central difference scheme (CDS), quadratic upwind interpolation for convective kinematics (QUICK) scheme (Leonard, 1979) and other higher-order schemes such as those introduced by Ferziger and Peric (1996).

The upwind scheme UDS is first-order in accuracy, which is numerically stable but highly diffusive in situations such as when the flow field is oblique to the grid lines in combination with a non-zero gradient of the dependent variable in the direction normal to the flow. Therefore it often leads to inaccuracy in the results and causes smearing of sharp gradients (Darwish and Moukalled, 1994). To increase the accuracy, higher order

schemes should be used. In this thesis, the QUICK scheme is used, which has third-order accuracy to discretise the convection term.

QUICK scheme

The QUICK scheme is to approximate the variable profile ϕ_e between P and E shown in figure 4.2 by a parabola instead of a straight line such as in the UDS scheme. A third point is needed to construct a parabola. By nature, the upstream point W is chosen, if the flow is from P to E. Approximating ϕ_e is obtained by following:

$$\phi_e = a_1\phi_E - a_2\phi_W + (1 - a_1 + a_2)\phi_P \quad , \tag{4.3.31}$$

where the coefficients a_1, a_2 are defined by the interpolation factors as:

$$\begin{cases} a_1 = \dfrac{(2 - f_{e,W})f_{e,P}^2}{1 + f_{e,P} - f_{e,W}} \\ \\ a_2 = \dfrac{(1 - f_{e,P})(1 - f_{e,W})^2}{1 + f_{e,P} - f_{e,W}} \end{cases} , \tag{4.3.32}$$

the interpolation factors take the form :

$$f_{e,P} = \frac{x_e - x_P}{x_E - x_P}, \quad f_{e,W} = \frac{x_e - x_W}{x_E - x_W} \quad . \tag{4.3.33}$$

Similarly, the values of ϕ at other control-volume cell surfaces can be obtained. The values obtained by the QUICK scheme were denoted with a superscript *H*; so the control-volume cell surface ϕ values calculated by the QUICK scheme are ϕ_e^H , ϕ_w^H, ϕ_n^H and ϕ_s^H.

Deferred Correction

Using a higher-order interpolation scheme or quadrate approximation scheme often leads to a large computational requirement; and the higher-order schemes also have unavoidable instability, which are harmful to numerical calculations. The deferred correction method proposed by Khosla and Rubin (1974) is a remedy for these problems; and the method is introduced as following:

In equations (4.3.3), the value of ϕ_f ($f = n, s, e, w$) is calculated using the first-order upwind scheme and obtained the discretised equation (4.3.11). For the convenience of description, the cell-face values of ϕ calculated by the first order upwind scheme are denoted as ϕ_f^U. Therefore, the cell-face convective fluxes in equation (4.3.3) can be replaced by their equivalent fluxes:

$$\mathcal{F}_f^C = F_f\phi_f^H = F_f\phi_f^U - F_f\left(\phi_f^U - \phi_f^H\right), \tag{4.3.34}$$

equation (4.3.3) is transformed to follows:

$$\begin{aligned}&\left(\mathcal{F}_n^D + F_n\phi_n^U\right) - \left(\mathcal{F}_s^D + F_s\phi_s^U\right) + \left(\mathcal{F}_e^D + F_e\phi_e^U\right) - \left(\mathcal{F}_w^D + F_w\phi_w^U\right) \\ &= \overline{S(\phi)} + S_{DC}\end{aligned}, \tag{4.3.35}$$

where S_{DC} is the contribution due to the adopted deferred correction procedure,

$$S_{DC} = F_n\left(\phi_n^U - \phi_n^H\right) - F_s\left(\phi_s^U - \phi_s^H\right) + F_e\left(\phi_e^U - \phi_e^H\right) - F_w\left(\phi_w^U - \phi_w^H\right). \tag{4.3.36}$$

The final discretised governing equations take a general form as follows:

$$a_P\phi_P = a_N\phi_N + a_S\phi_S + a_E\phi_E + a_W\phi_W + \overline{\overline{S(\phi)}} + S_{DC}, \tag{4.3.37}$$

where the discretisation coefficients, a_P, a_N, a_S, a_E, a_W and the source term $\overline{\overline{S(\phi)}}$ are the same as those in equation (4.3.11).

By now, the discretised equations for the governing equations are obtained. At a random grid point P in the computational domain, the dependent variables for solution are u_P, v_P, T_P, q_P, φ_P, E_{xP} and E_{yP}; and equations (4.3.37) (four equations when ϕ_P varies in 1, u_P, v_P, T_P), (4.3.21) and (4.3.29) are discretised. For the governing equation (3.6.5), it can be simply discretised by using central difference equation, results in two discretised equations for E_{xP} and E_{yP} respectively. Therefore, the number of

discretised equations equal to that of dependent variables; unique numerical solutions can be obtained if the boundary conditions are well-posed.

4.4 Pressure Correction Technique

In the discretized equations for flow fields, i.e., in equation (4.3.37), there is no independent equation for the pressure variable. This has made the solution of Navier-Stokes equations very complicated. Furthermore, the continuity equation does not contain the pressure. How to couple the pressure with velocity so as to satisfy the continuity equations has been the main task to solve the Navier-Stokes equations.

The pressure correction technique was developed by Patankar and Spalding (1972) and embodied in an algorithm called SIMPLE (Semi-Implicit Method for Pressure-Linked Equations), which has found widespread applications over the past thirty years for both compressible and incompressible flows. In this work, the focus is only given to the incompressible viscous flow.

4.4.1 Non-Staggered Grid Arrangement

Using central differences scheme for the incompressible continuity equation will result in the checkerboard velocity distribution, as well as for the pressure gradients illustrated in figure 4.3.

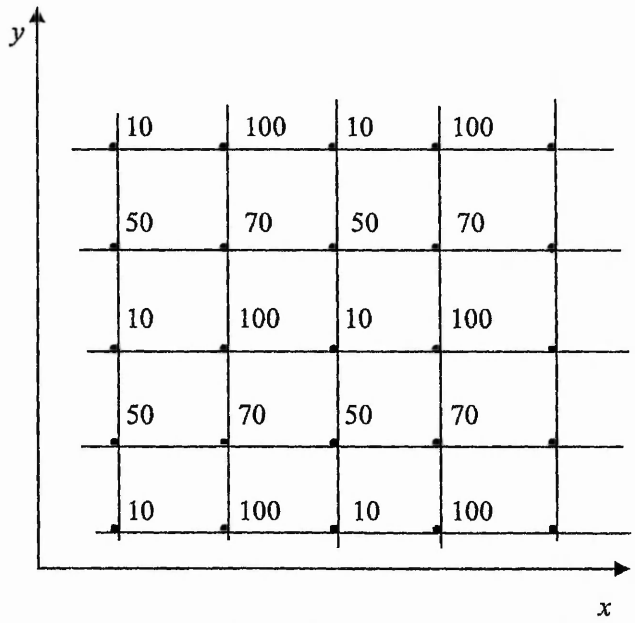

Fig 4.3 Discrete checkerboard pressure distribution

Clearly, the pressure field discretized in figure 4.3 gives zero pressure gradients in the x and y directions, respectively. For maintaining the central differencing scheme, the staggered grid arrangement (Patankar and Spalding, 1972) and the non-staggered grid arrangement with a momentum interpolation technique (Rhie and Chow, 1983) are two methodologies to solve this problem.

The non-staggered grid arrangement in which all the variables are stored at the same set of grid points is adopted for this work because of the significant advantages of this method over the staggered grid arrangement:

(i) all variables share the same location; hence, only one set of control volume is

needed;

(ii) in a discretized equation, the convection contribution to the coefficients is same for all variables;

(iii) for a complex geometry, Cartesian velocity components can be used in conjunction with non-orthogonal coordinates, yielding simpler equations than when numerical coordinate-oriented velocity components are employed (Peric, Kessler and Scheuerer,1988).

4.4.2 Pressure Correction Equation and Momentum Interpolation Scheme

In order to sort the checkerboard pressure distribution problem out, the coupling of pressure-velocity must be introduced. The coupling of pressure-velocity consists of two steps; one is momentum interpolation and the other is pressure correction.

4.4.2.1 Pressure Correction Equation

Setting $\phi = u$ and $\phi = v$ in equation (4.3.7), respectively, gives:

$$\begin{cases} u^* = h_u + B_u \dfrac{\partial p^*}{\partial \xi} + C_u \dfrac{\partial p^*}{\partial \eta} \\ v^* = h_v + B_v \dfrac{\partial p^*}{\partial \xi} + C_v \dfrac{\partial p^*}{\partial \eta} \end{cases}, \tag{4.4.1}$$

where

$$\begin{cases} B_u = \left(-\dfrac{ry_\eta \Delta\xi\Delta\eta}{a_P} \right)_P \\ C_u = \left(\dfrac{ry_\xi \Delta\xi\Delta\eta}{a_P} \right)_P \\ B_v = \left(\dfrac{rx_\eta \Delta\xi\Delta\eta}{a_P} \right)_P \\ C_v = \left(-\dfrac{rx_\xi \Delta\xi\Delta\eta}{a_P} \right)_P \\ h_u = \dfrac{\sum a_{NB} u^*_{NB} + \overline{\overline{S'(u)}}}{a_P} \\ h_v = \dfrac{\sum a_{NB} v^*_{NB} + \overline{\overline{S'(v)}}}{a_P} \end{cases} ; \qquad (4.4.2)$$

$\overline{\overline{S'(u)}}$ and $\overline{\overline{S'(v)}}$ are the rest terms of $\overline{S(\phi)}$ in equation (4.3.7) after the pressure gradients are taken out, for $\phi = u$ and $\phi = v$, respectively. p^* is an initial pressure, u^* and v^* are the values obtained using the initial pressure p^*.

In the iteration procedures, the flow fields of u^*, v^* and p^* (the superscript asterisk denotes an intermediate iteration value) cannot satisfy conservation of both continuity and momentum, therefore the corrections should be applied as

$$\begin{cases} u = u^* + B_u \dfrac{\partial p'}{\partial \xi} + C_u \dfrac{\partial p'}{\partial \eta} \\ v = v^* + B_v \dfrac{\partial p'}{\partial \xi} + C_v \dfrac{\partial p'}{\partial \eta} \\ p = p^* + p' \\ W_1 = W_1^* + W_1' \\ W_2 = W_2^* + W' \end{cases} \tag{4.4.3}$$

where u', v', W_1' and W_2' are the corrections of velocity, and p' is the pressure correction.

The correction of curvilinear velocities W_1 and W_2 given:

$$\begin{cases} W_2 = W_2^* + \left(B_u y_\eta - B_v x_\eta\right)\dfrac{\partial p'}{\partial \xi} + \left(C_u y_\eta - C_v y_\eta\right)\dfrac{\partial p'}{\partial \eta} \\ W_2 = W_2^* + \left(C_v x_\xi - C_u y_\xi\right)\dfrac{\partial p'}{\partial \eta} + \left(B_v x_\xi - B_u y_\xi\right)\dfrac{\partial p'}{\partial \xi} \end{cases} \tag{4.4.4}$$

Define the symbols:

$$B_1 = B_u y_\eta - B_v x_\eta = \left(-\frac{r\Delta\xi\Delta\eta}{a_P}\right)\alpha \tag{4.4.5a}$$

$$B_2 = B_v x_\xi - B_u y_\xi = \left(\frac{r\Delta\xi\Delta\eta}{\alpha_P} \right) \beta \tag{4.4.5b}$$

$$C_1 = C_u y_\eta - C_v x_\eta = \left(\frac{r\Delta\xi\Delta\eta}{\alpha_P} \right) \beta \tag{4.4.5c}$$

$$C_2 = C_v x_\xi - C_u y_\xi = \left(-\frac{r\Delta\xi\Delta\eta}{\alpha_P} \right) \gamma \tag{4.4.5d}$$

when the grid is not severely non-orthogonal, equation of (4.4.4) can be reduced as:

$$\begin{cases} W_1 = W_1^* + B_1 \dfrac{\partial p'}{\partial \xi} \\ W_2 = W_2^* + C_2 \dfrac{\partial p'}{\partial \eta} \end{cases}, \tag{4.4.6}$$

Combine equations (4.4.6) with equation (4.3.4), the continuity equation gives:

$$\begin{aligned} & r_n \Delta\eta \left[W_{1n}^* + W_{1n}' \right] - r_s \Delta\eta \left[W_{1s}^* + W_{1s}' \right] + \\ & r_e \Delta\xi \left[W_{2e}^* + W_{2e}' \right] - r_w \Delta\xi \left[W_{2w}^* + W_{2w}' \right] \\ & = 0 \end{aligned} \quad , \tag{4.4.7}$$

applying the central differences scheme for the correction pressure gradient :

$$W_{1n}' = B_{1n} \left(\frac{p_N' - p_P'}{\xi_N - \xi_P} \right) \quad , \tag{4.4.8a}$$

$$W_{1s}' = B_{1s} \left(\frac{p_P' - p_S'}{\xi_P - \xi_S} \right) \quad , \tag{4.4.8b}$$

$$W'_{2e} = C_{2e}\left(\frac{p'_E - p'_P}{\eta_E - \eta_P}\right) \quad , \tag{4.4.8c}$$

$$W'_{2w} = C_{2w}\left(\frac{p'_P - p'_W}{\eta_P - \eta_W}\right) \quad . \tag{4.4.8d}$$

The relations between the corrections of velocity and pressure are obtained as following:

$$\begin{cases} u' = \left(-\dfrac{\Delta\xi\Delta\eta}{a_P}\right)\left(y_\eta \dfrac{\partial p'}{\partial \xi} - y_\xi \dfrac{\partial p'}{\partial \eta}\right) \\ v' = \left(-\dfrac{\Delta\xi\Delta\eta}{a_P}\right)\left(-x_\eta \dfrac{\partial p'}{\partial \xi} + x_\xi \dfrac{\partial p'}{\partial \eta}\right) \end{cases} , \tag{4.4.9}$$

Rearranging equation (4.4.7), we have the pressure correction equation:

$$C_P p'_P = \sum_{NB} C_{NB} p'_{NB} + \dot{m}_P , \tag{4.4.10}$$

where $NB = N,\ S,\ E,\ W$,

$$C_N = \left(-r_n B_{1n} \Delta\eta\right)/\left(\xi_N - \xi_P\right) , \tag{4.4.11a}$$

$$C_S = \left(-r_s B_{1s} \Delta\eta\right)/\left(\xi_P - \xi_S\right) , \tag{4.4.11b}$$

$$C_E = \left(-r_e C_{2e} \Delta\xi\right)/\left(\eta_E - \eta_P\right) , \tag{4.4.11c}$$

$$C_W = \left(-r_w C_{2w} \Delta\xi\right)/\left(\eta_P - \eta_W\right) , \tag{4.4.11d}$$

$$C_P = C_N + C_S + C_E + C_W , \tag{4.4.11e}$$

and

$$\dot{m}_P = \left(W_{1s}^* r_s - W_{1n}^* r_n\right)\Delta\eta + \left(W_{2w}^* r_w - W_{2e}^* r_e\right)\Delta\xi . \qquad (4.4.11f)$$

4.4.2.2 Modified Momentum Interpolation Scheme

The momentum interpolation scheme by Rhie and Chow (1983) can cause numerical results dependent on the relaxing factor (Majumdar, 1988) and the linearity of the pressure field (Zhang, Yan and Hull, 2001). In this work, a modification to the momentum interpolation scheme for calculating cell-face curvilinear velocities is proposed.

Rhie and Chow's Momentum Interpolation Scheme

The coupling of velocity and pressure variables stored in non-staggered grids needs a special strategy. To supply this strategy, Rhie and Chow's momentum interpolation scheme uses the pressure gradient to evaluate the cell-face velocity and to eliminate 'checkerboard' fields. This mechanism can be explained by the derivations of the momentum interpolation scheme. For convenience of description, only the interpolation in ξ direction is shown here, as that for η is similar. As stated in section 4.4.2.1:

$$W_1 = H_1 + B_1 \frac{\partial p}{\partial \xi}, \qquad (4.4.12)$$

where B_1 is calculated according to equation (4.4.5a); H_1 is the difference between W_1 and the pressure gradient term. The momentum interpolation scheme is a formula to

calculate the cell-face velocities. For example, in order to calculate W_1 at cell-face n, equation (4.4.12) is first applied to grid nodes P and N as

$$\begin{cases} W_{1P} = H_{1P} + B_{1P}\left(\dfrac{\partial p}{\partial \xi}\right)_P \\ \\ W_{1N} = H_{1N} + B_{1N}\left(\dfrac{\partial p}{\partial \xi}\right)_N \end{cases}, \tag{4.4.13}$$

then the cell-face velocity W_{1n} is expected to take the form of

$$W_{1n} = H_{1n} + B_{1n}\left(\frac{\partial p}{\partial \xi}\right)_n . \tag{4.4.14}$$

An interpolation between W_{1P} and W_{1N} is obtained as

$$W_{1n} = \overline{W_{1n}} + \overline{B_{1n}}\left(\frac{p_N - p_P}{\xi_N - \xi_P} - \overline{\left(\frac{\partial p}{\partial \xi}\right)_n}\right), \tag{4.4.15a}$$

where the terms with top bars are the linear interpolation between the corresponding parts of W_{1P} and W_{1N}. Similarly,

$$W_{2e} = \overline{W_{2e}} + \overline{C_{2e}}\left(\frac{p_E - p_P}{\eta_E - \eta_P} - \overline{\left(\frac{\partial p}{\partial \eta}\right)_e}\right), \tag{4.4.15b}$$

The term in the square bracket has fourth-order accuracy and is designed to recognise the Pressure-velocity in a numerical calculation. The formula for W_{1s} and W_{2w} can be

obtained in a similar manner and have been omitted here. Denote two iteration steps with superscripts K and K+1, the value of ϕ obtained from Equation (4.3.7) for a new iteration but without relaxation is taken as ϕ^{new}, then:

$$\phi^{K+1} = \alpha_\phi \left[\frac{\sum a_{NB}\phi_{NB} + \overline{S(\phi)}}{a_P} \right]^{new} + (1-\alpha_\phi)\phi^K \; ; \tag{4.4.16}$$

and the cell-face velocity,

$$\begin{cases} W_{1n}^{K+1} = \alpha_\phi \left\{ \overline{W_{1n}} + \overline{B_{1n}} \left[\left(\frac{\partial p}{\partial \xi} \right)_n - \overline{\left(\frac{\partial p}{\partial \xi} \right)_n} \right] \right\}^{new} + (1-\alpha_\phi)\overline{W}_{1n}^K \\ W_{2e}^{K+1} = \alpha_\phi \left\{ \overline{W_{2e}} + \overline{C_{2e}} \left[\left(\frac{\partial p}{\partial \xi} \right)_e - \overline{\left(\frac{\partial p}{\partial \xi} \right)_e} \right] \right\}^{new} + (1-\alpha_\phi)\overline{W}_{2e}^K \end{cases}, \tag{4.4.17}$$

where α_ϕ is the under relaxation factor. Equation (4.4.17) are Rhie and Cow's momentum interpolation scheme to solve basic equations with under relaxed iteration.

Defects of Rhie and Chow's Scheme

Two defects of Rhie's scheme of momentum interpolation may be identified.

Defect 1: Relaxing Factor Dependency

As argued by Majumdar (1988), the momentum interpolation scheme, Equations (4.4.18a, b), can result in a relaxing-factor dependent numerical solution. This relaxing-

factor dependency can be easily explained. In Equations (4.4.17a, b), the cell-face velocity W_{1n}, is a compound of two parts. The first part is the "momentum interpolation" based on the values without relaxation, denoted as *MI*; and the second part is the "linear interpolation" based on the K's iteration, denoted as *LI*. Therefore, Equation (4.4.17) means:

$$W_{1n} = \alpha_\phi MI + (1-\alpha_\phi)LI\,. \tag{4.4.18}$$

However, the "momentum interpolation" and "linear interpolation" are two different interpolation methods, which mean $MI \neq LI$. This is to say, for a physical problem, different numerical results can be obtained only because a different value of the relaxing factor is used.

Defect 2: Dependency on Linearity of Pressure

In pervious work (Zhang, Yan and Hull, 2001), it was also observed that Rhie and Chow's momentum interpolation scheme equations (4.4.17) give a numerical solution dependent on the linearity of pressure. It was noticed that, for calculating the fully developed viscous flow in a curved and extending duct, the flow rates (this also means the main stream velocity) through different cross sections where mesh is non-uniform in streamwise direction, can vary considerably, although the numerical mesh is fine enough. This observation can be explained by the pressure-linearity dependency of the results by using Rhie and Chow's momentum interpolation scheme. For the convenience of explaining, the interpolation scheme without relaxation, equation

(4.4.15), is used for description.

In order to calculate the unknown terms in the right hand of equations (4.4.15), linear interpolation is used for both H_{1n} and B_{1n}, that is:

$$\begin{cases} H_{1n} = \overline{H}_{1n} = f_1 \cdot H_{1N} + (1 - f_1) \cdot H_{1P} \\ B_{1n} = \overline{B}_{1n} = f_1 \cdot B_{1N} + (1 - f_1) \cdot B_{1P} \end{cases}, \tag{4.4.19}$$

where f_1 is the geometrical interpolation factor. It is reasonable to take $H_{1n} = \overline{H}_{1n}$ as H_1 is only decided by the variable ϕ, which can be regarded as a continuous field. For the parameter B_{1n}, however, it is related to the numerical mesh because it contains mesh-dependent variables α, β or γ (see equation (4.4.5)). As the numerical mesh is possibly non-uniform, there is no reason to take $B_{1n} = \overline{B}_{1n}$. This non-equivalence is neglected in equation (4.4.15). In the calculations using equation (4.4.15), if W_{1n} is expected to converge at $\overline{W}_{1n}$, the term in the square bracket should be zero. This requirement can only be satisfied by regarding the pressure distribution as linear in the ξ- direction. Otherwise, the numerical results are inevitably pressure-linearity dependent.

Modified Momentum Interpolation Scheme

Based on the last section (4.4.2.2), the two defects of Rhie's momentum interpolation scheme can be eliminated with the modified approach being used in the present study. As the first defect is strongly related to the relaxation factor, which is inevitably to be used, the present modification should also start from this.

Consider equation (4.4.16) the iteration values without relaxation, denoted by the superscript *new*, should be obtained by equation (4.3.7) before relaxation is carried out. In the meanwhile, these *new* values need memories except those for levels K and K+1. All these are originally not good for an efficient algorithm and should be eliminated first. This can be done by carrying out the relaxation during iteration; that is, replacing equation (4.3.7) with equation (4.3.11), as has already been done. In this case, the iteration and relaxation are carried out in only one step, and the memory for the intermediate value without relaxation is saved.

The following is straightforward to eliminate the two defects by the relaxation in equation (4.4.17) and taking $B_{1n} \neq \overline{B}_{1n}$ into account. Similarly, setting ϕ=u and ϕ=v in equation (4.3.11) respectively, and then substituting them into equation (3.7.13), gives:

$$W_1^{K+1} = \left(H_1 + B_1 \frac{\partial p}{\partial \xi} \right)^{K+1} + (1-\alpha_\phi) W_1^K \quad . \tag{4.4.20}$$

Again, we apply W_1^{K+1} to nodes P and N, then interpolate to get W_{1n}^{K+1}, our modified momentum interpolation scheme is obtained as following:

$$W_{1n}^{K+1} = \overline{W_{1n}^{K+1}} + \left\{ B_{1n}\left(\frac{\partial p}{\partial \xi}\right)_n - \overline{\left[B_1\left(\frac{\partial p}{\partial \xi}\right)\right]}_n \right\}^{K+1} + \left(1-\alpha_\phi\right)\left(W_{1n}^{K} - \overline{W_{1n}^{K}}\right). \quad (4.4.21)$$

Contrast to equation (4.4.17), $B_{1n} \neq \overline{B}_{1n}$ has been taken into account in equation (4.4.21) therefore, the pressure-linearity dependency of the result is eliminated; In the mean time, the relaxation dependency of the numerical results has also been eliminated by equation (4.4.21), this can be demonstrated as follows.

When the calculation is converged, $W_{1n}^{K+1} = W_{1n}^{K}$ and $\overline{W_{1n}^{K+1}} = \overline{W_{1n}^{K}}$, therefore, equation (4.4.21) can be reduced to:

$$W_{1n} = \overline{W_{1n}} + \left\{ \left(-\frac{\Delta\xi\Delta\eta}{\rho a_P \varepsilon}\alpha \right)_n \left(\frac{\partial p}{\partial \xi}\right)_n - \overline{\left[\left(-\frac{\Delta\xi\Delta\eta}{\rho a_P \alpha_\phi}\alpha \right)\left(\frac{\partial p}{\partial \xi}\right)\right]}_n \right\} \; ; \qquad (4.4.22)$$

According to equation (4.3.12)

$$a_P \alpha_\phi = a_N + a_S + a_E + a_W \, . \qquad (4.4.23)$$

Therefore, W_{1n} is independent of the relaxation factor and the α_ϕ dependency of the numerical result is successfully eliminated.

4.4.3 SIMPLE method

The solution procedure is summarised as:

1) With approximate pressure and velocity fields obtained by a previous iteration or an initial guess, momentum equations (equation (4.3.11) with $\phi = u$ and $\phi = v$; or equation (4.3.37) when the QUICK scheme is used) are solved to obtain u^* and v^*;
2) A momentum interpolation is carried out according to the modified momentum equations, so that the curvilinear velocity components at control volume cell faces, W_{1n}^*, W_{1s}^*, W_{2e}^* and W_{2w}^* are obtained. These values are used to calculate the coefficients of the pressure equation;
3) Solving the pressure correction equation, i.e., equation (4.4.10), to obtain p';
4) Correcting the pressure and the velocity according to equation (4.4.9);
5) Calculating the temperature field by solving energy equation (4.3.11) (or equation (4.3.37) if using the QUICK scheme) with $\phi = T$;
6) Returning to step 1 if the convergent criteria are not satisfied. In this study, the convergence criteria are the dimensionless maximum mass residual, $\max(|\dot{m}_P|) < 1\times10^{-6}$ and the heat balance error, $\left|\overline{Nu}|_C - \overline{Nu}|_H\right| < 1\times10^{-3}$, where $\overline{Nu}|_C$ and $\overline{Nu}|_H$ are averaged Nusselt numbers on cold and hot walls, respectively.

4.5 Code Validation

The numerical methods presented in this chapter are developed into FORTRAN codes. A full list of the codes with necessary explanation of variables and subroutine functions are given in the appendix B. Validations are carried out for calculating heat and flow problems before studying the coupled electric, flow and thermal fields.

4.5.1 Roache Channel Flow

The Roache's (1981) channel flow problem is a well-known configuration designed for testing computer codes dealing with laminar flow in complex geometry. Napolitano and Orlandi (1985) presented a group of results presented in a modelling contest hosted by IHAR and pointed out the benchmark solution for this problem. The flow configuration is shown in figure 4.4.

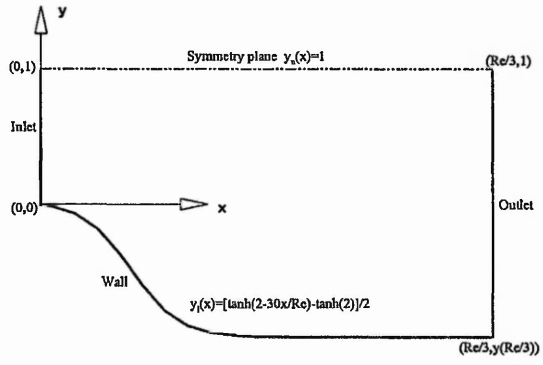

Figure 4.4 Geometry of the Roache channel

In this work, the calculations are carried out at Re=100. Figures 4.5 and 4.6 show the pressure and vorticity distributions along the wall. A grid-independent numerical result can be obtained using a mesh of 21×21; the error of imbalance mass source is 10^{-9}; and the minimum iteration steps to obtain its convergent results are 80. The results indicate that the present calculation is in good agreement with the benchmark solution.

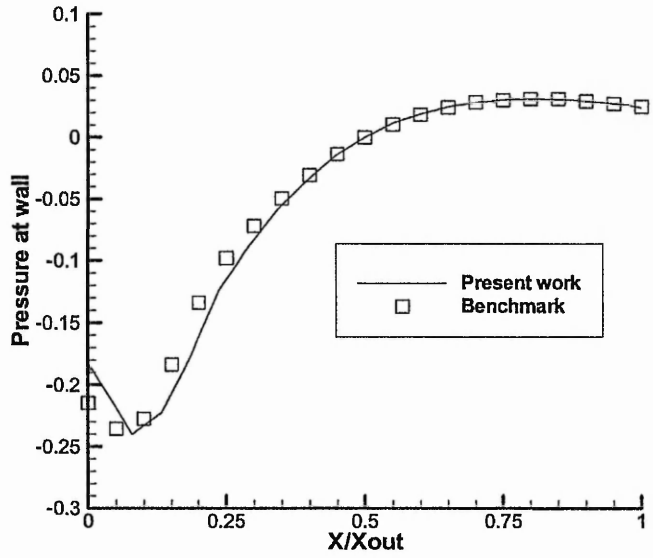

Figure 4.5 Pressure distribution at wall (Re=100)

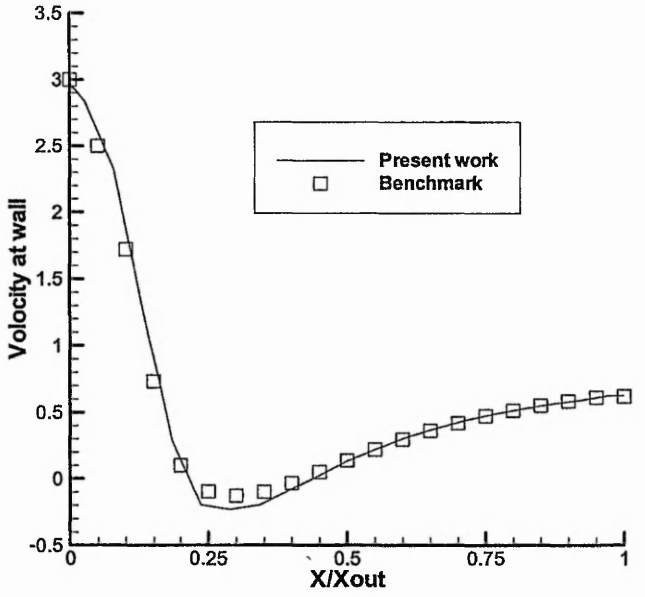

Figure 4.6 Vorticity distribution at wall (Re=100)

4.5.2 Natural convection in Annulus

Natural convection (or buoyancy-driven fluid flow) in an enclosure with differentially heated walls is an important model in heat transfer. Such a heat transfer model is closely related to the performance of many industrial processes and engineering devices. These devices or systems may include air conditioning in a vehicle, reactor insulations, cooling of radioactive waster contained, ventilation of rooms, fire prevention, solar energy collection and crystal growth in liquid. In the last twenty years, many experimental and numerical investigations have been carried out on this subject; Well-documented experimental data are available for natural convection in closed spaces and

this thesis use the annulus experimentally studied by Kuehn and Goldstein (1976) for validation of the codes.

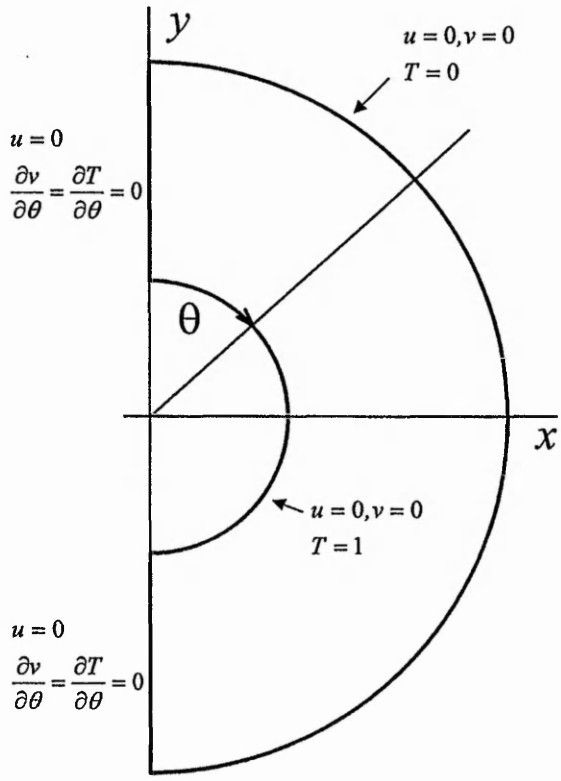

Figure 4.7. Computational domain and boundary conditions for annulus

The annulus has a value of ratio of gap width to inner diameter $L/D_{in} = 0.8$, the Rayleigh number $Ra = \frac{g\beta\Delta T D_{in}^{\ 3}}{\nu^2} Pr = 4.7\times10^4$, and the Prandtl number $Pr = 0.7$. The temperatures of both cylinders are circumferentially uniform. The inner cylinder is heated (T=1) and the outer cylinder is cooled (T=0). The velocity boundary conditions at the wall of inner and outer cylinders are imposed as zero. Because of the symmetry of the geometry, we separate the annulus along its vertical symmetric axis and take a half

as the computational domain, which is shown together with the boundary conditions in figure 4.7. The grid points of the mesh are 182×60 (in the θ and R directions, see figure 4.7). The comparisons of data of equivalent thermal conductivity $K_{eq}=\frac{R\ log(R_{out}/R_{in})}{T_{in}-T_{out}}\frac{\partial T}{\partial R}$, the temperature and angular velocity profiles are shown in figures 4.8, 4.9 and 4.10, respectively. Good agreements between calculation and experiment are obtained. The contours of temperature and the distribution of streamlines of the present calculation are shown in figure 4.11.

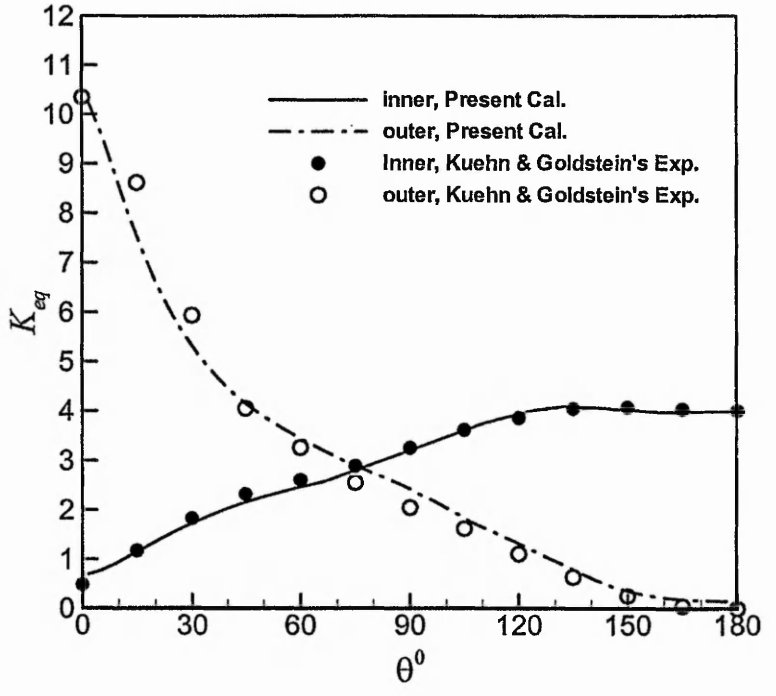

Figure 4.8 Comparison of K_{eq} on annulus walls

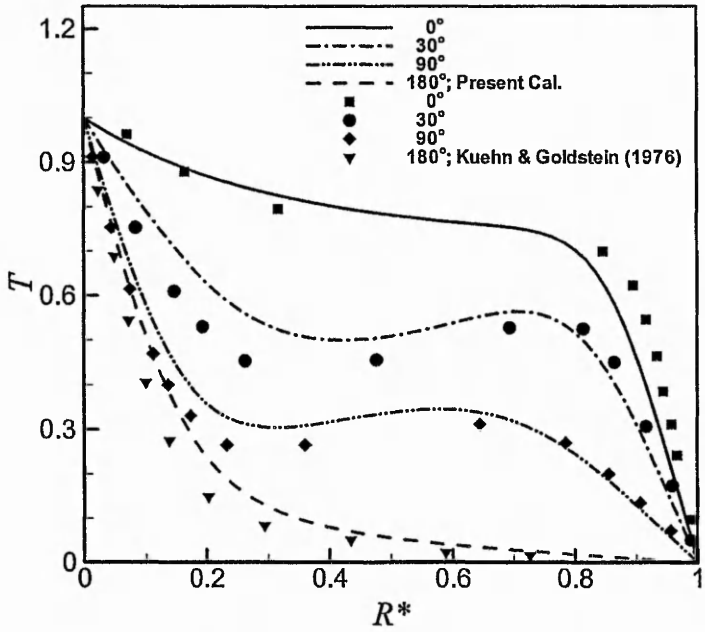

Figure 4.9 Comparison of temperature

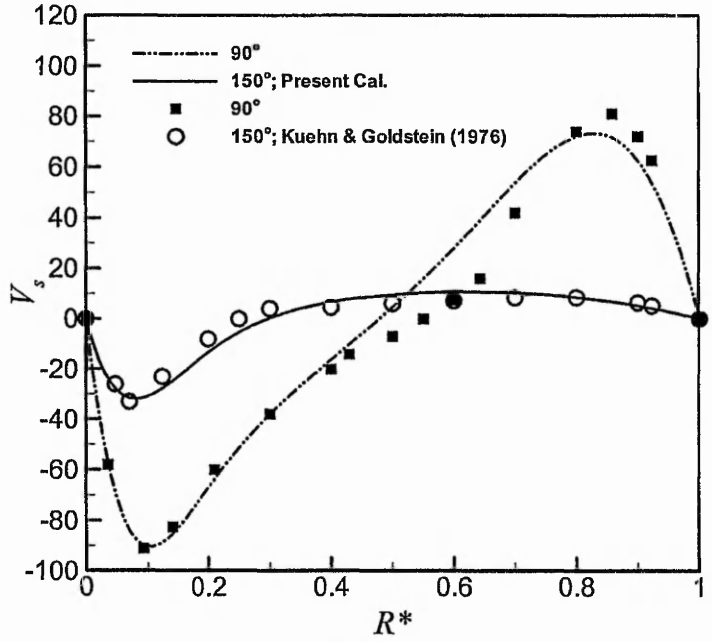

Figure 4.10 Comparison of circumferential velocity

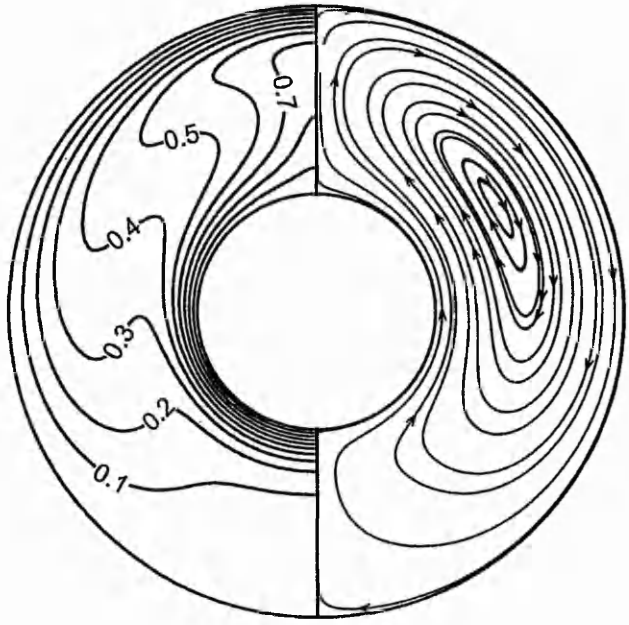

Figure 4.11 Temperature contour and streamlines in the annulus

4.5.3 Natural convection in inclined cavity

The inclined cavity natural convection problem is another benchmark testing case for validation of calculating heat-flow coupling of the code. The data select in this thesis are the benchmark numerical solution for the inclined angle of $\varphi = 90^\circ$ by De.Vahl.D and Jones (1981) and the Laser Doppler Velocimeter (LDV) measurements of velocity at $\varphi = 30^\circ$ and $\varphi = 70^\circ$ by Linthorst et al. (1981).

The physical model

The geometry of a two-dimensional cavity is shown in figure 4.12. The flow of air with Prandtl number $Pr = 0.71$ in the square is assumed to be incompressible. The wall at $x = 0$ and $x = H$ are differentially heated with the hot surface at $x = 0$. The surface at $y = 0$ and $y = H$ are insulated. The inclination angle is defined by the angle between the hot and horizontal walls.

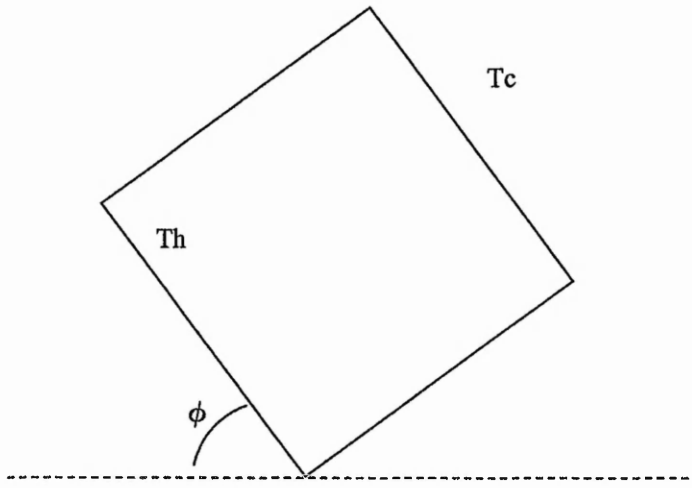

Figure 4.12 Geometry of inclined cavity

The local Nusselt number at a wall is calculated by:

$$Nu = -\frac{H}{\Delta T}\left(\frac{\partial T}{\partial x}\right)_x; \tag{4.5.1}$$

and the averaged Nusselt number:

$$\overline{Nu} = \frac{1}{H}\int_{y=0}^{H} Nu dy. \tag{4.5.2}$$

Natural convection at $\varphi = 90°$

At $\varphi = 90°$, the natural convection at $Ra = 10^3 \sim 10^6$ has been calculated. A comparison of the present results with the benchmark solution in (De.Vahl.D. and Jones, 1981) is presented in Table 4.1. Figs. 4.13 and 4.14 show isothermal and streamline distributions at different Rayleigh numbers. Figure4.15 gives the local Nusselt number along the hot wall. It can be seen from figure 4.14 (a) that, at $Ra = 10^3$, the streamline distribution only shows one vortex, its centre is in the cavity centre. While, figure 4.13 (a) shows that the corresponding isotherms are in parallel with the heated walls, indicating that most of the heat transferred is in heat conduction; this can also be seen in table 4.1, in which the mean Nusselt number is about 1.118. As Rayleigh number increases to as high as $Ra=10^4$, central streamlines are distorted into an elliptic shape (see Figure 4.14 (b)), the isotherms near the vertical walls become thicker. At $Ra=10^5$, the central streamline is further elongated and two secondary vortices appear inside the cavity. As the heat transfer in convection is much stronger than that in conduction, the temperature gradients in the centre of the streams are close to zero, or even negative, thus a negative vorticity is promoted. Indeed, this results in a development of the secondary vortex in the core area; the thermal contours near the vertical walls become even steeper. As the Rayleigh number increases to 10^6 as shown in Figure 4.14 (d), the secondary vortex moves close to the vertical walls and a third vortex appears in the core; the boundary layers adjacent to the vertical walls become thin. Furthermore, as the Raleigh number increases, a peak value of the Nusselt number appears near the bottom of the hot wall; this is as show in Figure 4.15.

Table 4.1 Comparison with benchmark solutions

	Ra= 10^3		Ra= 10^4		Ra= 10^5		Ra= 10^6	
	a	b	a	b	a	b	a	b
$\overline{Nu}$	1.118	1.118	2.238	2.245	4.505	4.526	8.903	8.917
Nu_{max}	1.506	1.506	3.527	3.534	7.717	7.745	18.562	18.266
Nu_{min}	0.691	0.693	0.586	0.601	0.729	0.732	1.002	1.018
u_{max}	3.657	3.632	16.178	16.164	34.77	34.984	64.94	66.483
v_{max}	3.702	3.697	19.643	19.536	68.25	68.428	221.29	221.034

a: benchmark solution b: present work

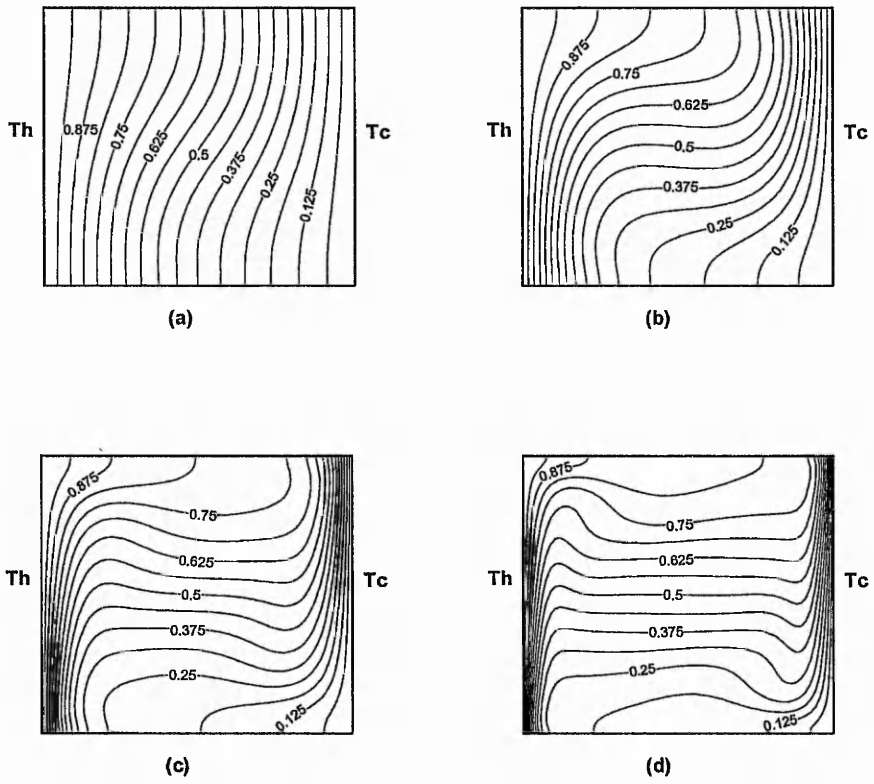

Figure 4.13 Temperature Isothermal at different Ra numbers

(a) Ra=10^3 (b) Ra=10^4 (c) Ra=10^5 (d) Ra=10^6

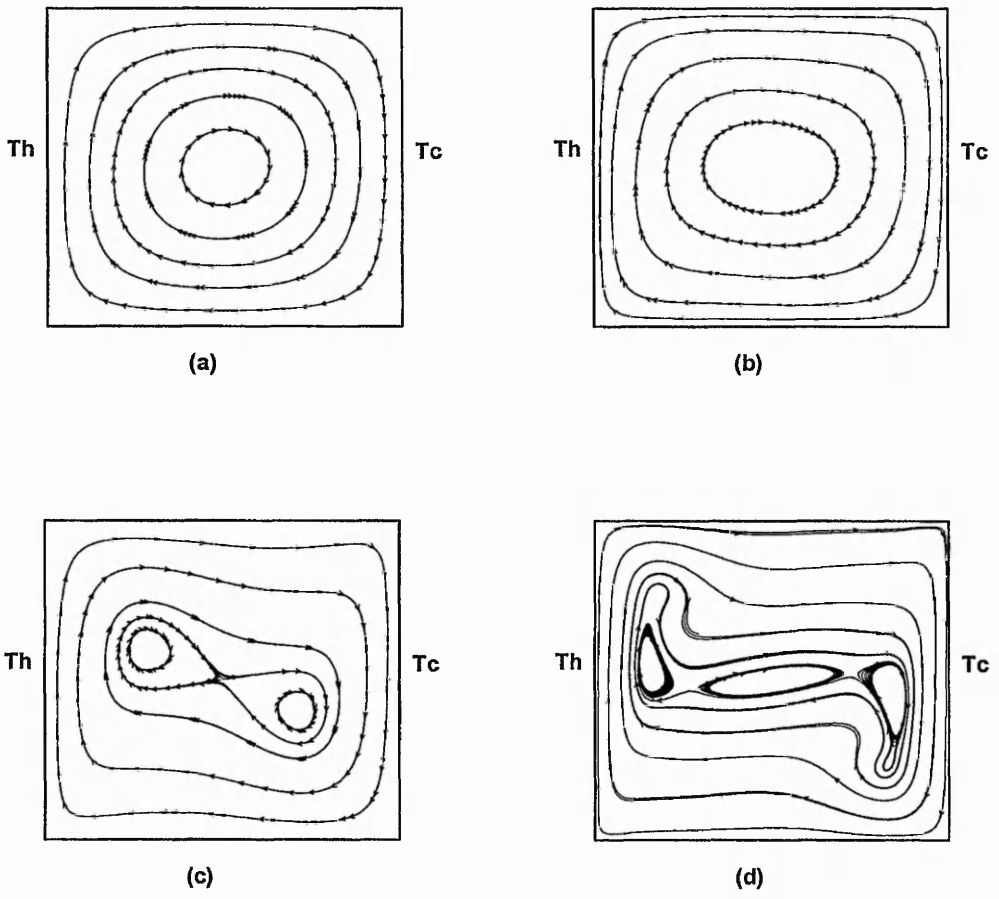

Figure 4.14 Streamlines at different Ra numbers

(a) $Ra=10^3$ (b) $Ra=10^4$ (c) $Ra=10^5$ (d) $Ra=10^6$

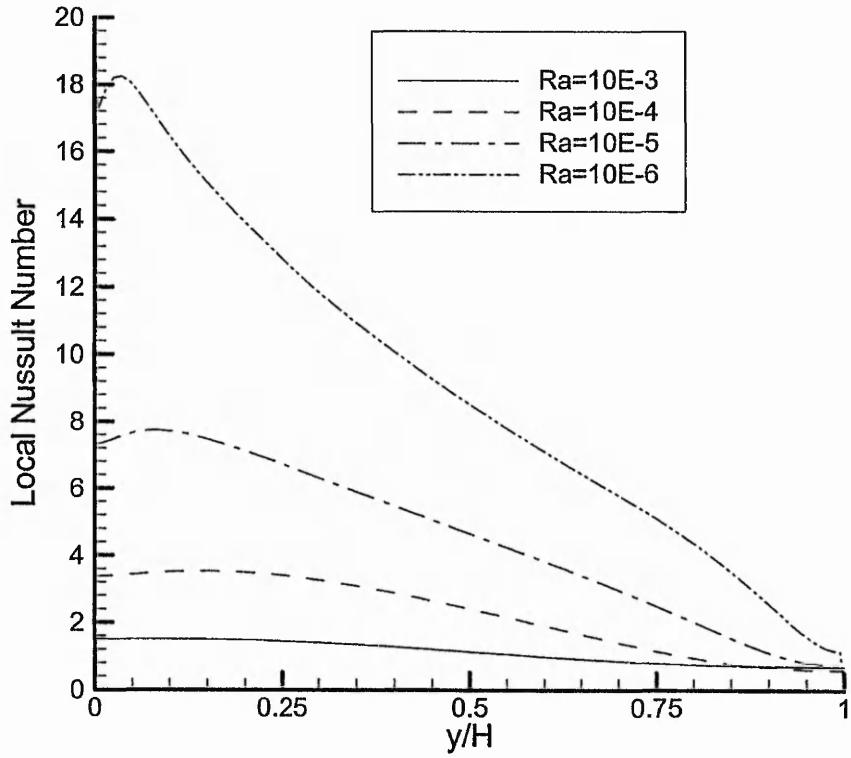

Figure 4.15 Local Nussult Number along the hot wall at different Rayleigh number

Natural convection at different inclined angles

Linthorst et al. (1981) measured the flow structure and velocity distribution using LDV with natural convection in inclined air-filled enclosures. The cases selected for validation of the codes are at $Ra = 1.3\times10^5$, $\varphi = 30°$ and $\varphi = 70°$ respectively; and the value of the height to width aspect ration A_x=1 (square cavity).

The convergent path of the calculation for the case of $\varphi = 30°$ is recorded and shown in

figure 4.16, where E_2 and E_3 are defined as follows:

$$E_2 = \sum_{\substack{k=1,M_1 \\ i=1,M_2}} \left| \dot{m}_P \right| , \tag{4.5.3}$$

$$E_3 = \max\left(\left| \dot{m}_P \right| \right) ; \tag{4.5.4}$$

$\dot{m}_P$ is given by equation (4.4.11). A good and smooth convergent path demonstrates the robustness of the code. The calculated u-velocity profiles (velocity component parallel to the isothermal walls) are compared with their measured values in figure 4.17. Very good agreement is achieved.

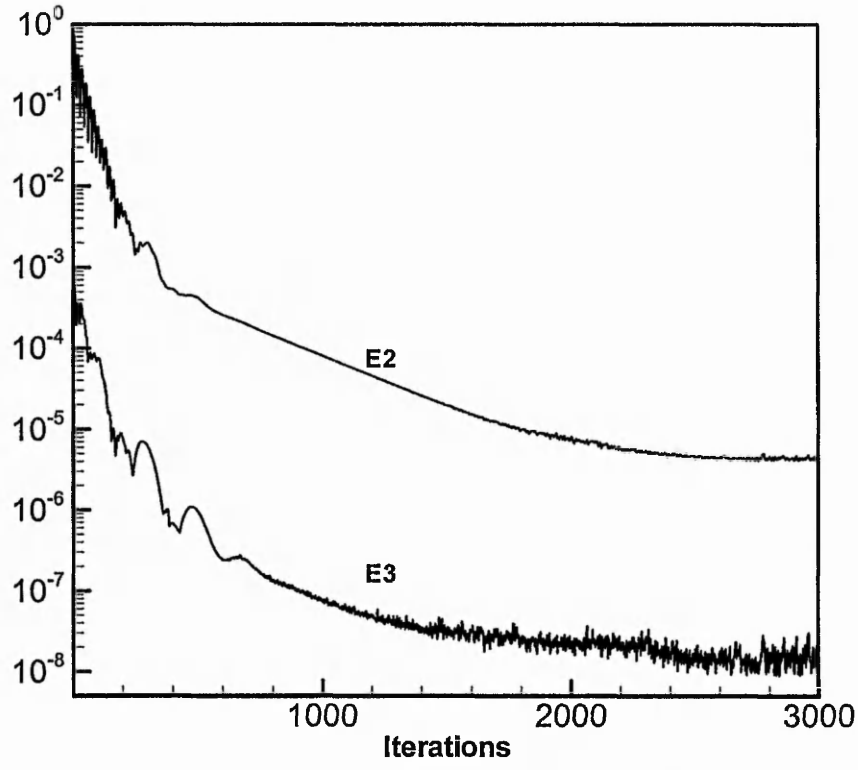

Figure 4.16 Convergent path of the inclined cavity at ϕ=30°

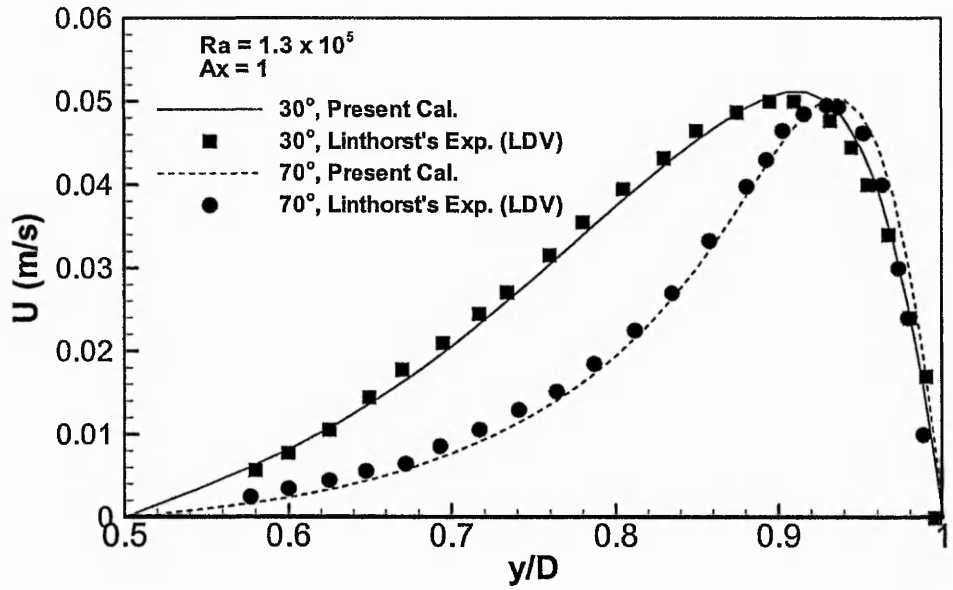

Figure 4.17 Comparison of *u*-velocity distribution at X/D=0.5

Based on the validation of the codes, natural convection in the inclined enclosure at *Ra* = 10^6 with different inclination angles, ranging from 19° to 180°, was further calculated. Figure 4.18 shows the associated temperature distributions. Figure 4.19 shows the streamlines of flow where the structures of vortex can be identified. In Figure 4.20 the local Nusselt number distribution along the hot wall for different inclination angles is presented. According to a combined experimental and numerical study (Hamady and Lloyd (1989), the flow in a square cavity at Ra=10^6 is two-dimensional and laminar for $\varphi \geq 20^\circ$; the present study shows steady numerical results for the flow can be obtained at $\varphi = 19^\circ$.

For heat conduction dominated the heat transfer, in which $\varphi = 180^\circ$ and the fluid is heated from above, the fluid theoretically stands still and the Nusselt number is purely determined by conduction. As $\varphi < 180^\circ$, the air in the cavity starts to move, the velocities along the hot and cold wall increase under rotation; the temperature gradient in the centre of the cavity is even steeper, and therefore, the mean Nusselt number grows rapidly.

At $\varphi = 90^\circ$, the fluid being heated from the side, the flow is thoroughly dominated by the boundary layer flow along the hot and cold walls. A further rotation will increase the velocities because of the increasingly unstable situation of the cavity by heating from below.

It is important to note that the flow structure starts to show unsteady at $\varphi = 19^\circ$ as two small vortices appear at the corners of boundary layers of the hot and cold walls. As for $\varphi = 0^\circ$, the flow is three-dimensional and cannot be described by a two-dimensional numerical program.

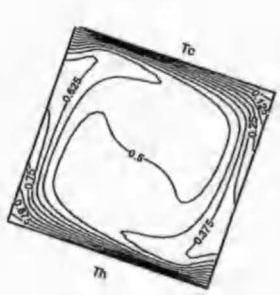
Tc
0.625
0.5
0.375
Th

(a)

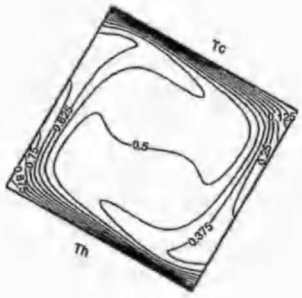
Tc
0.625
0.5
0.375
Th

(b)

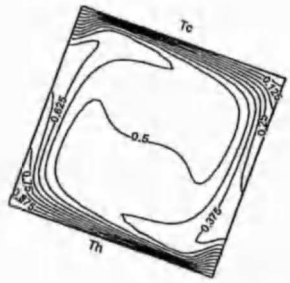
Tc
0.625
0.5
0.375
Th

(c)

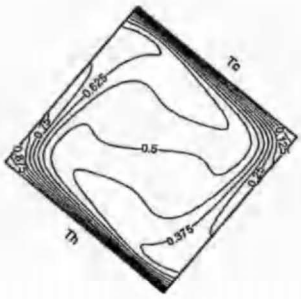
Tc
0.625
0.5
0.375
Th

(d)

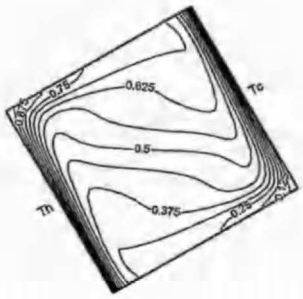
Tc
0.625
0.5
0.375
Th

(e)

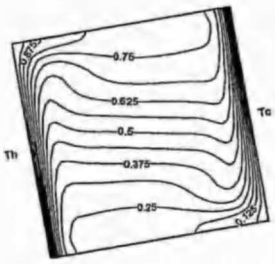
Tc
0.75
0.625
0.5
0.375
0.25
Th

(f)

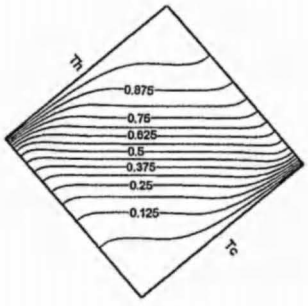
Th
0.875
0.75
0.625
0.5
0.375
0.25
0.125
Tc

(g)

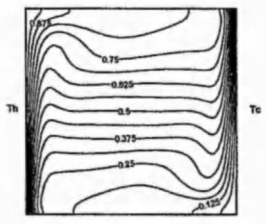
Th
0.875
0.75
0.625
0.5
0.375
0.25
0.125
Tc

(h)

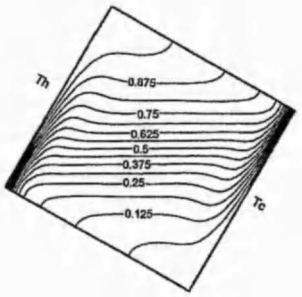
Th
0.875
0.75
0.625
0.5
0.375
0.25
0.125
Tc

(i)

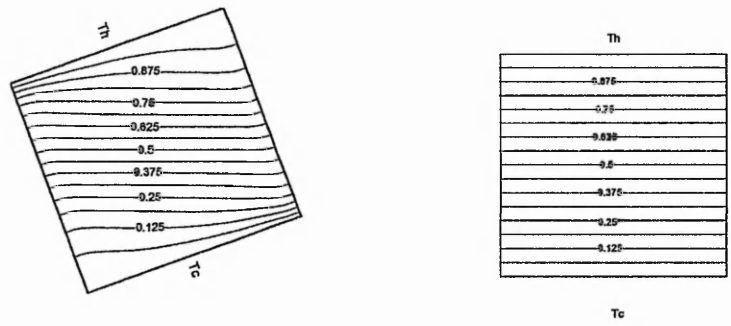

(j) (k)

Figure 4.18 Thermal Contour distribution at different angles for $Ra=10^6$

(a) ϕ=19°,(b) ϕ=20°, (c) ϕ=30°,(d) ϕ=40°,(e) ϕ=60°,(f) ϕ=80°,(g) ϕ=90°,(h) ϕ=120°,

(i) ϕ=140°,(j) ϕ=160°,(k) ϕ=180°

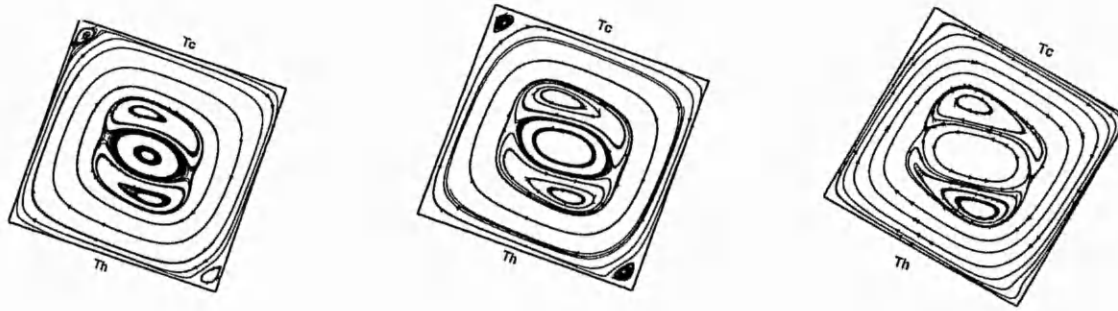

(a) (b) (c)

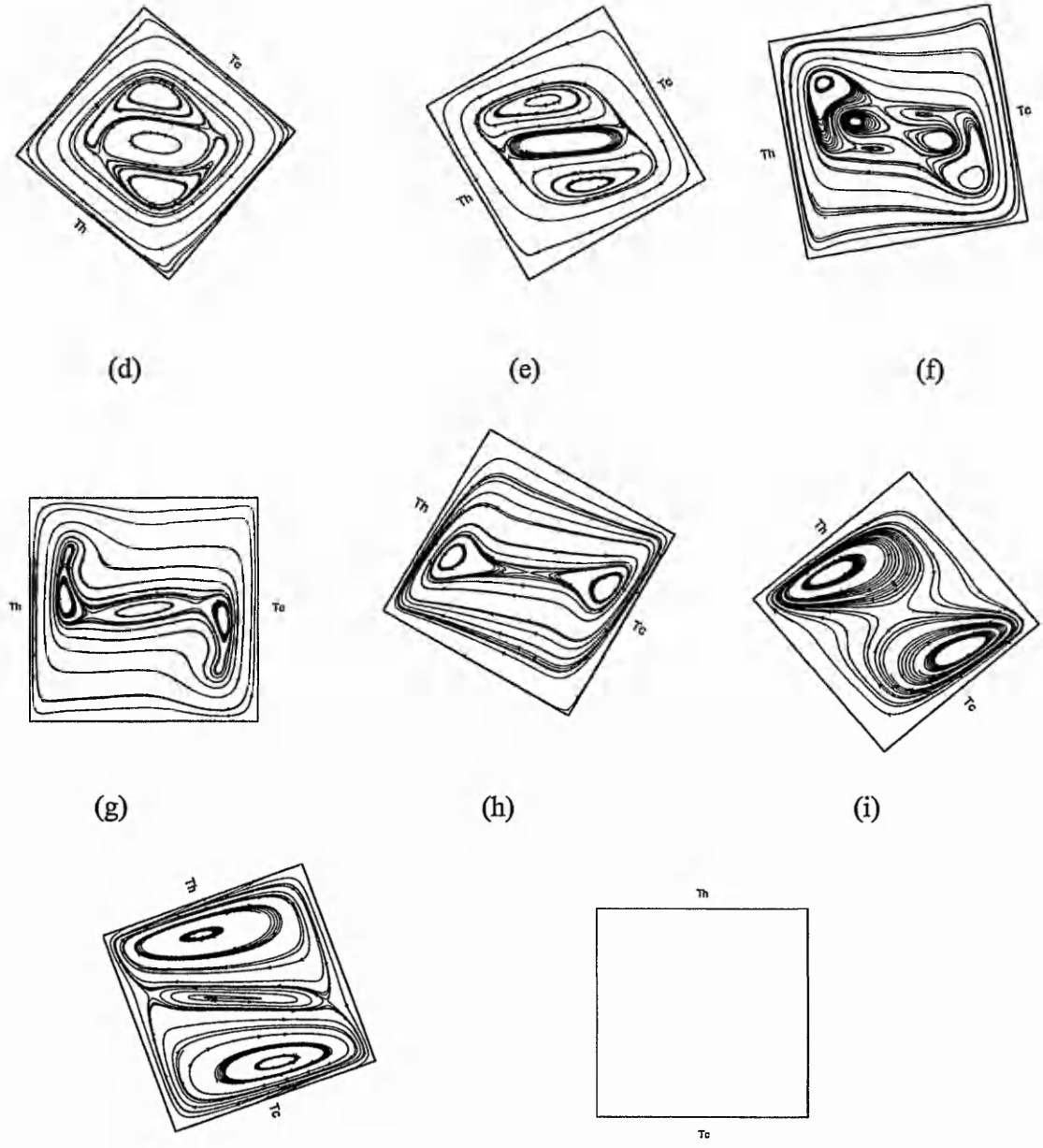

Figure 4.19 Streamlines distribution at different angles for Ra=10^6 (a) ϕ=19°,(b) ϕ=20°, (c) ϕ=30°,(d) ϕ=40°,(e) ϕ=60°,(f) ϕ=80°,(g) ϕ=90°,(h) ϕ=120°,(i) ϕ=140°,(j) ϕ=160°,(k) ϕ=180°

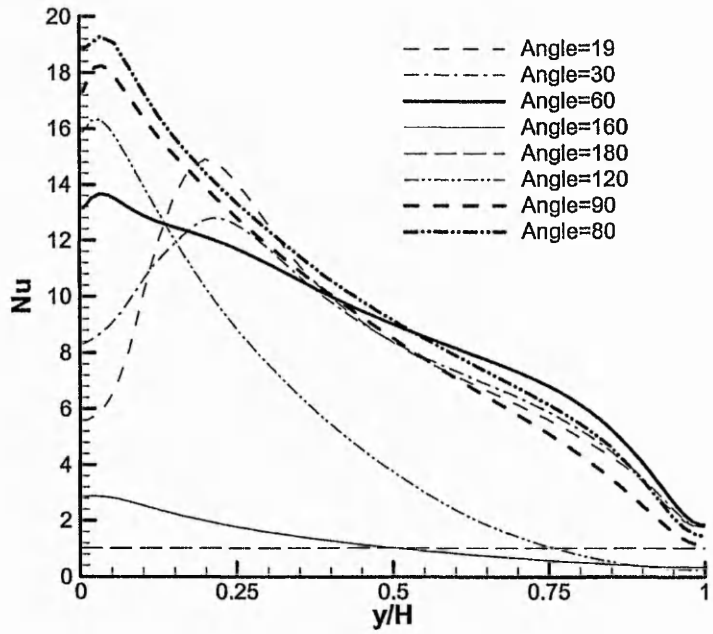

Figure 4.20 Local Nusselt number at some angles of inclination for Ra=10^6

4.5.4 Natural Convection in a Squeezed cavity

The application is the natural convection in a squeezed cavity as shown in figure 4.21, in which the inclined walls are kept at constant temperatures T_H and T_C, respectively, while the horizontal is

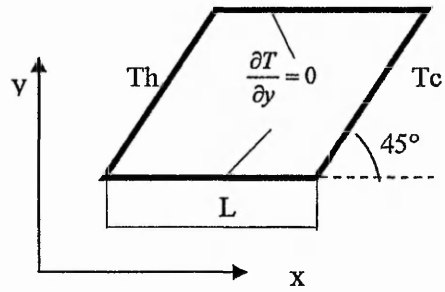

Figure 4.21 A squeezed cavity

assumed to be adiabatic. The inclination angle was chosen to be $\beta = 45^{\circ}$.

A benchmark solution for this natural convection problem has been reported by Demirdzic, Lilek and Peric. (1992) employing a multi-grid finite volume program. Using the same physical and geometric conditions, such as L=1, density $\rho = 1$, gravity constant g=1, expansion coefficient $\beta = 0.1$, specific heat $c_p = 1$, $T_H = 1$ and $T_C = 0$. The natural flow at Ra=10^6 is studied at Pr=0.1 and 10, respectively. A fine mesh with 224×192 grids was used for the calculation (figure 4.22). The results are shown in figure 4.23 and 4.24. The comparison of streamlines between the benchmark and the present solutions shows that the results are in good agreement with the benchmark solution.

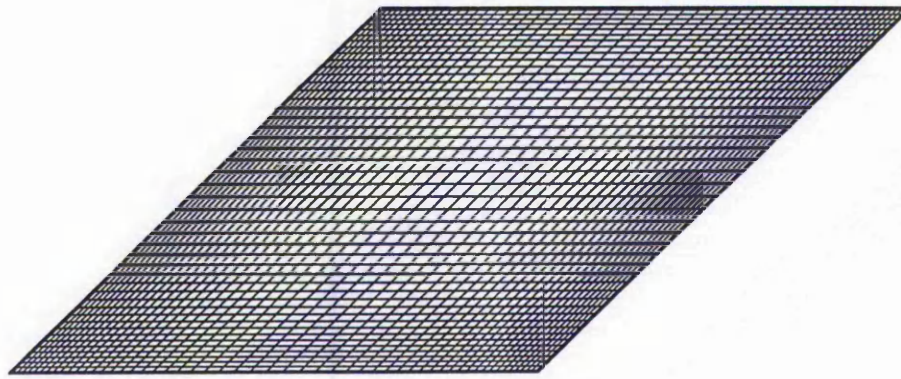

Figure 4.22 a mesh of the squeezed cavity (shown every other four points)

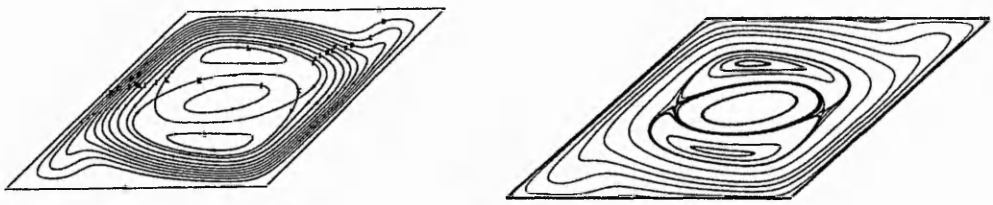

(a) (b)

Figure 4.23-1 streamlines comparison with benchmark solution

(a: benchmark, b: the present)

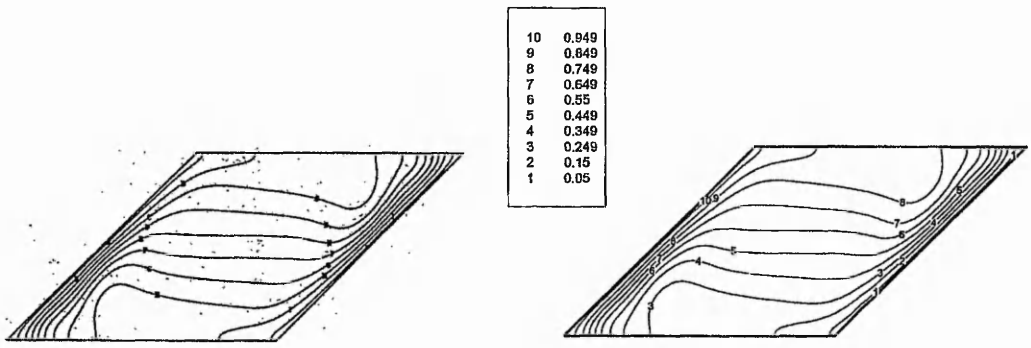

(a) (b)

Figure 4.23-2 Predicted isotherms with benchmark solution

(a: benchmark, b: the present) Pr=0.1

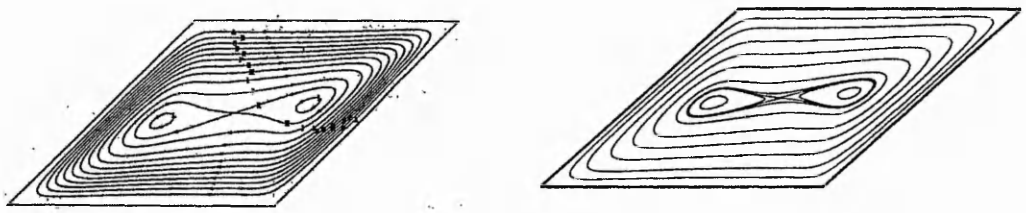

(a) (b)

Figure 4.24-1 Predicted streamline at Pr=10

(a) Benchmark (Demirdzic,1992), (b) present work

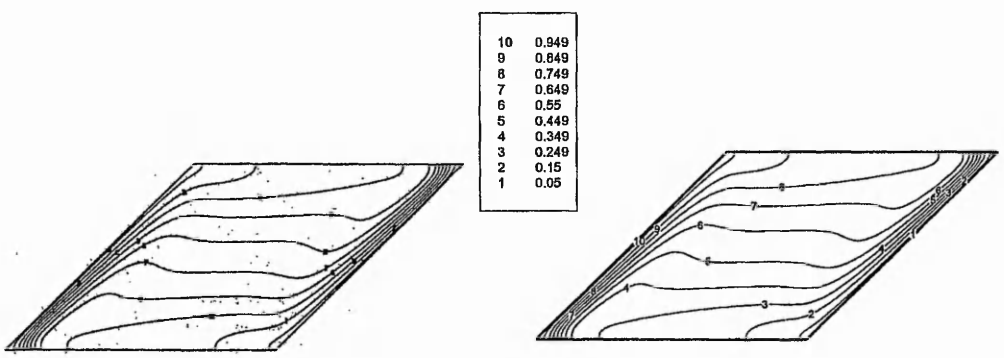

(a) (b)

Figure 4.24-2 Predicted isotherms at Pr=10

(a) Benchmark (b) present work

4.5.5 Laminar Flow through a Circular Pipe with Constriction

The laminar flow through a circular pipe with a sinusoidal constriction, experimentally studied by Young and Tsai (1973) and numerically studied by Rastogi (1984) and Karki and Patankar (1988) is selected to validate the code using body-fitted grids in axisymmetric coordinates system. The geometry is shown schematically in figure 4.25. Both the tube and the constriction are axisymmetric. The radius of the stenosis was specified as a cosine curve:

$$\frac{R}{R_0} = 1 - \frac{d}{2R_0}\left(1 + cos\frac{\pi x}{X_0}\right) \qquad -X_0 < x < X_0 \ . \tag{4.5.5}$$

The number of grid is taken as 102×50 in the $x-r$ coordinates. The density of grid points was higher near the wall and the grid was stretched in the axial direction with more grid points in the constricted region.

Table 4. 2 Model Geometries

Model no.	R_0 (in.)	d/R_0	X_0/R_0	% reduction in area
M-2	0.372	2/3	4	89
M-3	0.372	2/3	2	89

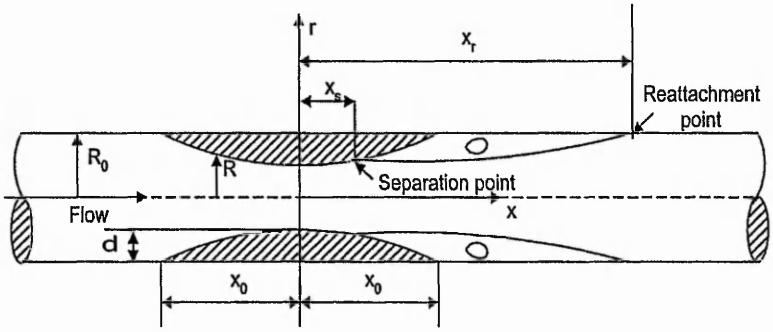

Figure 4.25 Geometric configuration of the pipe with a constriction

Results have been obtained for two geometries corresponding to models M-2 and M-3 of Young and Tsai (1973). The geometric characteristics of these stenoses are given in table 4.2. Computations were done at Re=50 and 100 for model M-2 and at Re=40 for model M-3.

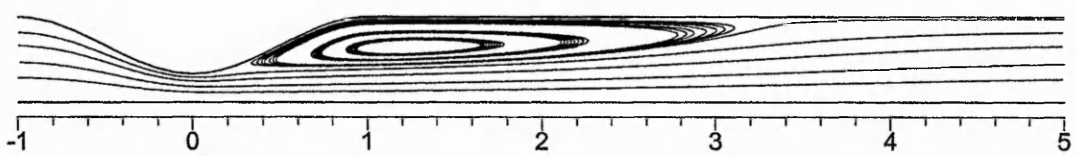

Figure 4.26 Flow pattern for Model M-3 at Re=40

Table 4. 3 Comparison of the present results with experiments

Re	Model no.	Separation point (X_s/X_0)		Reattachment point (X_r/X_0)	
		Experiment	Present	Experiment	Present
50	M-2	0.37	0.37	2.2	2.1
100	M-2	0.37	0.37	4.1	4.1
40	M-3	0.37	0.37	2.9	3.1

The flow pattern for model M-3 for Re=40 is plotted in figure 4.26. Table 4.3 gives a comparison between the present results and the experimental results of Young and Tasi (1973). The agreement between the two sets of results is good. The error of X_r/X_0 is acceptable considering the experimental error at low Reynolds numbers.

4.6 Summary

In this chapter, the computational domain and Navier-Stokes equations coupled with electric field equations are discretezed firstly; and then the SIMPLE procedure is applied for coupling the velocity and pressure. A modified momentum interpolation scheme is proposed.

An algebraic method is used to give an initial mesh; the Partial Equations to obtain the grid with second-order smoothness are used. The Control Volume method is used to discrete the governing equations. The QUICK scheme and deferred correction are employed for the convection term discretization.

Following the introduction of numerical methods, the algorithm and the developed FORTRAN codes are validated by cases with benchmark results or experimental data. These cases include the flow in a Roach Channel, natural convection in an annulus and in a square cavity, natural convection in a squeezed cavity and Laminar flow through a circular pipe with constriction. The validations show that the numerical method and the computer codes used in this work are reliable and robust.

Chapter 5

Numerical Study of EHD Effect on Natural Convection Heat Transfer

5.1 Introduction

Natural convection (or buoyancy-driven fluid flow) in enclosures with differentially heated walls is an important model of heat transfer in many industrial processes and engineering devices such as air conditioning system in a vehicle, reactor insulation, cooling of radioactive waste containers, ventilation of rooms, fire prevention, solar energy collection and crystal growth in a liquid.

When an external electric field is applied across a plane layer of a dielectric media, secondary flows in a flow field can be induced and heat transfer enhancement can be further obtained; this is an example of the EHD effect. This EHD enhancement is particularly attractive for enhancing the convective heat transfer of weakly conducting liquid through a narrow space at low Reynolds number, where the application of any conventional passively enhancement methods is neither easy nor effective (Bergles, 1978). As reviewed in chapter 2, many experimental studies on EHD enhancement of heat transfer have been carried out in the past three decades with most of the studies being experimental measurements and visualisations (Gross and Porter, 1966; Fujino, Yokoyama and Mori, 1989); numerical simulations of the EHD enhancement of natural

convection are very rare in literatures because the lacking of proper mathematical descriptions of the coupled electric, flow and thermal fields.

The status quo of the modelling the EHD effect and numerical simulation is not well connected. On one hand, some publications reported the modelling of the EHD effect on laminar flows but without numerical simulation, such as Worraker & Richardson (1981), Martin & Richardson (1984) and Dulikravich and Lynn (1995); and on the other hand, some numerical simulations are reported, such as those by Lee, Dulikeravich and Ahuja (1993) and Shu and Lai (1995), but in the mathematical models for these simulations, the electric field is decoupled with the flow and thermal fields.

In this chapter, numerical simulations of EHD effect on natural convection in a rectangular enclosure and a cylindrical enclosure are carried out; also the EHD effect on natural convection in different working fluid is simulated.

5.2 EHD effect on Natural Convection in Rectangular Enclosures

The configuration considered here is a two-dimensional horizontal rectangular chamber where the length is three times of the height, as shown in figure 5.1. The top (cool) and bottom (hot) walls are differentially heated.

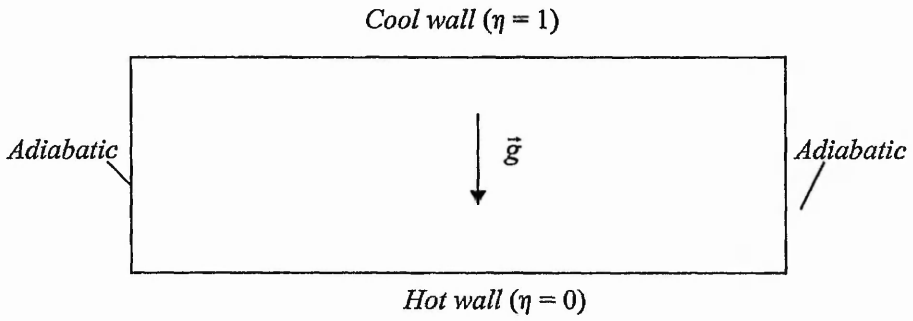

Figure 5.1 The horizontal rectangular chamber (where a/b=3)

5.2.1 The EHD Effect at Different Rayleigh Number

The following non-dimensional parameters are chosen in the calculations of the EHD effect on natural convection calculated for different Rayleigh numbers: $\mathrm{Pr}=1$, $E_C=1\times10^{-4}$, $S_E=1$, $N_E=1$, $D_e=1$, $\mathrm{Re}=Gr^{1/2}$ and $\mathrm{Pr}_E=1$. A mesh size of 120×60 is chosen for the calculation based on a grid independency as tested using the mesh sizes of 60×30, 120×60 and 240×120. The mean Nusselt number Nu_{av} calculated by three meshes are compared and tabulated in table 5.1. As can be seen, the relative error between the results of mesh 60×30 and mesh 120×60 is nearly 5% while that between mesh 120×60 and mesh 240×120 is less than 1%; therefore mesh 120×60 can be regarded as fine enough to produce grid-independent results and can be employed in the current simulation.

Table 5.1 Grid independent test

Mesh size	Nu_{av}	Relative error
120×60	1.893	-
60×30	1.989	5.071%
240×120	1.911	0.951%

Table 5.2: the comparison of mean Nusselt number at different Rayleigh number

Ra	Nu_{av} (without EHD effect)	Nu_{av} (with EHD effect)	Increase
3000	1.006	1.371	36.29%
3500	1.464	1.535	4.86%
4000	1.619	1.684	3.98%
4500	1.757	1.797	2.27%
5000	1.866	1.893	1.49%

The results at Ra = 3000, 4000 and 5000 are shown in figures 5.2.1 ~ 5.4.3. The mean Nusselt number and local Nusselt number along the hot wall is presented in table 5.2.

Figures 5.2.1~5.2.3 show the results of calculation at Ra =3000. The temperature distributions (figure 5.2.1) for without and with EHD effect exhibit a significant difference, it is clear that without an EHD effect, the system almost has a uniform temperature field; but when the effect are applied, the temperature distribution is rather non-uniform and should result in a significant heat transfer enhancement. Figure 5.2.2

shows the streamline, the visual differences between those with and without EHD effect are not very obvious; this means applying an electric field does not produce a topological change in the streamlines this time. However, corresponding to the temperature fields in figure 5.2.1, the distribution of local Nusselt number shown in figure 5.2.3 demonstrates the heat transfer enhancement by applying the EHD; as large as 140% maximum increase in local Nusselt number can be seen in the middle of the bottom wall.

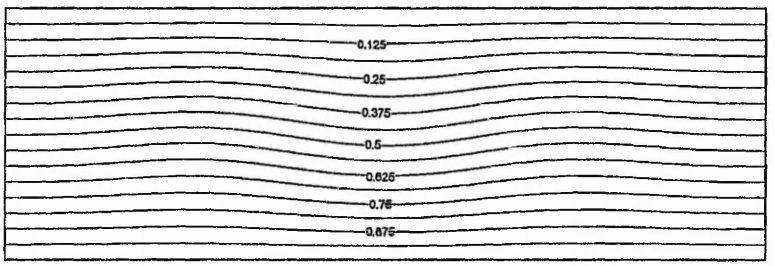

(a) the temperature distribution without EHD effect

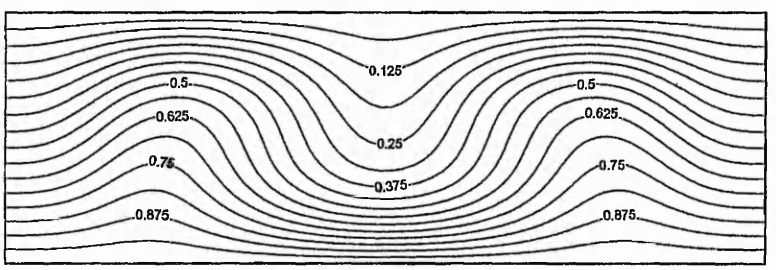

(b) the temperature distribution with EHD effect

Figure 5.2.1 The temperature distribution at $Ra = 3000$

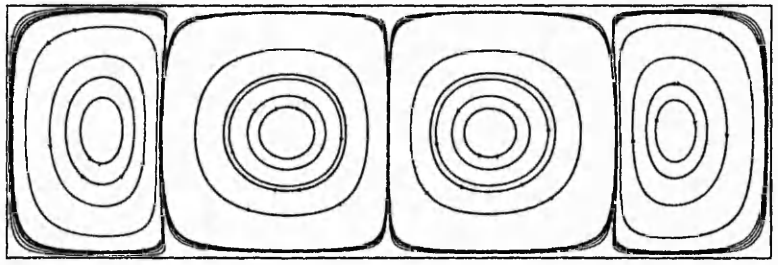

(a) without EHD effect

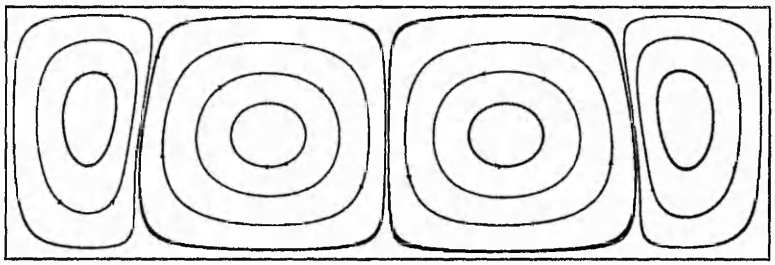

(b) with EHD effect

Figure 5.2.2 The streamlines at $Ra = 3000$

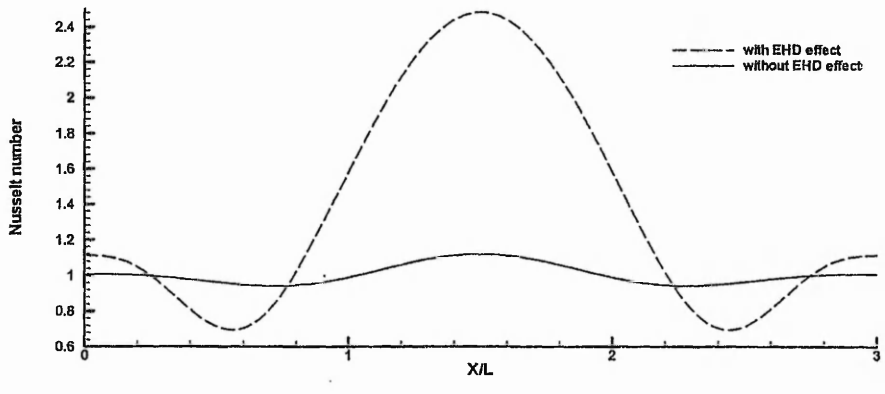

Figure 5.2.3 The local Nusselt number along the hot wall at Ra =3000

Figures 5.3.1~ 5.3.3 presents the results of the case *Ra*= 4000; the contours of dimensionless temperature, streamline structure, and local Nusselt number are shown in figures 5.3.1, 5.3.2 and 5.3.3 respectively. The differences in the flow fields and local Nusselt number distributions for with or without EHD are smaller than that at *Ra*=3000. This becomes clearer when the Rayleigh number increases to 5000. As shown in figure 5.4.1 and 5.4.2, both the temperature and streamline distributions for with or without EHD are similar. As a result, the difference in the Nusselt number distributions for with or without EHD, as shown in figure 5.4.3, is smaller than that in figure 5.2.3 (Ra=3000).

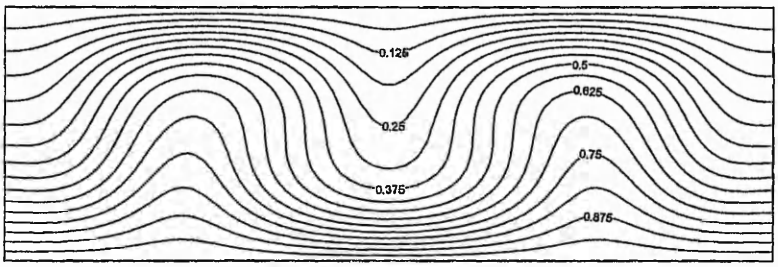

(a) without EHD effect

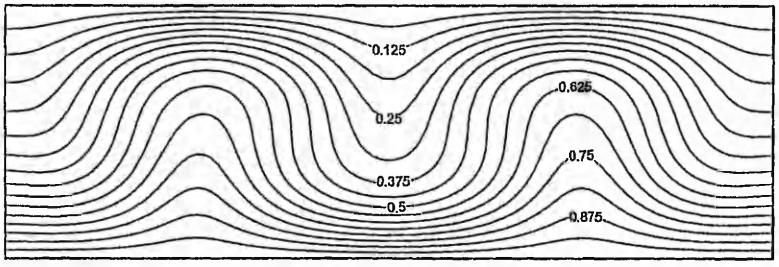

(b) with EHD effect

Figure 5.3.1 The temperature field at *Ra* = 4000

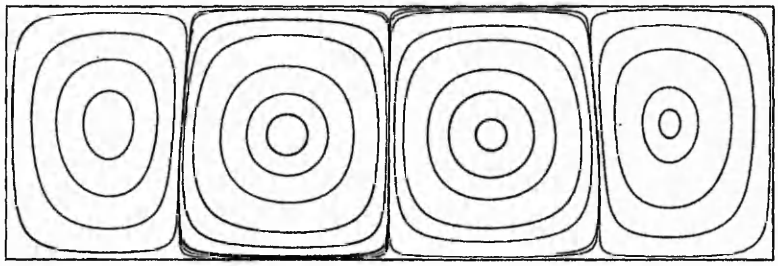

(a) without EHD effect

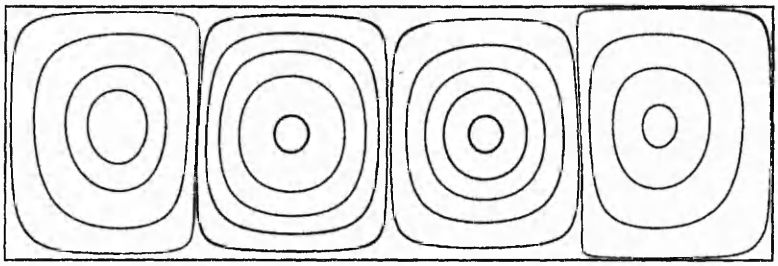

(b) with EHD effect

Figure 5.3.2 The streamline at $Ra = 4000$

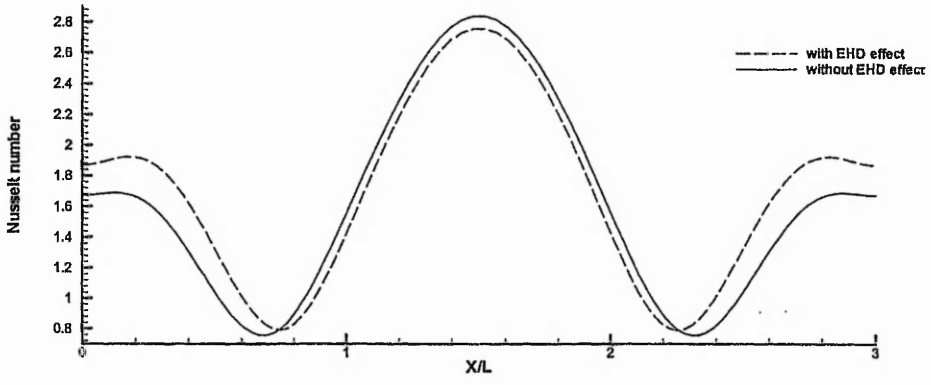

Figure 5.3.3 The local Nusselt number along the hot wall at $Ra = 4000$

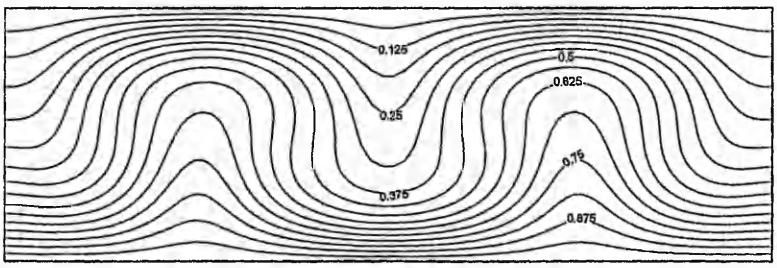

(a) without EHD effect

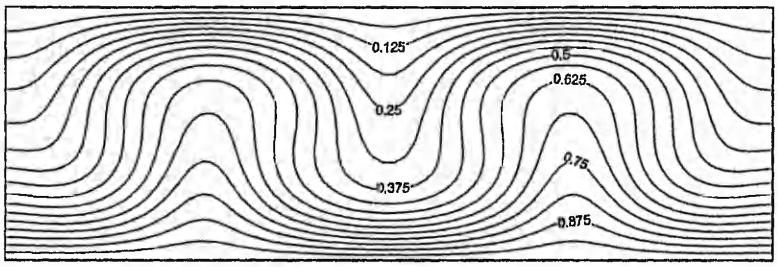

(b) with EHD effect

Figure 5.4.1 Temperature distribution at Rayleigh number of 5000

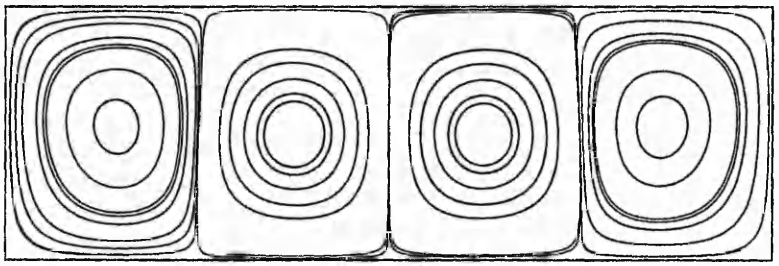

(a) without EHD effect

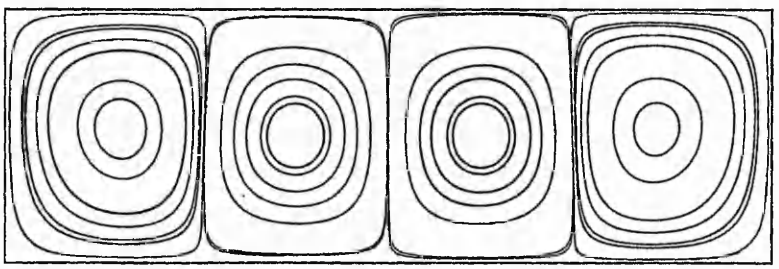

(b) with EHD effect

Figure 5.4.2 The streamline at Rayleigh number of 5000

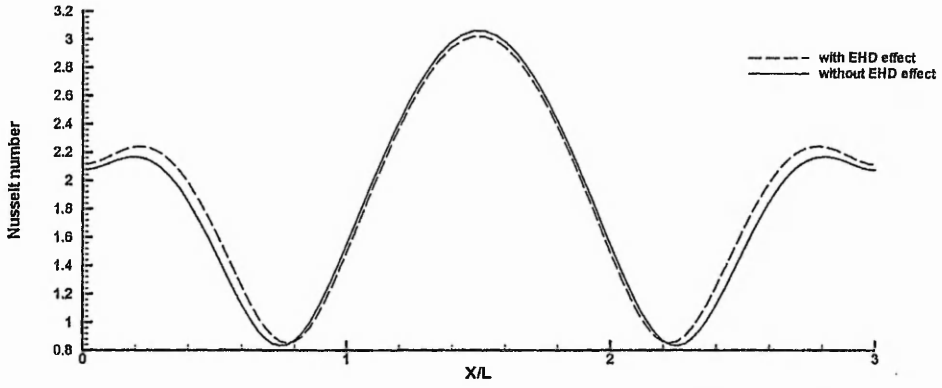

Figure 5.4.3 The local Nusselt number along the hot wall at *Ra*=5000

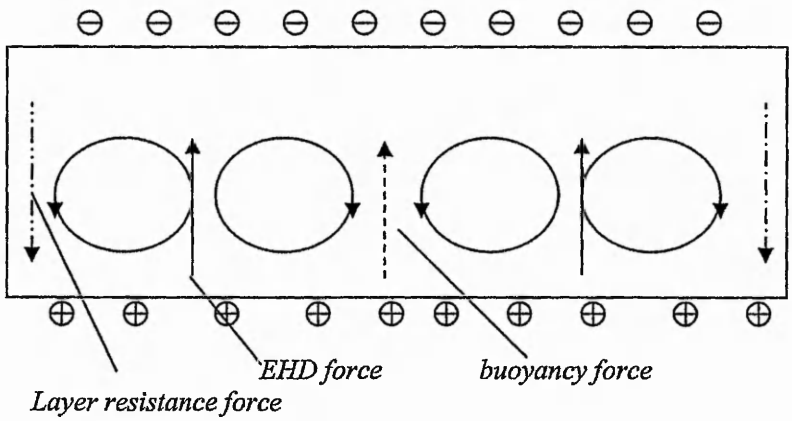

Figure 5.5 Force analysis (Gravity isn't shown in this figure)

Compare the distributions of local Nusselt number in figures 5.2.3, 5.3.3 and 5.4.3, there is a similarity between them; that is, by applying an electric field, the local heat transfer is enhanced near the side walls; but in the centre of the cavity, local heat transfer is enhanced at Ra= 3000 but is reduced at Ra= 4000 and Ra= 5000. This phenomenon can be partially explained by the force-analysis in figure 5.5. Due to the boundary layer resistance force, cold fluid is transported downward along the side walls; this results in a steeper vertical temperature gradient near the side walls. In the centre of the cavity, the direction of electric body force is opposite to the vortex motion and therefore the heat transfer is reduced locally.

The above calculations of the natural convection in two dimensional rectangular cavity demonstrate that the EHD enhancement of natural convection is limited; at Ra =3000, the enhancement is significant, but as the Rayleigh number increases, the enhancement will get less significant. This is consistent with the experimental results reported by Salehi, Ohadi and Dessiatioun(1997), and Shu and Lai, (1995). At a low Rayleigh number, the buoyancy force is much smaller than the EHD force, so that the EHD effect is significant; for example, with the EHD effect, the mean heat transfer coefficient at Ra =3000, as shown in table 5.2, can be increased by as much as 36%. The comparison of mean Nusselt number for with and without EHD cases is shown in figure 5.6. This phenomenon of the electric field cannot effectively enhance the natural convection at higher Rayleigh number maybe because of the assumption that the cavity size in the spanwise direction (normal to the x-y plane) is infinite. Because of this assumption, the vortices are straightened in the spanwise direction and the flow fields are therefore

stabilised artificially. In order to reveal the EHD effect on natural convection is rectangular cavities, fully three-dimensional calculations with the spanwise walls may be necessary; and this will be a further work.

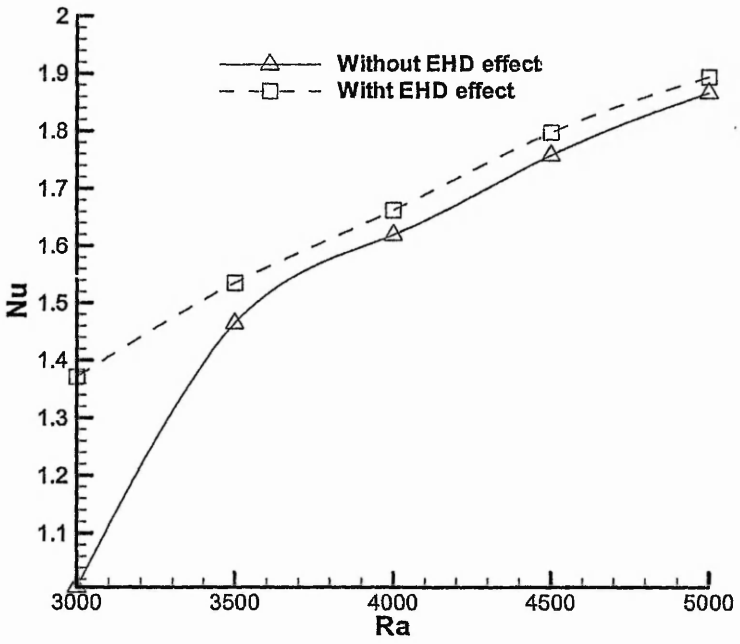

Figure 5.6 Comparison of mean Nusselt number for with and without EHD effect

5.2.2 The EHD Effect at Uniform or Non-Uniform Electric Fields

As reported by some recent researches (Yang and Lai, 1997; Ngo and Lai, 2001;Tan and Lai, 2001), the non-uniform electric fields are more effective to enhance convective heat transfer. A non-uniform electric field can be produced by wire electrodes or needle

electrodes. In this study, as the main purpose is to establish the computational model, the non-uniformity introduced by the injection of electric charge density from the electrodes is considered. By employing the same geometry as shown in figure 5.1, the effect of EHD on natural convection for different distributions of electric charge density is studied. The properties of the working fluid are: $\mu_0 = 1.002\times10^{-3} kgm^{-1}s^{-1}$, $a_0 = 0.5682 Wm^{-1}K^{-1}$, $\beta_0 = 1.96\times10^{-4} K^{-1}$, $\Pr = 7.396$, $\rho_0 = 1000 kgm^{-3}$. Non-dimensional parameters employed in the calculations are chosen as: $\mathrm{Re} = 30$, $Gr = 900$, $\Pr = 7.396$, $Ra = 6656.4$, $S_E = 0.852$, $N_E = 1.261$, $\Pr_E = 3.6\times10^{-3}$, $E_C = 1.28\times10^{-9}$. For a uniform electric field, the electric density is injected uniformly from the bottom wall with $q = 1$; for a non-uniform electric effect, sine wave distribution of q injected from the lower electrode is considered with the amplitude of the sine wave being 1. The calculated temperature field and velocity are and presented in figures 5.7.1 and 5.7.2 respectively. It is seen that both the temperature and streamline distributions are much different when uniform and non-uniform electric density q are injected from the bottom electrode (positive potential). The application of an uniform electric field has some effect on the flow and thermal fields, but it does not change the topology of flow structure; the vortices in figure 5.7.2(b) are similar to that in figure 5.7.2(a) although their size and distribution vary. On the other hand, when a non-uniform electric field is applied, the structure of streamlines and the topology of temperature contours are changed; the merge of vortices results in stronger rotational motion, and therefore, provides possibility of heat transfer enhancement.

The difference of the EHD effect with different electric density injections is also indicated in figures 5.7.3 and 5.7.4. The former shows the local Nusselt number distribution along the bottom wall; and the latter shows the distribution of electric density injected by the bottom electrode.

The comparisons of the mean Nusselt number for different electric density q injection are given in table 5.3. It is noted that with a non-uniform electric field, the mean heat transfer coefficient can be enhanced by more than 12%, but with a uniform field, only less than 0.5% of the enhancement can be achieved.

Table 5.3 The mean Nusselt number

	Nu_{av}	Increase
without an electric field	2.129	-
uniform electric density	2.139	0.47%
non-uniform electric density	2.396	12.5%

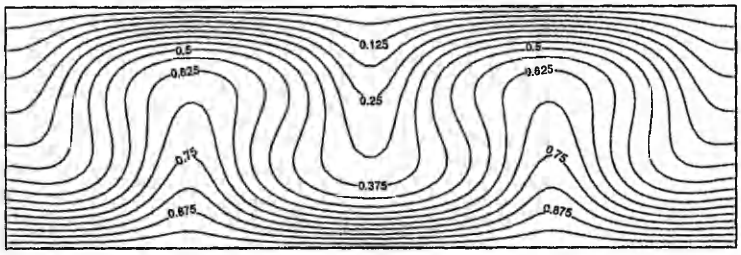

(a) without EHD effect

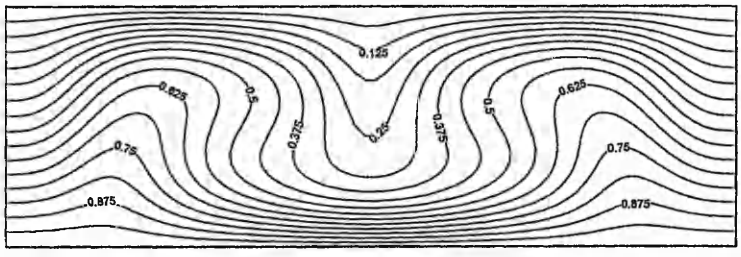

(b) with EHD effect at uniform electric density injection

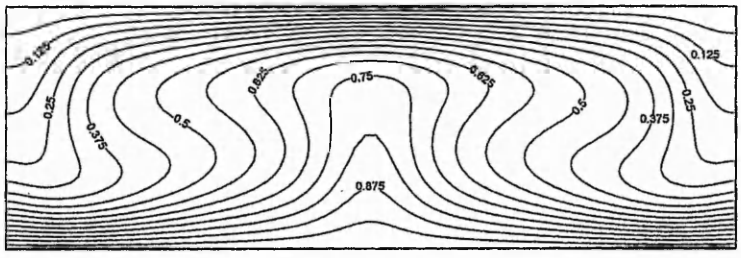

(c) with EHD effect at non-uniform electric density injection

Figure 5.7.1 The temperature distribution

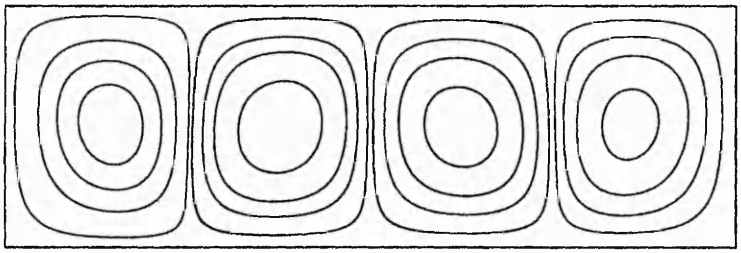

(a) without EHD effect

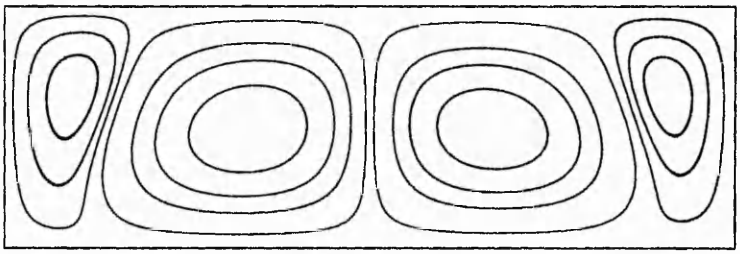

(b) with EHD effect at uniform electric density injection

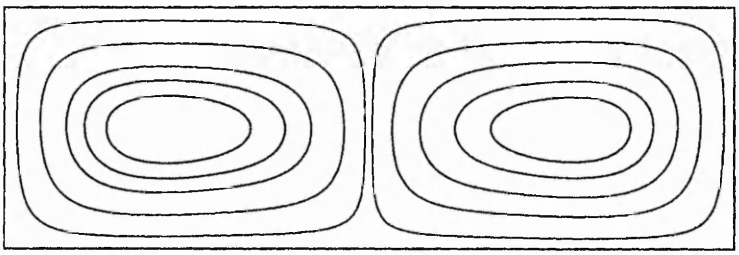

(c) with EHD effect at non-uniform electric density injection

Figure 5.7.2 The comparison of streamline

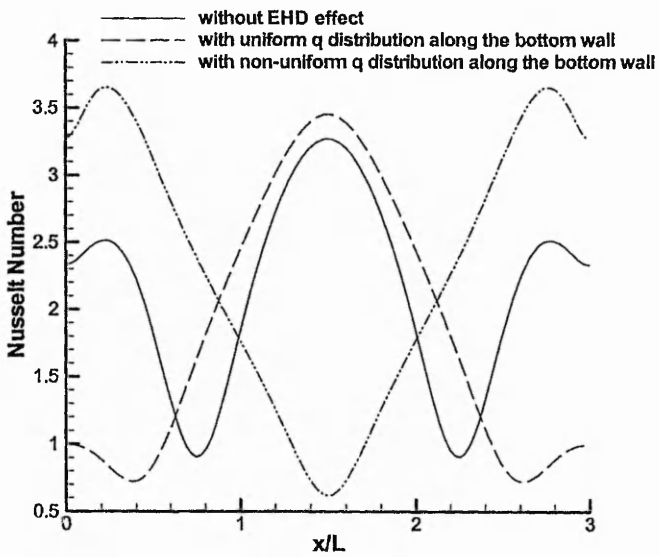

Figure 5.7.3 The comparison of local *Nu* along the bottom wall

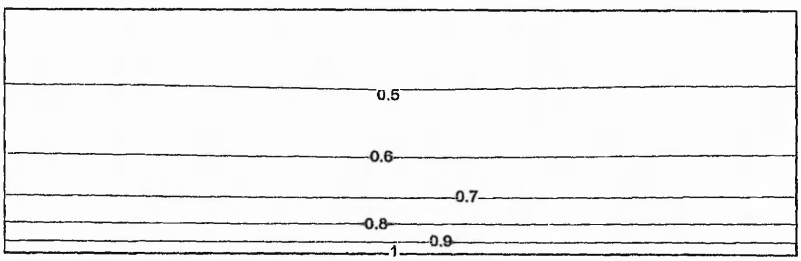

(a) uniform electric density injection

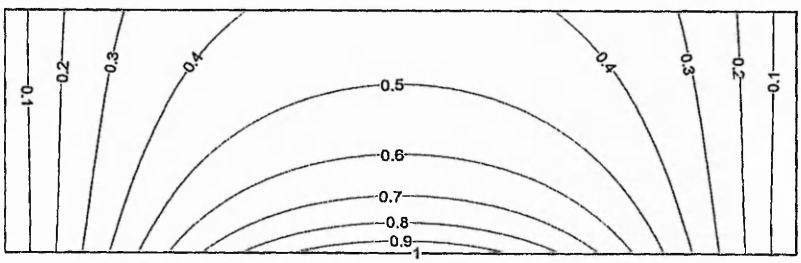

(b) non-uniform electric density injection

Figure 5.7.4 Distribution of the electric density *q*

5.3 EHD effect on Natural Convection in Cylindrical Enclosures

The horizontal cylindrical enclosure studied here is shown in figure 5.8. Without losing generality, the length is three times the height. The top (cool) and bottom (hot) walls are differentially heated. The following dimensionless parameters in the calculations are chosen as: $\mathrm{Pr}=1$, $E_C=1\times10^{-4}$, $S_E=1$, $N_E=1$, $D_e=1$, $\mathrm{Re}=Gr^{1/2}$ and $\mathrm{Pr}_E=1$. On this basis, the EHD effect on natural convection for different Rayleigh numbers is calculated; the results for *Ra*=3000, 4000, 6000 and 10000 are shown in figures 5.9~5.12.

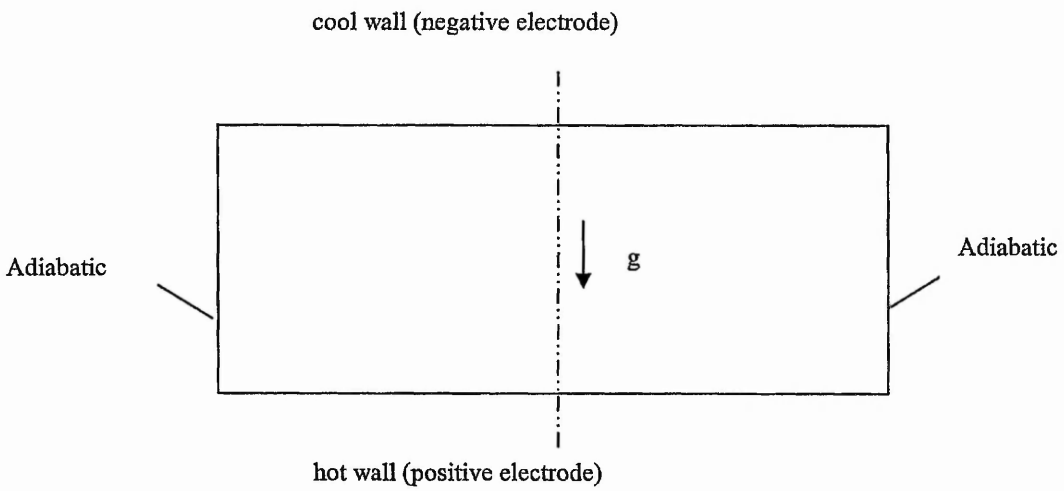

Figure 5.8 The geometry of the cylindrical enclosure (b=3a)

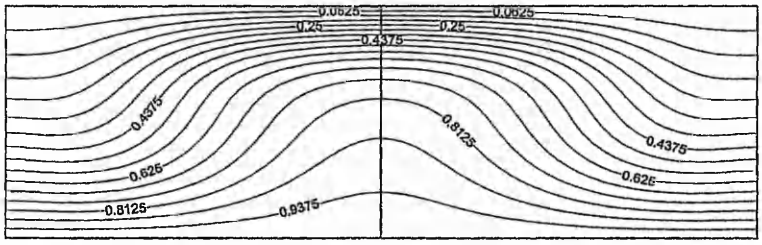

Without EHD effect

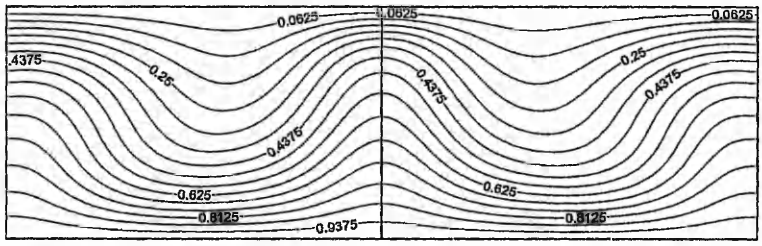

With EHD effect

Figure 5.9a temperature distribution

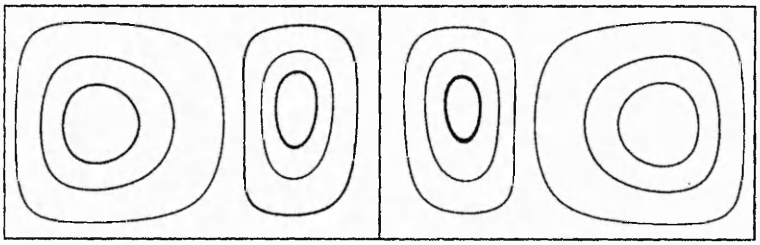

With EHD effect

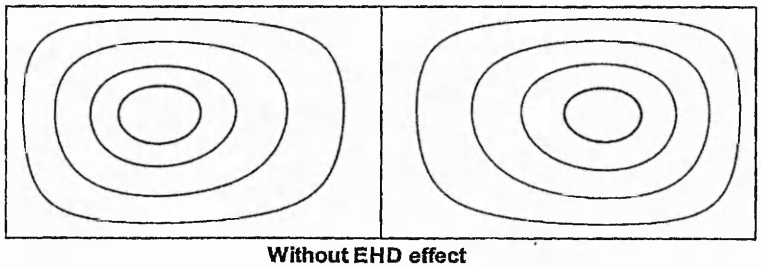

Without EHD effect

Figure 5.9b streamlines

Figure 5.9 Natural convection in a cylindrical enclosure at *Ra*=3000

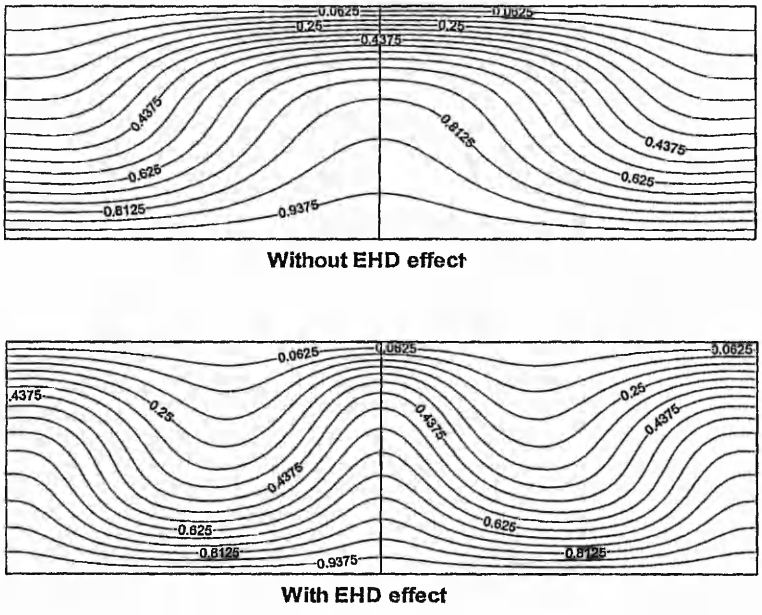

Figure 5.10a temperature distribution

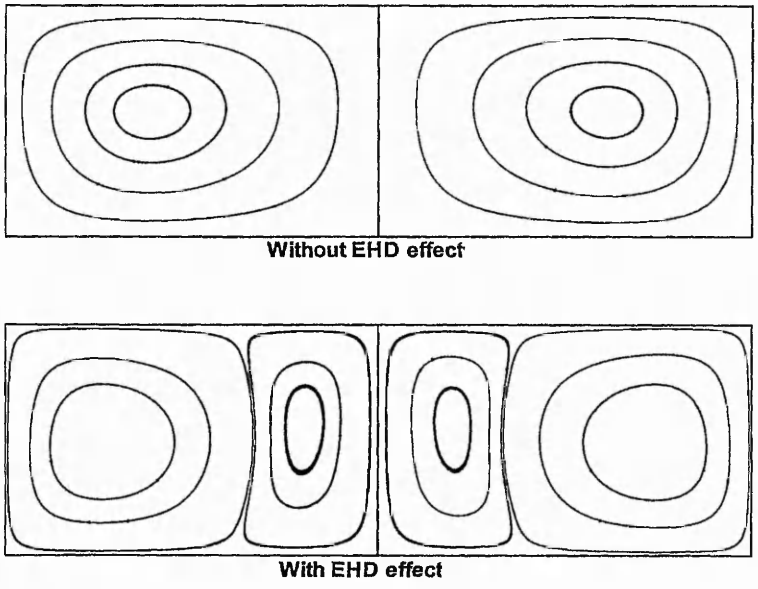

Figure 5.10b streamlines

Figure 5.10 Natural convection in a cylindrical enclosure at *Ra*=4000

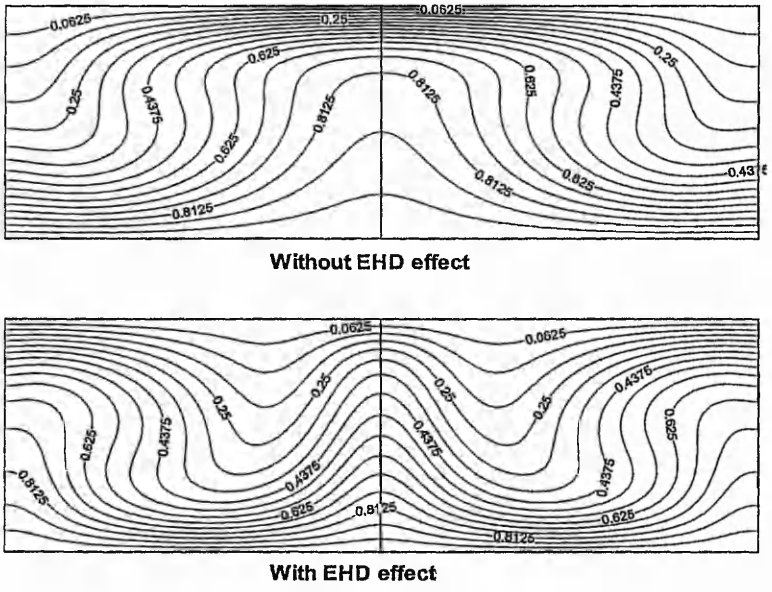

Figure 5.11a Isothermals

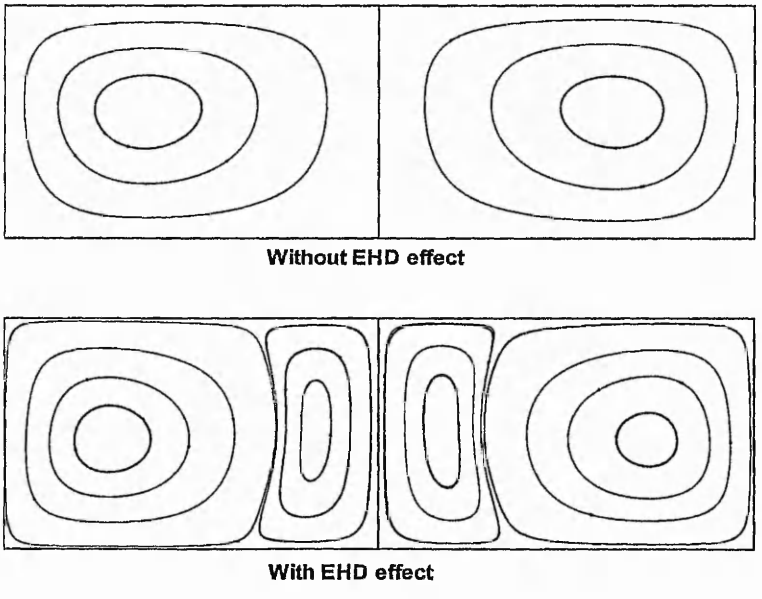

Figure 5.11b Streamlines

Figure 5.11 Natural convection in a cylindrical enclosure at *Ra*=6000

Generally, significant differences are demonstrated for with and without EHD for each individual case. For example, for the results for *Ra*=4000, shown in figure 5.10, the isothermals along the hot wall become thicker when EHD is applied (figure 5.10a) while the streamlines show a secondary vortex has been induced by the electric field. This secondary vortex has destabilizing effect on the thermal boundary and results in a significant increase in heat transfer rate.

As the Rayleigh number increases to *Ra*=6000, as showed in figure 5.11, the electrically induced secondary vortices are getting bigger in size and the heat transfer rate is increasing.

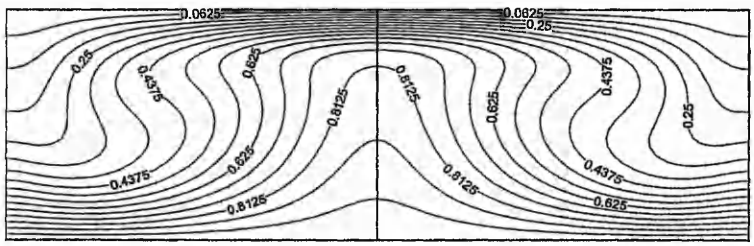

Without EHD effect

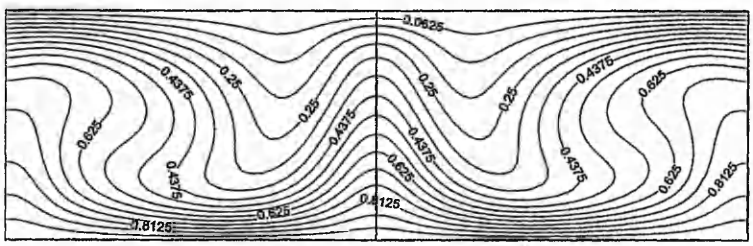

With EHD effect

Figure 5.12a Isothermals at Ra=10000

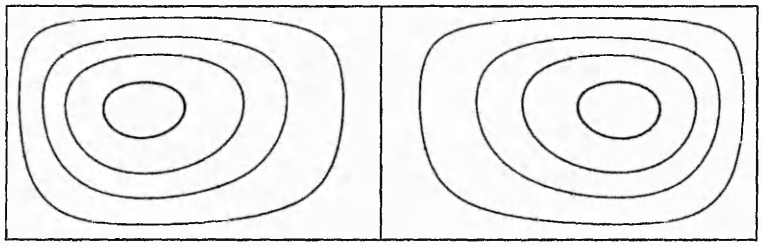

Without EHD effect

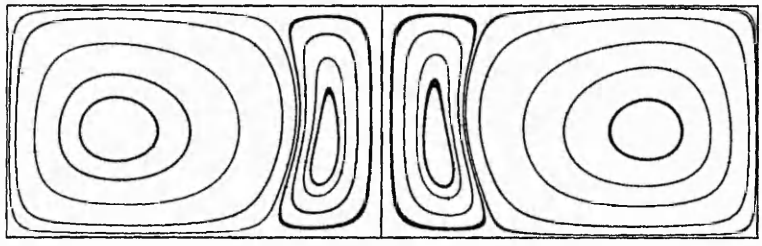

With EHD effect

Figure 5.12b Streamlines at Ra=10000

Figure 5.12 Natural convection in a cylindrical enclosure at Ra=10000

Table.5.4 Mean Nusselt number along the hot wall

Ra	4000	6000	10000
Nu_{av} without EHD effect	1.245	1.474	1.740
Nu_{av} with EHD effect	1.730	2.087	2.527
Increase	38.96%	41.59%	45.23%

At *Ra*=10000, the isothermals near the bottom wall become further thick and distorted; the mean Nusselt number Nu_{av} has is increased 45% by the EHD effect while that at *Ra*=4000 the increase rate is 39%, as shown in Table 5.4; the main vortices shown in Figure 5.12b are squeezed onto the central axis and the secondary flow dominates the flow field.

It is noticeable that the calculations of the cylindrical enclosure in this section show different tendency of the EHD effect with those in two-dimensional rectangular enclosures calculated in section 5.2 even when only uniform electric fields are applied. In the cylindrical enclosure, the EHD enhancement is very efficient and becomes more effective when the Rayleigh number increases; for two-dimensional rectangular enclosure, it has been noticed that the flows are much more stable and the heat transfer enhancements by the EHD effect are not significant. As analysed in section 5.2, the infinite spanwise size assumption of two-dimensional rectangular may stabilise the flows because the vortices in the spanwise are straightened. For a cylindrical enclosure, the size of normal to the *x-y* plane is limited; and the vortices in the enclosure are in a form of ring vortex, which possibly produce a self-sustaining vortex motion with higher instability of flows. These are possible reasons for the different tendency of EHD effect in the two kinds of enclosures. In order to thoroughly analyse and reveal the mechanism of EHD effect, fully three-dimensional and time-accurate simulations are necessary.

5.4 EHD Effect on Different Working Fluids

As the EHD heat transfer augmentation can largely reduce the size of heat exchanger, which uses the single-phase cooling oil with usually poor heat transfer characteristic in aircraft, and the EHD induced pump with no movable part in it, with all of these advantages, the EHD enhancement technique has become very attractive, but the lack of the understanding to some of the key problems makes EHD still unavailable. One of the key problems is to choose the right working fluid. There are only few papers published which concern the choice of a working fluid for EHD pumping and heat exchanger in aircraft. Crowley, Wright and Chato (1990) gave a fundamental analysis of the working fluid effect on the flow rate of an EHD pump. Paschkewitz and Pratt (2000) experimentally investigated the influence of fluid properties on EHD heat transfer enhancement. Because of the complexity of this phenomenon, so far no numerical investigation has been presented in publication.

Three working fluids having widely varying properties are numerically studied. The properties of the fluids are given in table 5.5. Polyalphaolefin (PAO) is a widely used aircraft avionics coolant used in aircraft heat exchangers that would benefit from EHD enhancement; ECO-C is biodegradable transformer oil; and Beta fluid is designed for the use as electrical cable oil, but has similar properties to those of aviation hydraulic oil. The fluid properties for PAO were obtained experimentally by Paschkewitz(1998). The properties for ECO-C and Beta were obtained from the manufacturer (DSI, Tyler,

TX). The ion mobility for all the fluids were given by using Walden's rule, which relates fluid viscosity to ion mobility (Crowley, Wright and Chato, 1990).

Table.5.5 Working fluid properties

Working fluid	PAO	ECO-C	Beta
Density at 20°C (kg/m^3)	790	850	860
Viscosity at 40°C(kg/m s)	5.214×10^{-3}	2.975×10^{-3}	9.288×10^{-2}
Electric conductivity (S/m)	2.7×10^{-10}	4.76×10^{-13}	6.25×10^{-13}
Thermal conductivity (W/m°C)	0.147	0.134	0.125
Dielectric constant	2.1	2.2	2.3
Ion mobility (m^2/Vs)	3.33×10^{-9}	6.72×10^{-9}	2.15×10^{-10}
Heat capacity (J/kg°C)	2050	547	670
Charge relaxation time	6.9	4090	3256

For convenience, the two-dimensional rectangular chamber shown in figure 5.1 is considered. In order to capture the flow and heat transfer details in the vicinity of the boundary, a specific mesh is generated shown in figure 5.13. A mesh size of 120×60 is chosen for the calculations. The non-dimensional parameters are shown in table 5.6. The results show in figures 5.14~ 5.16. The comparison of mean Nusselt number is given in table 5.7.

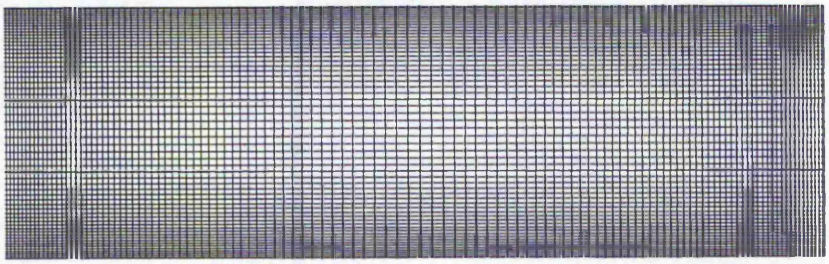

Figure 5.13 Computer generated mesh

Table 5.6 .Non-dimensional parameters

Fluid	Re	Pr	S_E	Pr_E	N_E	Ec
Beta	30	830	0.4070	10.0465	0.8170E-2	0.1171E-4
ECO-C	30	12.1	0.4434	0.1042	0.8545E-2	0.1334E-6
PAO	30	72	0.1314	0.3964	0.3255E-2	0.1060E-7

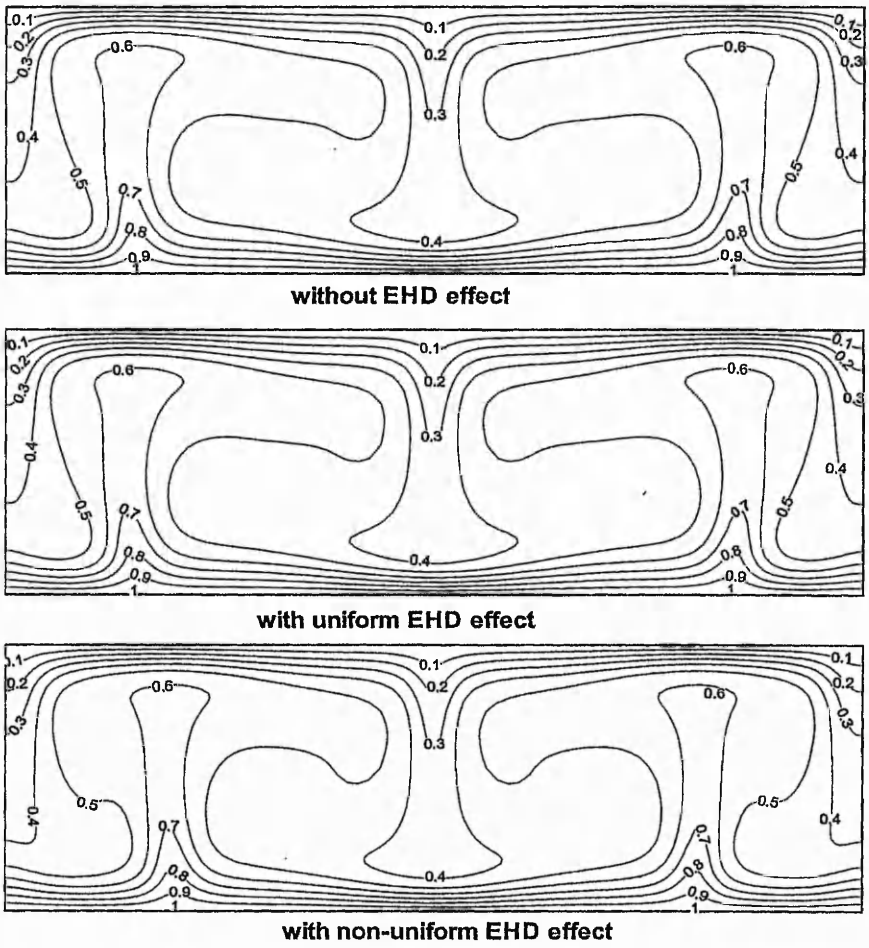

Figure 5.14a Comparison of thermal contours of Fluid Beta at ϕ=5000v

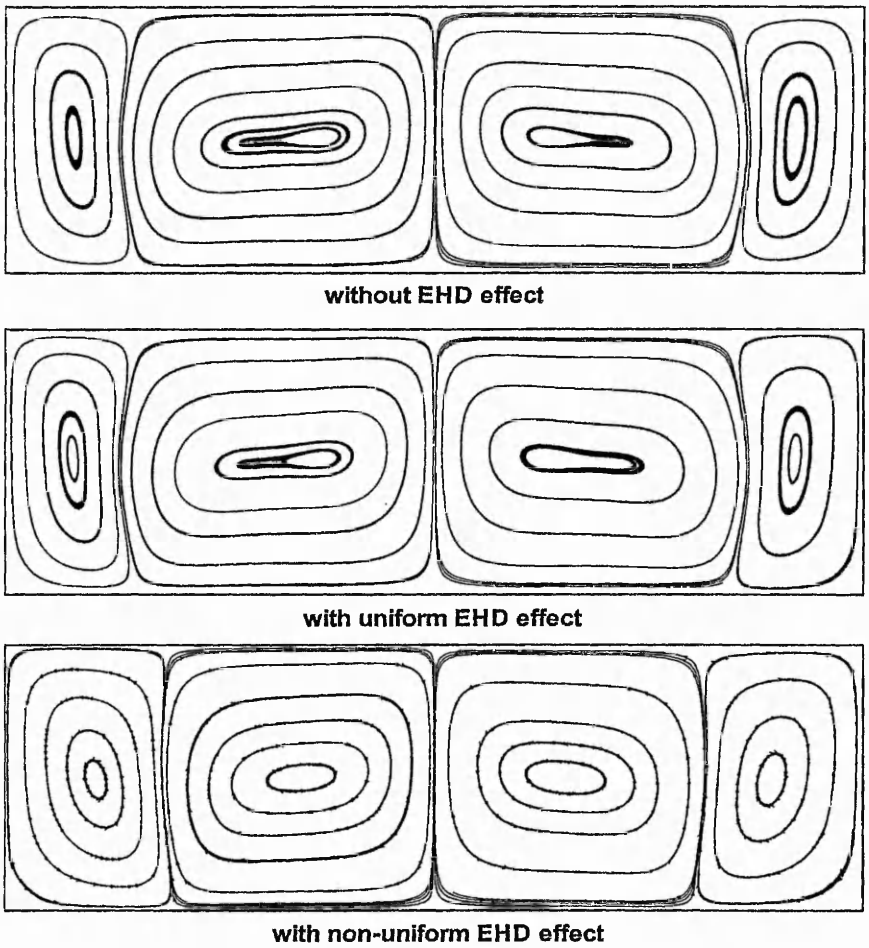

Figure 5.14b Comparison of streamlines of Fluid Beta at ϕ=5000v

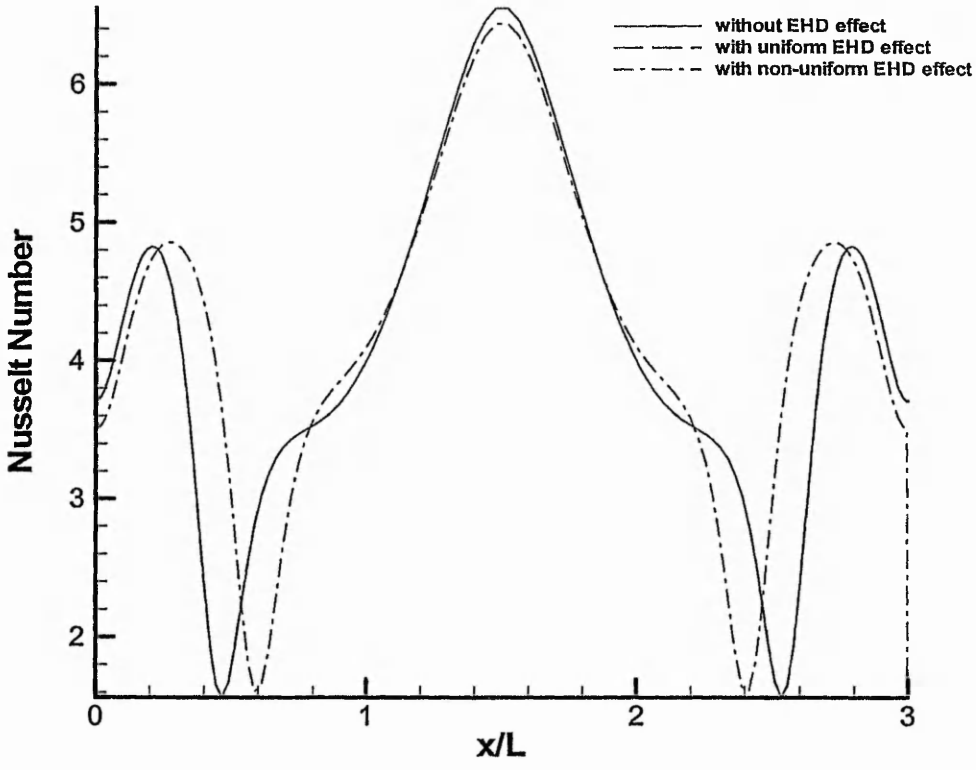

Figure 5.14c Comparison of local Nusselt number along the hot wall of Fluid Beta at ϕ=5000v

Figures 5.14a, b and c give the comparison of the thermal contours, streamlines and local Nusselt number distribution of fluid Beta at with and without EHD effect, respectively. Those figures show that there are not much significant difference between the thermal and flow fields before and after the application of the electric fields; this situation also happens to the application of a non-uniform electric field. The results

prove that the flow and thermal fields are very stable and the EHD effect are not strong enough to disturb the flow field and enhance the heat transfer in this case.

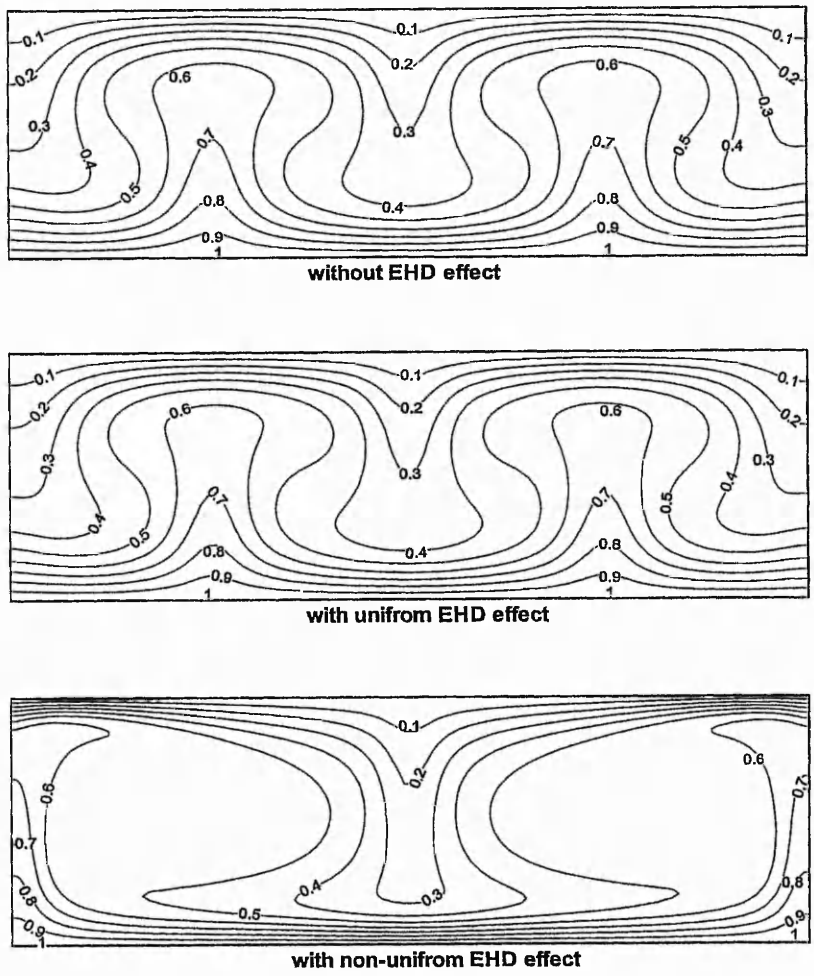

Figure 5.15a Comparison of thermal contours of fluid ECO-C at ϕ=5000v

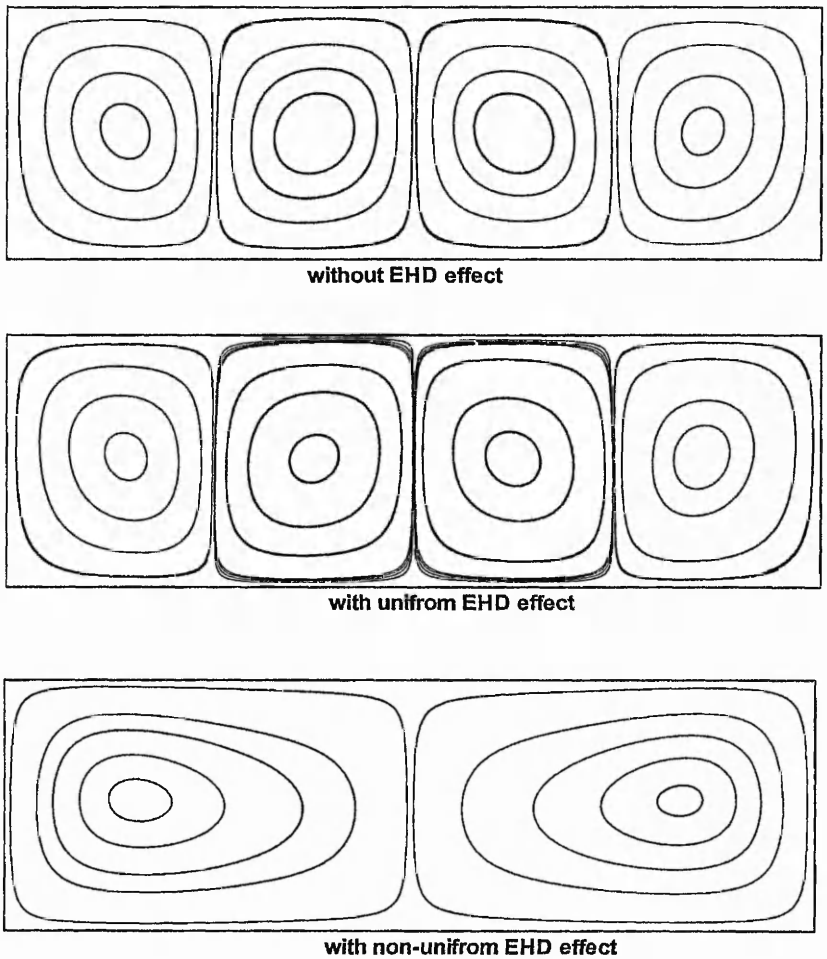

Figure 5.15b Comparison of streamlines of fluid ECO-C at ϕ=5000v

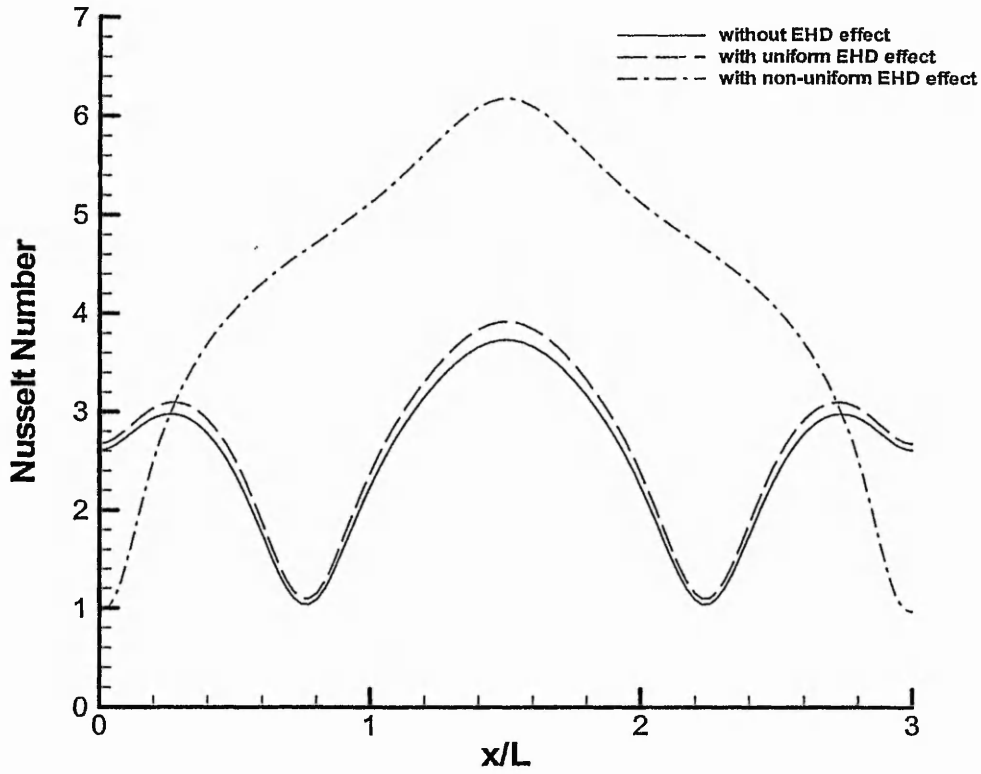

Figure 5.15c the comparison of local Nusselt number along the hot wall of fluid ECO-C

Figure 5.15a, b and c give comparisons of the thermal contours, streamlines and local Nusselt number distribution of fluid ECO-C with and without EHD effect, respectively. It can be seen that there is a big difference in the thermal contour distribution between no EHD effect and non-uniform EHD effect. The temperature gradient is steeper at the centre of the hot wall. In figure 5.15c, there are two bigger vortices apparent instead of four similar sized vortices. The local Nusselt number distribution shows that with the non-uniform electric field applied, the maximum of the local Nusselt number is much

higher than the case with uniform electric field. However, when the electric field applied is uniform, the effect of EHD on thermal and flow fields are not very effective and the enhancement of heat transfer by the EHD effect becomes very limited.

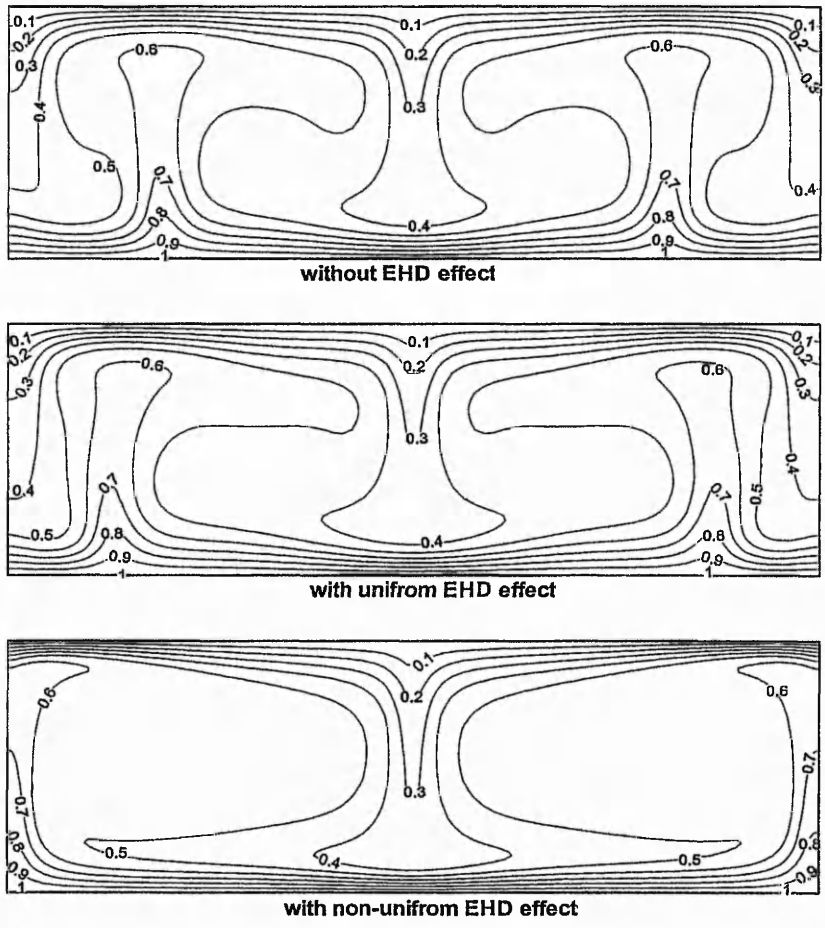

Figure 5.16a Comparison of thermal contours of fluid PAO at ϕ=5000v

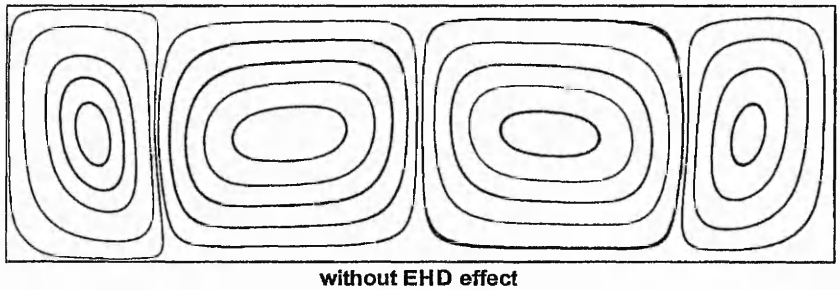

without EHD effect

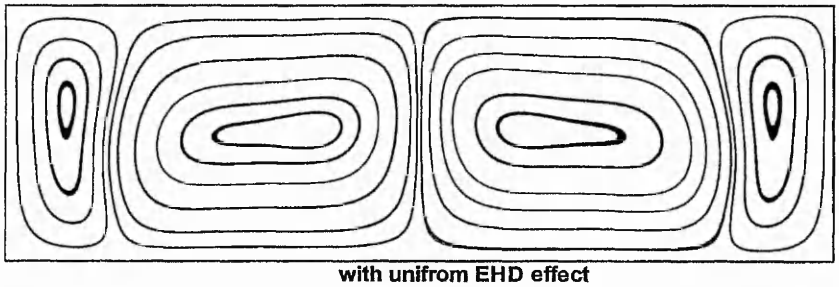

with unifrom EHD effect

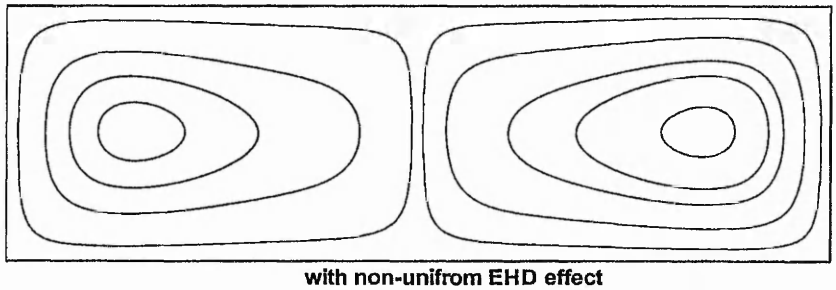

with non-unifrom EHD effect

Figure 5.16b Comparison of streamlines of fluid PAO at ϕ=5000v

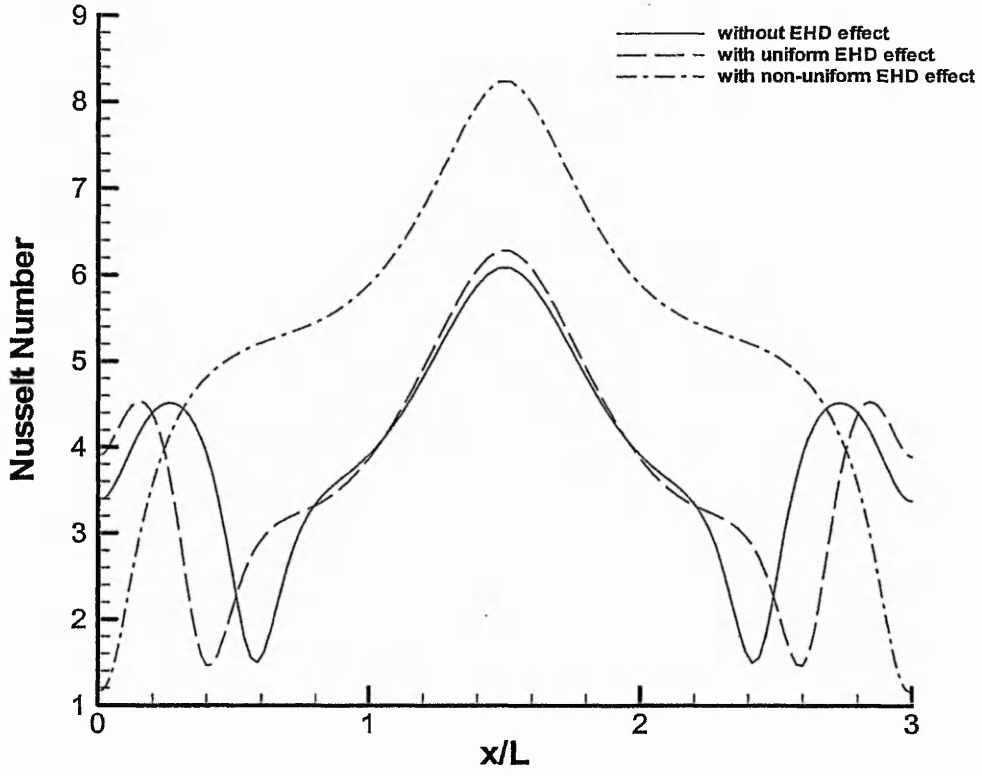

Figure 5.16c Comparison of local Nusselt Number along the hot wall at ϕ=5000v (fluid PAO)

Figures 5.16a, b and c give the comparison of the thermal contours, streamlines and local Nusselt number distribution of the fluid PAO with and without EHD effect, respectively. Similar to the fluid ECO-C, there is a big difference in the thermal contour distribution between without EHD effect and with non-uniform EHD effect. The temperature gradient is steeper at the centre of the hot wall. In Figure 5.16b, there are two bigger vortices apparent instead of four similar sized vortices. The local Nusselt

number distribution shows that with the non-uniform electric field applied, the maximum of the local Nusselt number is greatly increased. Different to the fluid ECO-C, the application of a uniform electric field also has some visual effect on the flow and thermal fields. Figure 5.16b shows that there are two vortices near the side walls become smaller compared with the no EHD case. In Figure 5.16c, it can be seen there is a shift of the local Nusselt number curve; the maximum of local Nusselt number is slightly higher than the case of no EHD effect.

Table 5.7 Comparison of the Nusselt Number of the three fluids at voltage of 5000v

Nu_{av}	Beta	ECO-C	Pao
Without EHD	4.1209	2.5204	3.9510
With non-uniform EHD	4.2567	4.7536	5.3690
The increase of $\overline{Nu}$	3.295%	89.26%	35.89%

Table 5.8 Properties of the three fluids (2)

	Beta	ECO-C	Pao
Viscosity at 40°C (mm^2/s)	6.6	3.5	108
Electrical conductivity, S/m	2.7×10^{-10}	4.76×10^{-13}	6.25×10^{-13}

Table 5.7 gives the comparison of the mean Nusselt number of the three different working fluids at the voltage of 5000v. The peak increase occurs for the Fluid ECO-C, with non-uniform electric field applied, there is an 89.26% increase of the mean Nusselt number.

Table 5.8 lists the properties which are quite different between the three fluids; it can be seen the fluid ECO-C has the lowest viscosity and Electrical conductivity compared to the other two fluids. The low viscosity is the dominant factor to distinguish the fluids. For the fluids Beta and ECO-C, which have similar magnitude of viscosity, the one with lower electric conductivity gives a higher heat transfer rate with non-electric field effect. Similarly, comparing fluid ECO-C with PAO, both have the same magnitude of electric conductivity, the one with lower viscosity gives a much higher heat transfer rate. These results are consistent in Paschkewitz and Pratt's work (2000), which found that the fluid with lower viscosity electrical conductivity gives a greater heat transfer enhancement for a given electrical power input.

5.5 Summary

In this chapter, the EHD effect on natural convection in rectangular and cylindrical enclosures are numerically studied. The results include: a) comparison of natural convection in a rectangular enclosure between with and without an uniform electric

field and at different Raleigh number; b) natural convection in a rectangular under uniform and non-uniform electric fields; c) natural convections in a cylindrical enclosure with and without applying an uniform electric field and at different Raleigh number; d) natural convection of three fluids in a rectangular enclosure with and without EHD effect and with non-uniform EHD effect. The main conclusions are:

(1). in a rectangular enclosure, the EHD enhancement is related to the Rayleigh number; an uniform electric field is more effective to enhance the heat transfer at lower Raleigh number case; as the Raleigh number increases, less enhancements are obtained;

(2). a non-uniform electric field is more effective than a uniform one to enhance the natural convection in a rectangular enclosure;

(3). in a cylindrical enclosure, a uniform electric field is more effective to enhance the heat transfer at higher Raleigh number; as the Raleigh number increases, more enhancements of heat transfer can be obtained;

(4). in a rectangular enclosure, the fluids with lower viscosity and lower electrical conductivity give greater heat transfer enhancements for a given electrical power input; between the viscosity and electrical conductivity, the viscosity is the dominant factor for obtaining good EHD effect. This conclusion agrees well with the experimental observations by the Paschkewitz and Pratt's (2000).

Chapter 6
EHD effect on Heat and Flow around R134a Bubble during Nucleate Boiling

6.1. Introduction

Nucleate boiling is an effective mode of heat transfer and it is very important for industries because of relatively small temperature differences result in high heat transfer rates. Due to the benefits of high heat transfer rates and the demand of removal of large amounts of heat from extended small heated surfaces, which often occurs in the fast growing microchips industries, gas-liquid two-phase heat transfer enhancement has been particularly paid attention by researchers; and a lot of effective techniques have been developed. The EHD method is an active technique for enhancing gas-liquid two-phase heat transfer in nucleate boiling and has demonstrated a great promise.

In order to understand the mechanism of EHD enhancement of nucleate boiling, numerous theoretical and experimental analyses have been conducted in the last few decades to investigate the effects of an electric field on bubble dynamics (Cheng and Chaddock, 1985; Feng and Beard, 1991; Karayiannis & Allen, 1991; Ogata and Yabe, 1993a, b; Yan, Neve, Karayiannis, Collins and Allen, 1996; He and Chang, 1995; Cho, Kang, Kweon and Kim, 1996; Seyed-Yagoobi, Geppert and Geppert, 1996; Karayiannis

and Xu, 1998a,b; Kweon and Kim, 2000; Zaghdoudi and Lallemand, 2001; Iacona, Herman and Chang, 2002; Madadnia and Koosha, 2003). Allen and Karayiannis (1995) gave a detailed review about the research on EHD enhancement on both single and two-phase flows. In general, the experiments have revealed that in nucleate boiling, an electric field can increase bubble frequency, reduce the departure size of bubbles, and increase the maximum value of heat flux. However, the mechanism of heat transfer enhancement by EHD, for example how the flow and temperature fields are altered by the electric force, keeps unveiled in the experimental studies. And it is obvious that using experimental methods such as nowadays particle image velocimetry (PIV) technology to study the details such as structure of vortices around a bubble surface is still expensive and with high cost. In this situation, numerical simulation becomes an efficient tool for analysing the heat and flow detail and their variation when an electric field is applied.

The establishment of the mathematical model is the first step of simulating the flow detail relevant to a gas-liquid interface of bubble under an electric field. Because of the nonlinearity of the problem, all the equations of the fields of electric current, heat and fluid flows must be coupled with each other to form a well-posed governing equation system; and the effects of nonlinear interaction between the fields, such as the electric body force and Joule heat, must be considered. Takata, Shirakawa, Tanaka, Kuroki and Ito (1996) tried to analyse the effects of electric body force on the interfacial flow, however, the temperature field was neglected in their study, and therefore, their mathematical model cannot be used to analyse the EHD enhancement of heat transfer.

Cho, Kang, Kweon and Kim (1996) also presented a mathematical model for analysing the effects of a uniform electric field on a bubble attached to a wall, and again, the temperature field was not considered in their governing equations; moreover, in their method, the pressure difference for determining the bubble shape was not available because they did not present any information of how the flow field was calculated. The calculation model of electric field proposed by Karayiannis and Xu (1998a), as we mentioned it in the chapter 2, is a novel attempt to analyse the EHD effect on bubbles because several bubbles can be considered, and only the electric field need to be calculated. However, as we reviewed, the flow field is decoupled with the electric and temperature fields in their model; and the sharp jump of permittivity across the bubble surface may induce difficulty for the differential operations in numerical calculation.

The second challenging task of simulating a gas-liquid interfacial flow of a bubble under an electric field is to highlight the flow fields at the vicinity of the gas-liquid interface. There is a large family of bubble shape determining strategies, such as the volume of fluids (VOF) methods, the level-set methods and the front-tracking methods. A good review of these methods has been provided by Shyy, Udaykumar, Rao and Smith (1996). Generally speaking, the volume-tracking methods (VOF and level-set) are robust in tracking the bubble deformation but poor in highlighting the flow details at the vicinity of gas-liquid interface; the front-tracking methods, such as the body-fitted coordinates transformation method by Ryskin and Leal (1984), are promising in revealing the interfacial flow details but weak in predicting highly deformable bubbles.

In this chapter, EHD effect on the heat and mass transfer around a bubble in nucleate boiling is numerically studied. A physically simplified model of a single R134a bubble during nucleate boiling will be presented. The mathematical model for coupled electric, flow and thermal fields established in chapter 3 is employed to study the EHD effect on a spherical bubble cap attached on the heated wall of a boiler, with an electric field applied. A numerically generated non-orthogonal curvilinear cylindrical body fitted mesh system is employed to map the bubble profile so that the flow details at the vicinity of the gas-liquid interface can be highlighted. Well-posed boundary conditions and a gas-liquid interfacial treatment are presented. Numerical simulation of the EHD enhancement of heat transfer around a bubble during nucleate boiling of R134a is carried out. The results are analysed.

6.2. Problem statement and assumptions

Early efforts to solve the flow field around a bubble were focused on a fixed shape such as spherical and spherical bubbles and this can be identified from work of Hadamard (1991), Rybczynski (1991), Levich (1947), Hamielec *et al.* (1967) and Brabston and Keller (1975). In order to study the mechanism of EHD enhancement of heat transfer, a gas bubble attached to the centre of a heated wall of an electrode is considered; the geometry is shown in figure 6.1. The electrodes are a pair of parallel round discs, with a voltage applied between them; the upper disk is connected to the

ground while the lower wall is superheated during nucleate boiling. The gap size between the electrodes is L; the diameter of the electrodes is denoted by W. In the figure, y and r are the axis of symmetry and the radial coordinate of the cylindrical system, respectively.

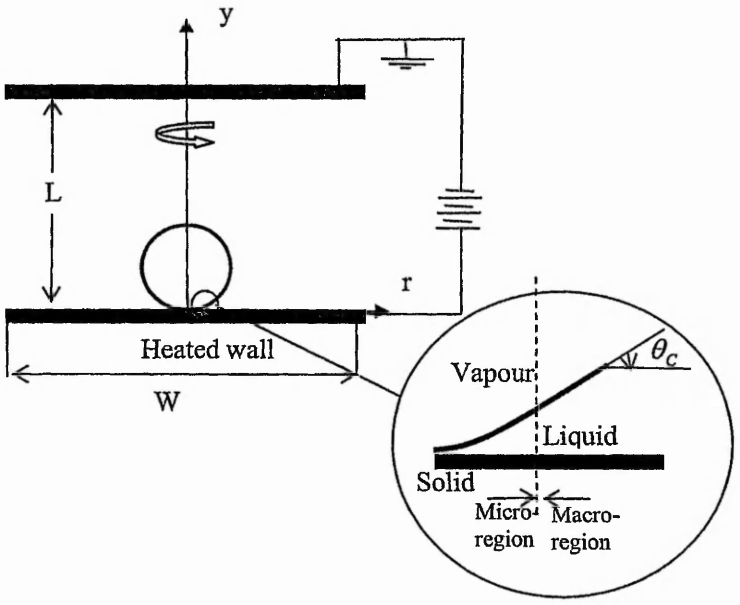

Fig 6. 1 A vapour bubble attached to a heated wall

During nucleate boiling, the heat transfer between the gaseous and liquid phases include two parts, i.e., heat transfer through the bubble cap and heat transfer through a microlayer underneath the bubble. The mechanism of nucleate boiling considering the vaporization of a microlayer was first suggested by Moore and Mesler (1961). They found the wall surface temperature occasionally dropped 20-30°F in about 2 milliseconds and suggested the rapid heat removal was possibly caused by vaporization

of the this water layer underneath a bubble. Later, Sharp (1964), Cooper and Lloyd (1966, 1969) and Jawurek(1969) experimentally demonstrated the vaporization of the microlayer at the base of bubbles during nucleate boiling. The existence of the microlayer is an undisputed fact, but its contribution to heat transfer in nucleate boiling is still not well defined. Depending on the boiling conditions, the estimate of its contribution to the energy required for bubble growth varies from less than 20 percent to nearly 100 percent (Voutsinos and Judd, 1975; Van Stralen et al, 1975; Judd and Hwang, 1976; Fath and Judd, 1978; Koffman and Plesset, 1983). In this study, our purpose is to qualitatively reveal the EHD effect on the heat transfer enhancement, vaporization of the micro-layer is temporarily not considered so as to eliminate the difficulties of calculating both the micro- and macro regions. In the meanwhile, the change of physical properties with the temperature distribution is also neglected so as to focus our attention on studying the EHD effect on the flow and temperature fields in the vicinity of liquid-vapour interface. In the boiling of low super heat, the variation of temperature in the whole flow field is weak and the neglecting of this change of fluid properties should be acceptable. And the pressure and temperature inside the bubble are considered as uniform (at saturation point); the electric field inside the bubble is also regarded as uniform. A full model taking into account of all factors such as the microlayer and the non-uniformity of fluid properties may be considered in our further work.

Summarily, considering the extreme complexities, the following assumptions are made to address the problem:

- The evaporation of the micro-layer is not considered in this study;
- The shape of the bubble is spherical or a truncated sphere;
- The contact angle θ_c is constant;
- The surrounding flow is laminar and incompressible, the properties of the fluid are constants;
- The pressure and temperature inside the bubble are uniform and at their saturation points; the electric field is also assumed to be uniform, i.e., the distribution of electric potential φ is assumed to be linear, and the electric field strength $\vec{E}$ is uniform;
- Because of the large time scale for bubble growth (compared with bubble departure), the heat and fluid flows are treated as steady problems.
- The electric field between the electrodes is uniform; an electric current in a dielectric liquid can be modelled as a direct motion of electrically charged particles injected in to a neutral fluid.

The assumptions and simplifications above are possibly not good agreement with the physical reality, for example, the spherical bubble shape and the constant contact angle θ_c. However, the purpose of making such assumptions is to reduce the physical complexity so as to highlight and analyse the effects of EHD on the heat and fluid flows around the gas-liquid interface of the bubble, and to further analyse the mechanism of heat transfer enhancement. This purpose is exactly the basic aim of the current research.

There is a section of checking the effects of the constant contact angle in chapter 8, where the acceptability of this assumption will be shown.

Table 6.1 Physical properties of R134a at 20°C

ρ (density)	1225.3 kg m^{-3}
ν (viscosity)	2.107×10^{-5} kg m^{-1} s^{-1}
k (thermal Conductivity)	8.33×10^{-2} $Wm^{-1}K^{-1}$
σ_{ST} (surface tension coefficient)	8.76×10^{-3} Nm^{-1}
c_p (specific heat transfer)	1.405 kJ kg^{-1} K^{-1}
ε (permittivitty)	8.416×10^{-11} Fm^{-1}

The dielectric liquid of R134a is selected as the working fluid for its environmentally friendly character. The physical properties of R134a are shown in table 6.1.

According to the correlation observed by Fritz (1935):

$$R_d = 0.0103\times\theta_c\times\left(\sigma_{ST}/\rho g\right)^{0.5} \tag{6.1}$$

where R_d is the bubble departure radius, σ_{ST} is the coefficient of surface tension, θ_c is the contact angle, ρ and g are the density of liquid and the gravity respectively. In this chapter, θ_c=15° is selected and the departure diameter $R_d = 1.57\times10^{-4}$m. In the configuration shown in figure 6.1, the gas size of electrodes L=1×10^{-3} m; the diameter of the electrodes is W= 3×10^{-3} m. The ratio of the electrodes gap and the diameter of the

electrode is L/W=0.333 in the present study; therefore, the electric field can be assumed uniform because $L/W \leq 0.375$ (Takuma, Kawamoto and Sunaga, 1985). The characteristic parameter l_0 for normalisation in equation (3.6.1) is the bubble diameter at departure point, $l_0 = 2R_d = 3.14\times10^{-4}$ m.

The electric mobility is obtained by Walden's rule. The relation is given by Adamczewski (1969) as:

$$b_0 = \frac{2\times10^{-11}}{\mu_0} \quad , \tag{6.2}$$

where μ_0 is the reference dynamics viscosity, $kg \cdot s / m^2$.

6.3. Mesh, Boundary Condition and Treatments

6.3.1 Non-orthogonal body-fitted mesh

In order to highlight the flow details in the vicinity of the gas-liquid interface of the bubble, a non-orthogonal body-fitted mesh system is employed to map the bubble profile. A typical mesh for the current numerical study is shown in figure 6-2a. This mesh is generated by the two-step method presented in chapter 4. The mesh size for the present calculation is 200×200, which was shown to be fine enough for eliminate the grid-independency of the results in our preliminary calculation.

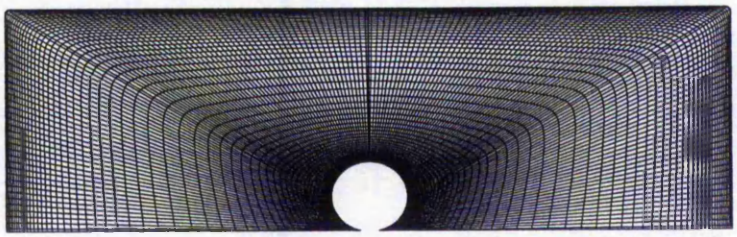

Figure 6.2a Body-fitted mesh for calculation

6.3.2 Boundary conditions

Considering the mentioned possible difficulty for differential operations in numerical calculation using Karayiannis and Xu's (1998a) model in which there is a sharp jump of permittivity across the bubble, we use a method of defining the bubble profile as a part of the computational domain; this is similar to the treatments of bubble surface by Ogata and Yabe (1991) and (1993a) and Yan et al. (1996). However, we will not employ the zero-electric-strength assumption in our model. Rather than that, we only assume the uniform distribution of fields inside the bubble. Based on this assumption, the mathematical descriptions for the boundary condition at the bubble surface become the zero second derivatives for the electric field (linear or uniform distributions) and saturation points for pressure and temperature.

Figure 6.2b illustrates the boundary conditions. Based on the mentioned assumptions in above, the following boundary conditions are imposed:

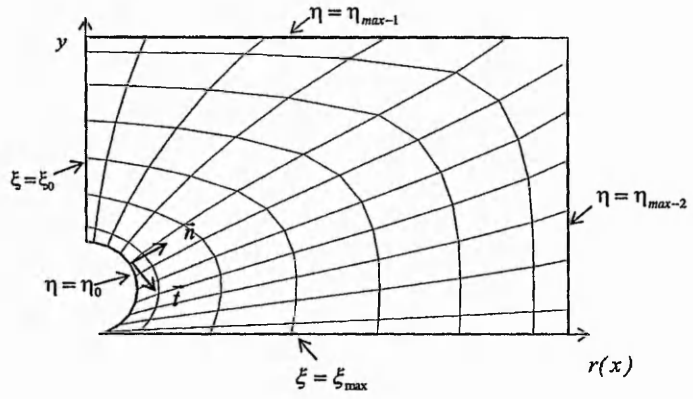

Figure 6.2b Illustration of mesh and boundaries

- At the bubble surface ($\eta=\eta_0$):

$$T=T_{Sat};\quad p=p_{sat};\quad \frac{\partial^2\varphi}{\partial^2 n}=-\frac{\partial E}{\partial n}=0;\quad \frac{\partial^2 q}{\partial^2 n}=0 \tag{6.3}$$

$$\tau_{\vec{t}}=0;\ V_{\vec{n}}=0. \tag{6.4}$$

where $\vec{n}$ and $\vec{t}$ are the unit normal and tangential vectors of the bubble surface; $\tau_{\vec{t}}$ is the tangential stress and $V_{\vec{n}}$ is the normal velocity.

- At bottom wall ($\xi=\xi_{\max}$):

$$u=0,\quad v=0,\quad \frac{\partial^2 p}{\partial y^2}=0,\qquad T=T_{sat}+\Delta T,\qquad \varphi=1,\quad q=1; \tag{6.5}$$

- At axis of symmetry ($\xi = \xi_0$):

$$u = 0, \quad \frac{\partial v}{\partial r} = 0, \quad \frac{\partial p}{\partial r} = 0, \quad \frac{\partial T}{\partial r} = 0, \quad \frac{\partial \varphi}{\partial r} = 0, \quad \frac{\partial q}{\partial r} = 0; \tag{6.6}$$

- At top wall ($\eta = \eta_{\max-1}$):

$$u = 0, \quad v = 0, \quad \frac{\partial^2 p}{\partial y^2} = 0, \quad T = T_{sat}, \varphi = 0, \quad \frac{\partial^2 q}{\partial^2 y} = 0; \tag{6.7}$$

- At right boundary ($\eta = \eta_{\max-2}$):

$$\frac{\partial u}{\partial r} = 0, \quad \frac{\partial v}{\partial r} = 0, \quad \frac{\partial^2 p}{\partial^2 r} = 0, \quad \frac{\partial^2 T}{\partial^2 r} = 0, \quad \frac{\partial^2 \varphi}{\partial^2 r} = 0, \quad \frac{\partial^2 q}{\partial^2 r} = 0. \tag{6.8}$$

6.3.3 Interfacial treatment

The slip and no penetration conditions at the bubble surface, namely, $\tau_{\tilde{t}} = 0$ and $V_{\tilde{n}} = 0$ in equation (6.4) need a special treatment because they cannot explicitly decide the boundary values of Cartesian velocity components u and v. Therefore, the tangential stress in the $\xi - \eta$ coordinates system is expanded as,

$$\tau_{\tilde{t}} = \frac{\mu}{\gamma \tilde{J}} \left\{ x_\xi \gamma \frac{\partial u}{\partial \eta} + y_\xi \gamma \frac{\partial u}{\partial \eta} + \frac{\partial u}{\partial \xi} \left[-\left(x_\xi \chi + y_\xi \tilde{J} \right) \right] + \frac{\partial v}{\partial \xi} \left[\left(x_\xi \tilde{J} - y_\xi \beta \right) \right] \right\}, \tag{6.9}$$

where α, β, γ and $\tilde{J}$ are geometrical metrics of the $\xi - \eta$ coordinates system and

calculated according to equations (3.6.15), (3.6.16), (3.6.17) and (3.6.18) respectively. Then $\tau_t = 0$ becomes:

$$A\frac{\partial u}{\partial \eta} + B\frac{\partial v}{\partial \eta} = C; \tag{6.10}$$

where $A = x_\xi \gamma$, $B = y_\xi \gamma$, $C = \frac{\partial u}{\partial \xi}\left(x_\xi \beta + y_\xi \tilde{J}\right) - \frac{\partial v}{\partial \xi}\left(x_\xi \tilde{J} + y_\xi \beta\right)$.

Combining equation (6.10) with $V_{\vec{n}} = 0$,

$$u = v \cdot x_\xi / y_\xi; \tag{6.11}$$

Denote the grid point at the bubble surface and the first nearest node with subscripts "1" and "2" respectively, equations (6.10) and (6.11) are discretised as:

$$\begin{cases} A\dfrac{u_2 - u_1}{\eta_2 - \eta_1} + B\dfrac{v_2 - v_1}{\eta_2 - \eta_1} = C \\ u_1 = v_1\left(x_\xi / y_\xi\right)_1 \end{cases} \tag{6.12}$$

In order to avoid the "divided by zero" situation, the boundary velocity is calculated as follows:

$$\begin{cases} u_1 = \dfrac{Au_2 + Bv_2 + C(\eta_2 - \eta_1)}{A + B\, y_\xi / x_\xi}, & v_1 = u_1 \cdot (y_\xi / x_\xi)_1 \qquad (if \ \ |x_\xi| \geq |y_\xi|) \\ v_1 = \dfrac{Au_2 + Bv_2 - C(\eta_2 - \eta_1)}{A(x_\xi / y_\xi)_1 + B}, & u_1 = v_1 \cdot (x_\xi / y_\xi)_1 \qquad (if \ \ |x_\xi| \leq |y_\xi|) \end{cases} . \quad (6.13)$$

6.3.4 Temperature Singularity at Triple Point

It is noticeable that the assumption of neglecting the micro-layer induces a singularity for the temperature at the triple point. This can be seen that equation (6.3) gives $T = T_{Sat}$ to the triple point, however, equation (6.5) give another value, $T = T_{sat} + \Delta T$. In order to remove this singularity, a treatment is carried out on the grids near the triple point.

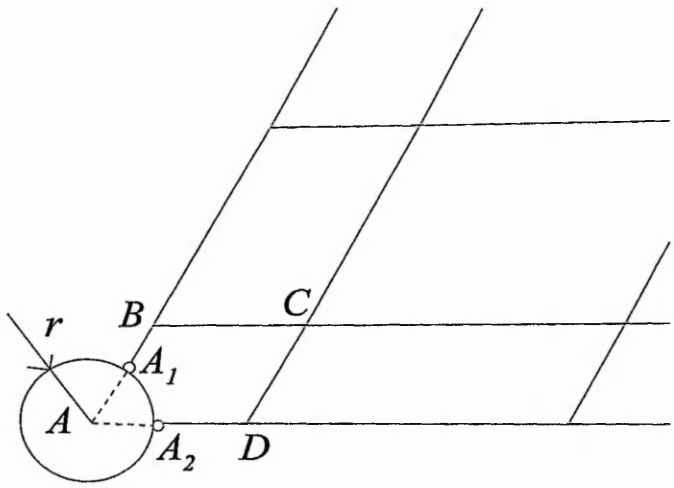

Figure 6.2c Grid treatments at triple point

As shown in figure 6.2c, the grid node A (coincide with the triple point) was replaced by

points A_1 and A_2, respectively, in two directions of the grid lines. Point A_1 and A_2 are at a distance of r to its original position A. The smaller distance r is closer to the original position. For the convenience of generating the mesh, r is set to be $r = 0.1 \times \min(|AB|, |AD|)$ in this thesis. Obviously, the temperature values at points A_1 and A_2 are $T = T_{Sat}$ and $T = T_{sat} + \Delta T$, respectively. Therefore, the treatment on the mesh has removed the temperature singularity; but it also has side effects on the accuracy of numerical result because the Jacobian value for the control volume $ABCD$ has been changed. However, these side effects are confined in the first control volume A_1BCDA_2 and therefore the general accuracy of the numerical results should be accepted.

6.4. Results and analysis

The electric potentials applied are 0v, 2000v, 4000v, 5000v, 8000v and 10000v, respectively. The dimensionless numbers are chosen as follows: $Gr = 6.625$, $\mathrm{Re} = 2.574$, the rest of dimensionless numbers are shown in table 6.2. Convergence paths in terms of the mass residuals for the calculation are shown in figure 6.3, where E_2 and E_3 have been defined in equations (4.5.3) and (4.5.4). The figure shows that the convergence of the calculation is smooth. Based on this, the numerical results are shown in figures 6.4 ~ 6.9.

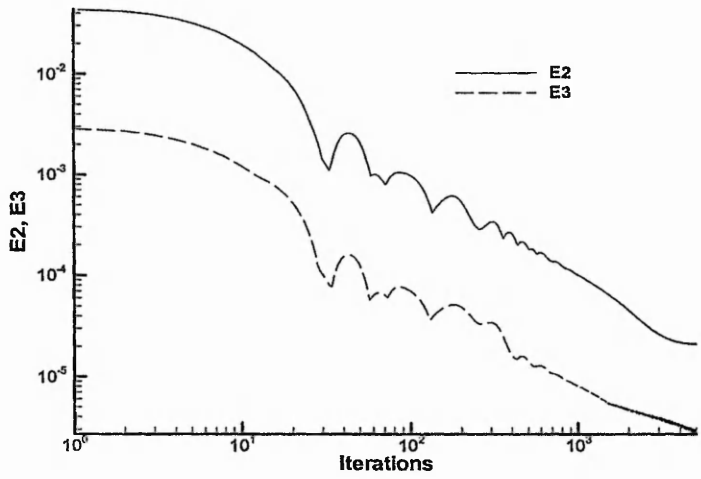

Fig 6.3 convergence paths

Table 6.2 dimensionless numbers

Voltages	2000v	4000v	5000v	8000v	10000v
S_E	3.9980	7.9960	9.9950	15.9920	19.9899
N_E	0.003713	0.001857	0.001485	0.0009285	0.0008426
Pr_E	0.01720	0.008600	0.006880	0.004300	0.003840

Figure 6.4 shows the change in the streamlines of the flow field has the electric potential varies from 0V, 2000V, 4000V, 5000V, 8000V to 10000V. Although the streamline topology does not change with the increase in voltage, the core of the ring vortex around the bubble moves in the direction of the heated wall and the diameter of the vortex becomes smaller and smaller. This changing of the ring vortex induces a

thinner shear-flow layer at the vicinity of the bubble surface and therefore, a steeper temperature gradient normal to the gas-liquid interface can be expected when the voltage is increased. This analyse is confirmed in figure 6.5, where the contours of temperature are presented. As shown in figure 6.5, again, a change of the contour line topology can not be identified; however, it is very clear that the contours are getting denser at the vicinity of the bubble surface when the voltage is increased step by step. As a result, the averaged value (along the bubble surface) defined as following:

$$Nu_{av} = \frac{\int_0^{\xi_{max}} Nu \cdot r \cdot \sqrt{x_\xi^2 + y_\xi^2} \cdot d\xi}{\int_0^{\xi_{max}} r \cdot \sqrt{x_\xi^2 + y_\xi^2} \cdot d\xi}, \tag{6.14}$$

increases with the voltage; these parameters are shown in figures 6.6 and 6.7, respectively. As mentioned above, the grid point at the triple point has been treated so as to remove the temperature singularity; the treatment has side effects on the numerical accuracy in the first control volume. In order to carry out a sensible comparison between calculations of with different voltages, the integration bound in equation (6.14) ξ_{max} takes the value of the second grid point, i.e., $\xi_{max} = \xi_B$ (see point B in figure 6.3c).

Figures 6.8 and 6.9 are the distribution of electric potential and the charge density in the fields. Because the general gradient of dimensionless variable φ in y direction is not changed at different voltage, the difference of φ contours in figure 6.8 is not apparent; however, the contours of q at 2000V and 10000V (figure 6.9) show the higher voltage can obtain a higher level of q at the negative electrode; this means q has the

characteristics of a transport variable. According to equation (3.3.7), the stronger transport of q results in a stronger electric body force which adds fuel to the motion of ring vortex and therefore enhances the heat transfer at the gas-liquid interface.

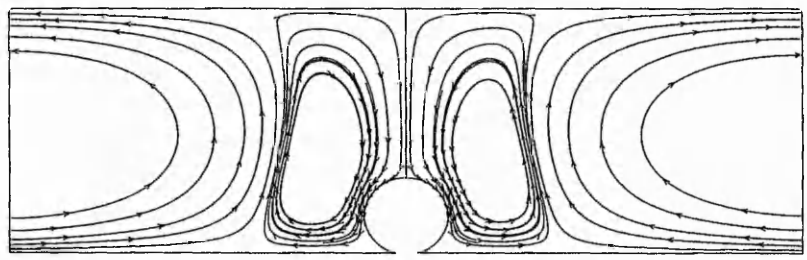

(a)

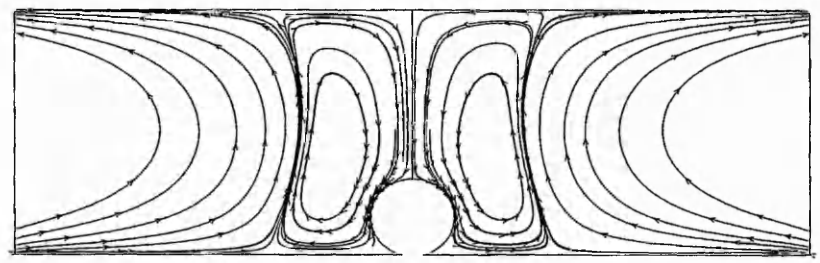

(b)

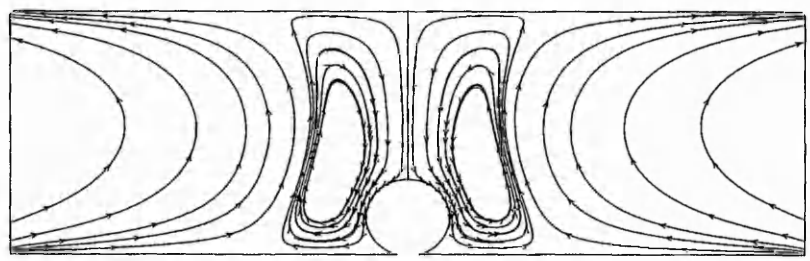

(c)

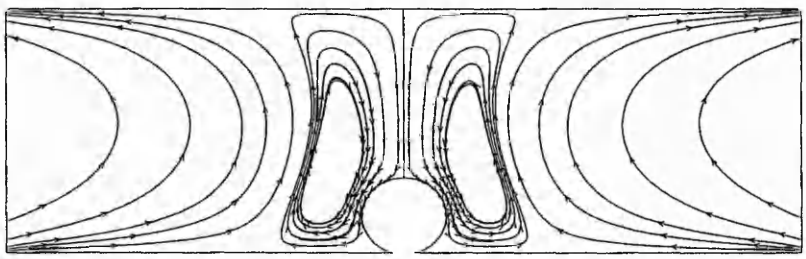

(d)

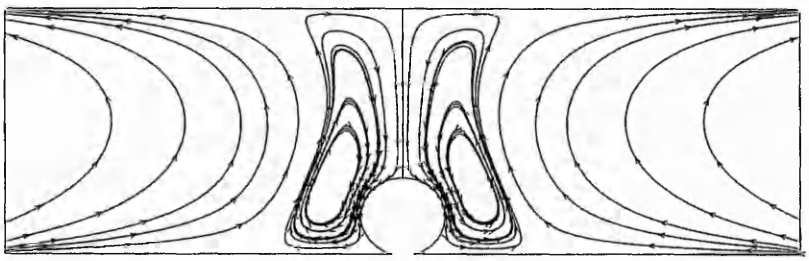

(e)

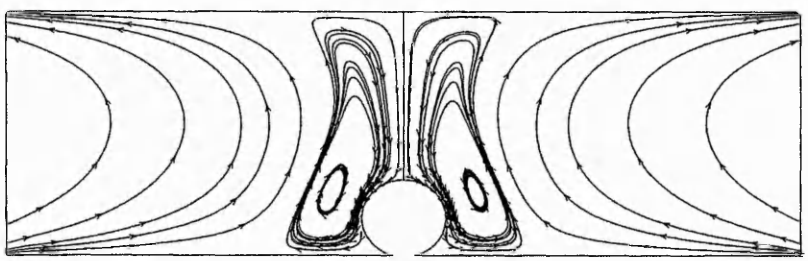

(f)

Figure 6.4 Streamlines around the bubble (a) $\varphi = 0$ (b) φ=2000v; (c) φ=4000v; (d) φ=5000v; (e) φ=8000v; (f) φ=10000v;

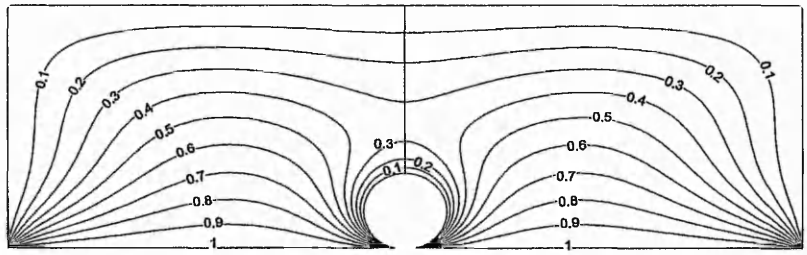
0.1
0.2
0.3
0.4
0.5
0.6
0.7
0.8
0.9
1

(a)

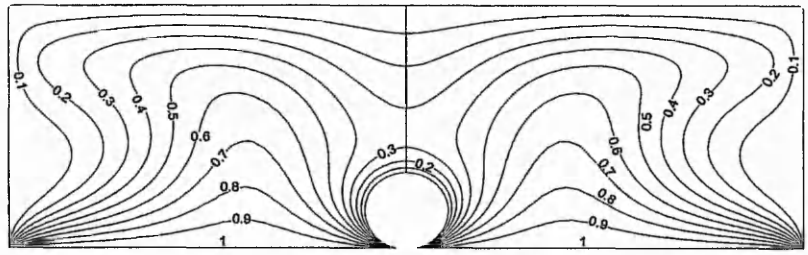
0.1
0.2
0.3
0.4
0.5
0.6
0.7
0.8
0.9
1

(b)

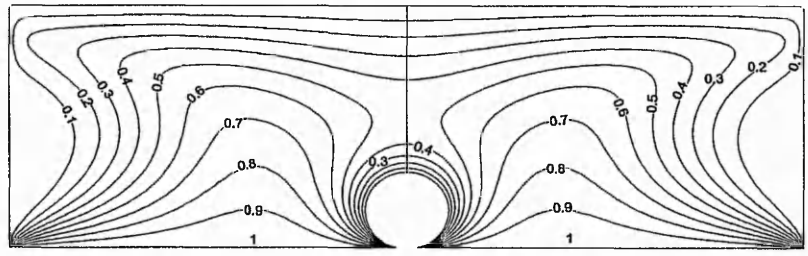
0.1
0.2
0.3
0.4
0.5
0.6
0.7
0.8
0.9
1

(c)

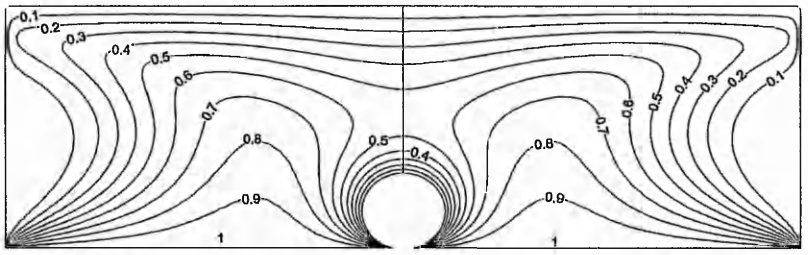

(d)

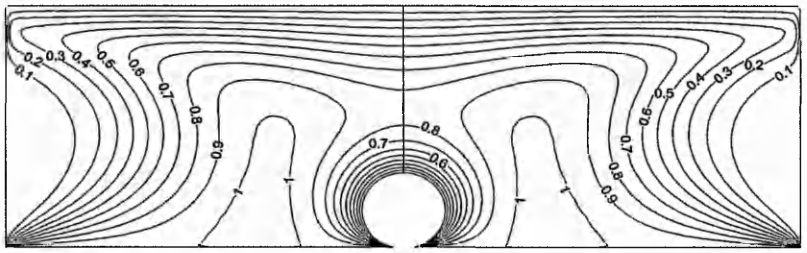

(e)

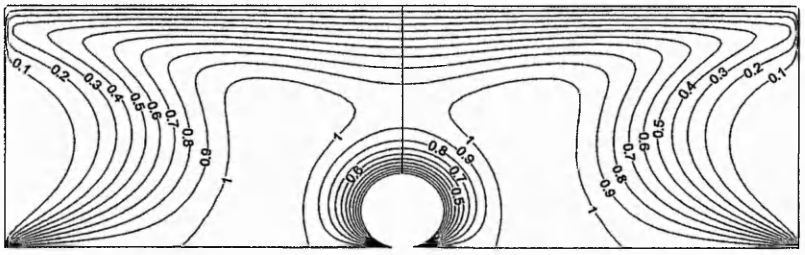

(f)

Figure 6. 5 Contours of temperature around the bubble (a) φ = 0 (b) φ =2000v; (c) φ =4000v; (d) φ =5000v; (e) φ =8000v; (f) φ =10000v;

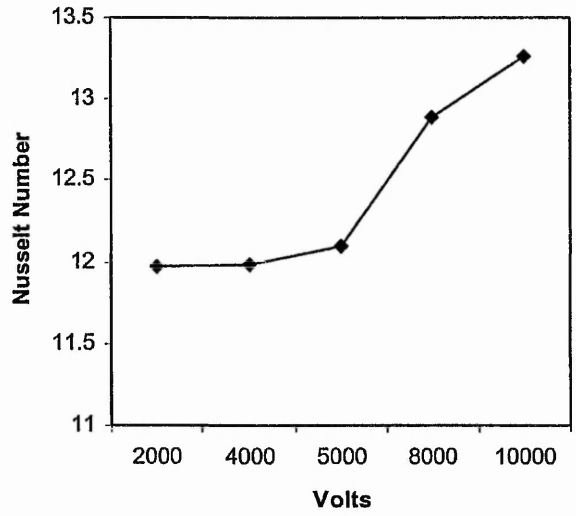

Figure 6.6 Average value of Nusselt number

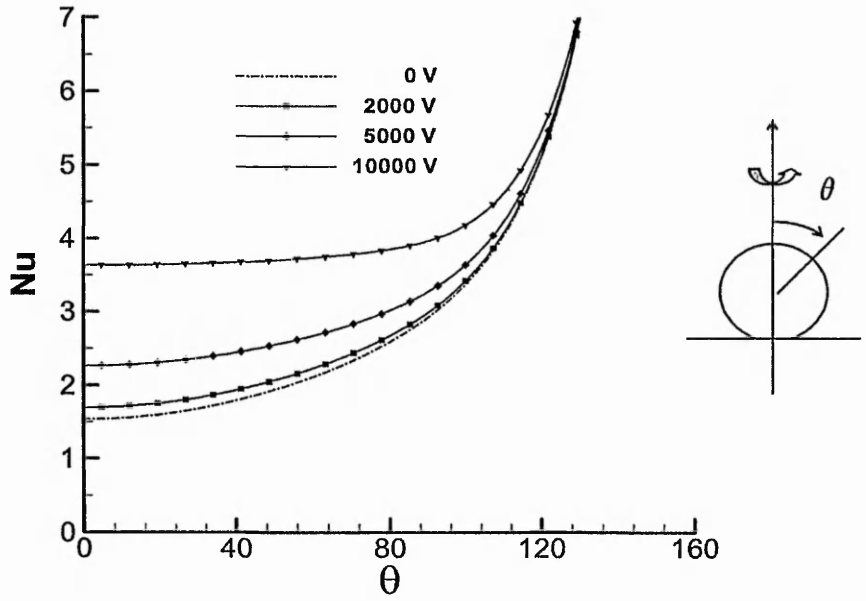

Figure 6.7 Local Nusselt number around the bubble

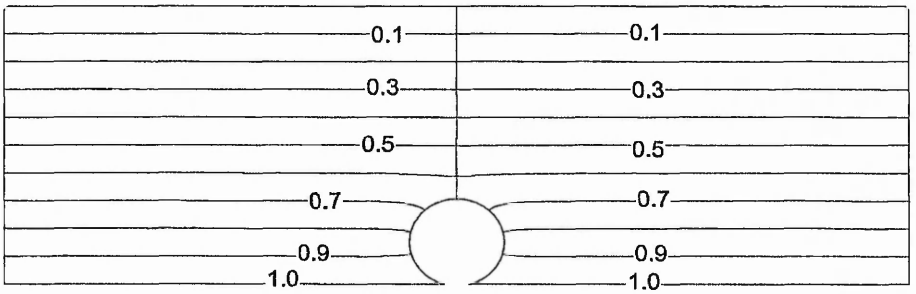

(a)

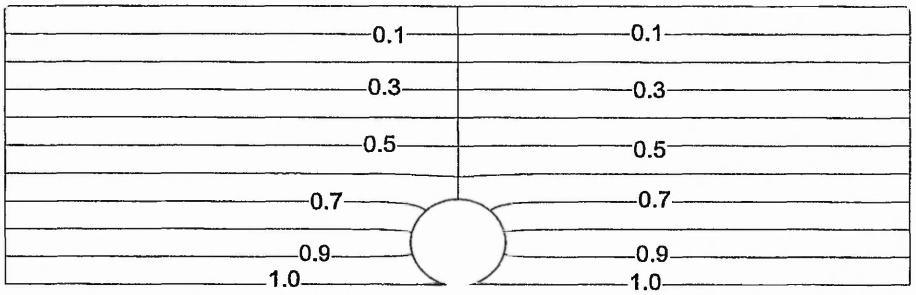

(b)

Figure 6.8 Distribution of electric potential (a) 2000V (b) 10000V

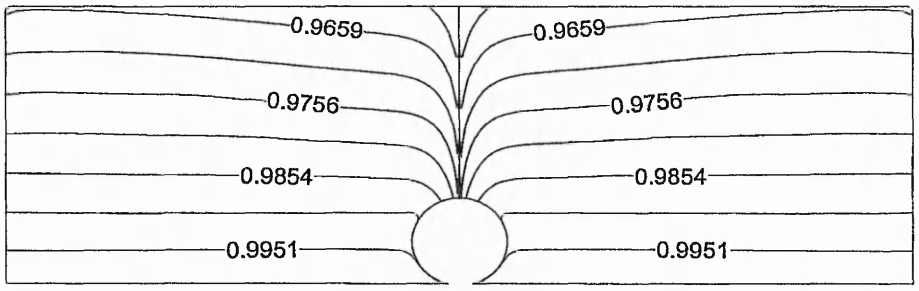

(a)

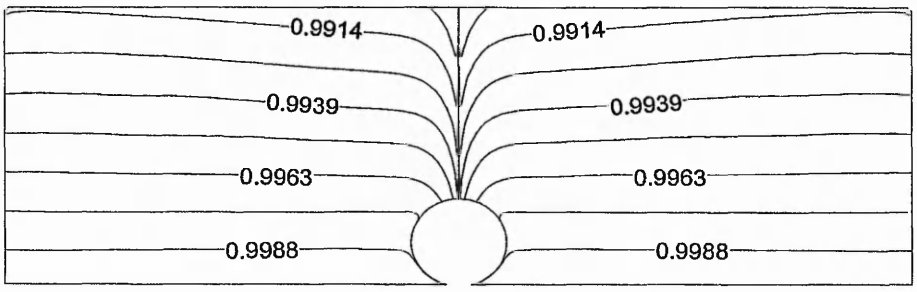

(b)

Figure 6.9 Distribution of charge density (a) 2000V (b) 10000V

6.5 Summary

This chapter used the mathematical model for the coupled electric, flow and thermal fields established in chapter 3 to analyse the EHD enhanced heat and fluid flow around a single bubble attached to a horizontal superheated wall of nucleate boiling. In order to

highlight the interfacial heat transfer phenomenon and its enhancement at the vicinity of a gas-liquid interface, assumptions such as spherical shape, constant contact angle, and negligible micro-layer are employed. Interfacial treatments are proposed and applied to calculate the velocity boundary value at the gas-liquid interface.

Numerical study of heat and flows around a bubble during nucleate boiling of R134a with different electric voltage applied between the electrodes is carried out. The calculation reveals that applying an electric field to nucleate boiling can enhance the motion of the vortex around the bubble by the electric body force; and reduce the thickness of shear flow layer. As a result, the heat transfer at the gas-liquid interface is enhanced.

Chapter 7
EHD Effect on Refrigerants with Different Relaxation Time

7.1 Introduction

In nucleate boiling, the charge relaxation time of the working fluid also plays an important role during bubble growth and departure in an electric field. When fluid is placed in an electric field, electric charge is generated. It takes a certain time for the influence of the electric field to take place. This time is called the relaxation time. The studies by Ogata and Yabi (1991, 1992, 1993a, 1993b) found that if the charge relaxation time is far greater than the bubble detachment period, the bubbles are not affected by the electric field. In this chapter the EHD effect on refrigerants with different charge relaxation time will be studied.

7.2 Relaxation Time

Consider a homogeneous fluid with electric conductivity σ and permittivity ε. Applying a current density $\vec{J}$, the density of free charges is q and the electric displacement $\vec{D}$, gives

$$\vec{D} = \varepsilon \vec{E} \quad . \tag{7.2.1}$$

In equation (3.3.4), if only the dominant term of $\vec{J}$ is considered, the equation is often reduced to

$$\vec{J} = \sigma \vec{E}, \tag{7.2.2}$$

Combine equations (6.19) and (3.3.3), then:

$$\nabla \cdot \left(\sigma \vec{E}\right) = \nabla \cdot \left(\frac{\sigma \vec{D}}{\varepsilon}\right) = -\frac{\partial q}{\partial t} \quad ; \tag{7.2.3}$$

If σ and ε are constants,

$$\nabla \cdot \vec{D} = -\frac{\varepsilon}{\sigma}\frac{\partial q}{\partial t} \quad . \tag{7.2.4}$$

Now using Maxwell's first equation,

$$div\vec{D} = q = \nabla \cdot \vec{D} = -\frac{\varepsilon}{\sigma}\frac{\partial q}{\partial t} \quad , \tag{7.2.5}$$

this gives a differential equation for q in which the variables can be separated

$$\frac{\partial q}{q} = -\frac{\sigma}{\varepsilon}\partial t \quad , \tag{7.2.6}$$

whose general solution is

$$\ln q = -\frac{\sigma}{\varepsilon}t + C \quad ; \tag{7.2.7}$$

where C is a constant of integration. Re-arranging equation (7.2.7),

$$q = \exp(-\frac{\sigma}{\varepsilon}t + C) \ , \tag{7.2.8}$$

and choosing $q = q_0$ at t=0, and then gives

$$q = q_0 \exp(-\frac{\sigma}{\varepsilon}t) = q_0 \exp(-\frac{t}{\tau}) \quad . \tag{7.2.9}$$

Equation (7.2.9) shows that there is a decay of charge density q which is exponential with time. The time constant

$$\tau = \varepsilon/\sigma \ , \tag{7.2.10}$$

is called the relaxation time. τ is a property of the media. For example, copper has the conductivity $\sigma = 5.8\times10^{7} sm^{-1}$, $\varepsilon \approx 1\times8.85\times10^{-12}$, so the relaxation time for copper is $\tau = 1.53\times10^{-19} s$; quartz has conductivity $\sigma \approx 1\times10^{-17} sm^{-1}$ and $\varepsilon \approx 4\times8.85\times10^{-12}$, its relaxation time $\tau = 3.5\times10^{6} s$.

The charge relaxation time represents the time needed by a free charge to relax from the fluid to the liquid interface. By comparing the relaxation time to the characteristic dynamical time t_c, which can be the period of the imposed electric field, the period of

the mechanical oscillations of a liquid-vapour interface, or the detachment period of bubbles, we can determine if the liquid behaves like an insulating fluid or not. Then if $t_c << \tau$, the fluid is highly insulating and the electric field is distributed within both liquid and vapour, without free electric charges. On the contrary, if $t_c >> \tau$, the electric field is totally excluded from the liquid, which behaves as a conducting fluid, and the entire voltage drop occurs at the liquid-vapour interface where electrical free charges appear.

The charge relaxation time is a critical but often neglected parameter in the formulation of models for EHD coupled heat transfer. It often determines the predominated terms in the electric body force (Jones, 1978). If the electric field is alternating at frequency of f, then for $f >> 1/\tau = \sigma/\varepsilon$, no free electric charge can build up at interfaces or in the bulk liquid, then the Columb force can be neglected. The studies by Ogata and Yabi (1991, 1992, 1993a, 1993b) found out that if the charge relaxation time is far greater than the bubble detachment period, the bubbles are not affected by the electric field.

According to equation (7.2.10), the differences in the relaxation time of the working fluids correspond to differences of conductivity and permittivity. This chapter compares the EHD effect on the working fluids with different relaxation time.

7.3 Numerical Results

In order to study the charge relaxation effect, EHD effect on heat and fluid flows around single bubbles of R134a, R123, R113 and R12 are calculated. The simplified bubble model established in chapter 6 is employed again so as to highlight the EHD effect on the heat and flow. The simulation is carried out at voltages of 2000V, 4000V, 5000V, 8000V and 10000V respectively, the contact angle is 15° and superheat is 4K. The mesh size is 200×200.The electrical properties of those fluids are shown in table 7.1 provided by (ASHRAE handbook, 1997). It is noticeable that the charge relaxation times of R134a and R123 have the same magnitude. Table 7.2 gives the heat and flow related dimensionless parameters for the calculations. The electric field related parameters are dependent to the voltage applied; table 7.3 gives the electric field related parameters at 5000V. The local Nusselt Number at voltage of 5000V and the increase of average Nusselt Number of R134a, R123, R113 and R12 are shown in figures 7.1 and 7.2 respectively. The comparisons of flow and thermal fields between with and without electric fields are shown at voltage of 5000V in figure 7.3 and 7.4, respectively.

Table 7.1 Electrical properties of refrigerants

Refrigerants	Relaxation time(s)	Permittivity $\varepsilon\times10^{12}$ (kg m s^{-2} V^{-2})
R134a	3.56×10^{-3}	84.1635
R123	1.76×10^{-3}	39.825
R12	0.104	18.054
R113	2.12	19.2045

Table 7.2 Dimensionless parameters for flow and thermal fields

Refrigerants	Re	Gr	Pr
R134a	2.574	6.625	3.55
R123	4.096	16.780	5.769
R113	3.298	10.874	8.6
R12	8.426	71.003	3.5

Table 7.3 Dimensionless parameters for electric field at $\varphi = 5000V$

Refrigerant	S_E	Pr_E	N_E	E_C
R134a	9.995	1.488×10^{-3}	6.881×10^{-3}	8.388×10^{-7}
R123	5.358	1.122×10^{-3}	4.732×10^{-5}	1.558×10^{-5}
R113	5.158	5.432×10^{-3}	9.284×10^{-3}	5.550×10^{-5}
R12	1.216	1.197×10^{-2}	9.960×10^{-5}	8.005×10^{-7}

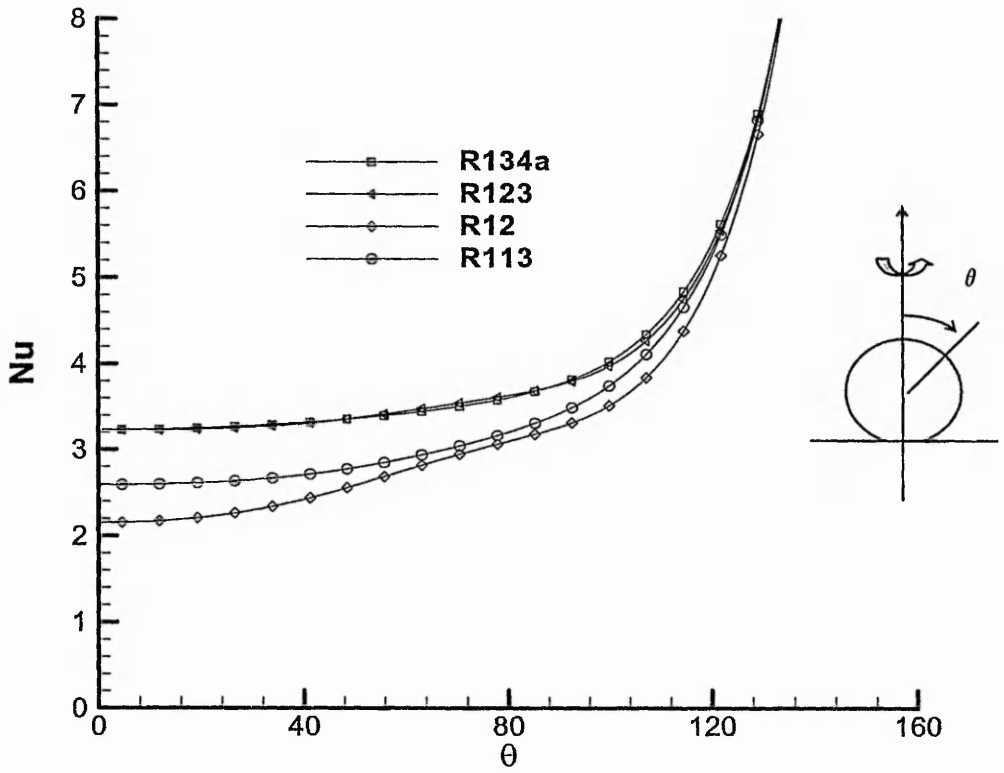

Figure 7.1 Local Nusselt number along the bubble surface at $\varphi = 5000V$

Figure 7.1 shows the Nusselt Number along the bubble surface. The *Nu* values of R134a and R123 are very closed to each other and higher than those of R12 and R113. Figure 7.2 shows clearly that with the increase of an applied electric field, the average value of *Nu* increases. R134a has the highest increase, then R123, R113. R12 has the lowest increase as compared to others. The difference is getting larger with the increase of the voltage applied.

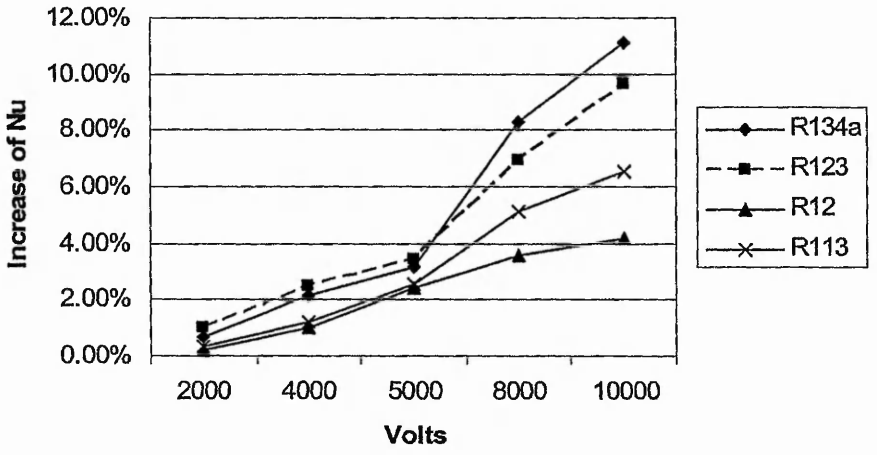

Figure 7.2 Increase of average Nusselt Number at different voltages

Figures 7.3 compares the distributions of thermal contours around the bubble of R134a, R123, R113 and R12 at voltages of 0V and 5000V; figure 7.4 compares the results of streamlines. For R134a, the thermal contours are noticeably different when the two different voltages are applied. R123 has a same situation with the R134a. For R113 and R12, the change of the electric voltage does not result in visual difference in the thermal contours. The same differences for the four fluids are also demonstrated by the streamlines shown in figure 7.4. These different responses to an electric field of the fluids can also be explained that the shorter relaxation time of the fluid is, the easier to enhance the heat transfer by applying an electric field.

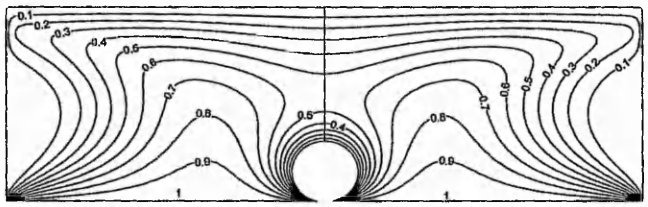

R134a with EHD

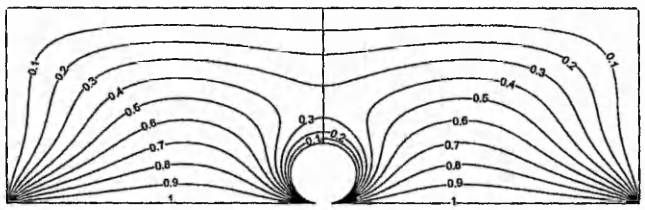

R134a without EHD

(a) The comparison of thermal contours of R134a

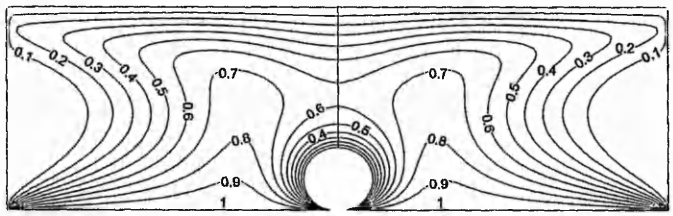

R123 with EHD

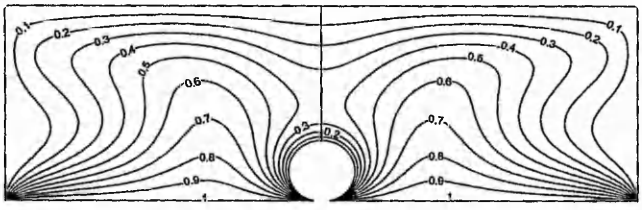

R123 without EHD

(b) The comparison of thermal contours of R123

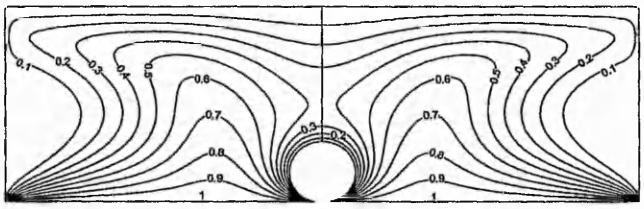

R113 with EHD

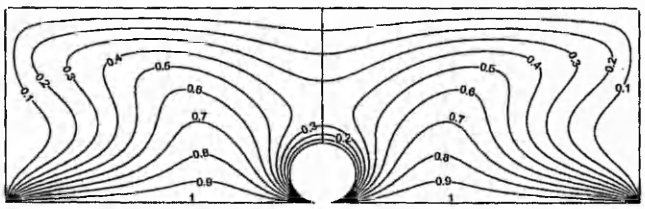

R113 without EHD

(c) The comparison of thermal contours of R113

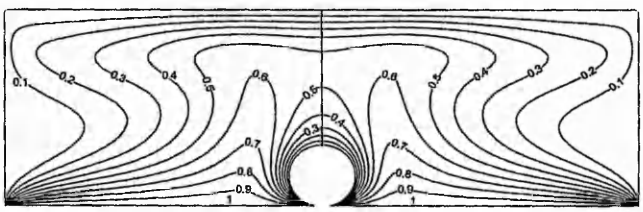

R12 with EHD

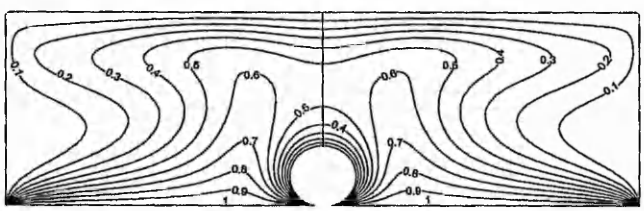

R12 without EHD

(d) The comparison of thermal contours of R12

Figure 7.3 The Comparisons of thermal contours (a) R134a (b) R123 (c) R113 (d) R12

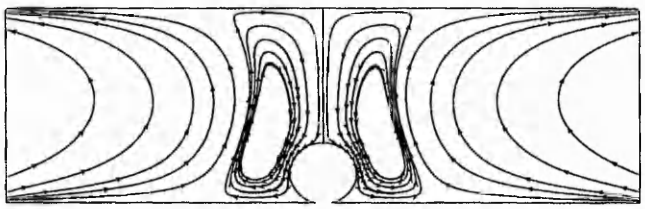

R134a with EHD

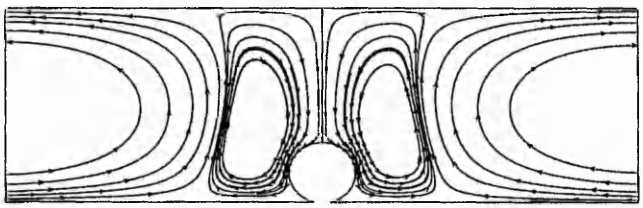

R134a without EHD

(a) The comparison of streamlines of R134a

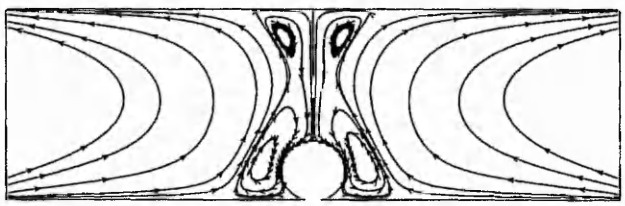

R123 with EHD

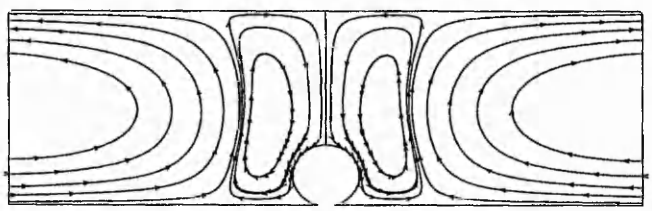

R123 without EHD

(b) The comparison of streamlines of R123

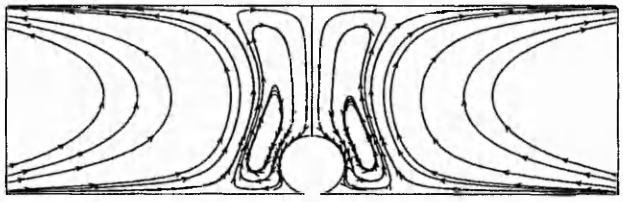

R113 with EHD

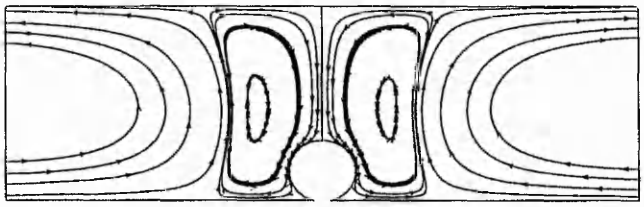

R113 without EHD

(c) The comparison of streamlines of R113

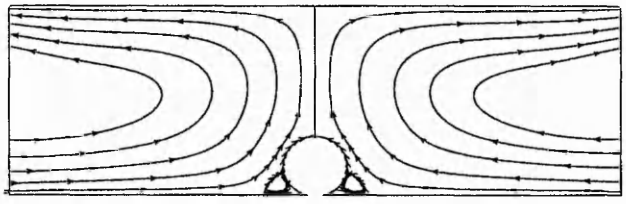

R12 with EHD

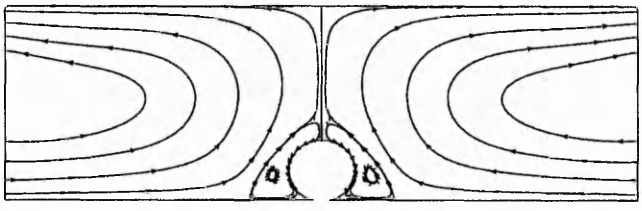

R12 without EHD

(d) The comparison of streamlines of R12

Figure 7.14 the comparisons of streamlines (a) R134a (b) R123 (c) R113 (d) R12

7.4 Summary

The effects of charge relaxation time on heat transfer enhancement by means of an electric field for refrigerants R134a, R123, R113 and R12 are numerically studied. The studies found that the smaller the charge relaxation time the refrigerant has, the easier to enhance the heat transfer by applying an electric field.

Chapter 8
EHD effect on Bubble Growth

8.1 Introduction

In nucleate boiling, the heat transfer rate could be attributed to vapour-liquid exchange during the growth and movement of bubbles (Forster and Grief, 1959 (tong's book)), and to the vaporization of (Moore and Mesler, 1961) or transient conduction to the microlayer and liquid-vapour interface (Han and Griffith, 1965b) before the bubble's departure.

Early models for the growth of a nucleate boiling bubble (Hsu and Graham, 1961; Van Stralen, 1967; Mikic etc, 1970) neglected the microlayer and modelled the bubble cap heat transfer by assuming a thin, typically uniform, thermal boundary layer along the bubble surface. The model of Van Stralen et al (1975) included several fitting parameters such as the microlayer thickness and the size of the area influenced by a growing bubble; their results were only applicable to the conditions where the parameters were specified.

Later than those, calculations of growing bubbles have been carried out by Lee and Nydahl (1989), Mei et al (1995), Hammer and Stephan (1996) and Fujita and Bai

(1998). In these studies, the model of the bubble was improved by reducing the assumptions. However, because of the extreme complexity, the assumptions such as the truncated sphere in shape and the constant contact angle were still commonly used. For example, in Fujita and Bai's (2000) calculations, they made no assumption about the bubble shape. The bubble shape was decided completely according to the balance of forces and calculated by solving the full Navier-Stokes equations; however, the assumption of constant contact angle are still employed in their calculation to reduce the complexity.

In this chapter, the EHD effect on different stages of a growing bubble attached to a horizontal wall are studied. Due to the complexity of the problem concerned in this work, only the steady heat and fluid flows around a truncated spherical bubble are considered. The assumption of constant contact angle is checked. Based on these, the coupled electric, flow and thermal fields around a growing R113 bubble at its 50%, 60%, 75% and 100% of departure radii are calculated.

8.2 Assumption of Constant Angle

The EHD effect on the heat and flow fields around a bubble at different angles is carried out. The refrigerant is R12, and the voltage applied is $\varphi = 5000V$; the relevant fluid

properties and dimensionless parameters have been presented in tables 7.1~ 7.3 in the last chapter. The results are shown in figures 8.1~ 8.3 and table 8.1.

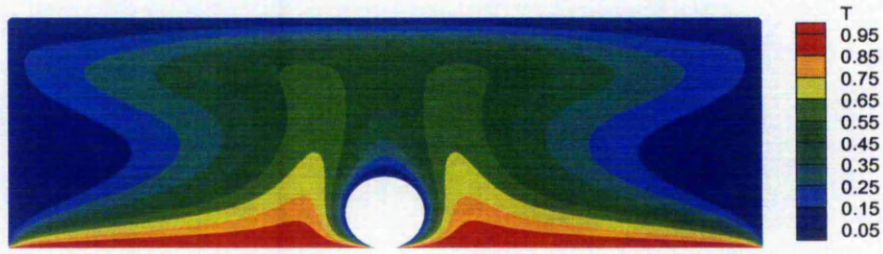

(a) $\theta_c = 15^\circ$

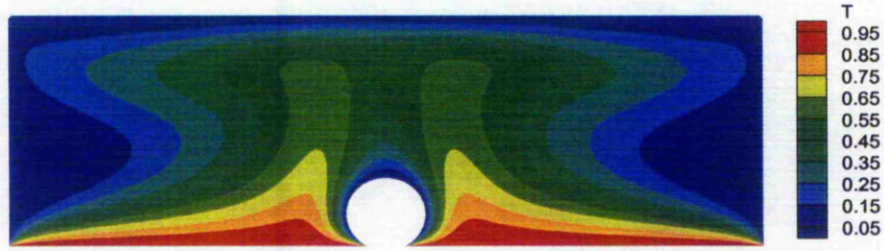

(b) $\theta_c = 30^\circ$

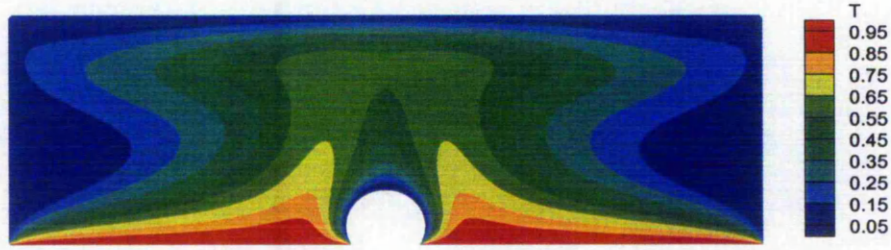

(c) $\theta_c = 60^\circ$

Figure 8.1 Thermal contours at different contact angles

The comparison of the thermal isothermals in figure 8.1 for three different contact angles and the comparison of the streamlines in figure 8.2 show that for a certain fluid, and at a certain voltage value, the variation of the contact angle has little effect on the thermal and flow fields, such as the ring vortex size. These effects can also be identified from the averaged Nusselt number shown in table 8.1 and figure 8.3. In table 8.1, the Nu_{av} values for the three angles are obviously different no matter whether an electric field is applied. However, the percentages of the increases of Nu_{av} for three contact angles are on the same level and very close. This fact proves that it is proper to use the constant contact angle assumption to analyse the effects of EHD on heat transfer in quality.

Table 8.1 Nu_{av} increase at different contact angles

Contact angle	Nu_{av} (without EHD)	Nu_{av} (with EHD)	Increase
15°	12.1881	12.4805	2.40%
30°	8.2920	8.5161	2.70%
60°	6.3331	6.4951	2.56%

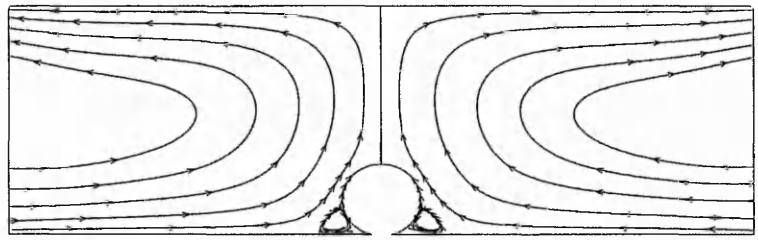

(a) $\theta_c = 15^\circ$

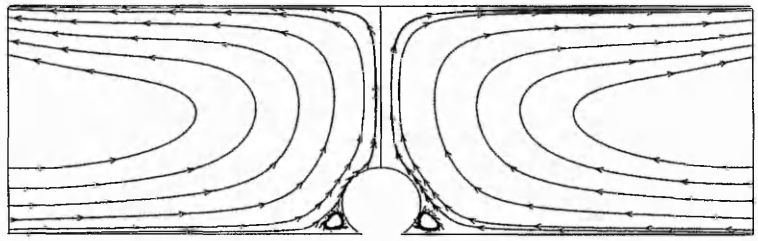

(b) $\theta_c = 30^\circ$

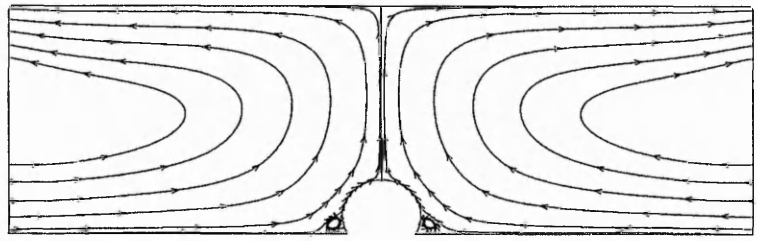

(c) $\theta_c = 60^\circ$

Figure 8.2 Streamlines at different contact angles

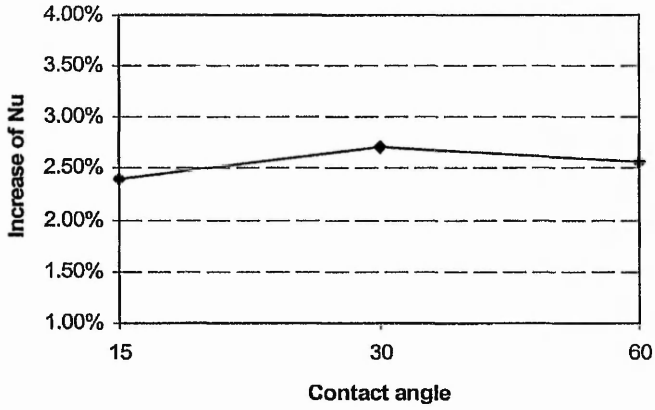

Figure 8.3 Nu_{av} increase at different contact angles

8.3 EHD effect on a Growing Bubble

The calculations for R113 at the contact angle of 15°, superheat of 4K and the bubble radii at $0.5R_d$, $0.6R_d$, $0.75R_d$ and $1\times R_d$ are carried out. The electric voltage is $\varphi = 5000V$. The dimensionless parameters for calculation have already been presented in the last chapter in tables 7.2 ~ 7.3. The numerical results are shown in figures 8.4~ 8.9.

Figures 8.4 and 8.5 show the temperature and flow fields around the bubble at different stages of the bubble growth. With the increase of the bubble radius, the vortex around the bubble also increases in size. It is interesting that a secondary ring vortex appear at

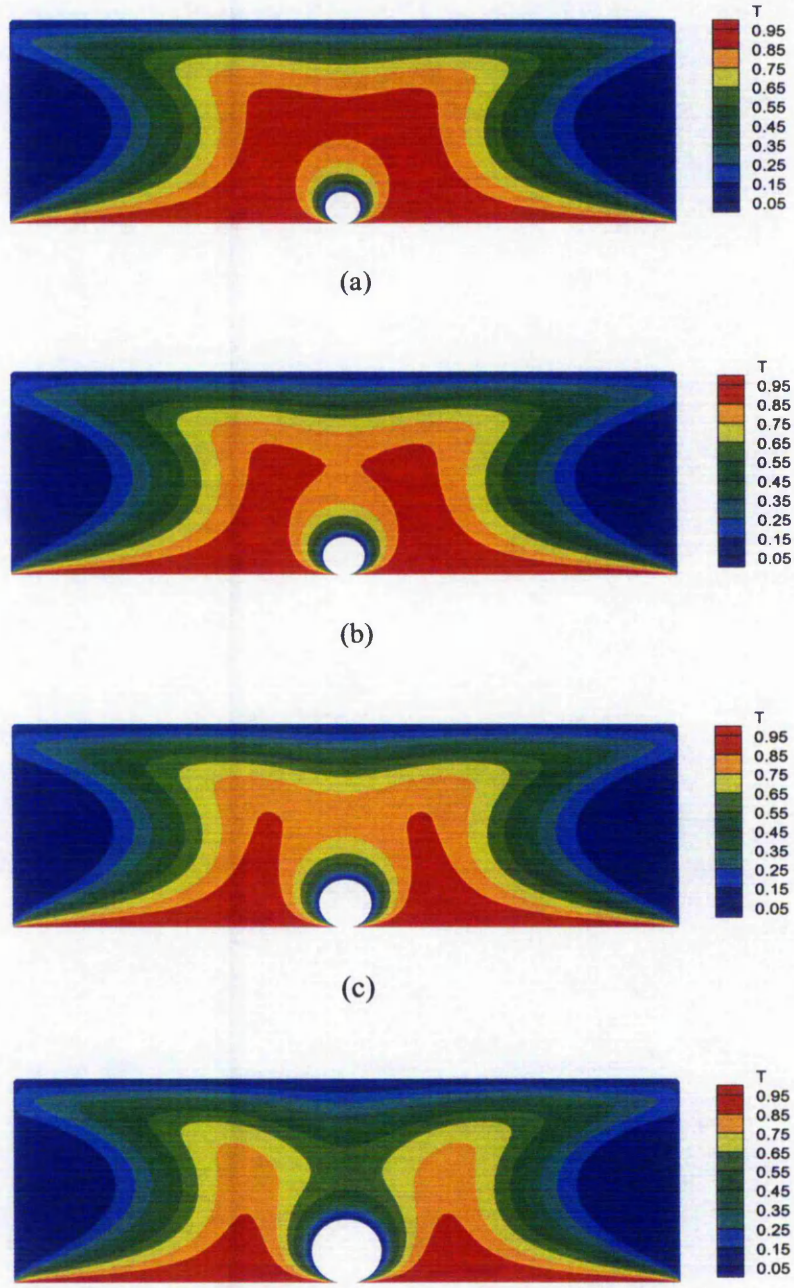

Figure 8.4 Temperature distributions at different bubble growing stages

(a) $R = 0.5R_d$, (b) $R = 0.6R_d$, (c) $R = 0.75R_d$, (d) $R = R_d$

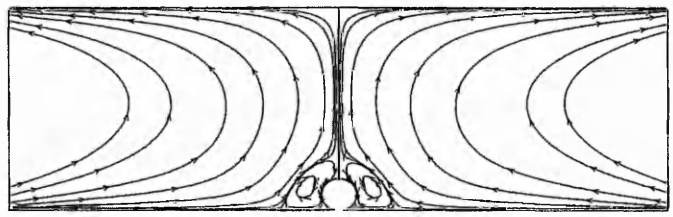

(a)

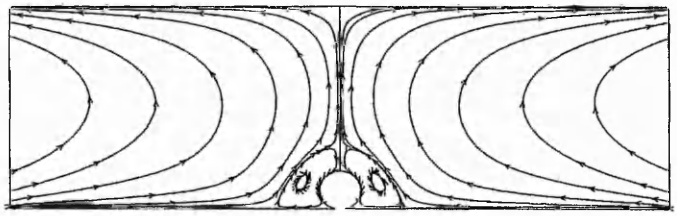

(b)

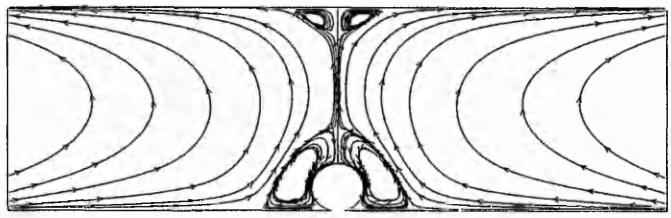

(c)

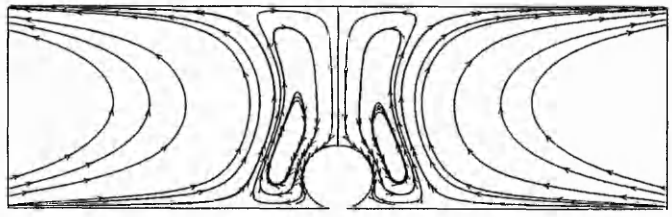

(d)

Figure 8.5 Streamlines at different bubble growing stages

(a) $R = 0.5R_d$, (b) $R = 0.6R_d$, (c) $R = 0.75R_d$, (d) $R = R_d$

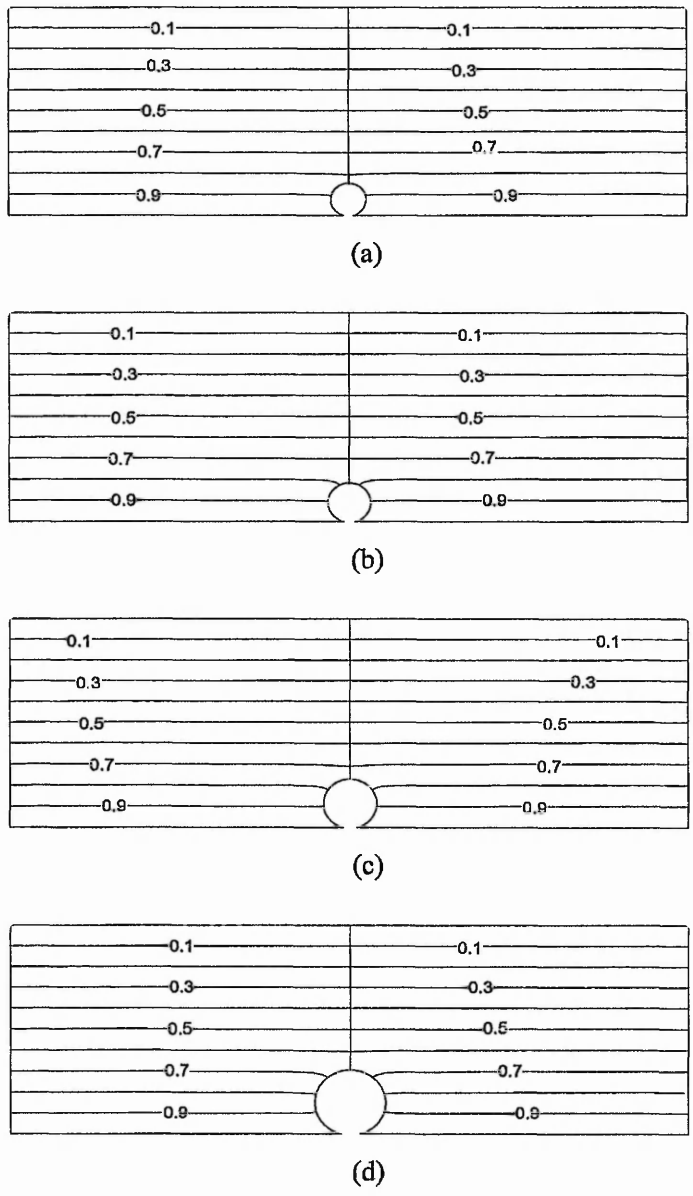

Figure 8.6 Contours of the dimensionless electric potential

(a) $R = 0.5R_d$, (b) $R = 0.6R_d$, (c) $R = 0.75R_d$, (d) $R = R_d$

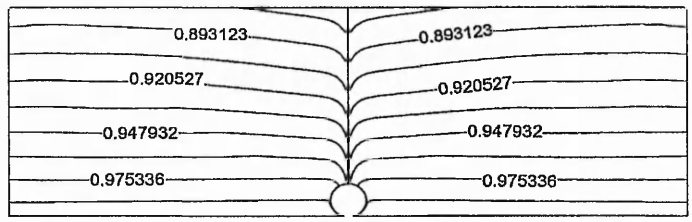

(a)

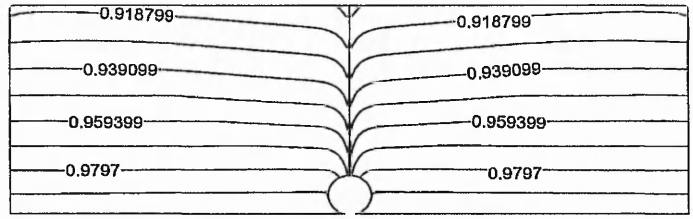

(b)

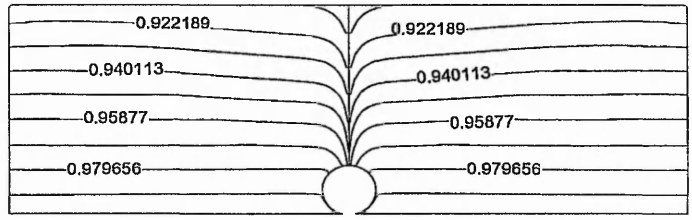

(c)

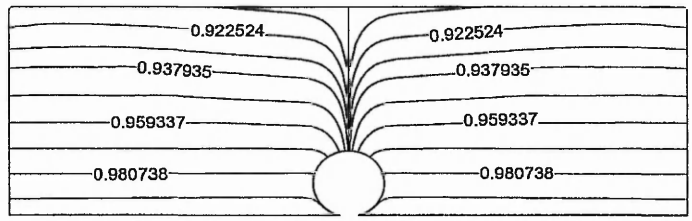

(d)

Figure 8.7 Charge distributions

(a) $R = 0.5R_d$, (b) $R = 0.6R_d$, (c) $R = 0.75R_d$, (d) $R = R_d$

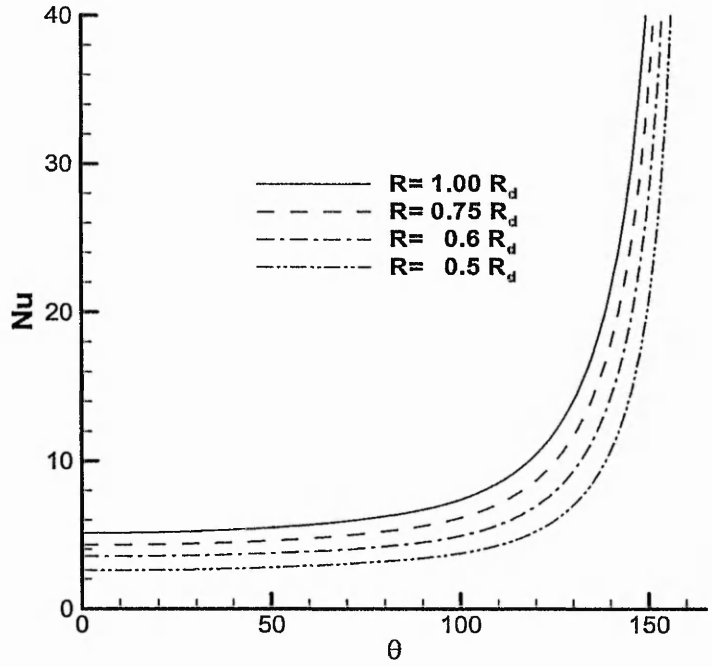

Figure 8.8 Local Nusselt Number at the bubble surface

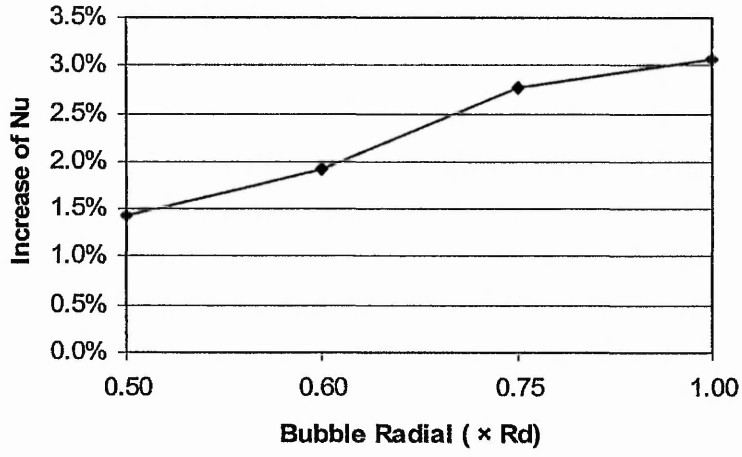

Figure 8.9 Increase of Nu_{av} at different bubble growth stages at $\varphi = 5000V$

about $R = 0.75R_d$ above the bubble near the negative electrode. As shown in figure 8.5, at $R = R_d$, this vortex has merged with the main ring vortex and formed a large circulation in the whole space in the vertical direction above the bubble. Corresponding to the topological change of the streamlines, the isothermals surrounding the bubble also change; the isothermal layers around the bubble become thinner with the increase of bubble radius. Because of this, the local Nusselt number along the bubble profile also increases with the bubble radius, as shown in figure 8.8. The increases of the averaged Nusselt number are shown in figure 8.9; the later stages have obtained more heat transfer enhancements than the earlier stages.

The results of electric fields are shown in figures 8.6 and 8.6, for the dimensionless potential and density of free change respectively. The distribution of dimensionless electric potential does not change significantly with the increase of bubble radius; however, the charge density shows property of transport variables, the value of q at the negative electrode becomes large with the increase of bubble radius, which produces stronger vortex motion observed in figure 8.5. Because the circulation of vortex transport fluids with lower q value to the top of the bubble, a trough of q is formed and can be observed on the top of the bubble, as shown in figure 8.6.

8.4 Summary

In this chapter, the EHD effect on the flow, temperature and electric fields at different bubble growth stages are numerically studied. In order to highlight the EHD effect on the different stages of the bubble growth, the heat and fluid flows are presumed to be steady while the bubble is supposed to be a truncated sphere and has constant contact angle. The constant-contact-angle assumption is checked by comparing between calculations with $\theta_c = 15^\circ$, 30° and 60°. Based on the comparison, the coupled electric, flow and thermal fields around a growing bubble at $R = 0.5R_d$, $0.6R_d$, $0.75R_d$ and $1.0R_d$ are numerically studied. The main conclusions are as follows:

(a). The constant-contact-angle assumption has influence on the results of the calculated heat transfer rate, but the heat transfer enhancements by EHD at different contact angle are on the same level and very close; so the assumption is valid for analysing the effects of EHD in quality;

(b). During the growth of the bubble, a second ring vortex, counter rotating with main vortex, forms near the negative electrode above the bubble. This vortex merges with the main one and forms a strong rotational motion which induces the change of isothermal and results in stronger heat transfer in the lateral stages of the bubble growth;

(c). The dimensionless potential field does not significantly change with the bubble radius;

(d). The density of free charges is a transport variable; because of the transport of vortex motion, a trough forms above the bubble with the increase of bubble radius.

Chapter 9

Conclusions and Recommendations for Further Work

The aim of this research is to understand the Electrohydrodynamic effects on single and two-phase heat transfer. To achieve this aim, a series of investigations have been carried out. They are: (1) the establishment of mathematical model for fully coupled electric, flow and thermal fields; (2) numerically study the EHD effect on heat transfer enhancement in natural convection in rectangular and cylindrical enclosures; (3) study the effects of fluid properties on natural convection enhanced by EHD; (4) EHD effect on the heat and flow fields around a single bubble during nucleate boiling; (5) study of the coupled electric, flow and thermal fields at different growing stages of the bubble.

To carry out such investigations, it is important to observe and understand the natural phenomenon by reviewing the works have been done by others on EHD effect on single and two-phase flows. On the basis of the analysis of these works, a mathematical model to describe the phenomenon of fully coupled electric, flow and thermal fields is established in chapter 3. The numerical methods and strategies for this mathematical model are introduced in chapter 4. These numerical methods are developed into FORTRAN codes, which are further widely validated by a series of benchmark testing cases such as the flow in the Roach Channel, natural convection in square cavities, natural convection in squeezed cavities and laminar flows through a circular pipe with

constriction. Based on these validations, the codes are employed to study the EHD effect on single phase heat transfer chapter 5, where the EHD effect on natural convection in rectangular and cylindrical enclosures are numerically investigated, and the EHD effect on fluids with different electrical properties are numerically simulated. Further to the simulations of single phase flows, an analytical model for the coupled electric, flow and thermal fields around a single bubble attached to a horizontal wall is established in chapter 6 and the results of numerical simulations are presented in chapters 6, 7 and 8, for refrigerants with different charge relaxation time and growing bubbles at different stages respectively. The conclusions of the research are summarised following the basic steps of the work.

9.1 Establishment of Physical and Mathematical models

9.1.1 Physical Aspects of the Coupled Electric, Flow and Thermal fields

The effects of applying an electric field on a flow include the electric body force and the Joule heat. In order to establish the mathematical model, a current in a dielectric field is physically modelled as a directed motion of electrically charged particles injected into a neutral fluid in this thesis. Based on this modelling, the electric field can be coupled with the flow and thermal fields in the form of the electric body force and Joule heat, while the flow and thermal fields play their effects on the electric field through the transport of the charged particles.

9.1.2 Mathematical Descriptions of the Coupled Electric, Flow and Thermal fields

The physical phenomenon of the coupled electric, flow and thermal fields are mathematically descried by combining the Maxwell's relation and the Gauss' law with the Navier-Stokes equations. Controlling equations of the free electric charges, electric potential are developed and coupled with those equations for heat and flows, by adding the electric body force into the momentum equation and adding the Joule heat to the energy equation. With these modelling, a mathematical model for fully coupled electric, flow and thermal fields are established.

The governing equations are non-dimensionlised and written in a generalized form and further transformed from the Cartesian coordinates system (x, y) to a general non-orthogonal body fitted coordinates (BFC) system (ξ,η). The advantage of the BFC form is that complex geometries can be fitted by body-conforming grids, whereby boundary conditions can be applied easily and the grid can be distributed preferentially in desired regions so as to obtain better resolution.

9.1.3 Analytical Models for Heat and Flows in the Vicinity of the Gas-Liquid Interface around a Single Bubble

In order to analyse the EHD effect on the heat transfer and fluid flow around the gas-liquid interface of a single bubble attached to a heated wall of nucleate boiling, a

simplified bubble model is proposed for consideration in order to highlight the interfacial heat transfer phenomenon and its enhancement in the vicinity of a gas-liquid interface, assumptions such as spherical shape bubble, constant contact angle, and negligible micro-layer are employed. Interfacial treatments are proposed and applied to calculate the velocity boundary value at the gas-liquid interface.

9.2 Numerical Methods and CFD codes

9.2.1 Finite Volume Method (FVM) with QUICK schemes

In this work, a calculating procedure for solving the coupled Navier-Stokes, energy and electric field equations based on a non-orthogonal BFC is proposed. The procedure generates the computational grids using a two-step strategy, namely, generating the initial grids by algebraic method and then smooths the mesh by solving the differential equations. Finite volume method is employed to discretise the governing equations. In order to obtain high numerical accuracy, the QUICK scheme is employed for discretisation. The coupling of pressure-velocity is carried out by a pressure correction procedure on non-staggered grids, where the defects of Rhie and Chow's momentum equation are analysed and eliminated. The algebraic equations are solved by the SIMPLE method.

9.2.2 Development of FORTRAN Codes

A FORTRAN code based on the numerical methods and strategies has been developed. The code generates the non-orthogonal BFC grids and solves the coupled controlling equations. Validations show that the code is an effective, reliable and robust tool for numerically simulating heat and fluid flows.

9.3 Numerical Results

Using these methods and the codes developed in this study, investigations on EHD effect on single and two phase flows have been carried out. The contributions of this thesis are:

(1) A detailed analysis of EHD effect on natural convections in rectangular and cylindrical enclosures;

(2) Studies of heat transfer enhancement using a non-uniform electric field and using different working fluids;

(3) Understanding of the EHD enhancement of heat and fluid flows around single bubbles of R134a and other fluids with different charge relaxation time during nucleate boiling;

(4) Investigation of EHD effect on different stages of bubble growth.

9.3.1 EHD effect on Natural Convection

The EHD effect on natural convection in rectangular and cylindrical enclosures is numerically studied. The results include: a) comparison of natural convection in a rectangular enclosure between with and without an uniform electric field and at different Raleigh number; b) natural convection in a rectangular under uniform and non-uniform electric fields; c) natural convections in a cylindrical enclosure with and without applying an uniform electric field and at different Raleigh number; d) natural convection of three fluids in a rectangular enclosure with and without EHD effect and with non-uniform EHD effect. The main conclusions are:

(1). in a rectangular enclosure, the EHD enhancement is related to the Rayleigh number; an uniform electric field is more effective to enhance the heat transfer at lower Raleigh number case; as the Raleigh number increases, less enhancements are obtained;

(2). a non-uniform electric field is more effective than a uniform one to enhance the natural convection in a rectangular enclosure;

(3). in a cylindrical enclosure, a uniform electric field is more effective to enhance the heat transfer at higher Rayleigh number; as the Raleigh number increases, more enhancements of heat transfer can be obtained;

(4). in a rectangular enclosure, the fluids with lower viscosity and lower electrical conductivity give greater heat transfer enhancements for a given electrical power input; between the viscosity and electrical conductivity, the viscosity is the dominant factor for obtaining better EHD enhancement. This conclusion agrees well with the available experimental observations.

9.3.2 EHD Enhancement of Heat Transfer around a Single R134a Bubble

EHD effect on an isolated R134a bubble attached to a horizontal surface in nucleate boiling are numerically studied. A simple physical model is employed to highlight the EHD effect on heat and fluid flows in the vicinity of the gas-liquid interface of a bubble. Coupled electric, flow and thermal fields are calculated and analysed when the electric voltage varies among 0V, 2000V, 4000V, 5000V, 8000V and 10000V. The analysis reveals that applying an electric field to nucleate boiling can enhance the motion of the vortex around the bubble by the electric body force; and reduce the thickness of shear flow layer. As a result, the heat transfer at the gas-liquid interface is enhanced.

9.3.3 EHD effect on Refrigerants with Different Charge Relaxation Time

In nucleate boiling, the charge relaxation time of refrigerants plays an important role during bubble growth and departure in an electric field. In order to study the charge relaxation time effects, EHD effect on heat and flow around single bubbles of R134a, R12, R123 and R113 have been calculated. The simulations are carried out at voltage of 5000V, contact angle of 15° and superheat of 4K. The studies found that the smaller the charge relaxation time the refrigerant has, the easier to enhance the heat transfer by applying an electric field

9.3.4 EHD effect on Different Stages of Bubble Growth

The EHD effect on the flow, temperature and electric fields at different bubble growth stages are numerically studied, with the assumptions of steady flow, truncated spherical bubble shape and constant-contact-angle. The constant contact angle is checked by comparing between the calculations at $\theta_c = 15^\circ$, 30° and 60°. The coupled electric, flow and thermal fields around a growing bubble at $R = 0.5R_d$, $0.6R_d$, $0.75R_d$ and $1.0R_d$ are numerically studied. The main conclusions are as follows:

(1). the constant-contact-angle assumption has influence on the results of the calculated heat transfer rate, but the heat transfer enhancements by EHD at different contact angle are on the same level and very close; so the assumption is valid for analysing the effects of EHD in quality;

(2). during the growth of the bubble, a second ring vortex, counter rotating with main vortex, forms near the negative electrode above the bubble. This vortex merges with the main one and forms a strong rotational motion which induces the change of isothermal and results in stronger heat transfer in the lateral stages of the bubble growth;

(3). the dimensionless potential field does not significantly change with the bubble radial;

(4). the density of free charges is a transport variable; because of the transport of vortex motion, a trough forms above the bubble with the increase of bubble radial.

9.4 Recommendation for the further work

Numerical simulation of heat transfer enhancement in single and two phase flows by

applying an electric field is a relatively new area of research and much work still needs to be bone to contribute a better understanding of the basic mechanism behind the physical phenomenon.

Firstly, for single phase flows such as natural convection in enclosures, our calculation reveals the application of an electric field has different heat transfer enhancing effects on the flows inside rectangular and cylindrical enclosures. When a uniform electric field is applied, better EHD enhancement effects are observed at lower Raleigh numbers for a rectangular enclosure, while it is at higher Raleigh number for a cylindrical enclosure. For this difference, we explained by the stabilisation effects on the flows of the spanwise infinite size in the rectangular enclosure. However, in order to check the validity of our explanation or find the real reason for this difference, fully three-dimensional simulation on heat and fluid flows are necessary. This could be a further work based on the current research.

Secondly, the current study on bubbles has several assumptions such as negligible micro-layer, steady flows, truncated spherical bubble shape and constant contact angle. Some of these assumptions are maybe not reasonable while we just use them to highlight the effects of EHD on the heat and flows around the bubble and to reduce the extreme complexity of the physical problem. For example, the bubble shape and contact angle change in the real world during bubble growth and the heat transfer through the micro-layer could be up to 80% of the total amount of heat for bubble growth. In order to study the mechanism of EHD enhancement on nucleate boiling, the interface and

bubble deformation, the micro-layer, and the unsteadiness of the flows should be considered in the further work.

Thirdly, the fluid properties are assumed to be constant in the current study. However, experimental studies have already proved that permittivity ε is variable at the vapour/liquid interface, the second and third term of the electric body force could be very strong when the surrounding liquid is not homogeneous, therefore the variety of permittivity should be taken into account in the future study.

Regarding to the present physical model, it is also assumed that all the properties inside the bubble are much smaller than those of the surrounding liquid. This assumption would not have a significant influence on external flow fields, but it could affect the temperature fields. Therefore, further simulation should pay attention to the double domain iteration method in order to understand the temperature fields in the vicinity of a vapour bubble and the effects of these fields on bubble deformation and growth or collapse.

References

ADAMCZEWSKI, I. 1969. Ionization, conductivity, and breakdown in dielectric liquid. London: Taylor and Francis.

ALLEN, P.H.G. and COOPER, P. 1987. The potential of electrically enhanced evaporators, *Proc. 3rd Int. Symp. On the Large Scale Applications of Heat Pumps*, Oxford, P2, pp. 221-229.

ALLEN, P.H.G. and **KARAYIANNIS, T.G.** 1995.Electrohydrodynamic enhancement of heat transfer and fluid flow, *Heat Recovery Systems& CHP*, Vol.15, No.5, pp. 389-423.

ASHGRIZ, N. and **POO, J.Y.** 1991 FLAIR: Flux Line-Segment Model for Advection and Interface Reconstruction, *Journal of Computational Physics*, Vol.93, pp.449.

BABSKI, V. G., ZHUKOV, M. V. and **YUDOVICH, V. I.,** 1989 Mathematical theory of electrophoresis, (translated by C. Flick), *Consultants Bureau*, New York.

BAI, Q and **FUJITA, Y.** 2000. Numerical simulation of bubble growth in nucleate boiling-effects of system parameters. *Multiphase Science and Technology*. Vol.12, Nos. 3 and 4, pp.195-214.

BARKHUDAROV, M.R. and **CHIN, S.B.** 1994 Stability of a Numerical Algorithm for Gas Bubble Modelling, *International Journal for Numerical Methods in Fluids*, Vol.19, pp.415-437.

BERGLES, A.E., 1978. Enhancement of heat transfer, *proceedings of the 6th International Heat Transfer Conference*, Hemisphere Publishing Corp., Washington, DC, Vol. 6, pp.89-108.

BOCHIROL, L., **BONJOUR, E.** and **WEIL, L.** 1960. Etude de I'actio de champs electriques sur les transfers de chaleur dans les liquids bouillants. *C.R.Hebd. Seances Acad. Sci,* Paris, pp76-78.

BROWN, C.E. and **MARTIN, S.A.** 1971. The effect of finite metal

conductivity on the condensation heat transfer for falling water results on vertical heat-transfer surface. *Journal of Heat Transfer*, Vol.93, pp 2627-2639.

BUGG, J.D., MACK, K. and **REZKALLAH, K.S.** 1998 A Numerical Model of Taylor Bubbles Rising Through Stagnant Liquid in Vertical Tubes, *International Journal of Multiphase Flow*, Vol.24, No.2, pp.271-281.

CHENG, K.J. and **CHADDOCK, J.B.**, 1985. Effects of an electric field on bubble growth rate, *International Communication. Heat Mass Transfer*, Vol.**12**, pp.259-268.

CHO, H.J., KANG, I.S., KWEON, Y.C. and **KIM, M.H.,** 1996. Study of the behaviour of a bubble attached to a wall in a uniform electric field. *International Journal of Multiphase flow*, Vol. **22**, No.5, pp.909-922.

COOPER, M.G. and **LLOYD, A.J.P.** 1969. The microlayer in nucleate pool boiling. International Journal of Heat Mass Transfer, Vol. 12, pp 895-913.

COOPER, P., 1990. EHD enhancement of nucleate boiling, *Journal of Heat Transfer, Trans. ASME*, Vol. **112**, pp. 458-464.

CROWLEY, J.M., WRIGHT G.S. and **CHATO, J. C.** 1990. Selecting a working fluid to increase the efficiency and flow rate of an EHD pump. *IEEE transaction on industry applications*. Vol. 26. No1., pp 42-49.

COURANT, R. 1956 Differential and integral calculus. *Blackie & Son, Ltd., London,* 133.

DARABI, J., OHADI, M. M. and **DESIATOUN, S. V.**, 1998. Heat transfer enhancement with falling film evaporation on vertical tubes using electric fields, *American Society of Mechanical Engineers, Heat Transfer Division, (Publication) HTD*, v 361-1, *Heat Transfer Division -1*, pp. 331-338.

DARABI, J., OHADI, M. M. and **DESIATOUN, S. V.**, 2000. Falling film and spray evaporation enhancement using an applied electric field, *Journal of Heat Transfer*, ASME, Vol. 122, n 4, pp. 741-748.

DARWISH, M.S. and MOUKALLED, F.H. 1994. Normalised variable and space formulation methodology for high-resolution schemes. *Numerical Heat Transfer, Part B: Fundamentals*, v 26, n 1, pp. 79-96.

DEMIRDZIC, I., LILEK, Z. and **PERIC, M.** 1992 Fluid Flow and Heat Transfer Test Problems for Non-Orthogonal Grids: Benchmark Solutions, *International Journal for Numerical Methods in Fluids*, Vol. 15, pp. 329-354.

DE.VAHL. DAVIS, G. and **JONES, I.P.**, 1981. Natural convection of air in a square cavity, A comparison exercise, in *numerical method in thermal problems*, (edited by R.M.Lewis, K Morgan and B.A. Schrfler), Pineridge Press,Swansea, pp.552-572.

DI MARCO, P. and **GRASSI, W.**, 1993. Saturated pool boiling enhancement by means of an electric field. *Journal of Enhanced Heat Transfer*, Vol. 1, n 1, 1993, pp. 99-114.

DULIKRAVICH, G. S. and **AHUJA, V.**, 1993. Computations of electro-thermo-convective phenomena in electro-rheological fluids, *American Society of Mechanical Engineers, Fluids Engineering Division (Publication) FED*, Vol. 164, pp. 29-42.

DULIKRAVICH, G.S. and **LYNN S.R.**, 1995. Electro-magneto-hydrodynamics: (Part 2) A survey of mathematical models. *American Society of Mechanical Engineers, Fluids Engineering Division (Publication) FED*, v 235, *Developments in Electrorheological Flows*, pp 59-69.

FENG, J.Q. and **BEARD, K.V.** 1991. Three dimensional oscillation characteristics of electrostatically deformed drops. *Journal of Fluid Mechanics*, Vol. 227, pp 429-447.

FERZIGER, J. H. and **PERIC, M.** 1996. Computational methods for fluid dynamics, Springer, New York.

FOSTER, H.K. and **GREIF, R.**, 1959, Heat transfer to boiling liquid, mechanism and correlations, ASME Journal of heat transfer, Vol. 81, pp43-53.

FRITZ, W. 1935. Maximum Volume of Vapour bubbles. *Physic*, Vol. 36, pp.379-384.

FUJINO, T., YOKOYAMA, Y. and **MORI, Y. H.**, 1989. Augmentation of laminar forced- convective heat transfer by the application of a transverse electric field, *Journal of Heat Transfer, Transactions ASME*, Vol. 111, n 2, pp. 345-351.

FUJITA, Y. and **BAI, Q.** 1998 Numerical Simulation of the Growth for an

Isolated Bubble in Nucleate Boiling, *Proceedings of the 11th IHTC*, Vol.2, August 23-28, 1998, Kyongju, Korea.

GARRIOCH, S.H. and **BALIGA, B.R.** 1998 Interface Tracking Using a Multi-Dimensional Advection Techiques Based on Skewed Subadvections, ASME paper FEDSM98-5207.

GROSS, M. J. and **PORTER, J. E.,** 1966. Electrically Induced Convection in Dielectric Liquids. *Nature*, No. 5066, pp. 1343-1345.

HAMADY, F. J., LLOYD, J. R., YANG, H. Q. and **YANG, K. T,** 1989. Study of local natural convection heat transfer in an inclined enclosure, *International Journal of Heat and Mass Transfer*, Vol. **32**, n 9, p 1697-1708.

HAMED, A. and **ABDANAH, S.** 1983. Internal three-dimensional viscous flow solution using the streamline function. *ASME, Journal of fluids engineering*, Vol. 108. pp.348-353.

HAMMER, J. 1996. Einfluss der Mikrozone auf den Wärmetübergang beim Blasensieden, Ph.D. thesis, University of Stuttgart, Stuttgart, Germany.

HAN, C.Y. and **GRIFFITH, P**., 1965.The mechanism of heat transfer in Nucleate pool boiling, Part II. the heat flux-temperature relation, *Int. J. Heat Mass Transfer*, Vol. 8 (6), pp. 905.

HARLOW, F.H. and **WELCH, J.E.** 1965 Numerical Calculation of Time-Dependent Viscous Incompressible Flow of Fluid with Free Surface, *Physics of Fluids*, Vol.8, PP.2182-2189.

HARVIE, D.J.E. and **FLETCHER, D.F.** 2000 A New Volume of Fluid Advection Algorithm: The Stream Scheme, *Journal of Computatioanl Physics*, Vol.162, pp.1-32.

HE, W. and **CHANG, J.S.** 1995. EHD enhanced mass transfer operations and chemical reactions. *In Handbook of electrostatic Processes*, Chapter 24, pp 527-553, Marcel Dekker, New York.

HIRT, C.W., AMSDEN, A.A., and **COOK, J.L.** 1974 An Arbitrary Lagrangian-Eulerian Computing Method for all Flow Speeds. J. Comp. Phys., 14, 227.

HIRT, C.W. and **NICHOLS, B. D.** 1981 Volume of Fluid (VOF) Method for

the Dynamics of Free Boundaries, *Journal of Computational Physics*, Vol.39, PP.201-225.

HSU, Y.Y. and **GRAHAM, R.W.**, 1961. An analytical and experimental study of the thermal boundary layer and ebullition cycle in nucleate boiling, *NASA TND-594, Lewis Res. Ctr.,* Cleveland, OH.

HUANG, M. and **LAI, F.C.**, 2003. Numerical study of EHD-enhanced forced convection using two-way coupling, *Journal of Heat Transfer*, Vol. 125, n 4, August, 2003, pp. 760-764.

IACONA, E., HERMAN, C. and **CHANG, S.** 2002. Electric field effects on injected air bubble at detachment in a low gravity environment. *12th international heat transfer conference*, Grenoble, France, August 18-23.

JAKOB, M and **FRITZ, W.** 1931 Versuche ūber den verdampfungsvorgang, Forsch. Ingenieurwes, Vol. 2, pp 435-447.

JONES, T.B., 1978. Electrohydrodynamically enhanced heat transfer in liquids – a review. In: Advances in Heat Transfer, Vol. 14, pp. 107-148, Academic Press.

KARAYIANNIS, T.G. and **ALLEN, P.H.G.**, 1991, electro-hydrodynamic enhancement of two-phase heat transfer, c413/036, ImechE, pp165-182.

KARAYIANNIS, T.G. 1993. Electrohydrodynamics boiling heat transfer enhancement in heat exchangers, *proceedings of ASME Winter Annual Meeting*, New Orleans, La. pp 1-8.

KARAYIANNIS, T.G. and **XU, Y.**, 1998a. Electric field effect in boiling heat transfer. Part A: Simulation of the electric field and electric forces. *Journal of Enhanced Heat Transfer*, Vol. 5, pp. 217-229.

KARAYIANNIS, T.G. and **XU, Y.**, 1998b. Electric field effect in boiling heat transfer. Part B: Electrode geometry. *Journal of Enhanced Heat Transfer*, Vol. 5, pp. 231-247.

KARKI, K. C. and **PATANKAR, S. V.**, 1988. Solution of Some Two-Dimensional Incompressible Flow Problems Using a Curvilinear Coordinate System Based Calculation Procedure, *Numerical Heat Transfer, part B*, Vol.**14**, pp. 309-321.

KAWAHIRA, H., KUBO, Y., YOKOYAMA, T. and **OGATA, J.**, 1990. Effect of an electric field on boiling heat transfer of refrigerant-11 - Boiling on a single tube, *IEEE Transactions on Industry Applications*, Vol. 26, n 2, Mar-Apr, pp. 359-365.

KENNING, D.B.R., 1999. What do we really know about nucleate boiling? 6UK National Heat Transfer Conference, Edinburgh, IMechE Conference Transacrions, pp. 143-167.

KHOSLA, P.K. and **RUBIN, S.G.** 1974. A diagonally dominant second-order accurate implicit scheme. *Computers Fluids*, Vol. 2, pp207-209.

KRAUS, J. D., 1992, Electromagnetics, McGraw-Hill Inc.

KRISHNA, R. and **BATEN, J. M.** 1999 Rise Characteristics of Gas Bubbles in a 2D Rectangular Column: VOF Simulations vs Experiments, *Int. Comm. Heat Mass Transfer*, Vol.26, No.7, PP.965-974.

KRONING, R. and **AHSMAN, G.** 1949. The influence of an electric field on convective heat transfer in liquids, *Application of .Science Research Section*, A2, pp.31-32.

KUEHN, T. H. and **GOLDSTEIN, R. J.** 1976 An experimental and theoretical study of natural convection in the annulus between horizontal concentric cylinders, *Journal of Fluid Mechanics*, Vol.74, Part 4, PP.695-719.

KUYPER, R. A., VAN DER MEER TH, H. and **HOOGENDOORN, C. J.**, 1993. Numerical study of laminar and turbulent natural convection in an inclined square cavity, *International Journal of Heat and Mass Transfer*, Vol. 36, n 11, p 2899-2911.

KWEON, Y.C. and **KIM, M.H.** 2000. Experimental study on nucleate boiling enhancement and bubble dynamic behaviour in saturated pool boiling using a non-uniform dc electric field. *International Journal of Multiphase Flow*, Vol. 26, pp 1351-1368.

KWEON, Y.C., KIM, M.H., CHO, H.J. and **KANG, I. S.**, 1998. Study on the deformation and departure of a bubble attached to a wall in d.c./a.c. electric fields, *International Journal of Multiphase Flow*, Vol. 24, n 1, Feb, 1998, pp. 145-162.

LACROIX, J. C., ATTEN, P. and **HOPFINGER, E. J.**, 1975. Electro-convection in a dielectric liquid layer subjected to unipolar injection, *Journal of Fluid Mechanics*, Vol. 69, pt 3, pp. 539-563.

LAFAURIE, B., NARDONE, C., SCARDOVELLI, R., ZALESKI, S. and **ZANETTIN, G.** 1994 Modelling Merging and Fragmentation in Multiphase Flows with SURFER, *Journal of Computational Physics*, Vol.113, pp.134.

LAI, H., YAN, Y. Y. and **GENTLE, C. R.** 2003 Calculation Procedure of Conjugate Viscous Flows about and inside Single Bubbles, *Numerical Heat Transfer*, Part B, Vol. 43, pp. 241-265.

LANDAU, L. D. and **LIFSHIZ, E. M.** 1963. Electrodynamics of Continuous Media. Pergamon, New York.

LEE, R.C. and **NYDAHL, J.E.** 1989 Numerical Calculation of Bubble Growth in Nucleate Boiling from Inception through Departure, *ASME Journal of Heat Transfer*, Vol.111, PP74-479.

LEE, S., DULIKRAVICH, G. S. and **AHUJA, V.**, 1993 Computations of electro-thermo-convective phenomena in electro-theological fluids, *American Society of Mechanical Engineers*, Fluids Engineering Division (Publication) FED, vol. 164, pp. 29-42.

LEONARD, B.P. 1979. A stable and accurate convection modelling procedure based on quadratic upstream interpolation. Comp. Meth.Appl.Mech.Engrg., 19, pp59-98.

LI, S. and **PETZOLD, L.** 1997 Moving Mesh Methods with Upwinding Schemes for Time-Dependent PDEs, *Journal of Computational Physics*, Vol.131, pp.368-377.

LI, W.Z. and **YAN, Y.Y.** 2002 A Direct-Predictor Method for Solving Terminal Shape of a Gas Bubble Rising through a Quiescent Liquid, *Numerical Heat Transfer*, Part B, Vol. 42 (1), pp. 55-71 (2002).

LI, W.Z., YAN, Y.Y. and **HULL, J. B.** 2003 The Propagation of Temperature and Concentration Fields around a Deformed Gas Bubble Rising in a Quiescent Hot or Bi-Solution Liquid, *Int. J. of Numerical Methods for Heat Fluid Flow*, Vol. 13, pp. 940-963.

LINTHORST, S. J. M., SCHINKEL, W. M. M. and **HOOGENDOORN, C.**

J. 1981 Flow structure with natural convection in inclined air-filled enclosures, *ASME Journal of Heat Transfer*, Vol.103, PP.535-539.

MACCORMACK, R.W. and **PAULLAY, A. J.** 1972 Computational efficiency achieved by time splitting of finite difference operators. AIAA paper, pp 72-154, San Diego.

MADADNIA, J. and **KOOSHA, H.** 2003. Electrohydrodynamics effects on characteristic of isolated bubbles in the nucleate pool boiling regime, *Experimental Thermal and Fluid Science*, Vol. 27, pp145-150.

MAJUMDAR, S. 1988. Role of under-relaxation in momentum interpolation for calculation of flow with non-staggered grids, *Journal of Numerical Heat Transfer*, v. 13, no. 1, pp. 125-132.

MANN, M. 2001. Ein Mikrozonenmodell zur Beschreibung der Blasenbildung und des Wärmeübergangs beim Sieden, *Ph.D. thesis*, University of Stuttgart, Stuttgart, Germany.

MARCO, P. DI. and **GRASSI, W.** 1993. Saturated pool boiling enghancement by means of an electric field. *Enhanced heat transfer*, Vol.1, pp.99-114.

MARKELS, M.. and **DURFEE, R.L.** 1964. The effect of applied voltage on boiling heat transfer, *AIChE J.* Vol.10, pp106-110.

MARKELS, M.. and **DURFEE, R.L.** 1965. Studies of boiling heat transfer with electric fields, *AIChE J.* Vol.11, pp 716-721.

MARTIN, P. J. and **RICHARDSON, A. T.,** 1984. Conductivity models of electrothermal convection in plane layer of dielectric liquid, *Journal of Heat Transfer, Transactions ASME*, Vol. 106, n 1, pp. 131-136.

MCDONALD, P.W. 1971. The computation of transonic flow through two-dimensional gas turbine cascades. *ASME* , pp71-89.

MIKIC, B.B., ROHSENOW, W.M. and **GRIFFITH, P.** 1970. On bubble growth rates. *Int. J. Heat Mass Transfer*, Vol. 13, pp 657.

MOORE, F. D. and **MESLER, R. B.** 1961. The measurement of rapid temperature fluctuations during nucleate boiling of water, *A.ICh.E.J* ,Vol. 17, pp620-624.

NAPOLITANO, M. and **ORLANDI, P.** 1985 Laminar flow in a complex geometry: A comparison, *Int. J. Numer. Meth. Fluids*, vol. 5, pp. 667-683.

NEVE, R.S. and **YAN, Y.Y.**, 1996. The enhancement of heat exchanger performance using combined EHD and passive methods. Int. J. of Heat Fluid Flow, Vol. 17, pp. 403-409.

NGO, C.C. and **LAI, F.C.** 2001, Effects of electric field on natural convection in an enclosure heated from below, *Proceedings of the national heat transfer conference, (NHTC2001-20200).*

OGATA, J., IWAFUJI, Y., SHIMADA, Y. and **YAMAZAKI, T.**, 1992. Boiling heat transfer enhancement in tube-bundle evaporators utilizing electric fields, ASHRAE Trans., Vol. 98(2), pp. 435-444.

OGATA, J. and **YABE, A.** 1991. Augmentation of nucleate boiling heat transfer by applying electric fields: EHD behaviour of boiling bubbles. ASME/JSME Thermal Engineering Proceedings 3:41-46.

OGATA, J. and **YABE, A.** 1993 a. Augmentation of nucleate boiling heat transfer by utilising the EHD effect - EHD behaviour of boiling bubbles and heat transfer characteristics. *Int. J. of Heat and Mass Transfer*, Vol. 36, no. 3, pp.783-791.

OGATA, J. and **YABE, A.** 1993 b. Basic study on the enhancement of nucleate boiling heat transfer by applying electric fields, *Int. J. of Heat and Mass Transfer*, Vol. 36, no. 3, pp. 775-782.

OLINGER, J.L. and **COLVER, C.P.** 1971. A study of the effect of a uniform electric field on nucleate and film boiling. *Chem. Engng Prog. Symp. Ser.* 67, pp19-29.

OH, S-D. and **KWAK, H-Y**, 1996. Study of bubble behavior and boiling heat transfer enhancement under electric field, *American Society of Mechanical Engineers*, Nuclear Engineering Division (Publication) NE, Vol. 19, pp 1-14.

OHADI, M.M., 1991. Electrohydrodynamic enhancement of single phase and phase change heat transfer in heat exchangers. *ASHRAE Journal*, pp. 42-48.

OSHER, S. and **SETHIAN, J.A.** 1988 Fronts Propagating with Curvature Dependent Speed: Algorithm Based on Halmilton-Jacobi Formulations, *Journal of Computational Physics,* Vo.79, PP. 12-49.

PASCHKEWITZ, J. S. and **PRATT, D. M.,** 2000. Influence of fluid properties on electrohydrodynamic heat transfer enhancement in liquids under viscous and electrically dominated flow conditions, *Experimental Thermal and Fluid Science*, Vol.

21, n 4, pp. 187-197.

PATANKAR, S. V. 1980. Numerical Heat Transfer and Fluid Flow. McGRAW-HILL book company.

PATANKAR, S. V. and **SPALDING, D.B.** 1972. A calculation procedure for heat, mass and momentum transfer in three-dimensional parabolic flows. *International Journal of Heat Mass Transfer*, vol.15, pp1787-1806.

PERIC, M., KESSLER, R. and SCHEUERER, G. 1988 comparison of finite-volume numerical methods with staggered and collocated grids. *Computers & Fluids*, v **16**, n 4, pp. 389-403.

POULTER, R. and **ALLEN, P.H.G.**, 1986. Electrohydrodynamically augmented heat and mass transfer in the shell/tube heat exchanger. *Heat Transfer, Proceedings of the International Heat Transfer Conference*, Vol. **6**, 1986, pp. 2963-2968.

PUCKETT, E.G., ALMGREN, A.S., BELL, J.B., MARCUS, D.L. and **RIDER, W.J.** 1997 A High-Order Projection Method for Tracking Fluid Interfaces in Varaibl Density Incompressible Flows, *Journal of Computational Physics*, Vol.130, PP. 269.

RAMASWAMY, B. 1990 Numerical Simulation of Unsteady Viscous Free Surface Flow, *Journal of Computational Physics*, Vol.90, PP. 396-430.

RASTOGI, A. K., 1984. Hydrodynamics in Tubes Perturbed by Curvilinear Obstructions, *ASME Journal of Fluids Engineering*, Vol.106, PP. 262-269.

RAUL, R. 1990. An application of the vorticity-vector potential method to laminar cube flow. *Int. J.for numerical method in fluids*. Vol. 10. pp 164-186.

RHIE, C. M. and **CHOW, W. L.** 1983. Numerical study of the turbulent flow past an airfoil with railing edge separation. *AIAA Journal*, v 21, n 11, p 1525-1532.

RIDER, W.J. and **KOTHE, D.B.** 1998, Reconstructing Volume Tracking, *Journal of Computational Physics*, Vol. 141, PP. 112.

RIZZIA, W. and **INOUYE, M.** 1973. Time split finite volume method for three dimensional blunt-body flows. *AIAA Journal*, Vol.11, pp 1478-1485.

ROACHE, P. 1981 Scaling of high Reynolds number weakly separated flows, *Symposium on Numerical and Physical Aspects of Aerodynamic Flows.*

ROHSENOW, W.M. 1952. A method of correlating heat transfer data for surface boiling of liquids. *Transaction of American society mechanics engineering*, No. 74, pp 969-976.

ROHSENOW, W.M. 1966. Nucleation with boiling heat transfer. *Industrial engineering chemistry*. No. 58 (1), pp 40-47.

RUDMAN, M. 1997 Volume-Tracking Methods for Interfacial Flow Calculation, *International Journal for Numerical Methods in Fluids*, Vol.24, PP. 671-691.

RYSKIN, G. and **LEAL, L.G.** 1984a Numerical Solution of Free-Boundary Problems in Fluid Mechanics. Part 1: The Finite-Difference Technique, *Journal of Fluid Mechanics*, Vol.148, PP.1-17.

RYSKIN, G. and **LEAL, L.G.** 1984b Numerical Solution of Free-Boundary Problems in Fluid Mechanics. Part 2: Buoyancy-Driven Motion of a Gas Bubble Through a Quiescent Liquid, *Journal of Fluid Mechanics*, Vol.148, PP. 19-35.

SALEHI, M., OHADI, M. M. and **DESSIATOUN, S.,** 1997. EHD enhanced convective boiling of R-134a in grooved channels - application to subcompact heat exchangers, *Journal of Heat Transfer, Transactions ASME*, Vol. 119, n 4, pp. 805-809.

SCHIMIDT, E. and **LEIDENFROST, W.,** 1953. Der Einfluss electrischer Felder auf den Wärmetransport in flűssigen elektrischen Nichtleitern. Forsh. Geb. *Ingenieurwes*. Vol.19, pp.65-80.

SENFTILEBEN, H., 1931. Physics. Z. 32, pp 550.

SENFTILEBEN, H., 1932. Physics. Z. 33, pp. 602.

SENFTILEBEN, H., 1934. Physics. Z. 35, pp. 661.

SENFTILEBEN, H. and **BRAUN, W.**, 1936. Der Einfluss elektrischer Felder auf den Wärmestrom in Gasen.Physics. Z. 102, pp.480-500.

SEYED-YAGOOBI, J. and **BRYAN, J.E.,** 1995. Enhancement of heat transfer and mass transport in single-phase flows with electrohydrodynamics, *Advances in heat transfer*, Vol. 33, pp 59-186.

SEYED-YAGOOBI, J., GEPPERT, C. A. and **GEPPERT, L. M.,** 1996, Electrohydrodynamically enhanced heat transfer in pool boiling. *Journal of Heat Transfer, Transactions ASME*, Vol. 118, n 1, p 233-237.

SHU, H. S. and **LAI, F. C.**, 1995. Effect of electrical field on buoyancy-induced flows in an enclosure, *Conference Record - IAS Annual Meeting*, Vol. **2**, pp. 1465-1471.

SHYY, W., UDAYKUMAR, H. S., RAO, M. M. and **SMITH, R. W.** 1996 *Computational Fluid Dynamics with Moving Boundaries*, Taylor & Francis.

SINGH, A., OHADI, M. M. and **DESSIATOUN, S.**, 1997. EHD-enhanced boiling of R-123 over commercially available enhanced tubes, *Journal of Heat Transfer, Transactions ASME*, Vol. 117, 4, pp. 1070-1073.

SNYDER , N.W. and **EDWARD, D.K.** 1956. Post conference comments, Summary of Conference on Bubble Dynamics and Boiling Heat Transfer Held the Jet Propulsion Laboratory, *JPL Memo* No. 20-137.

SOU, A., TOMIYAMA, A., ZUN, I. and **YABUSHITA, Y.** 1997 Comparison of Two Volume Tracking Algorithms for Bubbly Flow Simulation, in *Moving Boundaries IV---Computational Modelling of Free and Moving Boundary Problems*, Edited by R. Van Keer and C.A. Brebbia, Computational Mechanics Publications, Southampton, UK, Boston, USA.

STEPHAN, P. and **HAMMER, J.** 1994. A new model for nucleate boiling heat transfer, *Wärme- und Stoffübertragung*, vol. 30, pp. 119-125,

STEPHAN, P. and **HAMMER, J.** 1996. The role of micro-region phenomena on nucleate boiling, *2nd European Thermal Science and 14 UIT National Heat Transfer Conference*, Rome, Italy.

SUSSMAN, M., SMEREKA, P. and **OSHER, S.** 1994 A Level Set Approach for Computing Solutions to Incompressible Two-Phase Flow, *Journal of Computational Physics*, Vol.114, pp.146-159.

TAKAGI, S. and **MATSUMOTO, Y.** 1993 Numerical Analysis of a Single Rising Bubble Using Body-Fitted Coordinate System, *JSME International Journal*, Series B, Vol. 40, No.1, pp. 42-50.

TAKAGI, S. and **MATSUMOTO, Y.** 1995 A Rising Bubble in the Simple Shear Flow, ASME FED-Vol.210, pp.145-148.

TAKATA, Y, SHIRAKAWA, H., TANAKA, K., KUROKI, T. and **ITO, T.,** 1996. Numerical analysis of bubble growth under electric field, Nippon Kikai Gakkai Ronbunshu, B Hen/Transactions of the Japan Society of Mechanical Engineers, Part B, Vol. 62, 595, pp 1142-1147.

TAKUMA, T., KAWAMOTO, T. and **SUNAGA, Y.,** 1985. Analysis of calibration arrangements for a.c. field strength meters. *IEEE Trans*. Power App. Syst., PAS-104(2). pp.489-495.

TAN, K.T. and **LAI, F.C.** 2001. EHD-enhanced natural convection in an enclosure:effects of non-symmetric electric field, *Proceedings of the national heat transfer conference, (NHTC2001-20065).*

THOMAS, P.D. and **MIDDLECOFF, J.F.** 1980. Direct control of the grid point distribution in meshes generated by elliptic equations. *AIAA Journal*, Vol.18, n.6, pp.652-656.

THOMPSON, J. F. 1982 Elliptic grid generation, *Elsevier Publishing Co.*, Inc., New York, 79-105.

THOMPSON, J. F., WARSI, Z. U. A. and **MASTIN, C. W.** 1985 *Numerical Grid Generation, Fundamentals and Applications*, North-Holland, New York.

THOMPSON, J. F., F. C. THAMES, and **C. W. MASTIN** 1974 Automatic numerical generation of body-fitted curvilinear coordinate system for fields containing any number of arbitrary two dimensional bodies, *J. comp. Phys*, 15, 299.

TOMIYAMA, A., SOU, A., MINAGAWA, H. and **SAKAGUCHI, T.** 1993 Numerical Analysis of a Single Bubble by VOF Method, *JSME International Journal*, Series B, Vol.36, No.1, pp. 51-56.

UNVERDI, S.O. and **TRYGGVASON, G.** 1992 A Front-Tracking Method for Viscous, Incompressible, Multi-Fluid Flows, *Journal of Computational Physics*, Vol.100, pp. 25-37.

VAHL DAVIS, G. DE. and **JONES, I.P**. 1981. Natural convection of air in a square cavity, A comparison exercise, in *numerical method in thermal problems*, (edited

by R.M.Lewis, K Morgan and B.A. Schrfler), Pineridge Press,Swansea, pp.552-572, U.K.

WANG, S.Y., COLLIONS, M.W. and **ALLEN, P.H.G.**, 1990. Prediction of the effect of Electro hydrodynamic (EHD) enhancement on fluid flow and heat transfer, *proceedings of the first international conference*, in Portsmouth, UK.

WEBER, K.H. and **HALSEY, G.H.,** 1953. Free convection in electric fields, *Proceeding of Heat transfer Fluid Mechanics*, Inst. No.19.

WELCH, S.W.J. 1995 Local Simulation of Two-Phase Flows Including Interface Tracking with Mass Transfer, *Journal of Computational Physics*, Vol.121, PP.142-154.

WELCH, S.W.J. 1998 Direct Simulation of Vapour Bubble Growth, *International Journal of Heat and Mass Transfer*, Vol.41, No.12, PP. 1655-1666.

WORRAKER, W. J. and **RICHARDSON, A. T.**, 1979. The effect of temperature variations in charge carrier mobility on stationary electrohydrodynamic instability, *Journal of Fluid Mechanics*, Vol. 93, pp. 29-45.

WORRAKER, W. J. and **RICHARDSON, A. T.**, 1981. Nonlinear Electrohydrodynamic stability analysis of a thermally stabilized plane layer of dielectric liquid. *Journal of Fluid Mechanics*, Vol. 109, Aug, pp. 217-237.

YABE, A., 1993. Mechanism of electro-hydrodynamically (EHD) enhanced boiling and condensation. Computers and Computing in Heat Transfer Science and Engineering ed. By W. Nakuama and K. T. Yang. CRC.

YABE, A. and **MAKI, H.**, 1988. Augmentation of convective and boiling heat transfer by applying an electro-hydrodynamics jet. *International Journal of Heat and Mass Transfer*, Vol. 31, n 2, Feb, 1988, pp. 407-417.

YAN, Y.Y. 2000. Models for general phase change phenomena in heat exchangers and in industrial processes affected by applying an electric field. *International Journal of Transition Phenomena*, Vol.2, pp.287-197.

YAN, Y.Y., LAI, H., GENTLE, C.R. and **SMITH, J.M.** 2002 Numerical analysis of fluid flow inside and around a liquid drop using an incorporation of multi-block iteration and moving mesh, *Trans. IChemE, Part A: Chemical Engineering*

Research & Design, Vol. 80 (3), pp. 325-331.

YAN, Y.Y. and **NEVE, R.S.** 1996a. EHD augmentation of nucleate boiling at a Gewa-T surface. *Int. J. of Enhanced Heat Transfer*, Vol. 3, No. 3, pp. 211-219.

YAN, Y.Y., NEVE, R.S., KARAYIANNIS, T.G., COLLINS, M.W. and **ALLEN, P.H.G.** 1996b. EHD effects on nucleate boiling at passively enhanced surfaces. *Int. J. of Experimental Heat Transfer*, Vol. 9, No.3, pp. 195-211.

YAN, Y.Y., NEVE, R.S., and **COLLINS, M.W.**, 1997. The effect of an electric field on heat & mass transfer for dielectric crystallisation, *Trans. IChemE*, Vol.75, Part A, pp. 668-671, Oct.

YANG, H. and **LAI, F.C.** 1997. Effects of heat generation on EHD-enhanced natural convection in an enclosure, *Conference records of the IEEE Industry Application Society 32th IAS Annual meeting*, Vol.3, pp. 1851-1859.

YOUNG, D.F and **TASI, F. Y.,** 1973.Flow characteristics in models of arterial stenoses—I. Steady flow, *J. Biomech.* Vol. 6, PP. 395-410.

ZAGPDOUDI, M.C. and **LALLEMAND, M.,** 2001. Nucleate pool boiling under DC electric field, *Experimental Heat Transfer, Vol.* 14, pp157-180.

ZHANG, H.B., YAN, Y.Y. and **HULL, J.B.**, 2001 A modified momentum interpolation scheme and its application in numerical modelling of natural convection in enclosed cavities, *7th UK National Heat Transfer Conference*, Nottingham .

Appendix A

Deviation of Equation (4.3.20)

In equation (4.3.19)

$$a_P = a_P + a_S + a_E + a_W + (F_n - F_s + F_e - F_w)$$

In an electric field:

$$F_n - F_s + F_e - F_w$$

$$= r\left(W_1 + \frac{E_1}{\mathrm{Re}\,\mathrm{Pr}_E}\right)\Delta\eta\Big|_s^n + r\left(W_2 + \frac{E_2}{\mathrm{Re}\,\mathrm{Pr}_E}\right)\Delta\xi\Big|_w^e$$

$$= rW_1\Delta\eta\Big|_s^n + rW_2\Delta\xi\Big|_w^e + r\frac{E_1}{\mathrm{Re}\,\mathrm{Pr}_E}\Delta\eta\Big|_s^n + r\frac{E_2}{\mathrm{Re}\,\mathrm{Pr}_E}\Delta\xi\Big|_w^e$$

$$= \tilde{J}\left[\frac{\partial(\overline{ru})}{\partial\overline{x}} + \frac{\partial(\overline{rv})}{\partial\overline{y}}\right]\Delta\xi\Delta\eta + \frac{\tilde{J}}{\mathrm{Re}\,\mathrm{Pr}_E}\left[\frac{\partial(\overline{rE_x})}{\partial\overline{x}} + \frac{\partial(\overline{rE_y})}{\partial\overline{y}}\right]\Delta\xi\Delta\eta$$

Since

$$\frac{\partial(\overline{ru})}{\partial\overline{x}} + \frac{\partial(\overline{rv})}{\partial\overline{y}}$$

$$= rdiv(\vec{V})$$

$$= 0$$

$$\frac{\partial(\overline{rE_x})}{\partial\overline{x}} + \frac{\partial(\overline{rE_y})}{\partial\overline{y}}$$

$$= rdiv(\vec{\vec{E}})$$

$$div(\vec{\vec{E}}) = \overline{\nabla}\cdot(-\overline{\nabla}\overline{\varphi}) = N_E\overline{q}$$

Therefore:

$$\tilde{J}\left[\frac{\partial(\overline{ru})}{\partial\overline{x}}+\frac{\partial(\overline{rv})}{\partial\overline{y}}\right]\Delta\xi\Delta\eta+\frac{\tilde{J}}{\mathrm{Re}\,\mathrm{Pr}_E}\left[\frac{\partial(\overline{rE_x})}{\partial\overline{x}}+\frac{\partial(\overline{rE_y})}{\partial\overline{y}}\right]\Delta\xi\Delta\eta$$

$$=\frac{\tilde{J}}{\mathrm{Re}\,\mathrm{Pr}_E}N_E\overline{q}\Delta\xi\Delta\eta$$

Then the Equation (4.3.19) can be changed to Equation (4.3.20):

$$a_P=a_P+a_S+a_E+a_W+\frac{\tilde{J}}{\mathrm{Re}\,\mathrm{Pr}_E}N_E\overline{q}\Delta\xi\Delta\eta$$

Appendix B

List of FORTRAN Codes

The FORTRAN codes consist of four files with respective functions as follows:

INTGRID.F: generating the numerical grids; this file should be compiled and run independently before run the main code;

NS_Solver.F: the main code; this code should be compiled together with the files *COMMONBLOCK.F* and *PARAMETERS.F*. The function of *NS_Solver.F* is to solve the coupled flow, thermal and electric fields use the numerical methods presented in chapter 4;

PARAMETERS.F: setting up parameters for the case to be calculated;

COMMONBLOCK.F : definition of most of the arrays used in *NS_Solver.F*.

Because the main variables and arrays are explained in the codes when they appear at the first time, the lists of the above codes are directly given as follows (the case in the code as an example is the natural convection with EHD effects in a cylindrical enclosure):

INTGRID.F

```
      PARAMETER(M1=60,M2=40)
      DIMENSION X(M1,M2),Y(M1,M2),DEIT(M1),EITA(M1),DCET(M2),
     &          CETA(M2)

c     X and Y are the physical coordinates
c     EITA and are CETA are the transformed coordinates
      Q=1.02
      NN=(M1-2)/2
      BIANCHANG=1.5
```

```
      DEIT(2)=BIANCHANG*0.5*(1.-Q)/(1.-Q**NN)
      DO 100 K=3,(M1-2)/2+1
      DEIT(K)=DEIT(K-1)*Q
100   CONTINUE
      DO 105 K=(M1-2)/2+2,M1-1
      DEIT(K)=DEIT(M1+1-K)
105   CONTINUE
      EITA(1)=0.
      DO 110 K=2,M1
      EITA(K)=EITA(K-1)+0.5*(DEIT(K-1)+DEIT(K))
110   CONTINUE
      Q=1.05
      NN=(M2-2)/2
      BIANCHANG=1
      DCET(2)=BIANCHANG*0.5*(1.-Q)/(1.-Q**NN)
      DO 200 I=3,(M2-2)/2+1
      DCET(I)=DCET(I-1)*Q
200   CONTINUE
      DO 205 I=(M2-2)/2+2,M2-1
      DCET(I)=DCET(M2+1-I)
205   CONTINUE
      CETA(1)=0.
      DO 210 I=2,M2
      CETA(I)=CETA(I-1)+0.5*(DCET(I-1)+DCET(I))
210   CONTINUE
      DO 350 K=1,M1
      DO 360 I=1,M2
      X(K,I)=EITA(K)
      Y(K,I)=CETA(I)
360   CONTINUE
350   CONTINUE
      OPEN(2,FILE='INTGRID-1.DAT')
      WRITE(2,600)((X(K,I),Y(K,I),I=1,M2),K=1,M1)
      CLOSE(2)
      OPEN(3,FILE='DX1-DX2.DAT')
      WRITE(3,610)(DEIT(K),K=1,M1)
      WRITE(3,610)(DCET(I),I=1,M2)
      CLOSE(3)
600   FORMAT(1X,2F16.8)
610   FORMAT(1X,F16.8)
      STOP
      END
```

PARAMETERS.F

```
      PARAMETER(M1=60,M2=40)
C     1. For natural convection in closed space, Reynolds often defined as:
      Reynolds=SQRT(GRASHOF)
C     2. TIME0=XEL0/VELOCITY0
C     3. All variables, these are: Time, velocity, pressure, temprature, are dimensionless in
C     the program. If you want to recover the units, you can do this in subroutine OUTPUT.
      COMMON /REF_MUST/XEL0,REYNOLDS,GRASHOF,PRANDTL,SE,DE,
```

```
     &                                NE,PRE,EC
          COMMON /REF_MAYBE/DESITY0,VELOCITY0,TEMP0,DELTAT0,TIME0,
     &                                CBEITA0,GRAVITY0
          COMMON/COORDIN/KOODIN

          DATA  XEL0    /1./
          DATA  REYNOLDS /54.77226/
          DATA  GRASHOF  /3000./
          DATA  PRANDTL  /1./
          DATA  SE /1./
          DATA  ADE /1./
          DATA  ANE /1./
          DATA  PRE /1./
          DATA  EC /0.00001171/

C         KOORDIN=1: Cartesian coordinates; KOORDIN=2: cylindrical coordiantes
          DATA  KOODIN/2/
          DATA  DESITY0  /860./

C         relaxation factors for variables of solution
          DATA  ALFA,ALFAP,ALFAQU,ALFAFAI/0.6,0.4,0.3,0.1/
```

COMMONBLOCK.F

```
          COMMON /FLOWRT/Q
          COMMON /RELAXF/ALFA,ALFAP,ALFAQU,ALFAFAI
          COMMON /CONVEG/CONVEG,E1,E2,E3,E4
          COMMON /ERSPOT/KE1,KE2,KE3,IE3
          COMMON /COMFUN/X1(1000),FX1(1000),AXM1(1000),ADM1(1000),
     &           X2(1000),FX2(1000),AXM2(1000),ADM2(1000)
          COMMON /PHGRID/X(M1,M2),Y(M1,M2),
     &           Xs(M1,M2),Ys(M1,M2),Xw(M1,M2),Yw(M1,M2),
     &           RRP(M1,M2),RRs(M1,M2),RRw(M1,M2)
          COMMON /VOLSPA/DEITA(M1),DCETA(M2),EITA(M1),CETA(M2)
          COMMON /ARZIYA/
     &          XEITAP(M1,M2),XCETAP(M1,M2),YEITAP(M1,M2),YCETAP(M1,M2),
     &          XEITAs(M1,M2),YEITAs(M1,M2),XCETAs(M1,M2),YCETAs(M1,M2),
     &          XEITAw(M1,M2),YEITAw(M1,M2),XCETAw(M1,M2),YCETAw(M1,M2)
          COMMON /DULANG/AFAP(M1,M2),BETP(M1,M2),GAMP(M1,M2),
     &           AFAs(M1,M2),BETs(M1,M2),GAMs(M1,M2),
     &           AFAw(M1,M2),BETw(M1,M2),GAMw(M1,M2)
          COMMON /YACOBI/GHGP(M1,M2),GHGs(M1,M2),GHGw(M1,M2)
          COMMON /CHAZHI/F1(M1),F2(M2)
          COMMON /FFIELD/U(M1,M2),V(M1,M2),P(M1,M2),T(M1,M2),
     &           W1P(M1,M2),W2P(M1,M2),
     &           W1s(M1,M2),W2w(M1,M2)
          COMMON /COEFP1/CS(M1,M2),CN(M1,M2),CW(M1,M2),CE(M1,M2),
     &           CP(M1,M2),P1(M1,M2),SM(M1,M2)
          COMMON /CSMOVE/SU(M1,M2),SV(M1,M2),
     &           AS(M1,M2),AN(M1,M2),AW(M1,M2),AE(M1,M2),AP(M1,M2)
          COMMON /TSOURC/ST(M1,M2)
          COMMON /QUSOURC/SQU(M1,M2)
```

```
      COMMON /FAISOURC/SFAI(M1,M2)
      COMMON /BCDBCD/B1P(M1,M2),C2P(M1,M2),B1s(M1,M2),C2w(M1,M2)
      COMMON /PARTLP/DPDX1(M1,M2),DPDX2(M1,M2)
      COMMON /PARTLFAI/DFAIDX1w(M1,M2),DFAIDX2s(M1,M2),
     &            DFAIDX1(M1,M2),DFAIDX2(M1,M2)
      COMMON /QIUBIANWEFEN/
     &            DUDX1(M1,M2),DUDX2(M1,M2),DVDX1(M1,M2),DVDX2(M1,M2),
     &            DTDX1(M1,M2),DTDX2(M1,M2),DQUDX(M1,M2),DQUDY(M1,M2),
     &            DEXDX(M1,M2),DEYDY(M1,M2),DEXDY(M1,M2),DEYDX(M1,M2),
     &            DQUDX1(M1,M2),DQUDX2(M1,M2),
     &            DEXDX1(M1,M2),DEXDX2(M1,M2),
     &            DEYDX1(M1,M2),DEYDX2(M1,M2)
      COMMON /MOINTN/H1P(M1,M2),H2P(M1,M2)
      COMMON /EHD/FAI(M1,M2),QU(M1,M2),EX(M1,M2),EY(M1,M2),
     &            EEITAP(M1,M2),ECETAP(M1,M2),EEITAw(M1,M2),
     &            EEITAs(M1,M2),ECETAs(M1,M2),ECETAw(M1,M2)
```

NS_Solver.F

```
C=======================================================================*
C                                                                       *
C          N-S solver for 2D Heat and Fluid Flows Under Electric Field  *
C                                                                       *
C            This code is developed by Hongbo Zhang.  Last change: 26/12/2003 *
C                                                                       *
C=======================================================================*
      INCLUDE 'PARAMETERS.F'
      INCLUDE 'COMMONBLOCK.F'
      CALL GRIDPA
      CALL ASUME
      M=0
10    M=M+1
      CALL BLACK(M)
      IF(CONVEG.EQ.1) THEN
      GOTO 100
      ELSE
      GOTO 10
      END IF
100   CALL OUTPUT
      STOP
      END
C=======================================================================
C
C     TO CALCULATE THE PARAMETERS ABOUT GRIDS
C
      SUBROUTINE GRIDPA
      INCLUDE 'PARAMETERS.F'
      INCLUDE 'COMMONBLOCK.F'

      OPEN(UNIT=2,FILE='INTGRID-1.DAT')
      READ(2,*)((X(K,I),Y(K,I),I=1,M2),K=1,M1)
      CLOSE(2)
```

```
      OPEN(UNIT=4,FILE='DX1-DX2.DAT')
      READ(4,*)(DEITA(K),k=1,M1)
      READ(4,*)(DCETA(I),I=1,M2)
      CLOSE(4)
      EITA(1)=0.
      CETA(1)=0.
      DO 5  K=2,M1
      EITA(K)=EITA(K-1)+0.5*(DEITA(K-1)+DEITA(K))
5     CONTINUE
      DO 8 I=2,M2
      CETA(I)=CETA(I-1)+0.5*(DCETA(I-1)+DCETA(I))
8     CONTINUE
      DO 7 K=1,M1
      X1(K)=EITA(K)
7     CONTINUE
      DO 9 I=1,M2
      X2(I)=CETA(I)
9     CONTINUE

      DO 300 I=1,M2
      DO 302 K=1,M1
      FX1(K)=X(K,I)
302   CONTINUE
      CALL SPLINE(X1,FX1,AXM1,ADM1,M1)
      DO 304 K=1,M1
      XEITAP(K,I)=AXM1(K)
304   CONTINUE
      DO 306 K=1,M1
      FX1(K)=Y(K,I)
306   CONTINUE
      CALL SPLINE(X1,FX1,AXM1,ADM1,M1)
      DO 308 K=1,M1
      YEITAP(K,I)=AXM1(K)
308   CONTINUE
300   CONTINUE

      DO 310 K=1,M1
      DO 312 I=1,M2
      FX2(I)=X(K,I)
312   CONTINUE
      CALL SPLINE(X2,FX2,AXM2,ADM2,M2)
      DO 314 I=1,M2
      XCETAP(K,I)=AXM2(I)
314   CONTINUE
      DO 316 I=1,M2
      FX2(I)=Y(K,I)
316   CONTINUE
      CALL SPLINE(X2,FX2,AXM2,ADM2,M2)
      DO 318 I=1,M2
      YCETAP(K,I)=AXM2(I)
318   CONTINUE
310   CONTINUE

      DO 320 K=1,M1
```

```
                DO 325 I=1,M2
                AFAP(K,I)=XCETAP(K,I)**2+YCETAP(K,I)**2
                BETP(K,I)=XEITAP(K,I)*XCETAP(K,I)+YEITAP(K,I)*YCETAP(K,I)
                GAMP(K,I)=XEITAP(K,I)**2+YEITAP(K,I)**2
                GHGP(K,I)=XEITAP(K,I)*YCETAP(K,I)-XCETAP(K,I)*YEITAP(K,I)
325             CONTINUE
320             CONTINUE

20              CALL INFACTOR

                DO 900 I=1,M2
                DO 905 K=2,M1
                XEITAs(K,I)=F1(K-1)*XEITAP(K,I)+(1.-F1(K-1))*XEITAP(K-1,I)
                YEITAs(K,I)=F1(K-1)*YEITAP(K,I)+(1.-F1(K-1))*YEITAP(K-1,I)
                XCETAs(K,I)=F1(K-1)*XCETAP(K,I)+(1.-F1(K-1))*XCETAP(K-1,I)
                YCETAs(K,I)=F1(K-1)*YCETAP(K,I)+(1.-F1(K-1))*YCETAP(K-1,I)
905             CONTINUE
                XEITAs(1,I)=XEITAP(1,I)
                YEITAs(1,I)=YEITAP(1,I)
                XCETAs(1,I)=XCETAP(1,I)
                YCETAs(1,I)=YCETAP(1,I)
900             CONTINUE
                DO 910 K=1,M1
                DO 915 I=2,M2
                XEITAw(K,I)=F2(I-1)*XEITAP(K,I)+(1.-F2(I-1))*XEITAP(K,I-1)
                YEITAw(K,I)=F2(I-1)*YEITAP(K,I)+(1.-F2(I-1))*YEITAP(K,I-1)
                XCETAw(K,I)=F2(I-1)*XCETAP(K,I)+(1.-F2(I-1))*XCETAP(K,I-1)
                YCETAw(K,I)=F2(I-1)*YCETAP(K,I)+(1.-F2(I-1))*YCETAP(K,I-1)
915             CONTINUE
                XEITAw(K,1)=XEITAP(K,1)
                YEITAw(K,1)=YEITAP(K,1)
                XCETAw(K,1)=XCETAP(K,1)
                YCETAw(K,1)=YCETAP(K,1)
910             CONTINUE
                DO 950 K=1,M1
                DO 955 I=1,M2
                AFAs(K,I)=XCETAs(K,I)**2+YCETAs(K,I)**2
                BETs(K,I)=XEITAs(K,I)*XCETAs(K,I)+YEITAs(K,I)*YCETAs(K,I)
                GAMs(K,I)=XEITAs(K,I)**2+YEITAs(K,I)**2
                GHGs(K,I)=XEITAs(K,I)*YCETAs(K,I)-XCETAs(K,I)*YEITAs(K,I)
                AFAw(K,I)=XCETAw(K,I)**2+YCETAw(K,I)**2
                BETw(K,I)=XEITAw(K,I)*XCETAw(K,I)+YEITAw(K,I)*YCETAw(K,I)
                GAMw(K,I)=XEITAw(K,I)**2+YEITAw(K,I)**2
                GHGw(K,I)=XEITAw(K,I)*YCETAw(K,I)-XCETAw(K,I)*YEITAw(K,I)
955             CONTINUE
950             CONTINUE
                DO 400 I=1,M2
                DO 410 K=2,M1
                Xs(K,I)=F1(K-1)*X(K,I)+(1.-F1(K-1))*X(K-1,I)
                Ys(K,I)=F1(K-1)*Y(K,I)+(1.-F1(K-1))*Y(K-1,I)
410             CONTINUE
                Xs(1,I)=X(1,I)
                Ys(1,I)=Y(1,I)
400             CONTINUE
```

```
                DO 420 K=1,M1
                DO 430 I=2,M2
                Xw(K,I)=F2(I-1)*X(K,I)+(1.-F2(I-1))*X(K,I-1)
                Yw(K,I)=F2(I-1)*Y(K,I)+(1.-F2(I-1))*Y(K,I-1)
430             CONTINUE
                Xw(K,1)=X(K,1)
                Yw(K,1)=Y(K,1)
420             CONTINUE

                DO 500 K=1,M1
                DO 510 I=1,M2
                IF(KOODIN.EQ.1) THEN
                RRP(K,I)=1.
                RRs(K,I)=1.
                RRw(K,I)=1.
                ENDIF
                IF(KOODIN.EQ.2) THEN
                RRP(K,I)=X(K,I)
                RRs(K,I)=Xs(K,I)
                RRw(K,I)=Xw(K,I)
                ENDIF
510             CONTINUE
500             CONTINUE

                RETURN
                END
C===============================================================================
C
C               This sub calculate derivatives using cubic spline fitting
C               ADM = M: second derivative; AXM = m:  first derivative
C
                SUBROUTINE SPLINE(XX,YY,AXM,ADM,NN)
                DIMENSION XX(1000),YY(1000),ADM(1000),AXM(1000),
     &          AU(1000),AH(1000),AR(1000),D(1000),F(1000), BETA(1000),GAMA(1000)

                DO 100 N=1,NN-1
                AH(N)=XX(N+1)-XX(N)
                F(N)=(YY(N+1)-YY(N))/AH(N)
100             CONTINUE
                DO 110 N=2,NN-1
                AU(N)=AH(N-1)/(AH(N-1)+AH(N))
                AR(N)=AH(N)/(AH(N-1)+AH(N))
                D(N)=6.*(F(N)-F(N-1))/(AH(N-1)+AH(N))
110             CONTINUE

C               solve ADM (N=2,NN-1)
                ADM(1)=0.
                ADM(NN)=0.
                BETA(2)=AR(2)/2.
                GAMA(2)=D(2)/2.
                DO 200 N=3,NN-2
                BETA(N)=AR(N)/(2.-AU(N)*BETA(N-1))
200             CONTINUE
                DO 220 N=3,NN-1
```

```
                GAMA(N)=(D(N)-AU(N)*GAMA(N-1))/(2.-AU(N)*BETA(N-1))
220             CONTINUE
                ADM(NN-1)=GAMA(NN-1)
                DO 250 N=NN-2,2,-1
                ADM(N)=GAMA(N)-BETA(N)*ADM(N+1)
250             CONTINUE

C               solve AXM
                DO 300 N=1,NN-1
                AXM(N)=-ADM(N)*(XX(N+1)-XX(N))**2/(2.*AH(N))+
     &          ADM(N+1)*(XX(N)-XX(N))**2/(2.*AH(N))+
     &          (YY(N+1)-YY(N))/AH(N)-
     &          (ADM(N+1)-ADM(N))/6.*AH(N)
300             CONTINUE
                AXM(NN)=AH(NN-1)/6.*ADM(NN-1)+AH(NN-1)/3.*ADM(NN)+F(NN-1)
                RETURN
                END
C=======================================================================
C
C               calculate geometrical interpolation factors
C
                SUBROUTINE INFACTOR
                INCLUDE 'PARAMETERS.F'
                INCLUDE 'COMMONBLOCK.F'

                DO 100 K=1,M1-1
                F1(K)=DEITA(K)/(DEITA(K)+DEITA(K+1))
100             CONTINUE
                DO 200 I=1,M2-1
                F2(I)=DCETA(I)/(DCETA(I)+DCETA(I+1))
200             CONTINUE
                F1(M1)=0.
                F2(M2)=0.

                RETURN
                END
C=======================================================================
C
C               calculate derivatives of resolved functions
C
                SUBROUTINE QIUBIANDAO(FU,FX,FY,L)
                INCLUDE 'PARAMETERS.F'
                INCLUDE 'COMMONBLOCK.F'
                DIMENSION FU(M1,M2),DFUDX1(M1,M2),DFUDX2(M1,M2),FX(M1,M2),
     &          FY(M1,M2)

                DO 500 I=1,M2
                DO 510 K=1,M1
                FX1(K)=FU(K,I)
510             CONTINUE
                CALL SPLINE(X1,FX1,AXM1,ADM1,M1)
                DO 520 K=1,M1
                DFUDX1(K,I)=AXM1(K)
520             CONTINUE
```

```
500             CONTINUE
                DO 550 K=1,M1
                DO 560 I=1,M2
                FX2(I)=FU(K,I)
560             CONTINUE
                CALL SPLINE(X2,FX2,AXM2,ADM2,M2)
                DO 570 I=1,M2
                DFUDX2(K,I)=AXM2(I)
570             CONTINUE
550             CONTINUE
                IF(L.EQ.1) THEN
                DO 600 K=1,M1
                DO 610 I=1,M2
                FX(K,I)=-1./GHGP(K,I)*( DFUDX1(K,I)*YCETAP(K,I)-
     &                                  DFUDX2(K,I)*YEITAP(K,I) )
                FY(K,I)=-1./GHGP(K,I)*(-DFUDX1(K,I)*XCETAP(K,I)+
     &                                  DFUDX2(K,I)*XEITAP(K,I) )
610             CONTINUE
600             CONTINUE
                ENDIF
                IF(L.EQ.2) THEN
                DO 700 K=1,M1
                DO 710 I=1,M2
                FX(K,I)=1./GHGP(K,I)*( DFUDX1(K,I)*YCETAP(K,I)-
     &                                 DFUDX2(K,I)*YEITAP(K,I) )
                FY(K,I)=1./GHGP(K,I)*(-DFUDX1(K,I)*XCETAP(K,I)+
     &                                 DFUDX2(K,I)*XEITAP(K,I) )
710             CONTINUE
700             CONTINUE
                ENDIF

                RETURN
                END
C=======================================================================
C
C               assume the intial values for solving the fields by iteration
C
                SUBROUTINE ASUME
                INCLUDE 'PARAMETERS.F'
                INCLUDE 'COMMONBLOCK.F'

                DO 200 K=1,M1
                DO 210 I=1,M2
                U(K,I)=0.
                V(K,I)=0.
210             CONTINUE
200             CONTINUE
                TB=1.
                TT=0.
                FAIB=1.
                FAIT=0.
                QUB=1.
                QUT=0.
                DO 400 K=1,M1
```

```
                T(K,1)=TB
                T(K,M2)=TT
                QU(K,1)=QUB
C               QU(K,1)=QUB*SIN(3.141592654/3.*X(K,1))
                QU(K,M2)=QUT
                FAI(K,1)=FAIB
                FAI(K,M2)=FAIT
                DO 410 I=2,M2-1
                T(K,I)=T(K,1)+(TT-TB)/CETA(M2)*CETA(I)
                QU(K,I)=QU(K,1)+(QU(K,M2)-QU(K,1))/CETA(M2)*CETA(I)
                FAI(K,I)=FAI(K,1)+(FAIT-FAIB)/CETA(M2)*CETA(I)
 410            CONTINUE
 400            CONTINUE

                DO 205 K=1,M1
                DO 208 I=1,M2
                W1P(K,I)=U(K,I)*YCETAP(K,I)-V(K,I)*XCETAP(K,I)
                W2P(K,I)=V(K,I)*XEITAP(K,I)-U(K,I)*YEITAP(K,I)
 208            CONTINUE
 205            CONTINUE
                DO 225 I=1,M2
                DO 220 K=2,M1
                W1s(K,I)=F1(K-1)*W1P(K,I)+(1.-F1(K-1))*W1P(K-1,I)
 220            CONTINUE
                W1s(1,I)=W1P(1,I)
 225            CONTINUE
                DO 230 K=1,M1
                DO 235 I=2,M2
                W2w(K,I)=F2(I-1)*W2P(K,I)+(1.-F2(I-1))*W2P(K,I-1)
 235            CONTINUE
                W2w(K,1)=W2P(K,1)
 230            CONTINUE
                Q=0.
                DO 300 I=1,M2
                Q=Q+(W1s(2,I))*DCETA(I)
 300            CONTINUE
                RETURN
                END
C===============================================================================
C
C               This is the main work in every iteration step
C
                SUBROUTINE BLACK(M)
                INCLUDE 'PARAMETERS.F'
                INCLUDE 'COMMONBLOCK.F'
                DIMENSION PP1PX1(M1,M2),PP1PX2(M1,M2)

C               calculate the coefficients of the momentum equation
                CALL COEFMO(1)

C               solve the momentume equation
                CALL SOLVE(AS,AN,AW,AE,AP,U,SU,1)
                CALL SOLVE(AS,AN,AW,AE,AP,V,SV,1)
                CALL BOUNDARY(V,X1,M1,1)
```

```
C       momentum interpolation
        DO 460 K=2,M1-1
        DO 465 I=2,M2-1
        BCDXSH=-1.*DEITA(K)*DCETA(I)*RRP(K,I)/AP(K,I)
        B1P(K,I)=BCDXSH*AFAP(K,I)
        C2P(K,I)=BCDXSH*GAMP(K,I)
465     CONTINUE
460     CONTINUE
        DO 470 K=2,M1-1
        DO 480 I=2,M2-1
        H1P(K,I)=U(K,I)*YCETAP(K,I)-V(K,I)*XCETAP(K,I)
     &          -B1P(K,I)*DPDX1(K,I)
        H2P(K,I)=V(K,I)*XEITAP(K,I)-U(K,I)*YEITAP(K,I)
     &          -C2P(K,I)*DPDX2(K,I)
480     CONTINUE
470     CONTINUE

C       interplation to get W1s and W2w
        DO 510 I=2,M2-1
        DO 505 K=3,M1-1
        B1s(K,I)=AFAs(K,I)*(-1.*DCETA(I)*(EITA(K)-EITA(K-1))
     &          *RRs(K,I))*( F1(K-1)/AP(K,I)+(1.-F1(K-1))/AP(K-1,I))
        W1s(K,I)=F1(K-1)*H1P(K,I)+(1.-F1(K-1))*H1P(K-1,I)+
     &          B1s(K,I)*(P(K,I)-P(K-1,I))/(EITA(K)-EITA(K-1))
505     CONTINUE
        W1s(M1,I)=U(M1,I)*YCETAP(M1,I)-V(M1,I)*XCETAP(M1,I)
        W1s(2,I)=U(1,I)*YCETAP(1,I)-V(1,I)*XCETAP(1,I)
510     CONTINUE
        DO 500 K=2,M1-1
        DO 520 I=3,M2-1
        C2w(K,I)=GAMw(K,I)*(-1.*DEITA(K)*(CETA(I)-CETA(I-1))
     &          *RRw(K,I))*( F2(I-1)/AP(K,I)+(1.-F2(I-1))/AP(K,I-1))
        W2w(K,I)=F2(I-1)*H2P(K,I)+(1.-F2(I-1))*H2P(K,I-1)+
     &          C2w(K,I)*(P(K,I)-P(K,I-1))/(CETA(I)-CETA(I-1))
520     CONTINUE
        W2w(K,2)=V(K,1)*XEITAP(K,1)-U(K,1)*YEITAP(K,1)
        W2w(K,M2)=V(K,M2)*XEITAP(K,M2)-U(K,M2)*YEITAP(K,M2)
500     CONTINUE

C       Check the convergency of computation----------
        DO 610 K=2,M1-1
        DO 615 I=2,M2-1
        SM(K,I)=(W1s(K,I)*RRs(K,I)-W1s(K+1,I)*RRs(K+1,I))*DCETA(I)+
     &          (W2w(K,I)*RRw(K,I)-W2w(K,I+1)*RRw(K,I+1))*DEITA(K)
615     CONTINUE
610     CONTINUE
        Q2=0.
        Q3=0.
        DO 450 K=2,M1-1
        Q22=0.
        Q33=0.
        DO 454 I=2,M2-1
        Q22=Q22+abs(SM(K,I))
```

```
                Q33=ABS(SM(K,I))
                IF(Q33.GT.Q3) THEN
                Q3=Q33
                KE3=K
                IE3=I
                END IF
 454            CONTINUE
                IF(ABS(Q22).GE.Q2) THEN
                Q2=ABS(Q22)
                KE2=K
                END IF
 450            CONTINUE
                E2=Q2
                E3=Q3
                IF(MOD(M,5).EQ.0) THEN
                WRITE(*,*)'      PHYSICAL TIME STEP NO.',NT
                write(*,10)M,E2,E3
                write(*,11)KE2,KE3,IE3
                END IF
 10             format(1x,' itr=',i4,'  E2=',f10.6,'  E3=',f11.7)
 11             format(1x,' KE2=',i4,'  KE3=',i4,'  IE3=',i4)

 C              Pressure correct procedure
                DO 620 K=2,M1-1
                DO 625 I=2,M2-1
                IF(ABS(REAL(K-2)).LT.0.1) THEN
                CS(K,I)=0.
                ELSE
                CS(K,I)=(-1.*B1s(K,I)*RRs(K,I)*DCETA(I))/(EITA(K)-EITA(K-1))
                END IF
                IF(ABS(REAL(K-M1+1)).LT.0.1) THEN
                CN(K,I)=0.
                ELSE
                CN(K,I)=(-1.*B1s(K+1,I)*RRs(K+1,I)*DCETA(I))/ (EITA(K+1)-EITA(K))
                END IF
                IF(ABS(REAL(I-2)).LT.0.1) THEN
                CW(K,I)=0.
                ELSE
                CW(K,I)=(-1.*C2w(K,I)*RRw(K,I)*DEITA(K))/ (CETA(I)-CETA(I-1))
                END IF
                IF(ABS(REAL(I-M2+1)).LT.0.1) THEN
                CE(K,I)=0.
                ELSE
                CE(K,I)=(-1.*C2w(K,I+1)*RRw(K,I+1)*DEITA(K))/ (CETA(I+1)-CETA(I))
                END IF
                CP(K,I)=CS(K,I)+CN(K,I)+CW(K,I)+CE(K,I)
 625            CONTINUE
 620            CONTINUE

 C              solve pressure correction equation
                DO 630 K=1,M1
                DO 635 I=1,M2
                P1(K,I)=0.
 635            CONTINUE
```

```
630         CONTINUE
            CALL SOLVE(CS,CN,CW,CE,CP,P1,SM,-1)
            CALL BOUNDARY(P1,X1,M1,1)
            CALL BOUNDARY(P1,X1,M1,2)
            CALL BOUNDARY(P1,X2,M2,3)
            CALL BOUNDARY(P1,X2,M2,4)

C           correction of velocity
            DO 660 I=1,M2
            DO 662 K=1,M1
            FX1(K)=P1(K,I)
662         CONTINUE
            CALL SPLINE(X1,FX1,AXM1,ADM1,M1)
            DO 664 K=1,M1
            PP1PX1(K,I)=AXM1(K)
664         CONTINUE
660         CONTINUE
            DO 665 K=1,M1
            DO 667 I=1,M2
            FX2(I)=P1(K,I)
667         CONTINUE
            CALL SPLINE(X2,FX2,AXM2,ADM2,M2)
            DO 669 I=1,M2
            PP1PX2(K,I)=AXM2(I)
669         CONTINUE
665         CONTINUE

C           as B1s(2,i)=C2w(k,2)=0, no correction can be made for W1s(2,I) and W2w(k,2)
C           in the following loop, so don't care maybe P1(K,1).NE.P1(K,2)
            DO 640 K=2,M1-1
            DO 645 I=2,M2-1
            BCDXSH=-1.*DEITA(K)*DCETA(I)*RRP(K,I)/AP(K,I)
            U(K,I)=U(K,I)+BCDXSH*( YCETAP(K,I)*PP1PX1(K,I)-
     &                             YEITAP(K,I)*PP1PX2(K,I) )
            V(K,I)=V(K,I)+BCDXSH*(-XCETAP(K,I)*PP1PX1(K,I)+
     &                             XEITAP(K,I)*PP1PX2(K,I) )
            W1s(K,I) =W1s(K,I)+B1s(K,I)*
     &                 (P1(K,I)-P1(K-1,I))/(EITA(K)-EITA(K-1))
            W2w(K,I)=W2w(K,I)+C2w(K,I)*
     &                 (P1(K,I)-P1(K,I-1))/(CETA(I)-CETA(I-1))
645         CONTINUE
640         CONTINUE
            CALL BOUNDARY(V,X1,M1,1)
            DO 650 I=1,M2
            W1s(M1,I)=U(M1,I)*YCETAP(M1,I)-V(M1,I)*XCETAP(M1,I)
            W1s(2,I)=U(1,I)*YCETAP(1,I)-V(1,I)*XCETAP(1,I)
650         CONTINUE
            DO 690 K=1,M1
            W2w(K,2)=V(K,1)*XEITAP(K,1)-U(K,1)*YEITAP(K,1)
            W2w(K,M2)=V(K,M2)*XEITAP(K,M2)-U(K,M2)*YEITAP(K,M2)
690         CONTINUE

C           correct the pressure field
            DO 700 K=2,M1-1
```

```
                DO 710 I=2,M2-1
                P(K,I)=P(K,I)+ALFAP*P1(K,I)
710             CONTINUE
700             CONTINUE
                CALL BOUNDARY(P,X1,M1,1)
                CALL BOUNDARY(P,X1,M1,2)
                CALL BOUNDARY(P,X2,M2,3)
                CALL BOUNDARY(P,X2,M2,4)
                PREF=P(M1,M2)
                DO 750 K=1,M1
                DO 780 I=1,M2
                P(K,I)=P(K,I)-PREF
780             CONTINUE
750             CONTINUE

C               solve T equation
                CALL COEFMO(2)
                CALL SOLVE(AS,AN,AW,AE,AP,T,ST,1)
                CALL BOUNDARY(T,X1,M1,1)
                CALL BOUNDARY(T,X1,M1,2)

C               solve Q equation
                CALL COEFMO(3)
                CALL SOLVE(AS,AN,AW,AE,AP,QU,SQU,-1)
                CALL BOUNDARY(QU,X1,M1,1)
                CALL BOUNDARY(QU,X2,M2,4)
                CALL BOUNDARY(QU,X1,M1,8)

C               solve FAI equation
                CALL COEFMO(4)
                CALL SOLVE(AS,AN,AW,AE,AP,FAI,SFAI,-1)
                CALL BOUNDARY(FAI,X1,M1,2)
                CALL BOUNDARY(FAI,X1,M1,1)

                IF(E2.LT.1.e-6.and.E3.LT.1.e-7.and.EKEQU.LT.0.1) THEN
                CONVEG=1.
                ELSE
                CONVEG=0.
                END IF

                RETURN
                END
C===============================================================================
C               THIS SUB TO CALCULATE THE COEFECIENTS OF MOMENTUEM EQ.
C.
                SUBROUTINE COEFMO(L)
                INCLUDE 'PARAMETERS.F'
                INCLUDE 'COMMONBLOCK.F'
C
                FUN1(X1,X2)=AMAX1(0.,X2-0.5*ABS(X1))+ AMAX1(-1.*X1,0.)
                FUN2(X1,X2)=AMAX1(0.,X2-0.5*ABS(X1))+ AMAX1(0.,X1)
                FUN3(X1)  =AMAX1(X1,0.)
                FUN4(X1)  =AMAX1(-1.*X1,0.)
C
```

```
      IF(L.EQ.1) DIFF=1./REYNOLDS
      IF(L.EQ.2) DIFF=1./REYNOLDS/PRANDTL
      IF(L.EQ.3) GOTO 999
      IF(L.EQ.4) GOTO 799

      DO 99 K=2,M1-1
      DO 100 I=2,M2-1
      FS=W1s(K,I)*RRs(K,I)*DCETA(I)
      DS=DIFF*AFAs(K,I)*RRs(K,I)/GHGs(K,I)*DCETA(I)/(EITA(K)-EITA(K-1))
      FN=W1s(K+1,I)*RRs(K+1,I)*DCETA(I)
      DN=DIFF*AFAs(K+1,I)*RRS(K+1,I)/GHGs(K+1,I)*DCETA(I)
     &     /(EITA(K+1)-EITA(K))
      FW=W2w(K,I)*RRw(K,I)*DEITA(K)
      DW=DIFF*GAMw(K,I)*RRw(K,I)/GHGw(K,I)*DEITA(K)
     &     /(CETA(I)-CETA(I-1))
      FE=W2w(K,I+1)*RRw(K,I+1)*DEITA(K)
      DE=DIFF*GAMw(K,I+1)*RRw(K,I+1)/GHGw(K,I+1)*DEITA(K)
     &     /(CETA(I+1)-CETA(I))
      AS(K,I)=FUN2(FS,DS)
      AN(K,I)=FUN1(FN,DN)
      AW(K,I)=FUN2(FW,DW)
      AE(K,I)=FUN1(FE,DE)
      AP(K,I)=( AS(K,I)+AN(K,I)+AW(K,I)+AE(K,I) )/ALFA
100   CONTINUE
99    CONTINUE

      CALL QIUBIANDAO(FAI,EX,EY,1)

      IF(L.EQ.1) THEN
      DO 200 I=1,M2
      DO 210 K=1,M1
      FX1(K)=P(K,I)
210   CONTINUE
      CALL SPLINE(X1,FX1,AXM1,ADM1,M1)
      DO 220 K=1,M1
      DPDX1(K,I)=AXM1(K)
220   CONTINUE
200   CONTINUE
      DO 250 K=1,M1
      DO 260 I=1,M2
      FX2(I)=P(K,I)
260   CONTINUE
      CALL SPLINE(X2,FX2,AXM2,ADM2,M2)
      DO 270 I=1,M2
      DPDX2(K,I)=AXM2(I)
270   CONTINUE
250   CONTINUE
      DO 300 I=1,M2
      DO 310 K=1,M1
      FX1(K)=U(K,I)
310   CONTINUE
      CALL SPLINE(X1,FX1,AXM1,ADM1,M1)
      DO 320 K=1,M1
      DUDX1(K,I)=AXM1(K)
```

```
320             CONTINUE
300             CONTINUE
                DO 350 K=1,M1
                DO 360 I=1,M2
                FX2(I)=U(K,I)
360             CONTINUE
                CALL SPLINE(X2,FX2,AXM2,ADM2,M2)
                DO 370 I=1,M2
                DUDX2(K,I)=AXM2(I)
370             CONTINUE
350             CONTINUE
                DO 400 I=1,M2
                DO 410 K=1,M1
                FX1(K)=V(K,I)
410             CONTINUE
                CALL SPLINE(X1,FX1,AXM1,ADM1,M1)
                DO 420 K=1,M1
                DVDX1(K,I)=AXM1(K)
420             CONTINUE
400             CONTINUE
                DO 450 K=1,M1
                DO 460 I=1,M2
                FX2(I)=V(K,I)
460             CONTINUE
                CALL SPLINE(X2,FX2,AXM2,ADM2,M2)
                DO 470 I=1,M2
                DVDX2(K,I)=AXM2(I)
470             CONTINUE
450             CONTINUE

                DO 500 K=2,M1-1
                DO 550 I=2,M2-1
                SU1=(-1.)*DEITA(K)*DCETA(I)*RRP(K,I)*
     &              ( YCETAP(K,I)*DPDX1(K,I)-YEITAP(K,I)*DPDX2(K,I) )
                SU2=DIFF/GHGs(K+1,I)*(-1.*BETs(K+1,I)*RRs(K+1,I))*DCETA(I)
     &              *( F1(K)*DUDX2(K+1,I)+(1.-F1(K))*DUDX2(K,I) )
     &              - DIFF/GHGs(K,I)*(-1.*BETs(K,I)*RRs(K,I))*DCETA(I)
     &              *( F1(K-1)*DUDX2(K,I)+(1.-F1(K-1))*DUDX2(K-1,I) )
     &              +DIFF/GHGw(K,I+1)*(-1.*BETw(K,I+1)*RRw(K,I+1))*DEITA(K)
     &              *( F2(I)*DUDX1(K,I+1)+(1.-F2(I))*DUDX1(K,I) )
     &               - DIFF/GHGw(K,I)*(-1.*BETw(K,I)*RRw(K,I))*DEITA(K)
     &               *( F2(I-1)*DUDX1(K,I)+(1.-F2(I-1))*DUDX1(K,I-1) )
                SU3=AP(K,I)*U(K,I)*(1.-ALFA)
                SU6=SE*QU(K,I)*EX(K,I)*GHGP(K,I)*DEITA(K)*DCETA(I)*RRP(K,I)
                IF(KOODIN.EQ.2) THEN
                SU7=(-1.)/REYNOLDS*U(K,I)/RRP(K,I)*DEITA(K)*DCETA(I)*GHGP(K,I)
                ELSE
                SU7=0.
                ENDIF
                SV1=(-1.)*DEITA(K)*DCETA(I)*RRP(K,I)*
     &              ( XEITAP(K,I)*DPDX2(K,I)-XCETAP(K,I)*DPDX1(K,I) )
                SV2=DIFF/GHGs(K+1,I)*(-1.*BETs(K+1,I)*RRs(K+1,I))*DCETA(I)
     &             *( F1(K)*DVDX2(K+1,I)+(1.-F1(K))*DVDX2(K,I) )
     &             - DIFF/GHGs(K,I)*(-1.*BETs(K,I)*RRs(K,I))*DCETA(I)
```

```
     &          *( F1(K-1)*DVDX2(K,I)+(1.-F1(K-1))*DVDX2(K-1,I) )
     &          + DIFF/GHGw(K,I+1)*(-1.*BETw(K,I+1)*RRw(K,I+1))*DEITA(K)
     &          *( F2(I)*DVDX1(K,I+1)+(1.-F2(I))*DVDX1(K,I) )
     &          - DIFF/GHGw(K,I)*(-1.*BETw(K,I)*RRw(K,I))*DEITA(K)
     &          *( F2(I-1)*DVDX1(K,I)+(1.-F2(I-1))*DVDX1(K,I-1) )
                SV3=AP(K,I)*V(K,I)*(1.-ALFA)
                SV4=GRASHOF/REYNOLDS**2*T(K,I)
     &          *GHGP(K,I)*DEITA(K)*DCETA(I)*RRP(K,I)
                SV6=SE*QU(K,I)*EY(K,I)*GHGP(K,I)*DEITA(K)*DCETA(I)*RRP(K,I)
                SU(K,I)=SU1+SU2+SU3+SU4+SU5+SU6+SU7
                SV(K,I)=SV1+SV2+SV3+SV4+SV5+SV6
550             CONTINUE
500             CONTINUE
                ENDIF

                IF(L.EQ.2) THEN
600             DO 601 I=1,M2
                DO 610 K=1,M1
                FX1(K)=T(K,I)
610             CONTINUE
                CALL SPLINE(X1,FX1,AXM1,ADM1,M1)
                DO 620 K=1,M1
                DTDX1(K,I)=AXM1(K)
620             CONTINUE
601             CONTINUE
                DO 650 K=1,M1
                DO 660 I=1,M2
                FX2(I)=T(K,I)
660             CONTINUE
                CALL SPLINE(X2,FX2,AXM2,ADM2,M2)
                DO 670 I=1,M2
                DTDX2(K,I)=AXM2(I)
670             CONTINUE
650             CONTINUE
                DO 680 K=2,M1-1
                DO 685 I=2,M2-1
                ST2=DIFF/GHGs(K+1,I)*(-1.*BETs(K+1,I)*RRs(K+1,I))*DCETA(I)
     &          *( F1(K)*DTDX2(K+1,I)+(1.-F1(K))*DTDX2(K,I) )
     &          - DIFF/GHGs(K,I)*(-1.*BETs(K,I)*RRs(K,I))*DCETA(I)
     &          *( F1(K-1)*DTDX2(K,I)+(1.-F1(K-1))*DTDX2(K-1,I) )
     &          + DIFF/GHGw(K,I+1)*(-1.*BETw(K,I+1)*RRw(K,I+1))*DEITA(K)
     &          *( F2(I)*DTDX1(K,I+1)+(1.-F2(I))*DTDX1(K,I) )
     &          - DIFF/GHGw(K,I)*(-1.*BETw(K,I)*RRw(K,I))*DEITA(K)
     &          *( F2(I-1)*DTDX1(K,I)+(1.-F2(I-1))*DTDX1(K,I-1) )
                ST3=AP(K,I)*T(K,I)*(1.-ALFA)
                ST6=SE*EC*QU(K,I)*(U(K,I)*EX(K,I)+V(K,I)*EY(K,I)+
     &          (EX(K,I)**2+EY(K,I)**2)/(REYNOLDS*PRE))
     &          *GHGP(K,I)*DEITA(K)*DCETA(I)*RRP(K,I)
                ST(K,I)=ST2+ST3+ST5+ST6
685             CONTINUE
680             CONTINUE
                ENDIF
                RETURN
```

```
C       calculate the coefficients of QU equation
999     DO 2205 K=1,M1
        DO 2208 I=1,M2
        EEITAP(K,I)=EX(K,I)*YCETAP(K,I)-EY(K,I)*XCETAP(K,I)
        ECETAP(K,I)=EY(K,I)*XEITAP(K,I)-EX(K,I)*YEITAP(K,I)
2208    CONTINUE
2205    CONTINUE
        DO 2900 I=1,M2
        DO 2905 K=2,M1
        EEITAs(K,I)=F1(K-1)*EEITAP(K,I)+(1.-F1(K-1))*EEITAP(K-1,I)
2905    CONTINUE
        EEITAs(1,I)=EEITAP(1,I)
2900    CONTINUE
        DO 2910 K=1,M1
        DO 2915 I=2,M2
        ECETAw(K,I)=F2(I-1)*ECETAP(K,I)+(1.-F2(I-1))*ECETAP(K,I-1)
2915    CONTINUE
        ECETAw(K,1)=ECETAP(K,1)
2910    CONTINUE
        DO 2099 K=2,M1-1
        DO 2100 I=2,M2-1
        FS=RRs(K,I)*(W1s(K,I)+1./(REYNOLDS*PRE)*EEITAs(K,I))*DCETA(I)
        FN=RRs(K+1,I)*(W1s(K+1,I)+1./(REYNOLDS*PRE)*EEITAs(K+1,I)) *DCETA(I)
        FW=RRw(K,I)*(W2w(K,I)+1./(REYNOLDS*PRE)*ECETAw(K,I))*DEITA(K)
        FE=RRw(K,I+1)*(W2w(K,I+1)+1./(REYNOLDS*PRE)*ECETAw(K,I+1))
     &     *DEITA(K)
        AS(K,I)=FUN3(FS)
        AN(K,I)=FUN4(FN)
        AW(K,I)=FUN3(FW)
        AE(K,I)=FUN4(FE)
        IF(K.EQ.2) AS(K,I)=0.
        IF(K.EQ.(M1-1)) AN(K,I)=0.
        IF(I.EQ.(M2-1)) AE(K,I)=0.
        AP(K,I)=( AS(K,I)+AN(K,I)+AW(K,I)+AE(K,I)+(FN-FS+FE-FW))/ALFAQU
2100    CONTINUE
2099    CONTINUE
        DO 780 K=2,M1-1
        DO 785 I=2,M2-1
        SQU3=AP(K,I)*QU(K,I)*(1.-ALFAQU)
        SQU(K,I)=SQU3
785     CONTINUE
780     CONTINUE
        RETURN

C       coefficients of FAI equation
799     DO 899 K=2,M1-1
        DO 900 I=2,M2-1
        AS(K,I)=RRs(K,I)*AFAs(K,I)/GHGs(K,I)*DCETA(I)/(EITA(K)-EITA(K-1))
        AN(K,I)=RRs(K+1,I)*AFAs(K+1,I)/GHGs(K+1,I)*DCETA(I)
     &          /(EITA(K+1)-EITA(K))
        AW(K,I)=RRw(K,I)*GAMw(K,I)/GHGw(K,I)*DEITA(K)/ (CETA(I)-CETA(I-1))
        AE(K,I)=RRw(K,I+1)*GAMw(K,I+1)/GHGw(K,I+1)*DEITA(K)
     &          /(CETA(I+1)-CETA(I))
        AP(K,I)=( AS(K,I)+AN(K,I)+AW(K,I)+AE(K,I) )/ALFAFAI
```

```
900         CONTINUE
899         CONTINUE
            DO 1500 I=1,M2
            DO 1510 K=1,M1
            FX1(K)=FAI(K,I)
1510        CONTINUE
            CALL SPLINE(X1,FX1,AXM1,ADM1,M1)
            DO 1520 K=1,M1
            DFAIDX1(K,I)=AXM1(K)
1520        CONTINUE
1500        CONTINUE
            DO 1550 K=1,M1
            DO 1560 I=1,M2
            FX2(I)=FAI(K,I)
1560        CONTINUE
            CALL SPLINE(X2,FX2,AXM2,ADM2,M2)
            DO 1570 I=1,M2
            DFAIDX2(K,I)=AXM2(I)
1570        CONTINUE
1550        CONTINUE
            DO 1900 I=1,M2
            DO 1905 K=2,M1
            DFAIDX2s(K,I)=F1(K-1)*DFAIDX2(K,I)+(1.-F1(K-1))*DFAIDX2(K-1,I)
1905        CONTINUE
            DFAIDX2s(1,I)=DFAIDX2(1,I)
1900        CONTINUE
            DO 1910 K=1,M1
            DO 1915 I=2,M2
            DFAIDX1w(K,I)=F2(I-1)*DFAIDX1(K,I)+(1.-F2(I-1))*DFAIDX1(K,I-1)
1915        CONTINUE
            DFAIDX1w(K,1)=DFAIDX1(K,1)
1910        CONTINUE
            DO 1780 K=2,M1-1
            DO 1785 I=2,M2-1
            SFAI2= ANE*QU(K,I)*GHGP(K,I)*RRP(K,I)*DEITA(K)*DCETA(I)
            SFAI3=-BETs(K+1,I)*RRs(K+1,I)/GHGs(K+1,I)*DCETA(I)*
     &            DFAIDX2s(K+1,I)+ BETs(K,I)*RRs(K,I)/GHGs(K,I)*
     &            DCETA(I)*DFAIDX2s(K,I)-BETw(K,I+1)*RRw(K,I+1)/
     &            GHGw(K,I+1)*DEITA(K)*DFAIDX1w(K,I+1)+ BETw(K,I)*
     &            RRw(K,I)/GHGw(K,I)*DEITA(K)*DFAIDX1w(K,I)
            SFAI4=AP(K,I)*FAI(K,I)*(1.-ALFAFAI)
            SFAI(K,I)=SFAI2+SFAI3+SFAI4
1785        CONTINUE
1780        CONTINUE
C           WRITE(*,*)'HELLO'
            RETURN
            END
C=============================================================================
C
C           This subroutine solve algebraic equations by using ADI method
C
            SUBROUTINE SOLVE(CS,CN,CW,CE,CP,FY,SFY,L)
            INCLUDE 'PARAMETERS.F'
            DIMENSION CS(M1,M2),CN(M1,M2),CW(M1,M2),CE(M1,M2),CP(M1,M2),
```

```
     &          FY(M1,M2),SFY(M1,M2),FY1(M1,M2),
     &          A(1000),B(1000),C(1000),D(1000),PP(1000),Q(1000)

                NN=5
                IF(ABS(REAL(L+1)).LT.0.1) NN=10
                DO 50 K=1,M1
                DO 55 I=1,M2
                FY1(K,I)=FY(K,I)
55              CONTINUE
50              CONTINUE
                DO 1000 N=1,NN
                DO 100 I=2,M2-1
                DO 110 K=2,M1-1
                A(K)=CP(K,I)
                B(K)=CN(K,I)
                C(K)=CS(K,I)
                D(K)=CE(K,I)*FY(K,I+1)+CW(K,I)*FY(K,I-1)+SFY(K,I)
110             CONTINUE
                D(2)=D(2)+C(2)*FY(2-1,I)
                PP(2)=B(2)/A(2)
                Q(2)=D(2)/A(2)
                DO 120 K=2+1,M1-1
                PP(K)=B(K)/(A(K)-C(K)*PP(K-1))
                Q(K)=(D(K)+C(K)*Q(K-1))/(A(K)-C(K)*PP(K-1))
120             CONTINUE
                DO 130 K=M1-1,2,-1
                FY1(K,I)=PP(K)*FY1(K+1,I)+Q(K)
130             CONTINUE
100             CONTINUE
                DO 200 K=2,M1-1
                DO 210 I=2,M2-1
                A(I)=CP(K,I)
                B(I)=CE(K,I)
                C(I)=CW(K,I)
                D(I)=CS(K,I)*FY1(K-1,I)+CN(K,I)*FY1(K+1,I)+SFY(K,I)
210             CONTINUE
                D(2)=D(2)+C(2)*FY1(K,1)
                PP(2)=B(2)/A(2)
                Q(2)=D(2)/A(2)
                DO 220 I=3,M2-1
                PP(I)=B(I)/(A(I)-C(I)*PP(I-1))
                Q(I)=(D(I)+C(I)*Q(I-1))/(A(I)-C(I)*PP(I-1))
220             CONTINUE
                DO 230 I=M2-1,2,-1
                FY(K,I)=PP(I)*FY(K,I+1)+Q(I)
230             CONTINUE
200             CONTINUE
1000            CONTINUE
                RETURN
                END
C===============================================================================
C
C               this sub treat the boundary conditions
C
```

```
      SUBROUTINE BOUNDARY(FY,XX,NN,L)
      INCLUDE 'PARAMETERS.F'
      DIMENSION FY(M1,M2),XX(1000)

C     expolation boundary 1
      IF(L.EQ.1) THEN
      DO 100 I=1,M2
      FY(1,I)=FY(3,I)-(FY(3,I)-FY(2,I))/(XX(3)-XX(2))*(XX(3)-XX(1))
100   CONTINUE
      END IF

C     expolation boundary 2
      IF(L.EQ.2) THEN
      DO 200 I=1,M2
      FY(M1,I)=FY(M1-2,I)+(FY(M1-1,I)-FY(M1-2,I))
     &          /(XX(M1-1)-XX(M1-2))*(XX(M1)-XX(M1-2))
      FY(M1,I)=FY(M1-1,I)
200   CONTINUE
      END IF

C     expolation boundary 3
      IF(L.EQ.3) THEN
      DO 300 K=1,M1
      FY(K,1)=FY(K,3)-(FY(K,3)-FY(K,2))/ (XX(3)-XX(2))*(XX(3)-XX(1))
300   CONTINUE
      END IF

C     expolation boundary 1
      IF(L.EQ.4) THEN
      DO 400 K=1,M1
      FY(K,M2)=FY(K,M2-2)+(FY(K,M2-1)-FY(K,M2-2))
     &          /(XX(M2-1)-XX(M2-2))*(XX(M2)-XX(M2-2))
400   CONTINUE
      END IF

C     in case of 1 and 2 are adiabatic
      IF(L.EQ.6) THEN
      DO 600 I=1,M2
      FY(1,I)=FY(2,I)
      FY(M1,I)=FY(M1-1,I)
600   CONTINUE
      END IF

C     expolation boundary 4
      IF(L.EQ.7) THEN
      DO 700 K=1,M1
      FY(K,M2)=FY(K,M2-2)+(FY(K,M2-1)-FY(K,M2-2))
     &          /(XX(M2-1)-XX(M2-2))*(XX(M2)-XX(M2-2))
700   CONTINUE
      END IF

      IF(L.EQ.8) THEN
      DO 800 I=1,M2
      FY(1,I)=FY(2,I)
```

```
                FY(M1,I)=FY(M1-1,I)
 800            CONTINUE
                END IF

                RETURN
                END
C=======================================================================
C
C               This sub writes out the output results
C
                SUBROUTINE OUTPUT
                INCLUDE 'PARAMETERS.F'
                INCLUDE 'COMMONBLOCK.F'

C               IF YOU WANT TO RECOVER THE DIMENSIONS OF VARIABLES, YOU CAN
C               DO IT HERE YOU CAN ALSO DO IT LATER IF YOU HAVE NOT THE
C               "REF_MAYBE" VALUES IN THE 'PARAMETERS.F', THEN YOU SHOULD
C               MAKE THE FOLLOWING"DO 100 --- CONTINUE" AS COMMENTS
C
                OPEN(UNIT=2,FILE='RESULTS.PLT')
                WRITE(2,*)'TITLE="1"'
                WRITE(2,*)'VARIABLES="X","Y","U","V","P","T","QU","FAI","EX","EY"'
                WRITE(2,*)'Zone T="1",I=',M2,', J=',M1
                WRITE(2,15)((X(K,I),Y(K,I),U(K,I),V(K,I),P(K,I),T(K,I),
   &                        QU(K,I),FAI(K,I),EX(K,I),EY(K,I),I=1,M2),K=1,M1)
                CLOSE(2)
 10             FORMAT(1X,8E16.8)
 15             FORMAT(1X,10e16.8)
                RETURN
                END
```